Turbocharger performance and surge definition on a steady flow turbocharger test stand

Duda, Tomasz

Award date:
2017

Awarding institution:
University of Bath

Turbocharger performance and surge definition on a steady flow turbocharger test stand

PhD thesis
submitted by
Tomasz Lukasz Duda
of the
University of Bath
Department of Mechanical Engineering
August 2017

Supervisors: Dr Colin Copeland, Prof. Chris Brace

Table of Contents

List of Figures

List of Tables

Acknowledgements

I would like to express my deepest acknowledgements to my supervisor Dr Colin Copeland who was always there for me when I needed his help. I do not imagine going this long route without his enthusiasm, patience, understanding and motivation. I wish him all the best in his future professional career and lots of happiness in personal life.

I also thank my second supervisor Prof. Chris Brace for being a wonderful mentor and for giving me an opportunity to join Powertrain and Vehicle Research Centre at University of Bath. For many reasons he is a person I have greatly admired.

I am grateful to all my colleagues and co-workers I was honoured to work with, namely Richard Burke, Robert Gusthart, James Cansell, Tom Holley, James Burge, Calogero Avola, Pavlos Dimitriou, Ramkumar Vijayakumar, Huayin Tang, Nic Zhang.

I dedicate this dissertation to the memory of my dad Czeslaw, my amazing wife Anna and mum Teresa. I am sure this could have not been possible without their continual support.

Abstract

Turbocharger performance maps are vital components used in an engine-turbocharger matching process, a 1D engine performance development stage and a day-to-day operation of a turbocharged vehicle. The main aim of this thesis is the investigation of the turbocharger compressor performance when operating with an alternative to air substitute gas. This occurs, for instance, when turbocharging and low pressure exhaust gas recirculation (LP EGR) technologies are combined.

To conduct the experimental study of the turbocharger performance with substitute gas a steady-state turbocharger test facility with a compressor closed-loop mode has been designed and built within this thesis by the author. Also, for the most accurate performance map determination an uncertainty analysis of a selected turbocharger performance map and an extensive study on surge have also been carried out.

The sensor based uncertainty analysis has been a key aspect to help to understand the links between the accuracy of measured quantities and the overall uncertainty of the performance parameters. Such knowledge allowed for a selection of sensors targeting the most accurate data measurement. While investigating the uncertainty of the turbocharger performance maps heat transfer related efficiency uncertainty was also studied. Namely, a series of a semi-adiabatic tests were performed in the low turbocharger speed region which highlighted the issues related to a work and heat transfer separation and uncertainty of the extrapolated performance data. Also, a contribution to the turbocharger heat transfer modelling has been made by supporting the in-house lumped capacitance thermal node model with the 3D CHT (conjugate heat transfer) simulations [1, 2]. Finally, a study of a literature based compressor heat estimation method was performed as an alternative way of separating work and heat transfer (with low speed adiabatic mapping).

The experimental surge study was conducted in phases and included the analysis and comparison of the low and high frequency pressure data gathered at various locations downstream and upstream from the compressor and temperature data collected at close distance from impeller eye. It has been concluded that the post-compressor located pressure measurement is preferable (than the pre-compressor pressure measurement) as the FFT (Fast Fourier Transform) magnitude of the peak frequency associated with surge is independent on the distance of the sensor from the compressor. The useage of the temperature sensor installed at the closest distance from the compressor entry allowed an observation of the near surge temperature rise (a result of the air recirculation). However, due to the inconsistent rate of the temperature rise across the various speed lines along with the poor response it offers no benefit from the surge avoidance point of view. The comparison of the available surge metrics revealed that the resultant surge lines were drawn at different operating points especially at the higher turbocharger speed lines where the surge development investigated by the rise of the

low frequency FFT magnitude peaks was much more visible. The experimental tests performed in steady-state and pulsating flow conditions have indicated larger surge margin availability for the latter case [3].

Development of a turbocharger rig and gaining the confidence in turbocharger performance map generation allowed the author to carry out the investigation over compressor performance with a substitute gas. The study covered two cases of homogeneous and non-homogeneous gas introduction representing a well and a poorly mixed gases respectively. The substitute gas included various mixtures of CO2 and air and pure CO2. It has been highlighted that when comparing turbomachinery performance maps working with substitute gas non-dimensional speed and mass flow parameters shall be introduced. These parameters allow for the map corrections with respect to individual gas constant (R) and ratio of specific heats (γ). The experimentally obtained compressor performance maps with low CO2 concentration in CO2-air mixtures (3%, 5% and 10%) were successfully corrected with the use of non-dimensional speed and mass flow parameters. However, the compressor performance map obtained for the pure CO2 has revealed significant offsets in pressure ratio, efficiency, surge and choke flow locations. This is due to a significantly different γ. In the attempt of the further performance correction a method proposed by Roberts and Sjolander has been followed. As a result of such, a poor match between the measured and predicted values of compressor efficiency was achieved (n exponent = 0.8). A closer correlation was obtained if the n exponent was made a speed dependent variable. This observation has suggested that the measurement of compressor efficiency was affected by the heat transfer between the uninsulated turbomachinery components. Due to the time limitations this assertion has not been investigated experimentally. Realising this limitation, therefore, a series of adiabatic CFD simulations have been performed instead. These simulations have shown that for the case of pure CO2 a reasonable match between the simulated and predicted values of efficiency and pressure ratio was achieved. The experimental and numerical comparison of the compressor performance for homogeneously and non-homogeneously introduced substitute gas did not show any significant compressor performance changes. Finally, experimental study of selected configurations of the intake pipework and EGR mixing valve has shown that complex flow regimes can be developed within the LP EGR system affecting the compressor's surge margin, efficiency and width of the map. This demonstrates that the aerodynamic disturbances of an EGR mixing valve may have the largest influence on the compressor map compared to all other factors.

Abbreviations

ASME	American Society of Mechanical Engineers	NEDC	New European Drive Cycle
CA	Charge Air	NOx	Nitrogen Oxides
CBV	Compressor Back-Pressure Valve	NRV	Non-Return Valve
CFD	Computational Fluid Dynamics	NVH	Noise, Vibration, Harshness
CHT	Conjugate Heat Transfer	OEM	Original Equipment Manufacturer
CMV	Compressor Mass Air Flow Valve	PC	Personal Computer
CVND	Conventional Vaned Diffuser	PDE	Partial Differential Equation
DFT	Discrete Fourier Transform	PR	Pressure Ratio
DPF	Diesel Particulate Filter	RANS	Reynolds-Averaged Navier-Stokes
ECU	Electronic Control Unit	RSP	Rotor Speed Parameter
EVM	Eddy Viscosity Model	RSS	Root Sum Squared
FFT	Fast Fourier Transform	RST	Reynolds Stress Transport
FT	Fourier Transform	SAA	Same As Above
FVM	Finite Volume Method	SAE	Society of Automotive Engineers
HP EGR	High Pressure Exhaust Gas Recirculation	TIT	Turbine Inlet Temperature
HTM	Heat Transfer Model	VG	Variable Geometry
HTT	Honeywell Turbo Technologies	VGT	Variable Geometry Turbine
IGV	Inlet Guide Vanes	VIGV	Variable Inlet Guide Vanes
LP EGR	Low Pressure Exhaust Gas Recirculation	VNL	Vaneless Diffuser
LSVD	Low Solidity Vaned Diffuser	VNT	Variable Nozzle Turbine
MAF	Mass Air Flow Sensor	VTC	Variable Trim Compressor
MWE	Map Width Enhancement		

Nomenclature

Roman symbols

a	Reynolds independent losses	[/]
A_1	Compressor inlet cross section area	$[m^2]$
A_2	Compressor outlet cross section area	$[m^2]$
A_3	Turbine inlet cross section area	$[m^2]$
C_d	V-cone flowmeter coefficient	[/]
$c_{p,int}$	Specific heat of intake air	$[\frac{J}{kgK}]$
$c_{p,ex}$	Specific heat of exhaust gas	$[\frac{J}{kgK}]$
$c_{p,mix}$	Specific heat of a mixture of gases	$[\frac{J}{kgK}]$
$c_{p_{c,1}}$	Compressor inlet specific heat of air	$[\frac{J}{kgK}]$
$c_{p_{c,2}}$	Compressor outlet specific heat of air	$[\frac{J}{kgK}]$
$c_{p_{c,avg}}$	Average compressor specific heat of air	$[\frac{J}{kgK}]$
$c_{p_{t,3}}$	Turbine inlet specific heat of air	$[\frac{J}{kgK}]$
$c_{p_{t,4}}$	Turbine outlet specific heat of air	$[\frac{J}{kgK}]$
$c_{p_{t,avg}}$	Average turbine specific heat of air	$[\frac{J}{kgK}]$
D	Compressor impeller diameter	$[m]$
D_c	Compressor impeller tip diameter	$[m]$
D_t	Turbine rotor tip diameter	$[m]$
d_1	Compressor inlet internal pipe diameter	$[m]$
d_2	Compressor outlet internal pipe diameter	$[m]$
d_3	Turbine inlet internal pipe diameter	$[m]$
d_4	Turbine outlet internal pipe diameter	$[m]$
E	Total energy per unit mass	$[\frac{J}{kg}]$
$f_{1,2,3}$	Density correction factors	[/]
F_a	V-cone specific material thermal expansion factor	[/]
$\boldsymbol{f_b}$	The resultant of gravity and centrifugal forces per unit volume acting on the continuum	$[\frac{m}{s^2}]$
f_s	Sampling rate	$[Hz]$
k_1	V-cone flow constant	$[\sqrt{\frac{kgm^3}{s^2mbar}}]$
$\dot{m}_{air}$	Air mass flow rate	$[\frac{kg}{s}]$

$\dot{m}_c$	Compressor actual mass flow rate of air	$[\frac{kg}{s}]$
$\dot{m}_{c,cor}$	Compressor corrected mass flow	$[\frac{kg}{s}]$
$\dot{m}_{ex}$	Exhaust gas mass flow rate	$[\frac{kg}{s}]$
$\dot{m}_t$	Turbine actual mass flow rate of air	$[\frac{kg}{s}]$
$\dot{m}_{t,cor}$	Turbine corrected mass flow	$[\frac{kg}{s}]$
M_{air}	Molar mass of air	$[\frac{kg}{mol}]$
M_{co2}	Molar mass of CO2	$[\frac{kg}{mol}]$
M_{mix}	Molar mass of a mixture of gases	$[\frac{kg}{mol}]$
MFP	Mass flow parameter	$[\frac{kg}{s}\frac{\sqrt{K}}{kPa}]$
N	Engine speed	$[rpm]$
N_{act}	Turbocharger actual rotational speed	$[rpm]$
$N_{c,cor}$	Compressor corrected speed	$[rpm]$
$N_{t,cor}$	Turbine corrected speed	$[rpm]$
$NDMP$	Non-dimensional mass flow parameter	$[\frac{\frac{kg}{s}\sqrt{\frac{J}{kg}}}{Pa}]$
$NDSP$	Non-dimensional speed parameter	$[\frac{rpm}{\sqrt{\frac{J}{kg}}}]$
P	Pressure	$[Pa]$
P_{1s}	Pneumatically averaged compressor static inlet pressure	$[Pa]$
P_{2s}	Pneumatically averaged compressor static outlet pressure	$[Pa]$
P_{3s}	Pneumatically averaged turbine static inlet pressure	$[Pa]$
P_{4s}	Pneumatically averaged turbine static outlet pressure	$[Pa]$
P_{1t}	Compressor total inlet pressure	$[Pa]$
P_{2t}	Compressor total outlet pressure	$[Pa]$
P_{3t}	Turbine total inlet pressure	$[Pa]$
P_c	Compressor power	$[W]$
P_f	Turbocharger friction loss	$[W]$
P_t	Turbine power	$[W]$
PR_c	Compressor total-to-total pressure ratio	[/]
PR_t	Turbine total-to static pressure ratio	[/]
P_{cv1s}	Static pressure at the compressor mass flow meter entry	$[Pa]$
P_{tv3s}	Static pressure at the turbine mass flow meter entry	$[Pa]$
P_{ref}	Reference static pressure	$[Pa]$

Q	Total heat	$[W]$
$\dot{q}$	Heat flux	$[\frac{W}{m^2}]$
$\dot{Q}_c$	Compressor actual volumetric flow rate of air	$[\frac{m^3}{s}]$
$\dot{Q}_t$	Turbine actual volumetric flow rate of air	$[\frac{m^3}{s}]$
R	Individual gas constant	$[\frac{J}{kgK}]$
R_a	Actual individual gas constant	$[\frac{J}{kgK}]$
R_{mix}	Individual gas constant of a mixture of gases	$[\frac{J}{kgK}]$
R_{ref}	Reference gas constant	$[\frac{J}{kgK}]$
R_u	Universal gas constant	$[\frac{J}{molK}]$
Re	Reynolds number	[/]
Re_{ref}	Reference gas Reynolds number	[/]
$\boldsymbol{S}$	Strain tensor	$[\frac{N}{m^2}]$
SG	Specific gravity	[/]
S_E	Energy source per unit volume	$[\frac{J}{m^3}]$
SG_{co2}	Specific gravity of CO2	[/]
SP	Speed parameter	$[\frac{rpm}{\sqrt{K}}]$
$\boldsymbol{T}$	Viscous stress tensor	$[\frac{N}{m^2}]$
T_{2is}	Compressor isentropic outlet temperature	$[K]$
T_{1s}	Mathematically averaged compressor static inlet temperature	$[K]$
T_{2s}	Mathematically averaged compressor static outlet temperature	$[K]$
T_{3s}	Mathematically averaged turbine static inlet temperature	$[K]$
T_{4s}	Mathematically averaged turbine static outlet temperature	$[K]$
T_{1t}	Compressor inlet total temperature	$[K]$
T_{2t}	Compressor outlet total temperature	$[K]$
T_{3t}	Turbine inlet total temperature	$[K]$
T_{cv1s}	Static temperature at the compressor mass flow meter entry	$[K]$
T_{tv3s}	Static temperature at the turbine mass flow meter entry	$[K]$
T_{ref}	Reference temperature	$[K]$
U/C_s	Turbine blade speed ratio	[/]
$\boldsymbol{V}$	Continuum velocity	$[\frac{m}{s}]$
V_1	Compressor inlet gas velocity	$[\frac{m}{s}]$

V_2	Compressor outlet gas velocity	$[\frac{m}{s}]$
V_3	Turbine inlet gas velocity	$[\frac{m}{s}]$
V_{sw}	Engine swept volume	$[m^3]$
w	Mass fraction	[/]
y	Molar fraction	[/]
Y_{cv1}	Compressor V-cone gas expansion factor	[/]
Y_{tv3}	Turbine V-cone gas expansion factor	[/]
ΔP	Differential pressure across V-cone	$[mbar]$

Greek symbols

α_A	Compression heat transfer area partition parameter	[/]
γ_a	Actual ratio of specific heats	[/]
γ_{air}	Ratio of specific heats for intake air	[/]
γ_{ex}	Ratio of specific heats for exhaust gas	[/]
$\gamma_{c,1}$	Compressor inlet ratio of specific heats	[/]
$\gamma_{c,2}$	Compressor outlet ratio of specific heats	[/]
$\gamma_{c,avg}$	Compressor average ratio of specific heats	[/]
γ_{mix}	Ratio of specific heats for the mixture of gases	[/]
γ_{ref}	Reference ratio of specific heats	[/]
$\gamma_{t,3}$	Turbine inlet ratio of specific heats	[/]
$\gamma_{t,4}$	Turbine outlet ratio of specific heats	[/]
$\gamma_{t,avg}$	Turbine average ratio of specific heats	[/]
ε	Turbulence dissipation rate	$[\frac{J}{kgs}]$
η_c	Compressor isentropic efficiency	[/]
η_{ref}	Reference compressor isentropic efficiency	[/]
η_t	Turbine isentropic efficiency	[/]
η_{vol}	Engine volumetric efficiency	[/]
κ	Turbulence kinetic energy	$[\frac{J}{kg}]$
λ	Friction factor for fully turbulent pipe flow	[/]
λ_{ref}	Friction factor for a hydraulically rough pipe flow	[/]
ρ_1	Compressor inlet gas density	$[\frac{kg}{m^3}]$
ρ_2	Compressor outlet gas density	$[\frac{kg}{m^3}]$
ρ_3	Turbine inlet gas density	$[\frac{kg}{m^3}]$

ρ_{air}	Density of air	$[\frac{kg}{m^3}]$
ρ_{co2}	Density of CO2	$[\frac{kg}{m^3}]$
ρ_{cv1}	Compressor V-cone entry gas density	$[\frac{kg}{m^3}]$
ρ_{tv3}	Turbine V-cone entry gas density	$[\frac{kg}{m^3}]$
ρ_m	Intake manifold gas density	$[\frac{kg}{m^3}]$
σ	Compressor slip factor	[/]
$\boldsymbol{\sigma}$	Stress tensor (sum of normal stresses and shear stresses)	[Pa]

Non-Greek symbols

$\otimes$	The Kronecker product
∇	Nabla operator

Constants

P_{ref}	Reference pressure	$100.000\ [Pa]$
R_u	Universal gas constant	$8.3144598\ [\frac{J}{molK}]$
T_{ref}	Reference temperature	$298\ [K]$ (compressors), $873\ K$ (turbines)

1. Introduction and fundamentals

This chapter is an introduction to turbocharging fundamentals which will be referred to within this dissertation.

1.1 Turbocharging

The key aim of the automotive turbocharger is to increase the amount of air that is delivered to the internal combustion engine. More air in the cylinders means that more fuel may be burned and more power and torque generated when compared to the equivalent naturally aspirated engine. The turbocharged engine also benefits from increased volumetric efficiency since the exhaust energy is utilised and not wasted. The turbocharger is a forced induction device and consists of three basic components – a radial wheel turbine (or axial turbine for heavy duty/ high mass flow applications), a radial wheel compressor and a common shaft supported by bearings and enclosed within a bearing housing (Figure 1-1). The turbine is bolted to an exhaust manifold and extracts energy from the exhaust gas released at engine's cylinders during the exhaust stroke. The compressor (driven by the turbine and connected to the compressor by the shaft) draws in ambient air and compresses it to a higher pressure before it enters the intake manifold. As the compression of air also results with the temperature rise, an intercooler is introduced downstream from the compressor to cool the air down and thus increase its density (Figure 1-2).

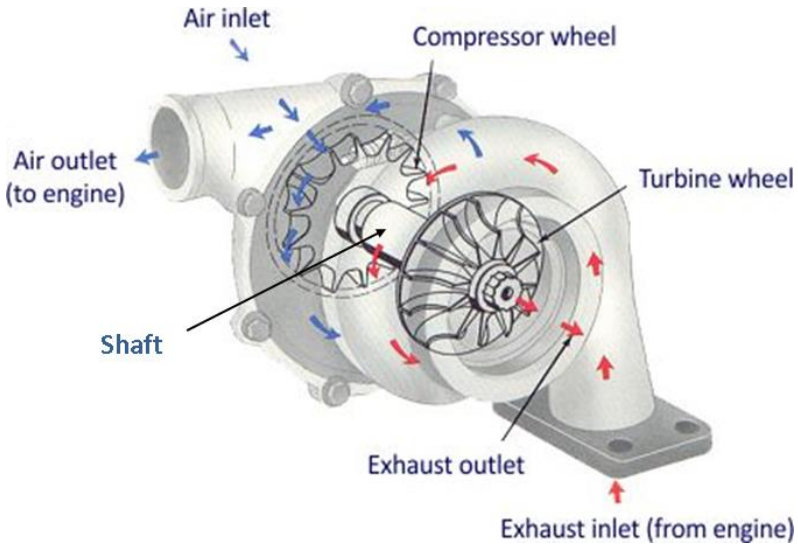

Figure 1-1. Typical automotive turbocharger [4]

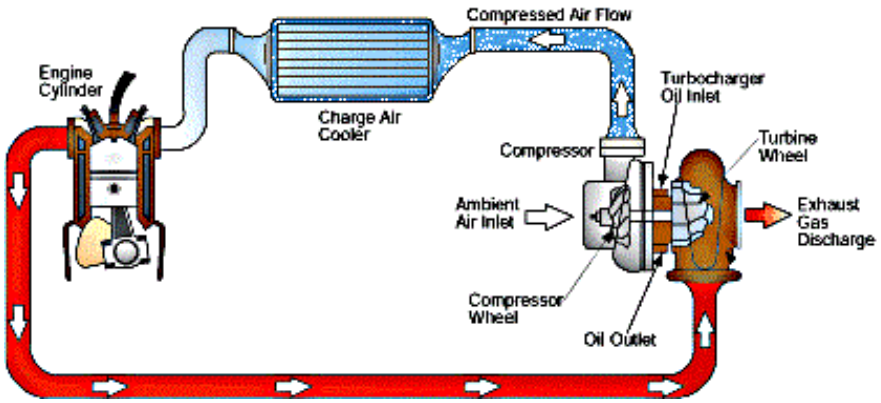

Figure 1-2. On-engine boosting system [5]

1.2 Turbocharger performance

Turbocharger turbine and compressor operation is characterised using performance maps that are generated as a result of steady-state mapping activity, carried out by turbocharger manufacturers at their test facilities. These maps are then delivered to powertrain OEM's along with the hardware. The maps are further used during turbocharger-engine matching activities, 1D wave-action engine simulations at a development stage and finally in everyday use of a turbocharged vehicle (data encoded within the engine ECU).

1.3 Compressor performance maps

The compressor performance maps are plots showing performance parameters – pressure ratio and isentropic efficiency as a function of the corrected mass flow and at constant corrected compressor speeds. A typical compressor performance map is shown in Figure 1-3.

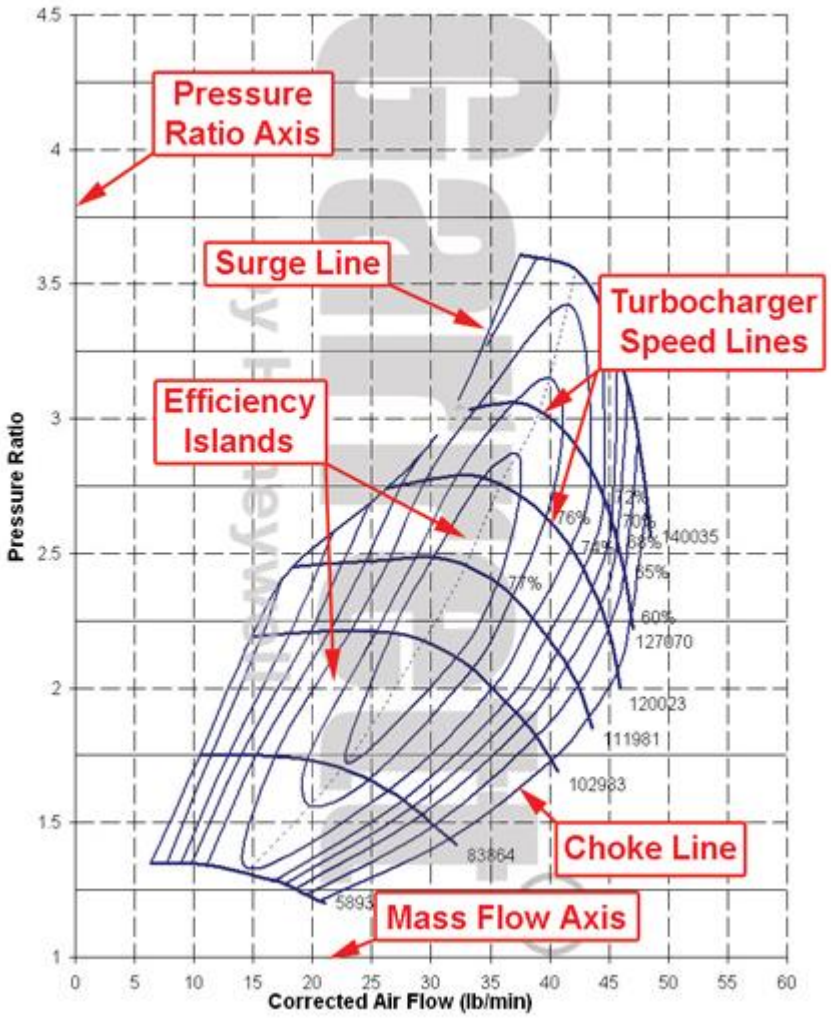

Figure 1-3. Compressor Performance Map [6]

The centrally located operating area is separated from the unstable regions marked with two boundary lines – the surge line on the left hand side at lower mass flows and the choke line on the right hand side at higher mass flows. The choke region is linked to a high gas velocity, low pressure ratios and low efficiency. A compressor is choking when the flow reaches the velocity of sound at some cross-section (normally at impeller eye in centrifugal compressors) [6]. When it happens no more air can be delivered through this cross section area at a given compressor speed (more mass flow through the compressor may be gained by increasing its rotational speed). However, turbocharger manufacturers define the choke line by the point where compressor efficiency drops below a certain unacceptable value. Longer operation at choke condition can result in the damage of the thrust bearing seal and cause a significant oil leakage to the compressor air path. This situation is more likely to occur on manually operated gas stands where the compressor is powered by a turbine. That is, when the turbocharger operates at the compressor's choke condition there is a significant pressure difference between the turbine and compressor side and lubricating oil is being pushed towards the lower pressure compressor. Surge, opposite to the choke region, is simply compressor instability at low

mass flow rates. More information regarding this phenomenon is given in the following sections of the thesis.

1.4 Turbine performance maps

Similarly to compressor, turbine performance maps are plots showing relationships between turbine performance parameters. These are expansion ratio, isentropic turbine efficiency and corrected mass rate and speed. Another parameter that is very widely used is the velocity ratio (or blade-speed ratio). This parameter is a non-dimensional ratio formed by dividing the tip speed of the turbine wheel by the “isentropic velocity” or “spouting velocity”. The isentropic velocity is defined as the velocity that would be attained with an isentropic expansion across the turbine pressure ratio. This parameter is useful since it provides an indication of how well the relative flow angle of the exhaust gases align to the blade angle for a given set of conditions. An example of the set of turbine maps is shown in Figure 1-4 - Figure 1-6.

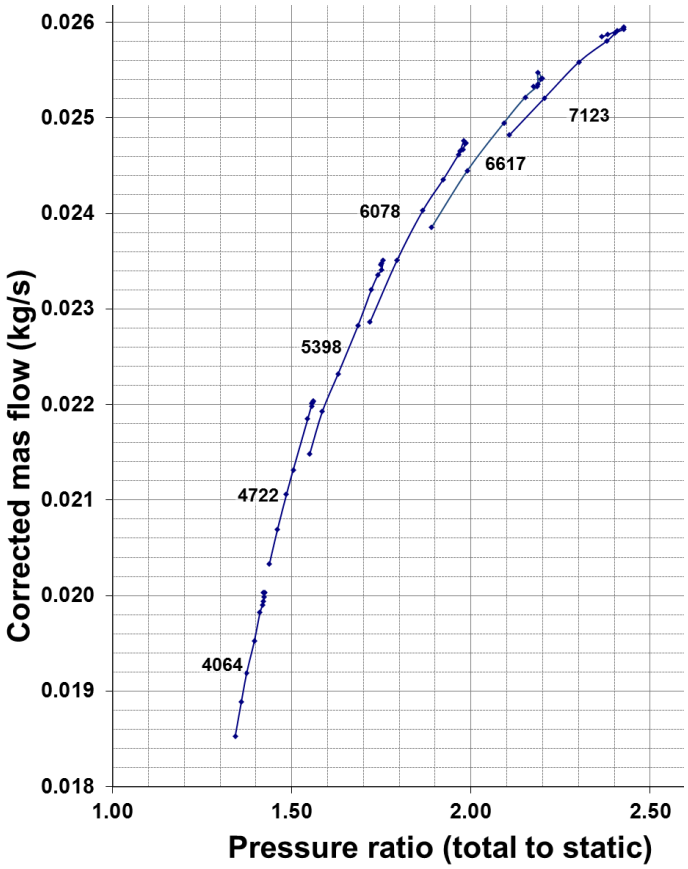

Figure 1-4. Turbine performance map. Corrected mass flow vs. pressure ratio

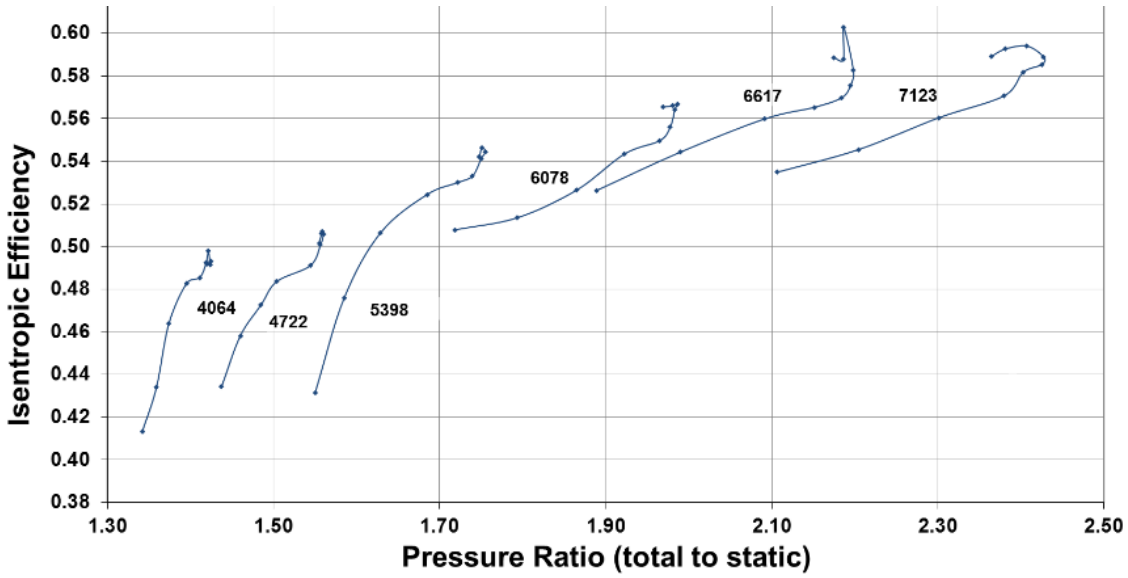

Figure 1-5. Turbine performance map. Isentropic efficiency vs. pressure ratio

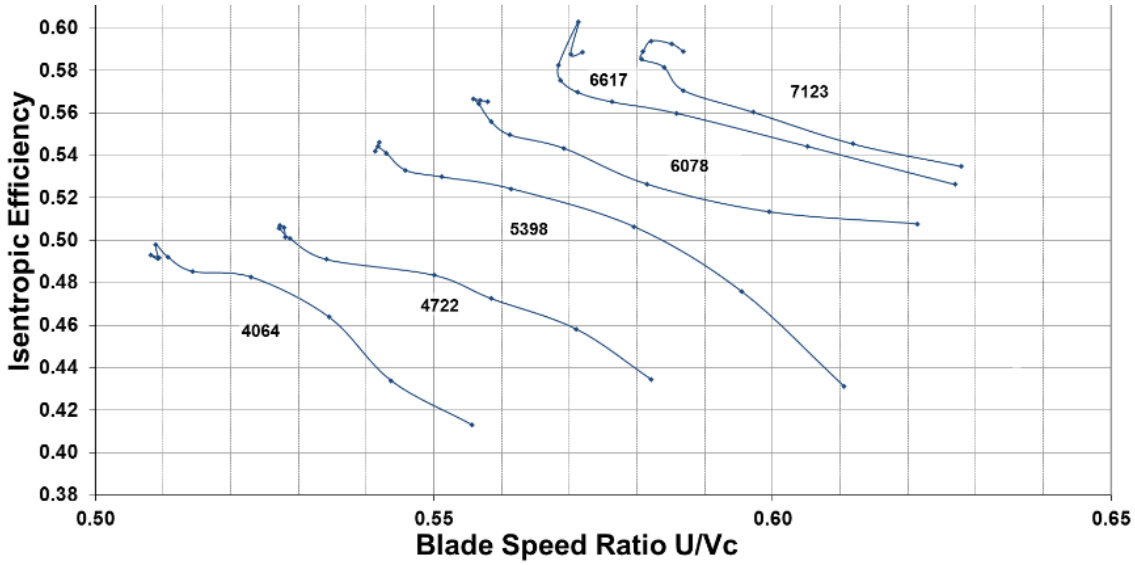

Figure 1-6. Turbine performance map. Isentropic efficiency vs. blade speed ratio

1.5 Compressor-turbine matching

The great majority of the automotive single-stage turbochargers consist of radial flow compressors and radial flow turbines mounted on a common shaft. Due to the fact that turbochargers are initially designed to work at steady-state conditions the main target is to match the compressor impeller and the turbine wheel to allow the turbine to operate at its peak efficiency. For this reason a unique relationship is derived from the compressor work transfer equation for a radial vaned impeller, the energy balance between compressor and turbine work and the definition of blade speed ratio:

$$\frac{D_c}{D_t} = \frac{1}{U/C_s} = \sqrt{\frac{\eta_t}{2\sigma}}, \qquad (1)$$

Where:

D_c – compressor impeller tip diameter,

D_t – turbine rotor tip diameter (radial flow),

η_t – turbine efficiency,

σ – compressor slip factor,

U/C_s – turbine blade speed ratio.

In the case of small automotive turbochargers consisting of compressor impellers with low vane numbers (slip factor approaching 0.8) and radial flow turbines of 0.7 isentropic efficiencies, the compressor impeller tip diameter should be approximately the same as the tip diameter of the turbine wheel or slightly smaller [7].

1.6 Engine - turbocharger matching

The main aim of a turbocharger – engine matching activity is selecting a turbocharger with a most suitable characteristics to an engine in order to obtain the targeted performance from that engine [7]. Generally three main steps can be distinguished in the process of a turbocharger – engine matching:

1) Establishing engine breathing requirements,
2) Selection of a compressor map to cover engine breathing requirements,
3) Selection of a turbine to drive the compressor to these operating points.

The first of the above listed steps is determined by the amount of air required by the engine which is a function of volumetric efficiency and scavenge flow, swept volume, speed, boost pressure and density of air in the intake manifold. For a four stroke engine the engine mass flow is calculated as follows:

$$\dot{m}_{air} \approx \eta_{vol} V_{sw} \frac{N}{2} \rho_m, \tag{2}$$

The next step - the choice of compressor is made accounting for the complete operating lines of the engine over its entire speed and load range superimposed on the compressor performance characteristic (Figure 1-7). The compressor “trim” or diffuser will be selected to allow for a suffiecient surge margin while ensuring that operating lines pass through the high-efficiency area.

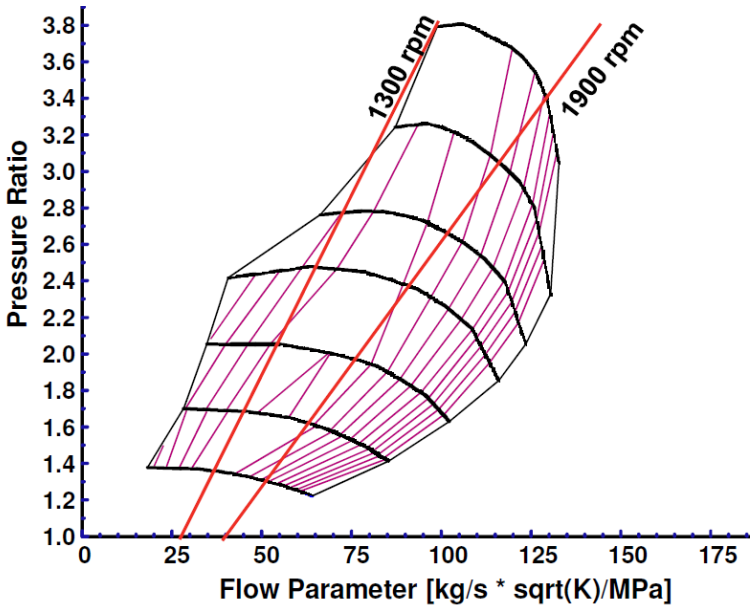

Figure 1-7. Engine breathing lines on a compressor map

In the third step, once the engine air flow has been established and compressor map selected the compressor power for these operating points must be calculated which can be completed as follows:

$$P_c = \frac{\dot{m}_{air}\, c_{p,int}\, T_{1t}\, (PR_c^{\left(\frac{\gamma_{air}-1}{\gamma_{air}}\right)}-1)}{\eta_c}, \tag{3}$$

Having calculated the compressor power a turbine is found that provides enough power to drive the compressor overcoming losses in the bearing system (an estimated bearing efficiency of 95-97% is usually chosen).

$$P_t = \frac{P_c}{\eta_{mech}}, \tag{4}$$

$$P_t = \dot{m}_{ex}\, c_{p,ex}\, \eta_t\, T_{3t}\left[1 - \left(\frac{1}{PR_t}\right)^{\left(\frac{\gamma_{ex}-1}{\gamma_{ex}}\right)}\right] \tag{5}$$

1.7 Exhaust Gas Recirculation

Exhaust gas recirculation (EGR) is an emission control technology targeting NOx emission reduction both in compression and spark ignition engines (Figure 1-8). NOx is formed in the combustion chamber at high temperatures when nitrogen and oxygen combine. The operation of EGR involves recirculating a controllable portion of exhaust gas from the exhaust manifold back in the intake manifold. The substitution of burnt gas for oxygen rich air reduces the proportion of the cylinder contents available for combustion which causes lower heat release rate and peak cylinder temperatures which reduces the

formation of NOx. The presence of an inert gas in the cylinder further limits the peak temperature (more than throttling alone in spark ignition engines).

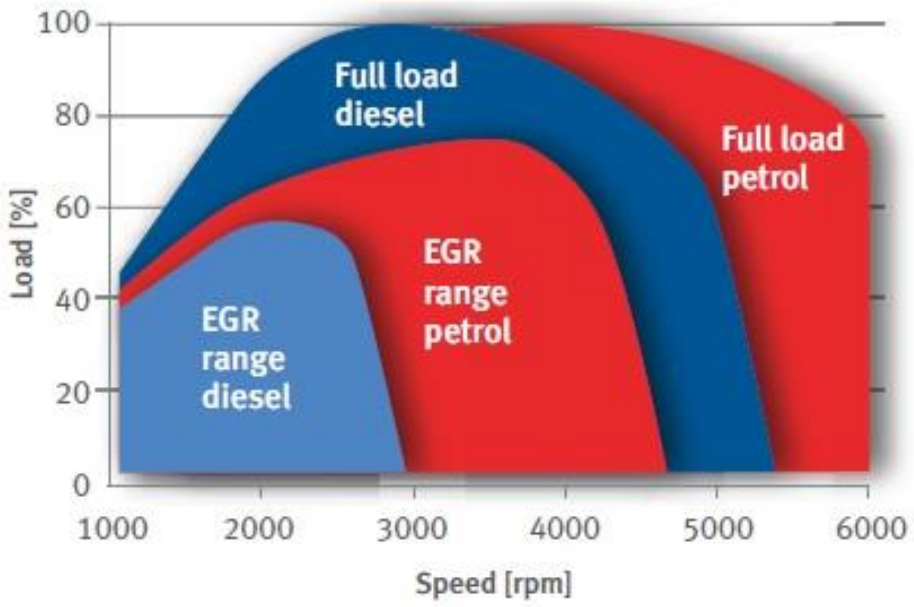

Figure 1-8. Typical EGR ranges of conventional petrol and diesel engines [8]

1.7.1 High Pressure Exhaust Gar Recirculation

Exhaust Gas Recirculation (EGR) is commonly applied at high pressure (HP EGR) as shown in Figure 1-9. The recirculated gas is passed through an EGR cooler which reduces its temperature (benefit of lower cylinder charge and peak temperatures; greater density of EGR gas – higher proportion of EGR gas can be used). The reduction of peak cylinder temperatures improves engine life, there is also a potential for reduction of throttling losses on spark ignition engines at part load. The disadvantages of using HP EGR systems are:

a) Reduction of turbine power due to a portion of exhaust gas being recirculated and not reaching the turbine,
b) Reduction of the peak power (reduction of oxygen available in the cylinder). For this reason the EGR is shut off when full power is demanded, therefore there is no control over NOx emission in this situation,
c) Increased production of particulates and risk of fouling,
d) Complex calibration of transient EGR behaviour,
e) Poor mixing and cylinder-to-cylinder distribution.

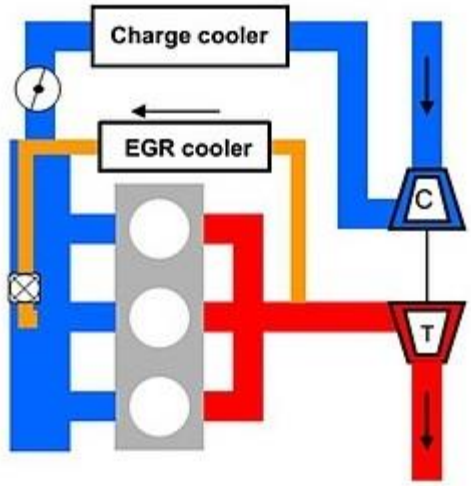

Figure 1-9. High Pressure Exhaust Gas Recirculation [9]

1.7.2 Low Pressure Exhaust Gas Recirculation

The need for achieving even higher exhaust gas recirculation rates in order to meet the Euro 6 legislation, introduces the concept of low pressure exhaust gas recirculation (LP EGR). In such a system, the exhaust gases are re-routed downstream of the turbine and the catalyst or diesel particulate filter (depending on the engine type that it's applied to) before being cooled down and returned upstream of the compressor where it is mixed with the fresh air flow (
Figure 1-10).

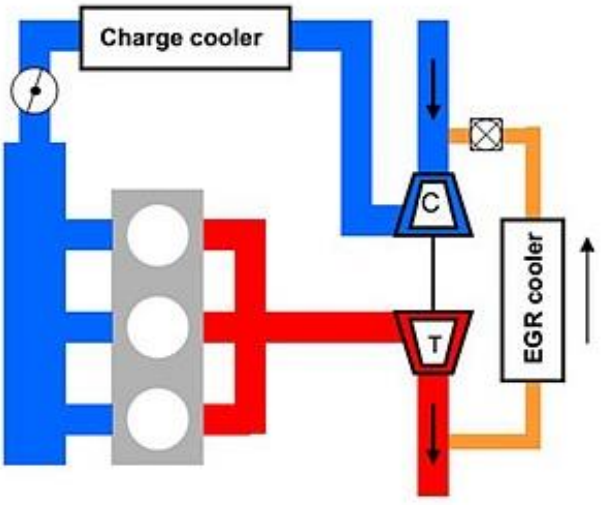

Figure 1-10. Low Pressure Exhaust Gas Recirculation [9]

The advantages of the LP EGR system over HP EGR are higher power input into the turbocharger, as the whole exhaust stream passes the turbine and lower temperature of the gas mixture entering intake manifold [10]. The drawbacks are:

a) Risk of water condensation and corrosion,
b) Poor transient response due to long piping,
c) The need for exhaust or intake air throttling to provide pressure difference driving the EGR flow,
d) Intercooler fouling risk,
e) Higher temperatures of the gas entering the compressor,
f) Higher mass flow of the gas and therefore more work is required to achieve a desired boost pressure.

2. Thesis objectives

The main aim of this thesis is the investigation of the turbocharger compressor performance with substitute gas. As the following literature review section demonstrates, there has been very little experimental data published in this area and that is the main motivation for this research. In order to conduct this study the ability to generate accurate and well-defined turbocharger performance maps is required. For this reason the main objectives of this thesis are as follows:

a) Build and commission a hot turbocharger gas stand with compressor closed-loop system,
b) Based on the available turbocharger map data, carry out an uncertainty analysis to understand the influence of sensor accuracies on characteristic performance parameters. Investigate on the efficiency measurement uncertainty due to the heat transfer phenomenon. Contribute to the experimental and modelling methods targeting the work and heat transfer separation.
c) Carry out an in-depth experimental analysis of compressor surge for better understanding of compressor performance map limits. Consider various size compressors and both steady-state and pulsating flow conditions.
d) Perform an experimental and numerical study (3D CFD) of the influence of variable fluid properties on the turbocharger performance maps and investigate on the existing correction methods. Consider various cases: homogeneous and non-homogeneous mixtures at the compressor entry. Finally, based on a selected combination of the EGR valve and intake pipework study (experimentally) the compressor performance changes due to the developed fluid flow regimes.

3. Literature review

The literature review is divided into several sections following the list of the thesis objectives. The first section is a review of commercial and academia located turbocharger testing facilities. Reviewing these has helped with the rig layout design, hardware and sensor selection and installation process. Next, the work that has been performed in the area of uncertainty of the turbocharger performance maps and so called low turbocharger speed region is summarised. As a result a method for uncertainty calculation has been selected and experimental procedure for low speed mapping has been elaborated. The following subchapter focuses on the surge phenomenon – a crucial limit of any automotive compressor performance map. Understanding physics of surge and surge line location determination has helped with the more precise performance map generation. Finally, the last section reviews on the effects of variable fluid properties on turbocharger performance.

3.1 Turbocharger test facilities

The increased demand for turbocharging in the automotive industry started after the 1973 oil crisis. The rising use of turbocharger performance maps introduced the need for regulating and standardising the process of map generation. Today, despite its imperfections as highlighted by Schwartz and Andrews [11], the most important document discussing the recommended test procedure for single rotor fixed or variable geometry turbochargers in steady-state conditions is “Turbocharger Gas Stand Test Code” published by Society of Automotive Engineers [12]. Additionally the recommendations regarding the distribution of pressure and temperature sensors can be found in “Supercharging Testing Standard” [13] and “Performance Test Code on Compressors and Exhausters” [14]. The great majority of turbocharger test facilities delivering hardware and performance maps for the automotive industry are owned by private companies and due to the confidentiality reasons the technical details of these rigs are not widely available. On the other hand there have been a large amount of research on turbochargers over years carried out within the academic environment, or other research institutions and therefore various rig installations exist. Generally, the turbocharger is tested on a typical gas stand as a full assembly including the turbine, compressor and bearing housing. In such configuration the compressor provides the load for the working turbine. An alternative method for providing load would be a dynamometer and although such arrangements exist, it is to extend the turbocharger turbine maps outside the operating range of the matched compressor. One of the first gas stands were designed and built by Wallace and Blair (Figure 3-1) and reported in 1965 by Benson and Scrimshaw [15]. The rig is impressive despite the rather crude way of turbocharger speed measurement (oscillograph indicated the rotational speed of the magnetic hub cap) and the use of mercury,

water and paraffin manometers for pressure measurements and thermocouples to measure the compressor side temperatures. The gas-stand was completely capable of producing performance maps at the turbine inlet temperature of 400°C.

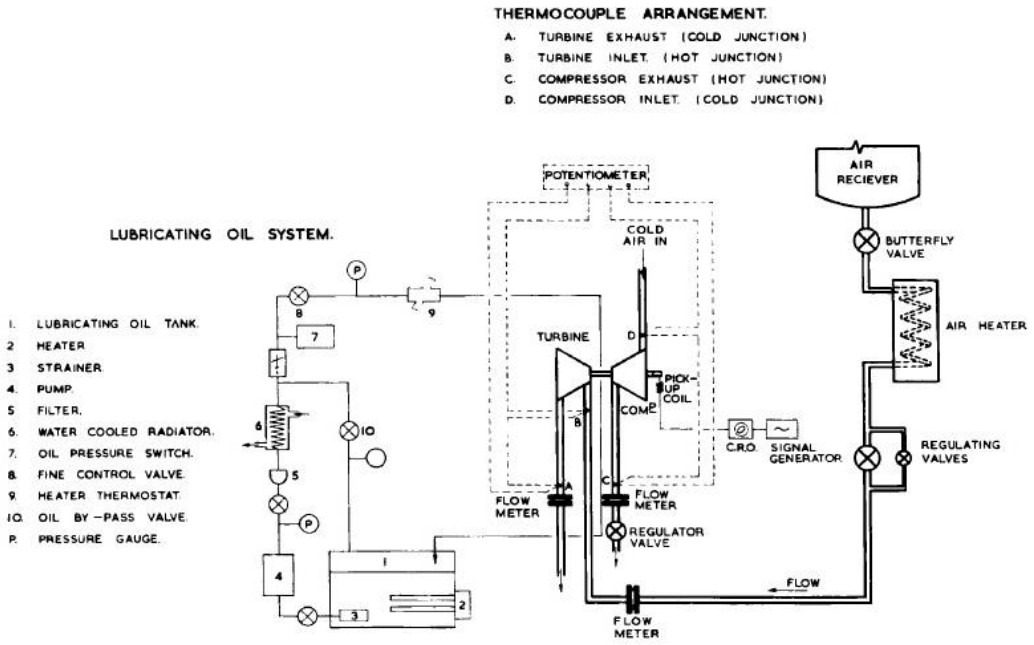

Figure 3-1. Schematic of turbocharger gas stand by Wallace and Blair [15].

Electric heaters continue to be used until today - the turbine inlet temperature can be easily controlled via adjustment of the electric power. A number of papers describing the experimental work performed on turbochargers operating on a gas stand have been published by Polytechnic University of Valencia. The rig that was used during the tests is reported by Payri et al [16] and shown in Figure 3-2 below. In this configuration also electric heaters are used. After passing through the turbine, the air is cooled (heat exchanger 2) allowing for the mass flow measurement by commercial hot wire flow meters (three of these placed in series). The setup of flow meters allows to make a statistical analysis of the flow values to control non-systematic errors and reduce systematic errors.

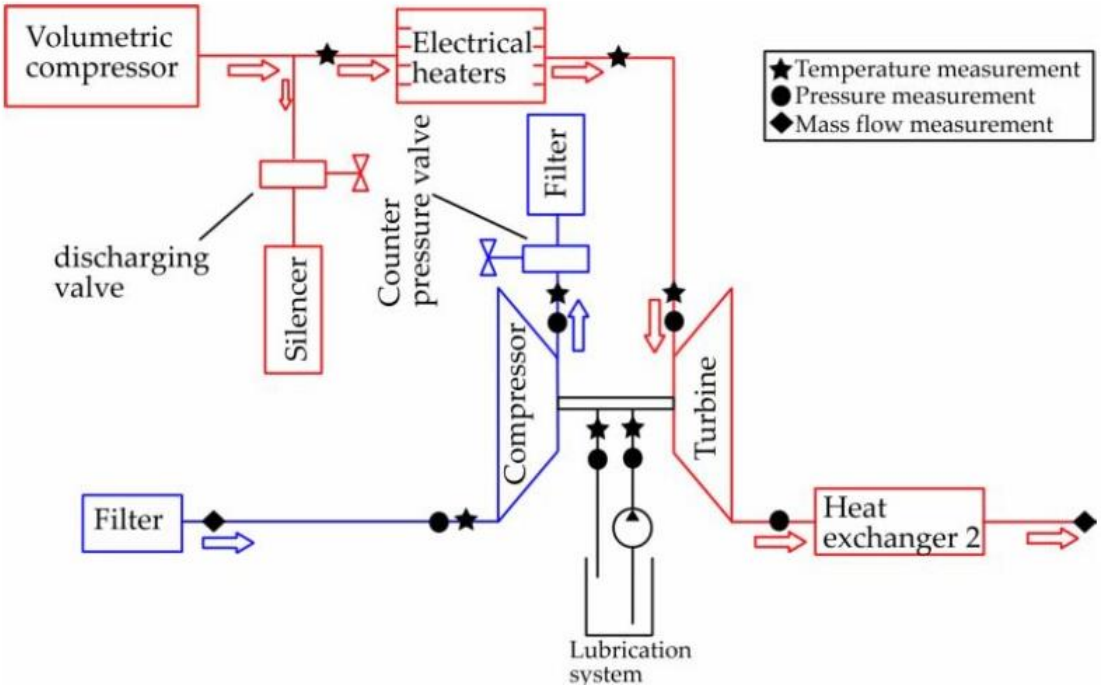

Figure 3-2. Schematic of turbocharger gas stand in Valencia [16].

Another turbocharger test stand, built at Imperial College, was used in the study of mixed flow turbines carried out by Arcoumanis and Martinez-Botas [17]. The rig layout is given in Figure 3-3.

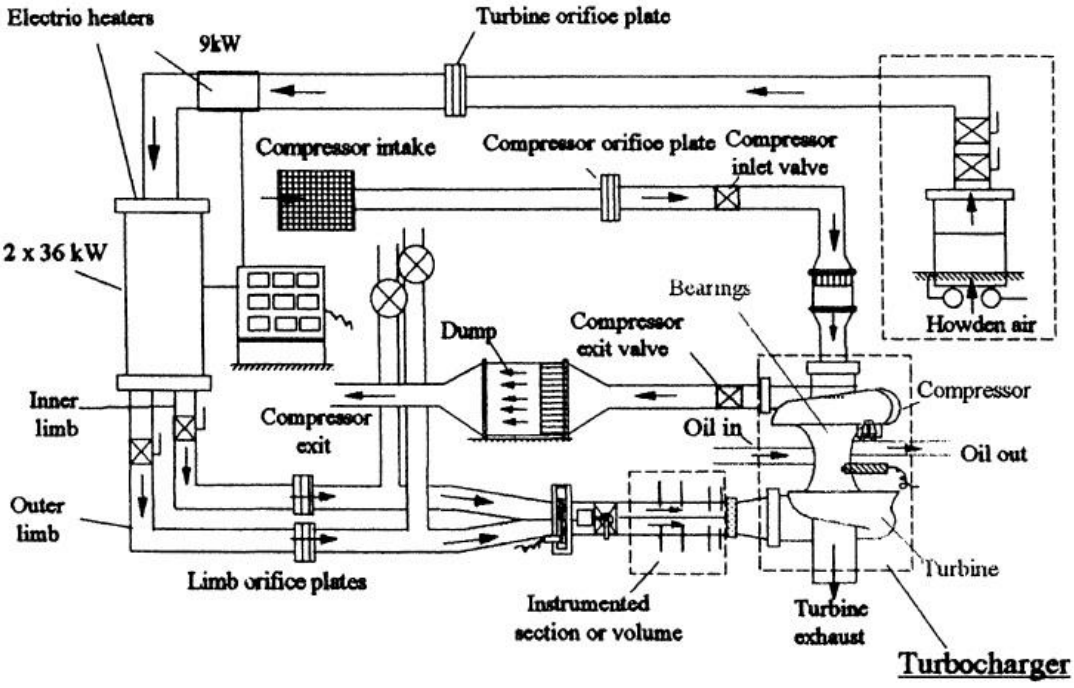

Figure 3-3. Schematic of turbocharger gas stand at Imperial College, London [17].

The capability of testing double entry and twin entry turbines is possible due to the parallel installation of electric heaters and relevant downstream parallel pipework legs. Although the capability of pulse generation prior to the turbine entry is not required by the Turbocharger Gas Stand Test Code such feature definitely helps with creation of engine-like conditions. For instance, such capability has been added at Centro Richerte Fiat Orbassano (Figure 3-4) to study the influence of pressure pulses on the turbine performance, at Polytechnic University of Valencia (used in the research on cold pulsating flows carried out by Serrano et al [18]) and Imperial College, London (used for mixed flow turbine study by Karamanis and Martinez-Botas [19]) with the use of rotary valve or set of rotary valves placed upstream from the turbine entry.

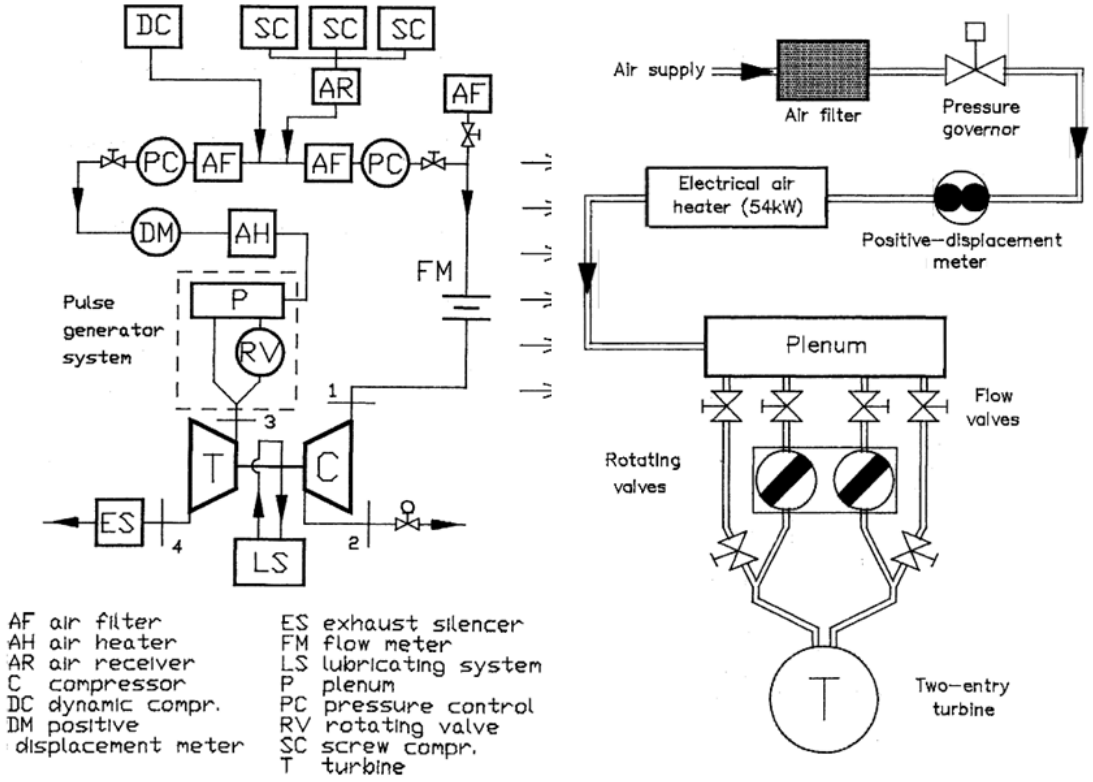

Figure 3-4. Schematic of turbocharger gas stand in Centro Richerte Orbassano, Italy [20]

An alternative to the previously mentioned extended turbine mapping utilising the turbine dynamometer is the use of so called compressor closed loop where the compressor discharge gas is cooled and returned at the compressor entry. The turbine map is extended by varying the compressor power which is done via the regulation of the compressor inlet pressure. An example of such configuration is given in Figure 3-5 representing the facility built at University of Aachen [21]. The compressor inlet pressure regulation takes place with the use of “closed loop inflation” and “closed loop blow off” valves.

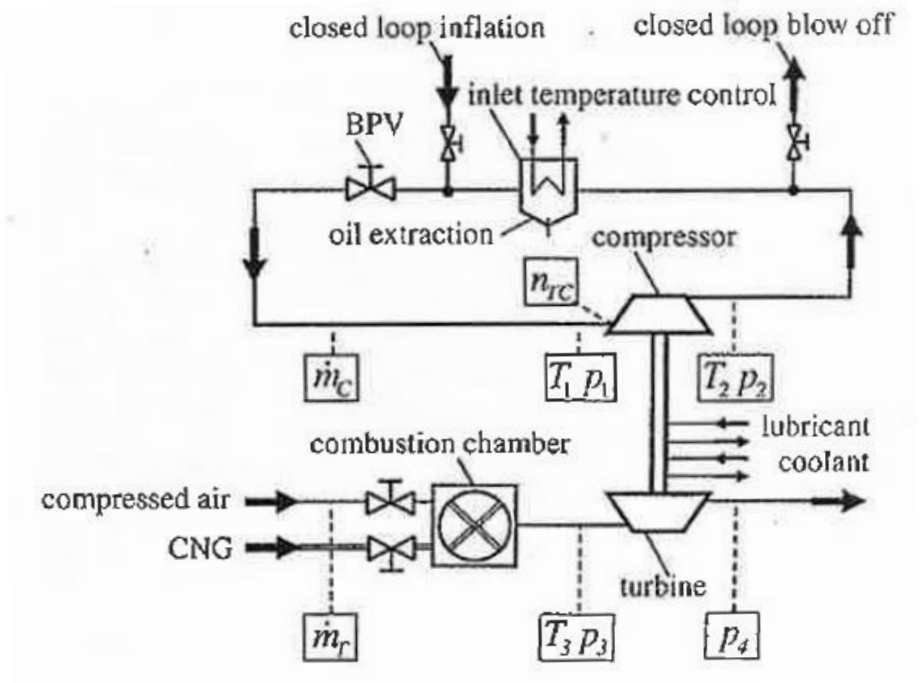

Figure 3-5. Schematic of turbocharger test stand with compressor closed-loop at University of Aachen [21]

Although there are no best practise recommendations for such configuration within the previously mentioned SAE or ASME codes such functionality will be added to the turbocharger test facility built within this thesis. The reason for this is that the closed loop arrangement is required for the intended tests on turbocharger compressor performance with substitute gas. Another way to increase the temperature of the gas prior to the turbine is the use of liquid fuel burners (as on earlier generation of turbocharger test stands) or more environmentally friendly natural gas burners where the natural gas is delivered from the supply line and therefore there is no need for the fuel tank and its periodical refilling [22]. Furthermore, natural gas combustion is complete and free from airborne particles that could foul the turbine parts, the combustion products are more homogeneous [23].

3.2 Turbocharger performance measurement uncertainty

According to JCGM100:2008 [24] uncertainty of measurement is a “parameter, associated with the result of a measurement, that characterizes the dispersion of the values that could reasonably be attributed to the measurand”. Although SAE standards [25], [26] give recommendations for the laboratory turbocharger test procedures they do not discuss the uncertainty determination and hence there is still little published in this area. The selection of a turbocharger for on-engine operation is based on performance maps measured on a test bench. The best possible matching and accurate determination of the mass flow range, boost pressure or compressor efficiency is dependent on the accurate measurement of the characteristic maps. The overall uncertainty of any given

turbocharger performance parameter given by such map is affected by the uncertainty of all relevant measured quantities – temperature, pressure, mass flow and speed. Kline and McClintock [27] and Mohtar et al [28] indicated the major sources of uncertainty in the above measurements and these are listed as follows:

- Temperature and pressure uncertainties:
  - Location error: incorrect position of the sensor in the air stream;
  - Installation error: heat transfer from and to the sensor due to the insufficient insulation;
  - Calibration errors: instrument drift, nonlinearities, and reference temperature errors;
  - Device errors: inherent accuracy limitation of the sensor;
  - Acquisition: amplifier, noise, read, and analogue–digital conversion errors.
- Flow measurement uncertainties:
  - Installation error: all flow meter types should follow required upstream length/flow conditioning specifications;
  - Range of the flow measurement: accuracy of the used flow meter drops when operating beyond the recommended range;
  - Flow pulsations: pulsation adversely affects most types of meters and will add to the uncertainty in the test measurement. However, as most flow measurement instruments provide a low-frequency output response, it is often difficult to determine pulsation magnitudes and frequencies.
- Rotational speed uncertainties:
  - Installation errors (due to non-proper location of the sensor in the casing),
  - Calibration errors.

Now, assuming that the chosen sensors are installed at correct locations, calibrated and used within their operating range and there is no errors associated with electrical noise, analogue–digital conversion etc. the only left source of uncertainty is device error (accuracy).

3.2.1 Turbocharger performance maps uncertainty analysis based on sensor accuracy and single-sample measurements

In order to determine the quality of the measured and calculated values an uncertainty analysis can be carried out. Two types of uncertainty evaluation can be distinguished: Type A evaluation – based on the statistical analysis of a series of observations and Type B – based on other than statistical analysis of a series of observations. The

latter type of evaluation is adequate for single-sample experiments which is of particular interest in this thesis.

In 2013 Erwann Guillou published a conference paper [29] where he carried out a type-B uncertainty analysis for evaluation of the propagation of measurement errors in the calculation of compressor performance parameters. In his work he used the same method as Kline and McClintock [27] or Mohtar et al [28] for calculating uncertainty of parameters that are dependent on few other variables (measured or calculated). The results of his study shown high sensitivity of the compressor efficiency uncertainty to the uncertainty in temperature measurements and high levels of pressure ratio uncertainty. Also the importance of operation in high confidence of rotational speed was highlighted to maintain a certain level of precision. Mohtar et al [28] studied the influence of different individual measurement uncertainties on the overall performance uncertainty of the radial compressor. They concluded that the inlet temperature sensor uncertainty has greater influence on total efficiency than the outlet sensor uncertainty. Regarding pressure measurements they noticed that outlet pressure uncertainty has a greater influence on the compressor efficiency uncertainty than the inlet pressure uncertainty. Finally the authors suggested that performing uncertainty analysis can also help in the process of instrumentation selection. Olmeda, P. et al [30] focused on a study of the uncertainties of turbine power calculating the propagated uncertainty using linear uncertainty propagation model. According to them when a high accuracy power measurement is required RTD sensors should be used. Also, improving mass flow rate measurement accuracy in the region of high mass flow rates and temperature measurement at low mass flow rates would drop the power measurement uncertainty. They presented a test rig optimisation technique compiling databases of sensors for the sake of test rig improvements. Bolz et al [31] performed a Gaussian type error propagation analysis showing that compressor pressure ratio uncertainty raises when increasing turbocharger speed and moving towards the region of high compressor pressure ratios. They also pointed out that the largest error in the efficiency is caused by uncertainty in pressure measurement followed by the temperature measurement before and after the compressor. Accordingly the compressor efficiency uncertainty is higher in the low turbocharger speed region as relative errors in pressure and temperature measurements are larger. In general this statement is in agreement with conclusions drawn by Sathvick Shiva Kumar et al [32] and Holger Mai et al [33].

3.2.2 Heat transfer effects on the turbocharger performance uncertainty

Despite the need for the accurate measurement of data in the low turbocharger speed region when simulating the New European Drive Cycle (Figure 3-6) or other similar driving cycle the turbocharger performance map data is usually limited at the low end of the map due to the test rig limitations and increasing heat transfer between the turbomachinery components. Instead, the extrapolated data is used.

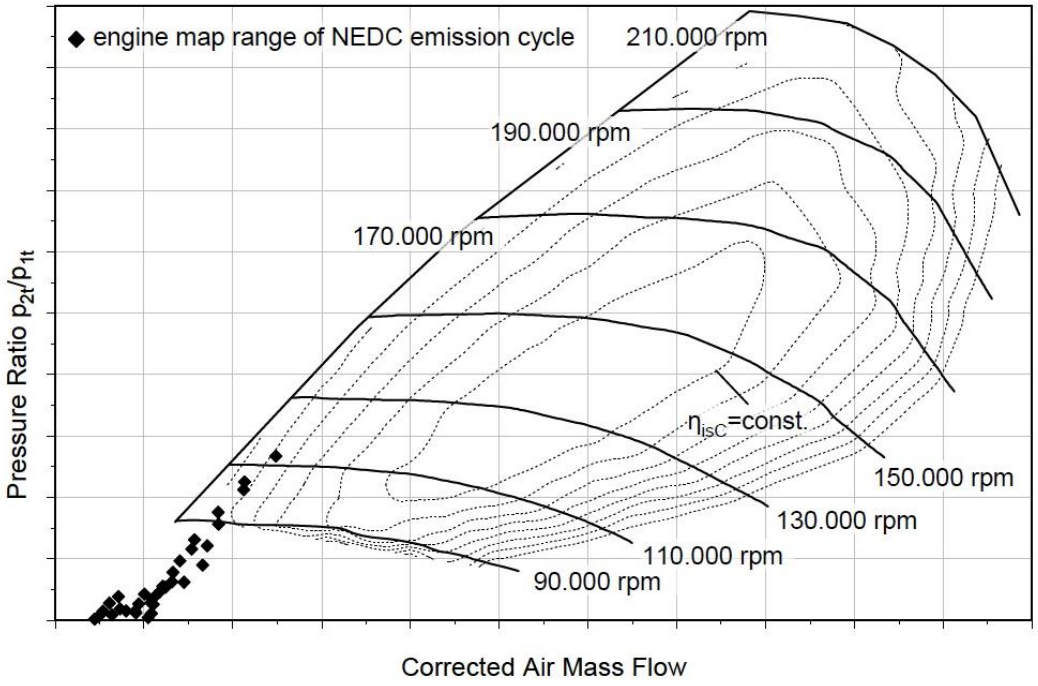

Figure 3-6. Engine map range of the NEDC emission test cycle, referring to the TC manufacturer's compressor map [34]

As a result of the heat transfer between the turbocharger hot and cold sides the measured temperature of gases flowing through the turbine and compressor combines the effects of mechanical work and heat transfer instead of the mechanical work only. The errors associated with the temperature measurement lead to the incorrect efficiency calculation. A number of publications exist that highlight the importance of uncertainty of turbocharger performance at low turbocharger region. Serrano et al [35] based on the experimental campaign carried out on selected turbochargers created their own heat transfer model (HTM). They have shown how heat fluxes become more important for the overall turbocharger prediction when the turbocharger load reduces. In some cases the heat transferred from the exhaust gases to the rest of the turbocharger via the turbine case can achieve up to 70% of the total turbine enthalpy drop. Chesse et al [36] demonstrated that the measurement of compressor adiabatic maps and with heat transfer allows for the calculation of the heat transfer from the turbine to the compressor which can

be further used for the evaluation of the compressor mechanical power and its outlet temperature. Otobe et al [34] generated performance maps at “hot”, “warm” and “cold conditions” to show the influence of the heat transfer on the maps. Concluding on this part of the literature review it shall be highlighted that for more accurate performance characterisation of turbomachinery, adiabatic mapping is a good alternative. This method of the turbocharger performance map characterisation will be studied in in more detail in later sections.

3.3 Compressor surge

Understanding compressor surge margin and related surge onset metrics is an important aspect of turbocharger performance mapping. Although this phenomenon is recognised and measured by turbocharger manufacturers there are different criteria used within industry for drawing surge lines on compressor performance maps and a unified or standardised definition still does not exist. That is particularly inconvenient for application engineers responsible for the engine-turbocharger matching process as they struggle to compare the low mass flow region of compressor performance maps limits originating from various suppliers. On one hand they need to be certain that the selected compressor will not surge or be too “noisy” (NVH issue) at any transient or steady-state engine operating point but on the other hand it has to be a best possible choice from the boost pressure, air flow range and efficiency point of view. The estimation of a surge line gets more difficult when the turbocharger works on engine – in a dynamic and characterised by pulsating flows environment, where the compressor intake duct is of a more complex shape, different size and volume if compared to steady-state gas stands. Creation of a standardised and obligatory code of practise for surge measurement within the turbocharging industry would definitely be beneficial but it is highly unlikely that this happens in the near future. The main limiting factor is the enormous cost that would have to be incurred – upgrading/replacement of instrumentation and other testing equipment to keep up with the new standard, updates of extensive databases etc. Therefore it is not a surprise that most turbocharging companies remain conservative with their own mapping techniques and reject the idea of such drastic changes. Seeing and understanding the above issues the author makes his best effort to study surge and contribute to the experimental surge detection.

3.3.1 Surge definitions

The simplest and shortest definition of surge is the compressor instability in the region of low mass flow rates. More complex definitions like those introduced by A. Whitfield and A. J. Sutton [37] describe surge as a violent breakdown of the flow through the com-

pressor with severe pressure fluctuations throughout the system and the air flow periodically reversing and discharging through the compressor inducer. According to the authors, this phenomenon can usually be attributed to rotating stall, which leads to increased losses and eventually to a pressure ratio versus mass flow characteristic that has a positive slope and is inherently unstable and can be easily triggered into violent surge. A. Engeda [38] describes surge as a system phenomenon where onset occurs when the operating point lies near the maximum pressure ratio associated with the operating speed. He also distinguishes between the onset of axial and radial compressors surge where the former is strictly associated with a preceding rotating stall whereas the latter can be totally independent of preliminary rotating stall. Bram de Jager [39] in his paper describes surge as a self-excited cyclic phenomenon, affecting the compression system as a whole and characterised by a large amplitude pressure and annulus averaged mass flow fluctuations even to the point of flow reversal. Other authors classify surge as “mild” or “deep” depending on the mass flow fluctuations - according to Fink et al [40] and Dehner [41, 42] or Hung Nguyen-Schafer [43] “mild surge” represents the conditions where average mass flow oscillates but remains in the forward direction at all times. These oscillations are characterized by the Helmholtz frequency. In the case when mass flow oscillations are severe and the mean flow reverses its direction during part of the cycle, the compressor is considered to operate in a “deep surge”. Another example is Bram de Jager’s [39] classification of surge that includes four stages:

- Mild surge - a phenomenon with small pressure fluctuations and a periodicity governed by the Helmholtz resonance frequency. Flow reversal does not occur.
- Classic surge - with larger oscillations and at a lower frequency than mild surge (although high frequency oscillations may be present also: the dynamics are non-linear and introduces higher harmonics), but no flow reversal.
- Modified surge - where the entire annulus flow fluctuates in axial direction but rotating stall is superimposed, so the flow is unsteady and non-axisymmetric. It is a mix of rotating stall and classic surge phenomena.
- Deep surge, a more severe version of classic surge, where even flow reversal is possible. This is an unsteady but axisymmetric limit cycle for the flow.

It is also well known that the dynamics of surge (amplitude and frequency) can be reduced or increased by modifying the system established downstream of the compressor [44]. Generally, it has been well established that surge is a problem dependent on several design and operation parameters.

3.3.2 Surge suppression and performance enhancement methods

As the automotive radial compressor surge becomes a limit in delivering lower end torque and can cause serious damage to the compression system, numerous attempts

have been made to avoid, delay or control it. Some of the methods can be applied at the compressor design stage, and this involves various modifications of the compressor components upstream and downstream from the impeller. Others are based on installation of additional components in the compressor inlet duct or include a combination of both mentioned methods.

Design stage based surge suppression methods

One of the most common ways of reducing the flow distortion (wake) from the impeller to the diffuser causing stall which progresses to surge is utilisation of backswept impellers (Figure 3-7) which also fulfil the demand for high efficiency compressors with a wide mass flow range.

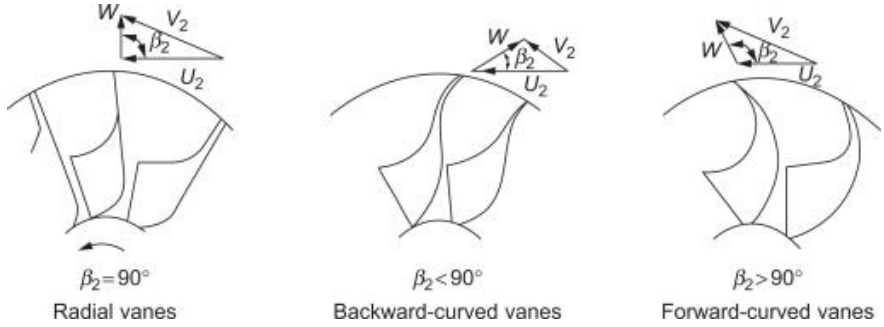

Figure 3-7. Various types of impeller blading [45]

Blade backsweep reduces the kinetic energy of the flow entering diffuser and therefore due to lower inlet losses its performance is improved. The application of a backsweep results in higher pressure ratios at low flow rates relative to radial impellers and the surge point is moved to lower flow rates. However, due to the increased stresses near the impeller tip the degree of backsweep has to be compromised between the performance advantages and mechanical limits [7].

Vaned diffusers can be considered as another compressor component targeting the improvement of the compressor performance and extending surge margin that is realised at the design process. The conventional full length vane diffusers where a throat is created tend to increase the flow blockage and therefore result in reduced flow range. Also the incidence effects can have the negative influence on surge at low flow rates [46]. To avoid the reduction of the flow range and optimise the incidence over operational range a variable vane mechanism is necessary. Aerodynamically different vane shapes were designed and tested (by the following researchers) with different angle settings and suggestions to incorporate these in a movable mechanism. Harp and Oatway [47] introduced a configuration where the vanes were pivoted close to the leading edge and the vane angle set in various settings. The vane pivot position was chosen so that the diffuser throat area was maximized at the minimum stagger angle to allow a high choked-flow rate. In such a way a variable channel diffuser, with straight-walled wedge vanes was

created, which provided surge-free operation over a broad flow range when used with a backswept impeller. Simon et al [48] focused on a combination of simultaneous adjustment of inlet guide vanes and diffuser vanes. They observed an increase in machine efficiency over the entire operating range without compromising on a wide operating range. Low Solidity Vaned Diffusers (LSVD) stand next to the conventional vaned diffusers and were first introduced by Senoo in a Japanese patent, 1978. The difference lies in the absence of the geometric throat which limits the minimum and maximum operating range in classic vaned diffusers. The “solidity” parameter is defined as chord blade length “l” to pitch length “s” ratio. The solidity and the blade length are combined together and determined in this way that the throat “t” is not created. A schematic drawing of an exemplary LSVD is presented in Figure 3-8.

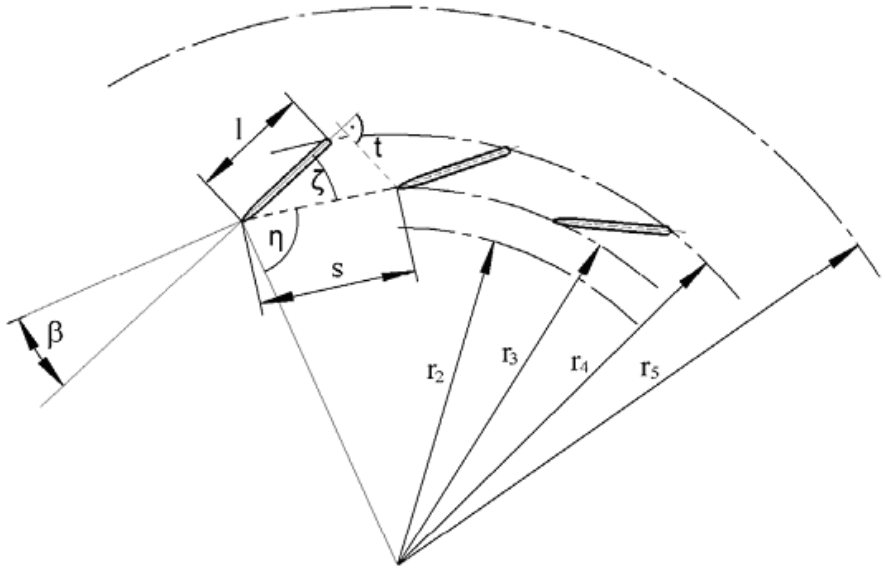

Figure 3-8. Schematic of Low Solidity Vaned Diffuser by Senoo [49]

Where:

l – blade length, s – pitch length, r2 – impeller tip radius, r3 – diffuser inlet radius, r4 – diffuser exit radius, r5 – diffuser outlet radius, β – blade angle with respect to tangential, η – angle between radius and pitch line, ζ – angle between blade and pitch line, t – throat

In 2001, Engeda [38] reviewed all previous work done in the topic of compressor diffusers including LSVDs and presented his own results where he compared four different LSVDs, two vaneless diffusers (VNL) and one conventional vaned diffuser (CVND). However, he didn’t make any breakthrough observations in the area of surge as neither his CVNDs nor LSVDs experienced surge at his test conditions. Despite all the work that has been done on vaned diffusers and their development, vaneless diffusers are still used in the majority of turbocharger compressors because of their simplicity and broad operating range. Narrowing of the diffuser passage width (so called “pinched diffusers”) has been investigated as a means of suppressing surge and extending the operating

range by many authors. As it has been discovered diffuser width has a very significant effect on the critical flow angle [50]. The critical flow angle is the most tangential angle with which the diffuser does not stall. The smaller the diffuser width, the more tangential the critical flow angle. Whitfield & Sutton [37], investigated the flexible wall (converging wall or pinched wall) and throttle ring arrangement (Figure 3-9) and they observed that both of these solutions moved the peak pressure ratio to lower flow rates, and at the near surge flow rates (where the device would be introduced, when operating in a variable geometry mode) improvements in both pressure ratio and efficiency were shown.

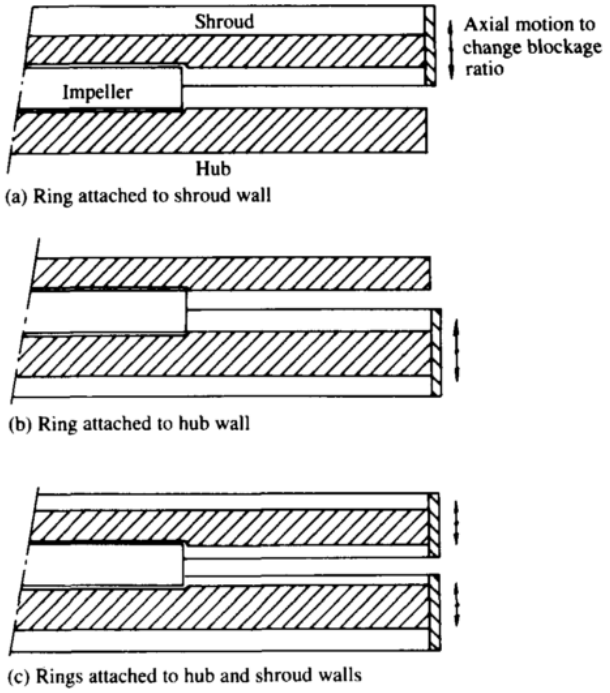

Figure 3-9. Diffuser throttle rings [37]

While the converging wall concept exhibited slightly better aerodynamic performance than the throttle ring, it has implementation difficulties with respect to material integrity under continuous flexing when developed to a fully variable geometry device. Abdel-Hamid [51] also experimented with the throttle rings on vaneless diffusers and his results were consistent with those of Whitfield and Sutton. Recently Jaatinen et al [52] also contributed in this area by experimenting on seven different pinched diffusers. According to their conclusions the pinch on the shroud side was the most advantageous of all tested configurations. Moreover, they concluded that pinched diffusers increase rotor efficiency. The pressure ratio increased over a wide operating range at the design and low rotational speeds, but decreased at the higher rotational speed. Higher efficiency and a lower pressure ratio, observed at the higher rotational speed, are possible only if the impeller work input is smaller. However, no conclusions were given regarding the surge suppression effects. Mohtar et al [53] investigated different pinched and grooved diffuser configurations and concluded that both of these methods can be advantageous in delaying diffuser

instabilities, hence shifting surge line to low flow rates. However they pointed out that pinched diffusers suffer from the creation of high pressure and efficiency losses, due to friction loss increase in the diffuser. Also, grooves may have a detrimental effect on both pressure ratio and efficiency if not optimised for number and location.

Another widely investigated method, next to impeller and diffuser modifications, realised at the design stage and targeting an improved performance and greater surge avoidance is the application of slotted compressor casing (also known as Map Width Enhancement (MWE) system). The idea behind this is to improve the surge margin by recirculating reversed flow to the impeller inlet when surge is imminent and improving the choke line by allowing additional air into the compressor. Fisher [54] was the first to contribute to the topic of classical bleed slots in the late 80's. Recently Chalet et al [55] tested 2 different MWE configurations by means of various hole number, its diameter and angles. The general conclusions are consistent with those presented by Sivagnanasundaram et al [56], and Liangjun Hu et al [57], Hua Chen et al [58] or Ding [59] and can be sum up as following: bleed slot is a cost effective casing treatment that improves the range of the centrifugal compressor. Stability near surge is improved by removal of low momentum fluid near the shroud region by the slots and recycling it to the inlet and reducing strength of shock waves on the blade suction surface. Compressor flow capacity near choke is increased by additional flow entering the blade passage through the slots. In order to improve the performance of the radial compressor incorporating a slotted casing the following considerations have to be taken into account: careful design of the port geometry to minimize losses, removing swirl from the port flow to minimize mixing loss with the main stream flow, enhancing recirculation flow with blade design more loaded near the inducer and by increasing the blade loading with counter swirl near the shroud [58].

Tip injection is another method for suppressing surge at low compressor air mass flows and is based on the same principles as the above mentioned recirculation casing treatment techniques but the injected air stream is either recirculated from the post compressor core flow or delivered from external sources. Most of the work in this topic has been performed in the aero-engine industry. Freeman et al [60] showed that injecting air into the blade tip in region of the compressor is more beneficial in terms of surge suppression than injecting it into the core of the main compressor flow. Suder et al [61] demonstrated the significant range extension potential with using four injectors spaced randomly about the circumference and injecting less than one percent of the annulus flow. Therefore, they considered a ''discrete casing treatment'' consisting of a recirculating system that would bleed high-pressure air from the rear of a blade and use it to supply discrete injectors upstream of the blade. Another advantage they pointed out is that by bleeding and injecting from different portions of the circumference, multiple recirculation of fluid

can be avoided. Finally, they suggested a use of a shut-off valve in the recirculation line, which could be turned off when not required, eliminating its inherent efficiency penalty and activated ‘‘on-demand’’ to recover from a fully developed stall. Stein et al [62] studied numerically by means of CFD blade tip flow separation leading to instabilities in centrifugal compressors which they tried to diminish or eliminate via the application of steady and pulsed jets. Steady jets were found to be effective in controlling these instabilities. Jets pulsed at higher harmonics of the stall frequency produced larger shear stresses than low-frequency jets and better energized the injected particles.

Hirano et al [63] recirculated part of the flow at the scroll outlet and injected it via an injection nozzle installed on the inner wall of the suction pipe of the compressor. The experimental results revealed that the optimum circumferential position, which most effectively reduced the flow rate for the surge inception, existed at the opposite side of the tongue of the scroll, against the rotational axis and did not depend on the compressor system and the rotational speeds.

The air injection has also been studied experimentally and numerically in vaned diffusers. Spakovszky [64] showed that an improvement in the stable range could be obtained by injecting air through the shroud surface of the vaneless space in a direction that was tangent to impeller rotation. Skoch [65] tested other variants of shroud-side injection. Significant results were obtained when the injectors were oriented to produce a vaneless space jet that was tangent to the impeller, but travelled in a direction that was opposite to impeller rotation. Results from shroud surface experiments proved to be very promising and showed that both a significant improvement in stable flow range as well as an ability to recover from fully developed surge could be obtained from control actions taken on the shroud surface. Skoch continued his work at the U.S Army Research Laboratory and at the end of 2004 he published another paper investigating the air injection through the hub surface of a vaned diffuser [65]. He oriented the nozzle orientations in such a way that they concentrated air injection on the suction side of vanes, on both the suction and pressure sides and finally on the pressure side. Surge margin improved by a small amount as the injector nozzles were turned from the suction-side to pressure-side orientations and stage efficiency was maintained. The suction-side position pointed the injector opening in a direction that was aligned with the tangential component of fluid flow in the vaneless space. As the nozzles were rotated toward the pressure-side orientation, a flat side of the injector passage became opposed to the tangential component of flow in the vaneless space and the nozzles became obstructions to the flow. Generally, the results of hub injection experiments and the comparison to successful shroud-side results suggested that successful stability improvement techniques must act upon flow within the vaneless space of the diffuser. The hub nozzles were located just upstream of the leading edges of the diffuser vanes. The injected air jets travelled immediately into the

diffuser passage which proved to be an ineffective means to improve stability, at least in this compressor.

Off-design surge suppression and performance enhancement methods

Next to the above mentioned methods that are realised at the design stage for surge margin improvement and/or widening radial compressor's operating range, there are also those which may be applied externally to the base compressor hardware, namely Inlet Guide Vanes (IGV) and variable trim compressors (VTCs). The first technique has been studied by many researchers over a couple of decades and some concepts were even used in mass production. The idea behind the application of IGV's (within the compressor air inlet system) is to modify so called "velocity triangle" (Figure 3-10) of the flow which has a direct influence on the enthalpy rise (which depicts the work input) that is expressed by the Euler momentum formula (Equation (*6*)).

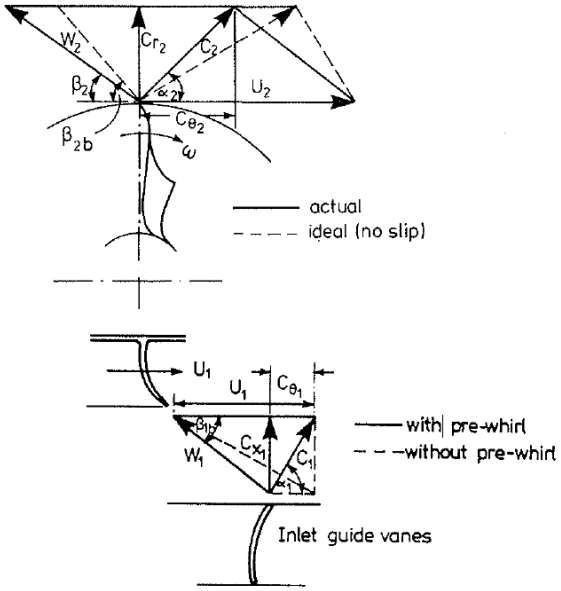

Figure 3-10. Compressor velocity triangle [7]

$$\Delta h = U_2 C_{\theta 2} - U_1 C_{\theta 1} \qquad (6)$$

Based on the above equation it can be seen that creating the tangential velocity component $C_{\theta 1}$ at the compressor impeller inlet by introducing positive pre-whirl (same direction as the rotation of impeller) reduces the work input of the impeller resulting in a lower pressure ratio for a given impeller speed. However, at the same time the angle of incidence defined as an angle between the relative velocity of the flow and the impeller blade is reduced which lowers the possibility of the flow separation on the suction side of the blade. The onset of surge is moved to lower mass flow rates. Therefore, it would be ideal to construct a device causing a negative swirl in the stable operational region of the map to raise the pressure ratio and positive swirl near the low flow stability region to suppress the onset of surge. For the optimal minimum incidence angle within the entire range of

compressor rotational speeds such a device would need to be fitted with variable vane angle mechanism. This seems to be a very challenging and difficult task which can only be successful if realised at a reasonable cost despite very harsh packaging constraints. The theory on the modifications of velocity vectors has resulted in various designs over the years. F.J. Wallace, A. Whitfield et al [66] tested various vane angles for both positive and negative pre-whirl created by the in-house made pre-whirl device incorporating either flat plate or curved vanes (Figure 3-11).

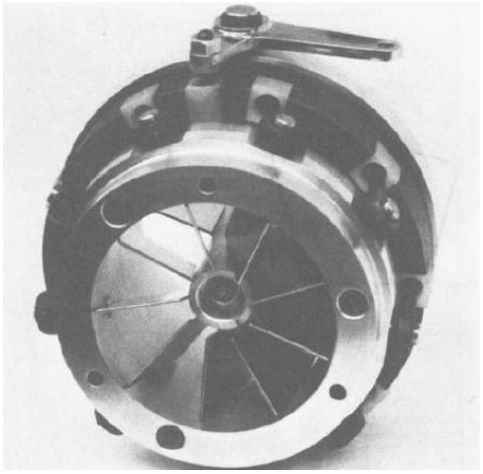

Figure 3-11. Pre-swirl device designed by Wallace, A. Whitfield et al [66]

The results of the experimental tests showed that stable operation can be extended to low flow rates by the introduction of positive pre-whirl. However, the higher vane angle that was introduced the greater isentropic efficiency drop was observed. Another interesting approach was presented in 1998 in Journal of Turbomachinery by Whitfield and Abdullah [67] - volute swirl generator was used for introducing pre-whirl upstream from the impeller. Despite its positive influence of the surge (surge pressure pulsations were not detected at the lowest flow rate tested when full swirl was generated by the volute) the device turned to become noisy when in operation. The authors also pointed out some packaging difficulties regarding the installation of dual inlet system being the simplest option from the control and mechanical point of view. J. Galindo et al [68] came up with an interesting idea of so called " Swirl Generator Device" (Figure 3-12) and by a series of tests performed on a gas stand they proved that it would improve the uniformity of air reaching the compressor inlet and improve the compressor's stable operating region.

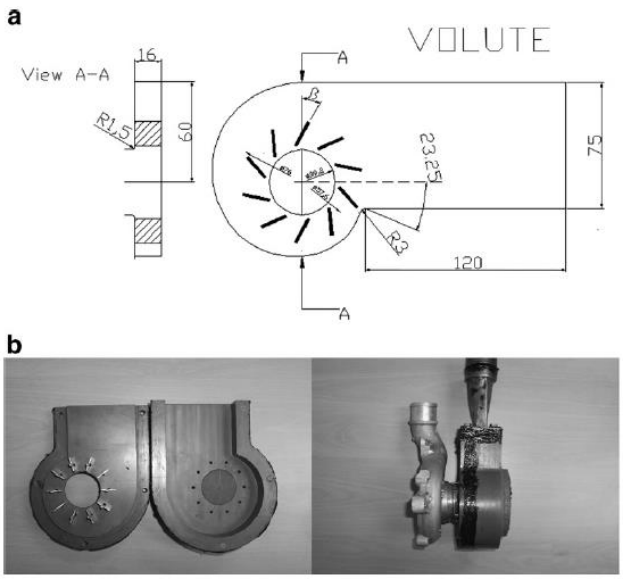

Figure 3-12. Swirl Generator designed in Valencia [68]

Also the packaging constrains were taken on board and the device designed was compact and installed in a close proximity from the compressor's inducer – normally occupied by a bend of the inlet duct. 90 degree bend has been proven to have a detrimental effect on the surge margin and therefore the elimination of this component was clearly a great advantage of the device. To make the device beneficial across the entire compressor map and with only low efficiency losses caused by its vanes a variable actuated mechanism would be needed. H. Mohtar, P. Chesse et al [69] tested their own pivoting vane mechanism (Figure 3-13) showing map extension potential at low flow rates when positive pre-whirl was applied but also pointing out some efficiency and pressure ratio degradation at high flows.

Figure 3-13. Pivoting vane mechanism [69]

Mohseni et al [70] studied numerically and experimentally three different guide vane profiles, including a symmetric reference profile, a two-piece tandem profile with a variable angle, and an s-cambered profile, together with two auxiliary profiles. Different setting angles, covering negative and positive inlet swirls, and at different operating points were considered. The results showed that tandem and s-cambered vanes had superior aerodynamic performance in comparison with the symmetric reference profile and extended

the operating range of the compressor over which the efficiency remains high. The tandem profile showed better aerodynamic performance than the s-cambered profile at negative inlet swirl, while the asymmetric s-cambered profile offered an extended range of high efficiency at positive pre-whirl. Figure 3-14 below shows a novel vane used by the authors where part of is movable and can be adjusted for a specific angle.

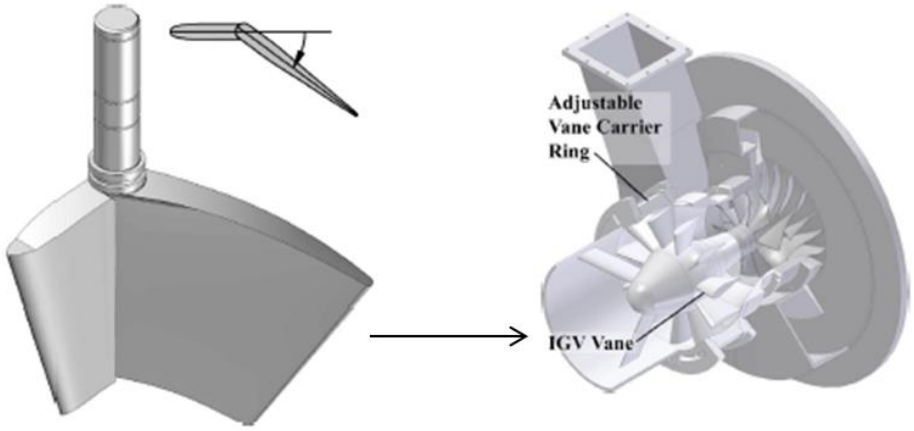

Figure 3-14. IGV mechanism designed by Mohseni et al [70]

All the above examples of the application of inlet guide vanes proved to be influential on the performance maps in steady-state conditions. M. Toussaint and P. Podevin [71] studied the effects of pre-whirl generated by several and of various design devices (Figure 3-15) during transient acceleration tests.

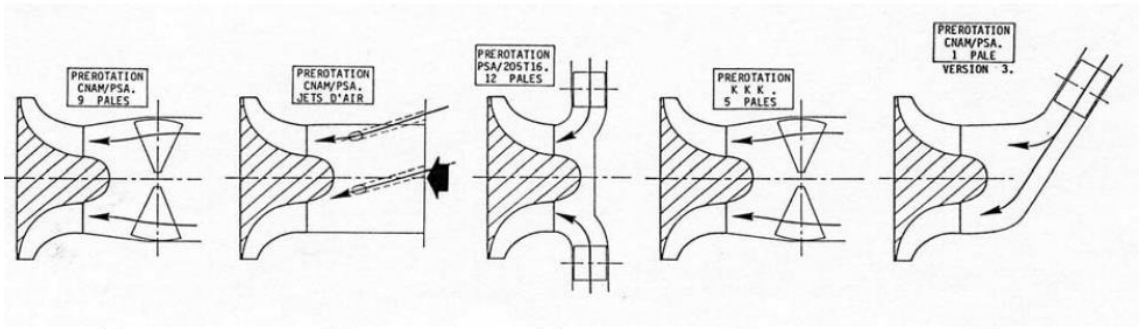

Figure 3-15. The five tested pre-rotators [71]

The figure above illustrates the schematic of all 5 tested configurations. Axial vane pre-rotators (a and d) were composed of 9 and 5 vanes whereas radial type pre-rotators of 12 and 1 vane (c and e respectively). The last configuration included a stream of a peripheral jet air which is another method for introducing pre-whirl at the compressor inlet. This particular method will be reviewed in more detail in the next section. The most important conclusions from this research is that modification of the inlet velocity triangle affects the compressor power absorbed from the turbocharger shaft (based on Euler equation) and therefore turbocharger speed can be either increased or decreased

changing the time-to-torque characteristics (turbo lag). However, it must be remembered that on a real engine operation the mass flow delivered to the engine is not regulated by pre-whirl devices therefore it cannot be concluded that IGV increases/decreases the engine power.

Variable trim compressor is fairly a new concept introduced in 2012 and based on reducing the effective maximum peripheral velocity for particles of air impacting front edges of the compressor blades (compressor inlet diameter is reduced). This is done by using a conical element directly at the compressor inlet (Figure 3-16) – altering the inlet cross section changes compressor's trim [72].

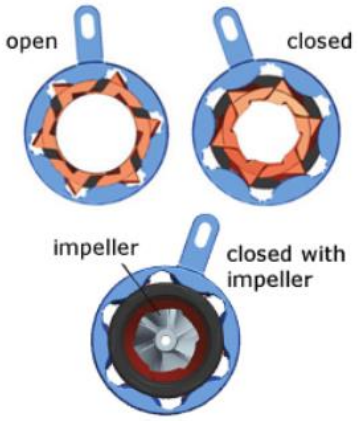

Figure 3-16. Variable trim compressor [72]

A series of numerical simulations and as well as turbocharger based experimental tests have demonstrated the potential in respect of shifting the surge line and improving compressor's efficiency. For a proper on-engine operation an electrically operated variable mechanism would be required to adjust the trim of the compressor according to an operating point.

Combination of surge suppression techniques

One of the techniques combining at least two methods for the suppression of surge or enhancement of the compressor performance was mentioned in paragraph 3.3.2 and this included air/nozzle injection operating together with the vaned diffusers. Another one includes either fixed or variable inlet guide vanes (VIGV). Iwakiri and Uchida [73] tested experimentally and modelled numerically the latter case adjusting the axial vane angle between 0 and 80 degrees. However no information was given regarding the variable mechanism. Tomita et al [74] seemed to be aware of potential issues or difficulties with the operation of the variable mechanism therefore he decided to study numerically the first case incorporating fixed angle IGV (Figure 3-17).

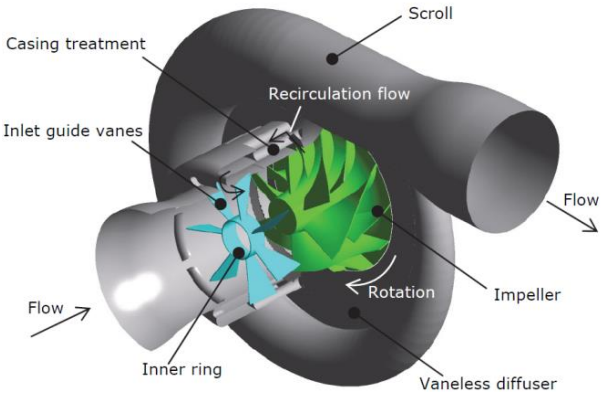

Figure 3-17. IGV arrangement studied by Tomita [74]

The number of vanes [41] was achieved optimising for efficiency and surging characteristics of the compressor under consideration. The inner ring was installed to decrease vibration and eliminate its tip leakage vortex. IGV were oriented to generate negative pre-whirl although no information regarding vane angles were provided. Generally, the overall conclusions drawn from the last 2 mentioned research studies were that the counter-rotating flow increased the compressor's pressure ratio along the entire operating range. At the same time flow unsteadiness was controlled by the casing treatment.

3.3.3 Compressor surge measurement

Despite the fact that compressor surge has been studied, defined and classified by a number of researchers [37-40, 42, 44, 75, 76] SAE J1826 code of practice [25] does not provide values of any physical parameters to quantify surge on a steady-flow test stand. It is only described as the area of severe flow reversal combined with audible coughing and banging. Similarly ASME standard for compressor measurement [77] only identifies symptoms of surge as noise, mass flow fluctuations, a drop in pressure ratio and outlet pressure or outlet temperature fluctuations. The lack of a clear and standardized definition gives a field for various interpretations of surge onset hence different surge metrics exist within industry. Galindo et al [44, 78-81] studied surge in steady-state and pulsating flow engine conditions. According to his findings surge can be indicated by the low frequency oscillations of the compressor mass flow, turbocharger speed or post compressor pressure (the most sensitive out of three). When the compressor is in surge, the FFT pressure spectrum showed higher low frequency contents than in stable operation (main frequency peak between 5 and 15Hz depending on the compressor size, the installation arrangement and operating conditions). Andersen [75] used a number of temperature sensors (Pt100) distributed axially across the inlet pipe and a 0.25mm exposed junction thermocouple installed at a distance of 2mm from inducer to measure the temperature across the entire compressor map. He concluded that the inducer temperature rise when approaching hard surge is of various magnitudes across the high pressure region of

compressor speeds therefore he found it to be useless as a surge indicator. However it could be still a valuable information when tackling NVH issues. Both Galindo and Andersen suggested that FFT analysis of pressure oscillations is necessary to detect surge in the pulsating flow. The most difficult situation for the surge onset interpretation occurs in real on-engine operation where the FFT analysis of the pressure signal is disturbed by the low frequency oscillations induced by the engine. However, a clear correlation between the noise level in car and inducer temperature rise can be observed. Another interesting surge related finding has been described by Boyce [82] in a paragraph on surge detection and control. Namely, in a limited number of tests it has been noted that when the second harmonic of the blade passing frequency reaches the same order of magnitude as the blade passing frequency, the unit is very close to surge.

3.3.4 Compressor surge modelling

Modelling of surge onset phenomenon and its active control has been extensively studied for axial compressors via so called lumped parameter technique. Most of the models are based on Greitzer's proposal introduced in 1976 [83] – this model accounted for filling and emptying of the discharging volume during surge and fluid flow delay across the compressor. In 1981 it was applied to centrifugal compressors by Hansen et al [76] and extended by Fink et al [40] for centrifugal compressors with varying speed. With the increase of the computational power many more advanced models of axial and centrifugal compression were created over the years for predicting compressor performance and surge instabilities. However, the original Greitzer model is still used mainly due to its simplicity and low order. On the other hand the lumping nature of the model limits the geometry and dimensions of the components that the Greitzer model can effectively describe. It is also inadequate to predict the dynamics associated with fluid flow in distributed systems such as acoustic waves and flow pulsations in pipelines [84].

Another way to gain an insight into the flow through the compressor is the application of three-dimensional computational fluid dynamics (CFD) The CFD codes solve Navier-Stokes governing partial differential equations (PDE) via various techniques among which a control-volume technique seems to be the most popular. This technique converts the governing equations into a set of algebraic equations which can be solved numerically. The discretisation process is performed using computational mesh. However, as there is no standardised definition describing the surge onset in experimental environment similarly there is also no clear indication on how to judge surge onset based on the CFD calculations. Some researchers run their compression models via steady-state calculations (Frozen Rotor approach) and the onset of surge is indicated when those are not capable of providing converged solutions. Convergence was defined by certain levels

of RMS residuals, the imbalances of mass, energy, momentum and fluctuation of isentropic efficiency [85], [86], [87]. Some authors run all calculations in steady-state ignoring the convergence factors and judged surge onset based on the static pressure drop when moved towards the lower mass flow rates on the same speed line – the gradient of the static pressure line becomes positive [56]. Other numerical methods for the surge onset judgement include running steady-state calculations and looking for the flow reversals at the tip clearance by examination of velocity vectors which is strongly related to surge limits [73]. Some authors switch to fully transient calculations (rotor-stator or sliding mesh approach) when experiencing difficulties with convergence near surge and examine pressure oscillations, velocity vectors and contours [88]. Finally, only fully transient calculations with moving mesh and proper time stepping are performed for the surge onset determination based on pressure fluctuations at the compressor outlet duct [89].

3.3.5 Surge stabilisation/avoidance

There are several ways of dealing with surge and these can be classified as follows [90]:

- Surge avoidance via an open loop strategy where the compressor is prevented to operate in a region near and beyond the surge line
- Surge detection and avoidance via a closed loop strategy where the system starts acting when the onset of surge is detected
- Active surge control where the flow instabilities are stabilised by one or more actuators acting on appropriate signals from a controller that receives relevant information from sensors

Because the operating point of the compressor is established by three parameters (mass flow, compressor speed, and pressure rise) all the above techniques aim at influencing at least one of these factors. Increasing mass flow may be realised by discharging into a by-pass or by feeding back excess flow through a recirculation loop or by blowing excess flow with a vent (bleeding). Compressor speed increment can be realised by modifying the torque on the compressor by changing fuel consumption of a driving turbine or by changing the voltage to a motor. Finally, modifying the pressure rise can be achieved by manipulating valves in the flow [39].

3.4 Turbocharger compressor performance with substitute gas

3.4.1 General approach

In order to directly compare turbocharger compressor performances operating with substitute gas the use of principles of similitude and dimensional analysis is required. As a result of such analysis the performance of machine or geometrically similar machines can be assessed more easily at different operating conditions. Existing designs can also

be scaled to different sizes [91]. Following the principles of dimensional analysis it is shown that the turbomachinery performance characteristics for any ideal gas can be described as function of non-dimensional mass flow parameter, non-dimensional speed, Reynolds number and λ (ratio of specific heats). The formulas for the non-dimensional mass flow parameter and non-dimensional speed are shown in Equation 7 and Equation 8 respectively. Correction for variable gas properties is achieved thanks to the use of individual gas constant (R) and ratio of specific heats (λ).

$$NDMP = \frac{\dot{m}_c \sqrt{\frac{RT_{01}}{\gamma}}}{P_{01}\pi\frac{D^2}{4}}, \tag{7}$$

$$NDSP = \frac{N_{act} D\pi}{60\sqrt{(RT_{01}\gamma)}}, \tag{8}$$

As stated in the principles of the non-dimensional analysis Reynolds number is one of the parameters affecting turbocharger performance. In the actual machine the Reynolds number is dependent on the size of the compressor, the operating conditions and the type of gas used. The changes in compressor performance due to changes in Reynolds number involve a change in efficiency, a shift in flow and change in the pressure rise. One can imagine that the understanding of the Reynolds number effects on the turbocharger compressor performance is really important when the application requires much higher Reynolds numbers than those achieved for the prototype stage tested in a test stand. This is the case for many multistage compressors used for petroleum, chemical or aerospace industry where the new Reynolds number can be more than hundred times higher when compared with the prototype. In this study only one selected turbocharger compressor is investigated therefore Reynolds number effects are expected to be of much smaller significance than given in the example above however it is still worth looking into this phenomenon. In the case when substitute gas are used the Reynolds number change is due to the viscosity or density change of the passing gas. Lots of work on Reynolds number effects have been carried out for the purpose of aerospace industry. As example of an early work it can be given work of Weigel and Ball [92] who conducted experimental studies to support the closed Brayton cycle system for space vehicle onboard power generation. Namely, they studied the effect of Reynolds number on the performance of small centrifugal compressor applicable to these systems and operating with argon. In 1979 Wiesner [93] published a paper in which he summarised on this topic based on the references dated back to forties of the previous century. Most often to account for efficiency loss due to Reynolds number change a very well-known but given in different variations empirical formula was given in literature (Equation (*9*)).

$$\frac{1-\eta}{1-\eta_{ref}} = a + (1-a)[\frac{Re_{ref}}{Re}]^n \tag{9}$$

However the identification of suitable values for n and Reynolds independent losses, a, has caused substantial difficulties and no general agreement has been reached for different machine types in the literature. Simon and Bülskämper [94] and Strub et al [95] and others recognized the variation of n related to the variation in friction factor expected in an equivalent pipe flow and they modified Equation (*9*) as follows:

$$\frac{1-\eta}{1-\eta_{ref}} = a + (1-a)\frac{\lambda}{\lambda_{ref}} \qquad (10)$$

By doing so the Reynolds number effects and related relative roughness are accounted for in the value of friction factor λ. Casey [96], described an alternative method for prediction of a single-stage efficiency change with Reynolds number based on a simplified loss model. More recently he published a journal article where he presented a unified correction method for Reynolds number, size and roughness effects on the performance of compressors [97].

The effects of λ on the turbocharger compressor with substitute gas have not been investigated to such extent as Reynolds number and only limited number of publications exist. Roberts and Sjolander [98] carried out experimental and numerical investigation for three different working fluids – air, argon and CO2. Although they could not run their tests at constant Reynolds number due to the test rig limitations they managed to do so with their CFD simulations. Comparing both experimental and numerical results they concluded that difference in compressor behavior is mainly due to the differences in γ rather than Reynolds number. They also found that the value of the mass flow parameter at choking condition varies inversely with γ. Finally they have developed a method to predict changes in pressure ratio, choking mass flow and efficiency when substitute gas are used.

3.4.2 LP EGR – an application for compressor operation with substitute gas

The main interest in investigating on turbocharger compressor performance with substitute gas is linked with the application of LP EGR. When the turbocharger compressor operates at LP EGR mode a mixture of exhaust gas and fresh air is compressed. The composition of the mixture is not fixed at all engine operating points but dependant on the EGR rate demand. The latter is based on the engine's calibration strategy and dependant on engine speed and load. Generally, there is a constant tendency for emission reduction in automotive industry and that can be also achieved by increasing EGR rates during engine operating cycles. The consequences of the compressor operation with a mixture of exhaust gas can be divided for those which mainly affect its fatigue or lifespan and therefore performance (indirectly) and those directly affecting its thermodynamic and aerodynamic performance – due to change in gas properties and as described in the

preceding paragraph. While this thesis focuses on the compressor performance change due to different properties of the substitute gas also a brief information regarding the first aspect is given. The lifespan of the compressor working at the LP EGR mode can be shortened due to so called droplet strike or particulate strike. The droplet strike occurs if the condensed droplets of water hit the surface of impeller and these can be formed if the temperature drops below the dew point. Among others, the droplet strike has been studied at Borg Warner by Karstadt, S. et al [99] by means of experimental tests where various types of water admission, droplet size and wall film at various compressor speeds were investigated. They concluded that increasing droplet diameter showed an effect by physical damage of the leading edge, and the decrease in efficiency that correlated to the surface damage of the blades. Particulate strike happens if impeller is hit by the solid particles (most of which originate from the combustion process) that were not captured by the particulate filter. Therefore to increase the resistance of the compressor against these lifespan shortening phenomena various coating treatments are available and commonly used. The experimental work on droplet and particulate and strike and impeller coatings are most often carried out internally by turbocharger manufacturers as they must deliver the application best suited product. Amongst many researchers investigating on various impeller surface treatments it can be mentioned work on anodising, plating or polymeric-based coatings performed by Burkinshaw et al [100] or nickel-phosphor coating by Munz et al [101]. Apart from the droplet and particulate strike the next important effect of compressor operation at LP EGR mode is stressing the compressor due to the increased inlet temperatures. Despite the fact that the recirculated exhaust gas is routed via an EGR cooler, compressor inlet temperatures are increased. This results in higher compressor outlet temperatures if compared with standard compression where only air is passed through the machine. Due to the compressor outlet temperature limitations set for about 210°C in case of commonly used materials (aluminium alloys) alternative solutions by means of other materials should be taken into account to maintain the thermal integrity of the turbocharger.

The study on the performance of the turbocharger compressor with substitute gas of different properties than reference gas (air) is one of the focal points of this thesis. Due to the particular interest in compressor operation at LP EGR mode the issues regarding the modelling aspects of this process are revealed here. Currently, long before any internal combustion engine gets in production it goes through many development stages. 1D performance modelling of the engine combined with a boosting system is now a standard. Such 1D codes due to their simplicity do not require full geometry of the turbocharger hardware to predict its performance. Instead, turbine and compressor maps are provided by the supplier. In most cases the supplier shall be interpreted as turbocharger

manufacturer – performance maps are generated as a result of steady-state flow mapping activity carried out on facilities popularly known as gas-stands where air flows through the compressor. Now, if LP EGR is engaged and mixture of exhaust gas and air passes through the compressor, it is the responsibility of the engine development engineer/modeller to include for any implicating changes of the turbocharger performance. However, in most cases this fact is ignored. This is surely not a valid approach since the rates of the LP EGR are constantly rising. Incorrect prediction of the turbocharger operating point will result in further propagation of errors and affect vital engine performance variables like specific fuel consumption or engine torque. The questions that shall be asked is how to correct original maps if those effects turn to be significant. Answering these questions requires to understand the current form the turbocharger performance maps are delivered at. In general, performance maps can be summarised as a series of performance data points – each of which describes the operating condition by speed, pressure ratio, mass flow and thermodynamic efficiency (more details in paragraph 1.3.). Most often mass flow through the compressor and rotational speed of the shaft are expressed as a function of other variables such as corrected mass flow (Eq.(*11*)) or mass flow parameter (Eq. (*12*)) and corrected speed (Eq. (*13*)) or speed parameter (Eq. (*14*)).

$$\dot{m}_{c,cor} = \dot{m}_c \frac{\sqrt{\frac{T_{1t}}{T_{ref}}}}{\frac{P_{1t}}{P_{ref}}}, \tag{11}$$

$$MFP = \dot{m}_c \frac{\sqrt{T_{1t}}}{P_{1t}}, \tag{12}$$

$$N_{c,cor} = N_{act} \sqrt{\frac{T_{ref}}{T_{1t}}}, \tag{13}$$

$$SP = \frac{N_{act}}{\sqrt{T_{1t}}}, \tag{14}$$

All the above equations make a valid way to describe turbocharger compressor performance if the same gas is compressed between the compared applications and this is due to a lack of any corrections linked to specific gas properties. The reason behind this is that both the gas-stand operation during mapping activity as well as standard on-engine operation occurs with air being passed through the turbocharger compressor. Therefore mass flow and speed are only corrected for a change in temperature or pressure. Surely this is not the case when LP EGR is engaged. It has been explained that in order to directly compare turbocharger compressor performance with substitute gas non-dimensional parameters need to be introduced. From the perspective of 1D modelling

code this means that appropriate correction formulas should be applied to existing air-generated maps. More information on this can be found in the following section.

3.4.3 Correction procedures for ratio of specific heats and gas constant

The fact of ignoring of any corrections of turbocharger performance maps at LP EGR operation by engine performance modelling engineers is either caused by lack of awareness of this topic or estimating those effects as negligible for the correct prediction of turbocharger operating points. With the increasing EGR rates this situation may change and errors emerging due to lack of correction activities may prove significant. GT Power - one of the most recognisable 1D engine simulation codes developed by Gamma Technologies has already a built in feature for correcting turbocharger maps. Apart from the long route EGR correcting for different Ratio of Specific Heats and Gas Constants is required for the following engine configurations [102]:

- Spark-ignition engines operating at a rich air-fuel ratio, yielding a gas that has significant amounts of carbon monoxide, lowering the inlet temperature.
- Diesel engines operating at part load conditions, for which the high air-fuel ratios will produce lower inlet temperatures at the turbine and produce a composition of the exhaust that is difference that the map measurement.
- Two-stage turbocharged engines, for which inlet temperature of the high-pressure compressor is significantly higher than the test value, and the inlet temperature of the low-pressure turbine is significantly lower than the test value.
- Natural gas engines that introduce fuel into the airflow before a compressor.

The correction process in GT Power happens during simulation run-time and is divided for two steps. First, the compressor corrected speed is corrected by multiplying it by the following factor: $\sqrt{\frac{\gamma_{ref}*R_{ref}}{\gamma_a*R_a}}$. Then after the speed is corrected the corrected mass flow is looked-up and multiplied by $\sqrt{\frac{\gamma_a*R_{ref}}{\gamma_{ref}*R_a}}$. The theory behind the corrections is based on the same non-dimensional mass flow and speed parameters as given in [103]. It is assumed that the by reaching the compressor entry the exhaust gas and fresh air are fully mixed (homogeneous mixture).

4. Turbocharger test stand facility development

Automotive radial turbochargers are characterised by performance maps and these are generated on steady-state flow facilities also known as gas stands. Such a flow rig has also been designed and developed by the author of this thesis with help and supervision of other researchers and technicians. This chapter provides the basic information regarding the rig layout and principles of a turbocharger performance map generation process.

In a very general summary there are three main modules that can be distinguished within the facility: turbine module, compressor module, and lubrication module (Figure 4-1, Figure 4-2, Figure 4-5). Additionally the turbocharger can be provided with the cooling water if equipped with water cooled bearing housing or water cooled compressor (Figure 4-6).

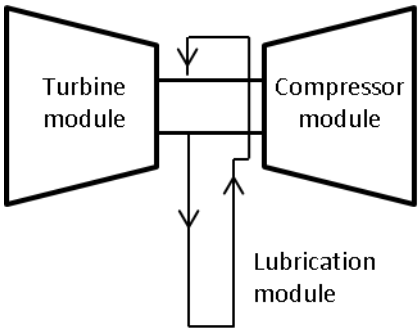

Figure 4-1. General turbocharger module arrangement

4.1 Turbocharger gas stand modules

4.1.1 Turbine feed module

The turbine feed module (Figure 4-2) consists of an air supply and heating system and is designed to deliver compressed and hot air to the turbine blades.

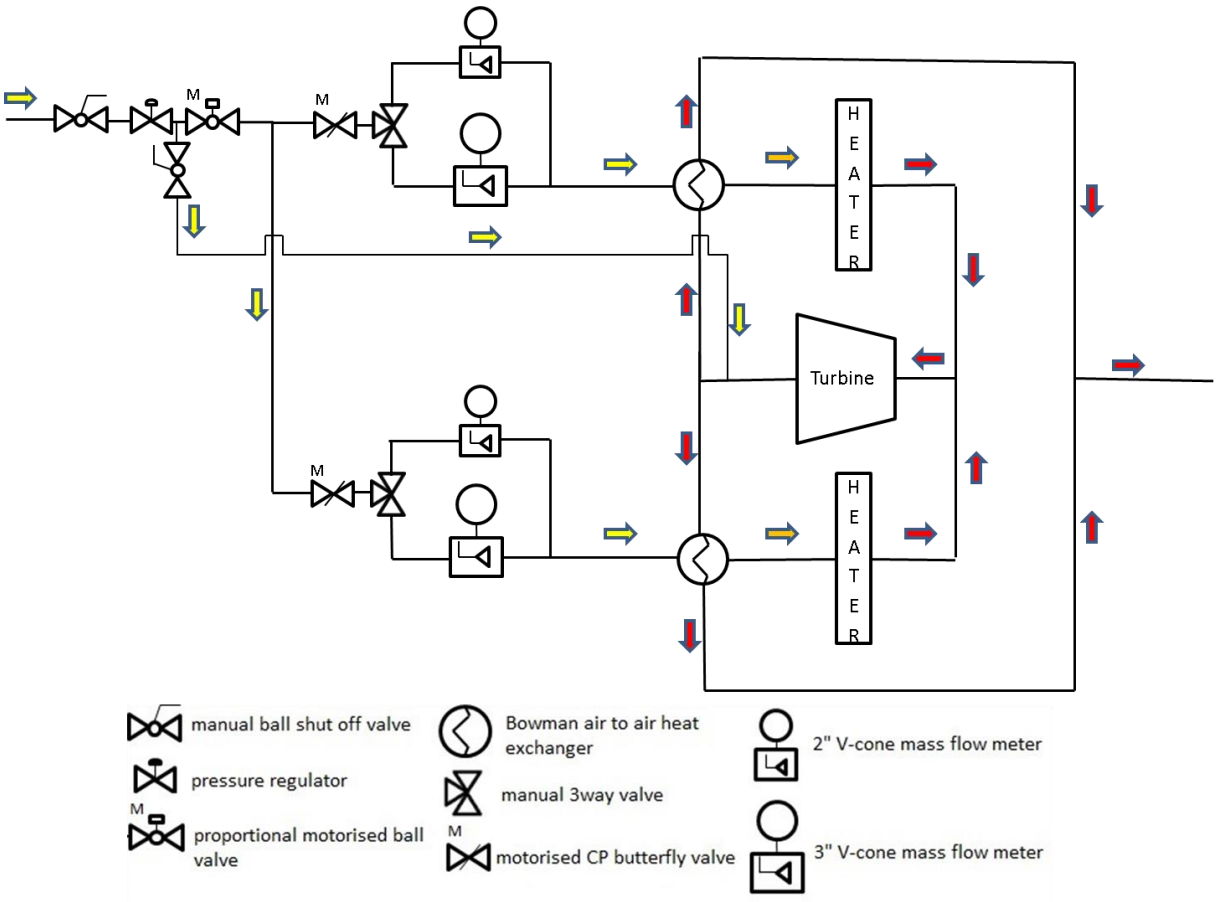

Figure 4-2. Turbine feed module

The supply air is compressed externally from the testing facility via two industrial rotary type compressors. The moisture is removed via a refrigerated compressed air drier and therefore the air arriving at the test facility is cold and dry. The control of the mass flow rate of the supply air is achieved via a number of sequential motorised valves. The parallel arrangement of the pipework where the mass flow rate can be controlled in each leg separately allows for testing of twin or double entry turbines. After the mass flow measurment point (two various range V-cones), the supply air gets through the recuperator/heat exchanger where it is heated up by the returning exhaust flow. The power of the electric heaters is controlled by the operator via the CP acquisition system. As a heater protection feature there is a bypass circuit allowing for mixing the hot post turbine air with the cold fresh air.

4.1.2 Compressor module

The standard arrangement of the compressor module is a common gas stand layout where air is drawn from the inside of the test cell upstream from the compressor and discharged to ambient after the compression process takes place. Similarly to the turbine module, there are two alternative mass flow measurement devices operating in various flow ranges. The motorised gate valve located downstream from the compressor is used

to control the pressure that it develops (and therefore the power of the compressor) and can push the compressor into surge at low mass flow rates. To reduce the noise generated during the compressor operation an inline racing silencer has been installed. The standard compressor module layout is shown in Figure 4-3.

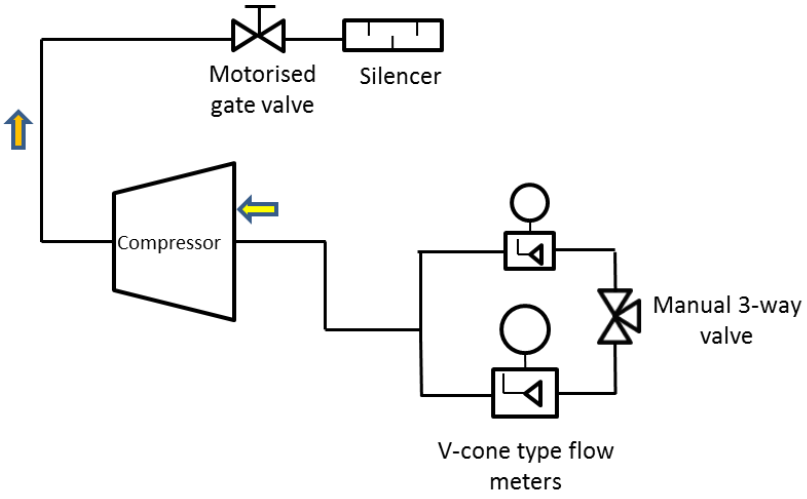

Figure 4-3. Compressor module – standard arrangement

The “closed loop” arrangement of the compressor module (Figure 4-4) is typically used to extend the range of turbine maps. This technique adjusts the compressor power and therefore the turbine load by varying the compressor inlet pressure. However, the closed-loop mode is a key arrangement allowing for compressor performance map generation with substitute gas (more details is given in section 7.1). When operating at the closed loop mode, the Bowman air-to-water heat exchanger is used to cool down the compressed air before it returns to the compressor entry. The mass of air that is circulating within the loop can be modified via a motorised pressure regulator on the low pressure side of the back pressure valve. An oil separator has been included in the system to drain the compressor loop pipes. The situation where lubricationg oil gets through the compressor seals into the compressor loop is likely to happen especially when turbine side pressure is much higher than the compressor side pressure (occurs when compressor inlet pressure is much lower than atmospheric).

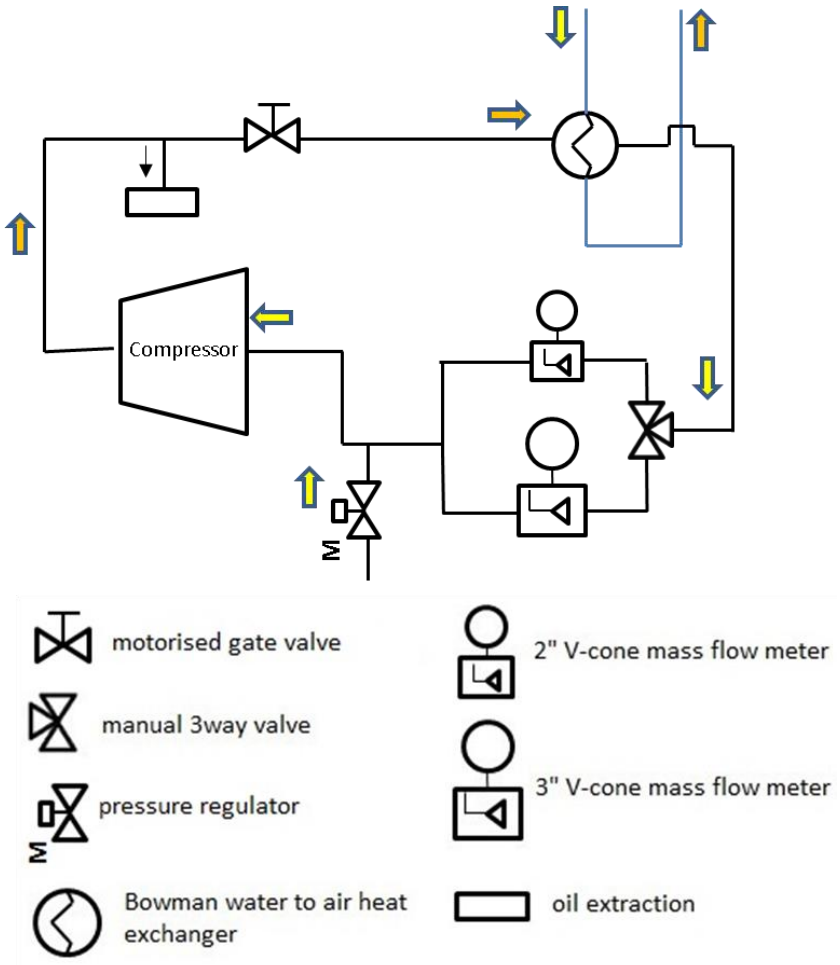

Figure 4-4. Compressor module – closed loop

4.1.3 Lubrication module

Finally, the lubrication module can be seen in Figure 4-5. The turbocharger bearing housing is fed by the engine oil conditioned by Regloplas 300s unit which is equipped with variable speed magnetic drive pump allowing for the oil flow and pressure control. The unit also has a built-in air to water heat exchanger, an immersion heater (for oil temperature control) and oil mass flow meter. Additionally an Oval Gear flow meter has been installed with signal converter for precise flow measurements and direct communication with the data acquisition PC.

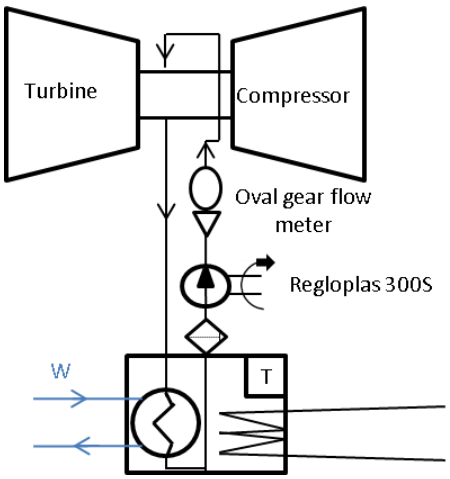

Figure 4-5. Lubrication module

4.1.4 Bearing housing/compressor cooling module

Normally the turbocharger housings are tested dry but if the turbocharger is equipped with the liquid-cooled bearing housing (or liquid-cooled compressor) the cooling water can also be provided (Figure 4-6). In this case the supply condition of the liquid shall be agreed upon by the tester and end user and recorded on the performance maps [12].

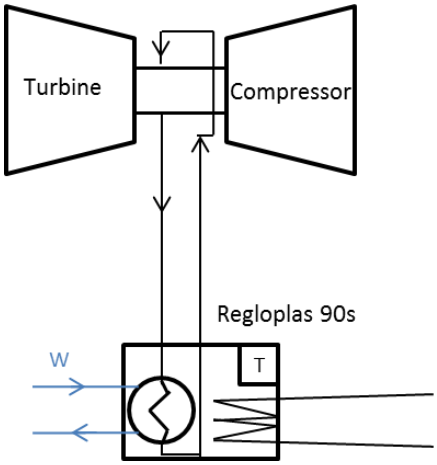

Figure 4-6. Bearing housing cooling module

4.2 Turbocharger Maps

4.2.1 Mapping methodology

Compressor and turbine maps are generated as a result of mapping activity. The data is collected simultaneously for both components. The standard turbocharger mapping is performed at a constant turbine inlet temperature which can be controlled by adjusting the power of electric heaters. Usually, the turbine inlet temperature varies between 550°C and 600°C depending on the turbocharger manufacturer.

Before the process of mapping is begun a warm up stage takes place during which the electric power of the heaters is gradually increased until the desired turbine inlet temperature is reached. Oil and coolant (for water-cooled bearing housings) temperatures are fixed at 90°C. A number of operational points is measured across the constant compressor speed lines (typically 7-10 points per speed line) starting at high flow rates and low pressure ratios (choke) and finishing in the region of low mass flow rates and high pressure ratios (surge). The compressor mass flow rate is adjusted by controlling the back-pressure valve (closing the valve reduces the mass flow through the compressor). The turbocharger speed is controlled by adjusting the turbine mass flow rate and pressure along with the compressor power (mass flow control).

4.2.2 Compressor maps

A compressor performance map is a plot of mass flow rate (corrected mass flow or mass flow parameter) and total-to-total pressure ratio at various rotational speeds (corrected speed or speed parameter) and with superimposed lines of isentropic efficiency. Alternatively, the compressor efficiency is plotted separately against the total-to-total pressure ratio or the corrected mass flow. The central stable operating area of the performance chart is separated from two unstable regions by two boundary lines – the surge line on the left hand side at lower mass flows and the choke line on the right hand side at higher mass flows. The choke region is linked to high gas velocity and low efficiency. A compressor is choking if no more air can be squeezed through a certain cross section area at a given compressor speed (more mass flow through the compressor may be gained by increasing its speed). It is a common practise among turbocharger manufacturers to define the choke line by the point where compressor efficiency drops below a certain unacceptable value. Surge is simply compressor instability at low mass flow rates. The surge onset criterion is based on the fluctuations of the post compressor static pressure.

The compressor performance parameters are calculated as follows:

a) Compressor total-to-total pressure ratio, PR_c

$$PR_c = \frac{P_{2t}}{P_{1t}}, \tag{15}$$

b) Compressor corrected mass flow, $\dot{m}_{c,cor}$

$$\dot{m}_{c,cor} = \dot{m}_c \frac{\sqrt{\frac{T_{1t}}{T_{ref}}}}{\frac{P_{1t}}{P_{ref}}}, \tag{16}$$

c) Compressor corrected speed, $N_{c,cor}$

$$N_{c,cor} = N_{act}\sqrt{\frac{T_{ref}}{T_{1t}}}, \tag{17}$$

d) Compressor isentropic efficiency, η_c

$$\eta_c = \frac{T_{1t}[(\frac{P_{2t}}{P_{1t}})^{\left(\frac{\gamma_{c,avg}-1}{\gamma_{c,avg}}\right)}-1]}{T_{2t}-T_{1t}}, \quad (18)$$

In order to calculate the above performance parameters, the following formulas are used:

- Compressor total inlet pressure, P_{1t}

$$P_{1t} = P_{1s} + [\frac{\rho_1 V_1^2}{2}], \quad (19)$$

- Compressor total outlet pressure, P_{2t}

$$P_{2t} = P_{2s}[\frac{T_{2t}}{T_{2s}}]^{\left(\frac{\gamma_{c,2}}{\gamma_{c,2}-1}\right)}, \quad (20)$$

- Compressor total inlet temperature, T_{1t}

$$T_{1t} = T_{1s} + [\frac{V_1^2}{2c_{p_{c,1}}}], \quad (21)$$

- Compressor total outlet temperature, T_{2t}

$$T_{2t} = T_{2s} + [\frac{V_2^2}{2c_{p_{c,2}}}], \quad (22)$$

- Compressor inlet gas density, ρ_1

$$\rho_1 = \frac{P_{1s}}{RT_{1s}}, \quad (23)$$

- Compressor outlet gas density, ρ_2

$$\rho_2 = \frac{P_{2s}}{RT_{2s}}, \quad (24)$$

- Compressor inlet gas velocity, V_1

$$V_1 = \frac{\dot{m}_c}{\rho_1 A_1}, \quad (25)$$

- Compressor outlet gas velocity, V_2

$$V_2 = \frac{\dot{m}_c}{\rho_2 A_2}, \quad (26)$$

- Compressor inlet cross section area, A_1

$$A_1 = \frac{\pi d_1^2}{4}, \quad (27)$$

- Compressor outlet cross section area, A_2

$$A_2 = \frac{\pi d_2^2}{4}, \quad (28)$$

- Compressor inlet specific heat of air, $c_{p_{c,1}}$

$$c_{p_{c,1}} = R\frac{\gamma_{c,1}}{\gamma_{c,1}-1}, \quad (29)$$

- Compressor outlet specific heat of air, $c_{p_{c,2}}$

$$c_{p_{c,2}} = R\frac{\gamma_{c,2}}{\gamma_{c,2}-1}, \quad (30)$$

- Compressor average specific heat of air, $c_{p_{c,avg}}$

$$c_{p_{c,avg}} = \frac{(c_{p_{c,1}}+c_{p_{c,2}})}{2}, \quad (31)$$

- Compressor inlet ratio of specific heats, $\gamma_{c,1}$

$$\gamma_{c,1} = 1.42592 - 8.03974(10^{-5})T_{1s} \quad (32)$$

- Compressor outlet ratio of specific heats, $\gamma_{c,2}$

$$\gamma_{c,2} = 1.42592 - 8.03974(10^{-5})T_{2s} \quad (33)$$

- Compressor average ratio of specific heats, $\gamma_{c,avg}$

$$\gamma_{c,avg} = \frac{\gamma_{c,1}+\gamma_{c,2}}{2}, \quad (34)$$

- Compressor actual mass flow rate of air, $\dot{m}_c$

$$\dot{m}_c = \rho_{cv1}\dot{Q}_c, \quad (35)$$

- Compressor actual volumetric flow rate of air, $\dot{Q}_c$

$$\dot{Q}_c = F_a C_d Y_{cv1} k_1 \sqrt{\frac{\Delta P}{\rho_{cv1}}}, \quad (36)$$

- Compressor V-cone gas expansion factor, Y_{cv1}

$$Y_{cv1} = 1 - (0.649 + 0.696\beta^4)\frac{\Delta P_{cv1}}{1.4P_{cv1s}}, \quad (37)$$

- Compressor V-cone entry gas density, ρ_{cv1}

$$\rho_{cv1} = \frac{P_{cv1s}}{RT_{cv1s}}, \quad (38)$$

4.2.3 Turbine maps

Similarly to compressors, radial turbines are commonly characterised by performance parameters. These are:

a) Turbine total-to-static pressure ratio, PR_t. The formulation, in contrast to the compressor, does not take post turbine kinetic energy of air into account as it is not further utilised.

$$PR_c = \frac{P_{4s}}{P_{3t}}, \quad (39)$$

b) Turbine corrected mass flow, $\dot{m}_{t,cor}$

$$\dot{m}_{t,cor} = \dot{m}_t \frac{\sqrt{\frac{T_{3t}}{T_{ref}}}}{\frac{P_{3t}}{P_{ref}}}, \quad (40)$$

c) Turbine corrected speed, $N_{t,cor}$

$$N_{t,cor} = N_{act}\sqrt{\frac{T_{ref}}{T_{3t}}}, \quad (41)$$

d) Turbine efficiency, η_t

$$\eta_t = \frac{P_c/\eta_{mech}}{\dot{m}_t c_{p_{t,avg}} T_{3t}[1 - (\frac{1}{PR_t})^{(\frac{\gamma_{t,avg}-1}{\gamma_{t,avg}})}]} \quad (42)$$

To calculate the above parameters the following formulas are used:

- Turbine total inlet pressure, P_{3t}

$$P_{3t} = P_{3s}[\frac{T_{3t}}{T_{3s}}]^{\left(\frac{\gamma_{t,3}}{\gamma_{t,3}-1}\right)}, \quad (43)$$

- Turbine total inlet temperature, T_{3t}

$$T_{3t} = T_{3s} + [\frac{V_3^2}{2c_{p_{t,3}}}], \quad (44)$$

- Turbine inlet gas density, ρ_3

$$\rho_3 = \frac{P_{3s}}{RT_{3s}}, \quad (45)$$

- Turbine inlet gas velocity, V_3

$$V_3 = \frac{\dot{m}_t}{\rho_3 A_3}, \quad (46)$$

- Turbine inlet cross section area, A_3

$$A_3 = \frac{\pi d_3^2}{4}, \quad (47)$$

- Turbine inlet specific heat of air, $c_{p_{t,3}}$

$$c_{p_{t,3}} = R\frac{\gamma_{t,3}}{\gamma_{t,3}-1}, \quad (48)$$

- Turbine outlet specific heat of air, $c_{p_{t,4}}$

$$c_{p_{t,4}} = R\frac{\gamma_{t,4}}{\gamma_{t,4}-1}, \quad (49)$$

- Turbine average specific heat of air, $c_{p_{t,avg}}$

$$c_{p_{t,avg}} = \frac{(c_{p_{t,3}} + c_{p_{t,4}})}{2}, \quad (50)$$

- Turbine inlet ratio of specific heats, $\gamma_{t,3}$

$$\gamma_{t,3} = 1.42592 - 8.03974(10^{-5})T_{3s}, \quad (51)$$

- Turbine outlet ratio of specific heats, $\gamma_{t,4}$

$$\gamma_{t,4} = 1.42592 - 8.03974(10^{-5})T_{4s}, \quad (52)$$

- Turbine average ratio of specific heats, $\gamma_{t,avg}$

$$\gamma_{t,avg} = \frac{(\gamma_{t,3}+\gamma_{t,4})}{2}, \quad (53)$$

- Turbine actual mass flow rate of air, $\dot{m}_t$

$$\dot{m}_t = \rho_{tv3}\dot{Q}_t, \quad (54)$$

- Turbine actual volumetric flow rate of air, $\dot{Q}_t$

$$\dot{Q}_t = F_a C_d Y_{tv3} k_1 \sqrt{\frac{\Delta P}{\rho_{tv3}}}, \quad (55)$$

- Turbine V-cone gas expansion factor, Y_{tv3}

$$Y_{tv3} = 1 - (0.649 + 0.696\beta^4)\frac{\Delta P_{tv3}}{1.4 * P_{tv3s}}, \quad (56)$$

- Turbine V-cone entry gas density, ρ_{tv3}

$$\rho_{tv3} = \frac{P_{tv3s}}{RT_{tv3s}}, \quad (57)$$

- Compressor power, P_c

$$P_c = \dot{m}_c c_{p_{c,avg}} (T_{2t} - T_{1t}) \quad (58)$$

4.2.4 Turbomachinery performance measurement

Measurement of static temperature and pressure that are further used in the calculation of performance parameters is based on SAE's and ASME's codes of practise. In particular these are SAE J1826 Turbocharger Gas Stand Test Code, SAE J1723 Supercharger Testing Standard and ASME PTC 10 1997 Performance Test Code on Gas Turbines. Volumetric flow measurement both on the turbine and compressor side of the testing facility is captured by differential pressure type V-cone flow meters. The principal theory among these is Bernoulli's theorem for the conservation of energy in a closed pipe. This states that for a constant flow, the pressure in a pipe is inversely proportional to the square of the velocity in the pipe. Finally, turbocharger speed is measured with an eddy current speed sensor.

5. Uncertainty of the turbocharger performance maps

Researchers who ever performed an experimental testing must have wondered how confident could they be regarding the measured results. It is no surprise that with every measurement there is the dilemma of the measurement error and overall uncertainty of the system. It is no different when it comes down to the turbocharging testing and turbocharger performance map generation. For this reason, based on the selected turbocharger this chapter discusses the uncertainty regarding the data measurement during the turbocharger performance map generation. This exercise helped to identify and understand the dominant sources of uncertainties which are caused either by chosen sensors and their accuracies and other errors associated with the commonly used mapping approach (heat transfer due to high temperature gradient between the turbine and compressor). The errors were identified across the entire turbocharger map and therefore allowed the author to target the map accuracy improvement in the specific regions of performance charts. The first part of the uncertainty analysis considers a situation, where a perfect installation of relevant measurement instrumentation is assumed and therefore it is acknowledged that the only source of measurement uncertainty is due to the device error. As a result of such uncertainty analysis, compressor and turbine performance maps with the superimposed error bars were generated. This allowed assessment of the quality of the gathered data and show the potential for improving the accuracy of the obtained data in the particular region of the map once the significance of the respective measurement had been addressed. The accuracy of the compressor and turbine maps were compared over several scenarios with respect to various pressure and temperature sensors. In the second part of this chapter attention was brought to the performance uncertainty due to the heat transfer effects in the low turbocharger speed region. The chosen turbocharger has been mapped in hot conditions (500°C at the turbine inlet) and two semi-adiabatic conditions with different temperatures of the lubricating oil. The experimentally approached data was then compared with the Wave (1D model) extrapolated data. Finally, as an alternative to experimentally obtained data a work contributing to the turbocharger heat transfer modelling is summarised. This part of the study is described in two separate subsections. The first one discusses a 3D conjugate heat transfer modelling approach that was used to understand the thermal behaviour of the turbocharger and feed the in-house lump capacitance turbocharger heat transfer model whereas the second one presents a validation of a literature based function that estimates the amount of heat transferred to the compressor at various operating points across the performance map.

5.1 Uncertainty of the turbocharger maps with respect to the sensor accuracy

In order to understand how the particular measured physical quantities affect the overall uncertainty of the turbocharger performance maps Type B evaluation (adequate for single-sample experiments) has been carried out. The uncertainty of a single performance parameter when several independent variables are used is based on RSS (Root Sum Squared) given in Equation (*59*). Therefore to calculate the final uncertainty of such parameter partial derivatives with respect to each variable need to be calculated. All the formulas used to calculate the uncertainties of compressor and turbine performance parameters are shown in Appendix A and B respectively.

$$\delta G = \sqrt{\sum_{i=1}^{n} \left(\frac{\partial G}{\partial Y_i} \delta Y_i\right)^2} \tag{59}$$

Uncertainty of any physical measurement that is taken during the performance mapping is commonly expressed by standard deviation (Equation (*60*)) and is proportionally dependent on the accuracy of the used sensor.

$$SD = \frac{e}{\sqrt{3}} \tag{60}$$

The list of sensors utilised during the performance map measurement of the relevant turbocharger is given in Table 1.

Table 1. List of sensors – turbocharger gas stand

Sensor location	Measured quantity	Sensor model	Manufacturer	Accuracy	Operating range	Number of	Mechanical Averaging	Mathematical Averaging
Inside the test cell	Atmospheric Pressure	PX409-32BV	Omega	0.08%	0-104.8kPa absolute	1	/	/
Compressor housing	Turbocharger speed	DZ135	Micro Epsilon	0.22361%	0-400000 rpm	1	/	/
Compressor Intake pipework	Smaller Vc-cone Differential Pressure	Sitrans P DSIII transmitter	Siemens	0.51%	0-60 mbar	1	/	/
	Larger V-cone Differential Pressure	Sitrans P DSIII transmitter	Siemens	0.51%	0-250mbar	1	/	/
Turbine feed pipework	Smaller Vc-cone Differential Pressure	Sitrans P DSIII transmitter	Siemens	0.51%	0-250mbar	1	/	/
	Larger V-cone Differential Pressure	Sitrans P DSIII transmitter	Siemens	0.51%	0.250mbar	1	/	/
Prior to Smaller Compressor V-cone	Static Temperature	Pt100	TC Direct	±	(-50°C to 200°C)	1	/	/
	Static Pressure	PX312-030AV	Omega	0.25%	0-206.8kPa absolute	1	/	/
Prior to Larger Compressor V-cone	Static Temperature	Pt100	TC Direct	±	(-50°C to 200°C)	1	/	/
	Static Pressure	PX312-050AV	Omega	0.25%	0-344.7kPa absolute	1	/	/
Prior to Smaller Turbine V-cone	Static Temperature	Pt100	TC Direct	±	(-50°C to 200°C)	1	/	/
	Static Pressure	PX312-100GV	Omega	0.25%	0-689.5kPa above atm.	1	/	/
Prior to Larger Turbine V-cone	Static Temperature	Pt100	TC Direct	± (0.3+0.0005*t)	(-50°C to 200°C)	1	/	/
	Static Pressure	PX302-100AV	Omega	0.25%	0-689.5kPa absolute	1	/	/
Pre-Compressor Measuring section	Absolute Static Pressure	PXM419-3.5BAV	Omega	0.08%	0-350kPa absolute	1	YES	/
	Static Temperature	Pt100	TC Direct	± (0.3+0.0005*t)	(-50°C to 200°C)	4	/	YES
Post-Compressor Measuring section	Static Pressure	PXM419-002BGV	Omega	0.08%	0-200kPa above atm.	1	YES	/
	Static Temperature	Pt100	TC Direct	± (0.3+0.0005*t)	(-50°C to 200°C)	4	/	YES
Pre-Turbine Measuring section	Static Pressure	PXM419-007BGV	Omega	0.08%	0-690kPa above atm.	1	YES	/
	Static Temperature	1.5mm k-thermocouple	TC Direct	higher of 2.5°C or 0.75%	(-50°C to 1100°C)	4	/	YES
Post-Turbine Measuring section	Static Pressure	PXM419-007BGV	Omega	0.08%	0-690kPa above atm.	1	YES	/
	Static Temperature	1.5mm k-thermocouple	TC Direct	higher of 2.5°C or 0.75%	(-50°C to 1100°C)	4	/	YES

Generally, the selection of sensors is not an easy task, with the compromise made between the application requirements, cost, range and accuracy. The SAE turbocharger gas stand code of practise [25] sets the accuracy limitation on pressure (±0.5%), temperature (±0.5%), airflow (±1%), speed (±0.5%). In order to correctly interpret these limitations and calculate the relevant sensor uncertainty the following subsections give details regarding the sensor accuracies.

5.1.1 Pressure sensors

According to *IEC 61298-2 (*International Electro-technical Commission) and regardless of the type of the used pressure sensor the accuracy of sensor must include hysteresis, non-repeatability and non-linearity.

Hysteresis is the maximum difference in sensor output at a pressure when that pressure is first approached with an increasing value and then approached with pressure decreasing during a full span pressure cycle.

Non-repeatability is the maximum difference in output when the same pressure is applied, consecutively, at the same conditions and approaching from the same direction.

Non-linearity - Best Fit Straight Line (BFSL) Non-Linearity or Terminal Point Non-Linearity are usually given out of three available methods. Different non-linearity percentages can be achieved (Figure 5-1.

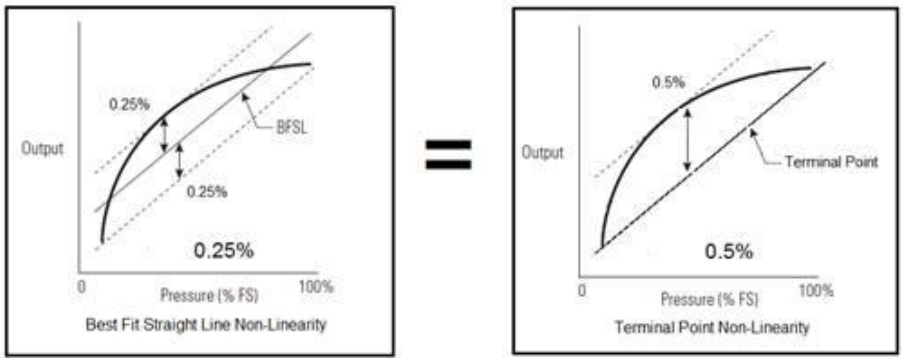

Figure 5-1. Non-linearity of measurement

The IEC standard does not specify how these factors are combined into a single (total) accuracy and therefore care is needed when comparing and selecting pressure sensors. There are three available methods to combine hysteresis, non-repeatability and non-linearity into a total (combined) accuracy: Rum of Sum Squared, Root of Mean Squared and Summed Factors. The methods in which the values are combined have an impact on the total accuracy as shown in Figure 5-2.

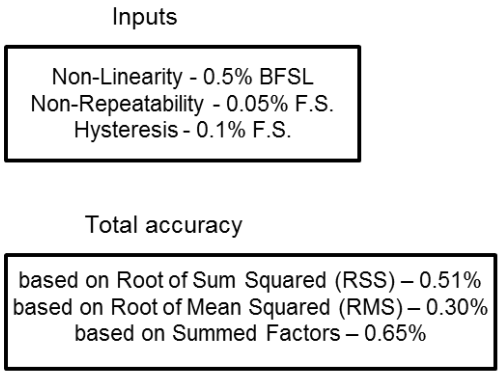

Figure 5-2. Example of sensor (total) accuracy based on various combining methods

The accuracy of the pressure sensors is usually given either as a percentage of the reading or a percentage for the full scale (range) of the sensor. In the former case the accuracy of sensor is calculated by multiplying the accuracy percentage by the pressure reading. Therefore, the lower the pressure measurement, the better the accuracy. Pressure sensors that have a percent reading specification are usually provided with a “floor” specification. The floor specification takes into account uncertainties such as resolution and measurement noise which may be negligible at higher pressures but are of much more significance at lower pressures. For instance, an accuracy specification may read 0.2% of reading for 30 to 100% of range and 0.05% of full scale below 30% of the range. The 0.05% of full scale specification is considered the floor specification. This method of

specification is often used because it aligns well with the typical performance of pressure gauges. Generally, the closer you measure to atmospheric pressure the better the performance of the gauge. Accuracy as a percentage of full scale is calculated by multiplying the accuracy percentage by the full scale pressure. This is a more simple method of specification and is most commonly used in industry because it is easy to calculate and interpret. Denoting the accuracy as percent full scale is a more conservative way of specifying the pressure sensor because typically the sensor doesn't perform the same over its full range. As mentioned before it usually will perform more accurately as you approach atmospheric pressure. Following this method to gain the most accurate measurement, sensors of narrowest range shall be used. To conclude on the above methods one method of specification is not better than another, it is just different. The accuracy of the measurement depends mainly on the pressure that is measured. It is important to know how to interpret the different specifications types and be able to compare one versus another. All the pressure sensors used at the turbocharger gas stand at Bath University are specified to have the accuracy based on the latter method (based on full scale measurement). Below, some examples are given on the calculation of overall uncertainty of pressure measurement. All the calculations were carried out in Microsoft Excel spreadsheet where all the required formulas were implemented.

5.1.2 Temperature sensors

Two types of temperature sensors are commonly used during turbocharger performance mapping exercise at steady-state gas stands: resistance temperature detectors (RTDs) and thermocouples. The sensing element of RTD is made of platinum, copper or nickel. The most often used are platinum resistance thermometers (PRTs). Thermocouples are less accurate than PRTs in low temperatures but can be used also at high temperatures unsuited for PRTs and for this reason thermocouples are used mainly to measure high temperature turbine gas whereas PRTs are used elsewhere at lower temperatures.

PRT tolerances based on resistance v temperature tables and defined by *IEC 60751* and *ASTM E-1137* are given below in Table 3 and Table 3 respectively.

Table 2. PRT classes as given by IEC 60751

Class and accuracy calculation formula	Range
Class C = ±(0.60 + 0.01t)	dependant on the sensor construction
Class B = ±(0.30 + 0.005t)	SAA
Class A = ±(0.15 + 0.002t)	SAA
Class AA = ±(0.10 + 0.0017t)	SAA
Class 1/5DIN = ±1/5(0.3 + 0.005|t|)	SAA
Class 1/10DIN = ±1/10(0.3 + 0.005|t|)	SAA

Table 3. PRT grades as given by ASTM E-1137

Class and accuracy calculation formula	Range
Grade A = ±[0.13 +0.0017|t|] °C	dependant on the sensor construction
Grade B =±[0.25 +0.0042|t|] °C	SAA

Thermocouple tolerances as specified by *IEC 60584-2* and *ASTM E230* and are given in Table 4.

Table 4. Typical thermocouple accuracies

Model	Alloys	Standard	Class	Temperature range	Accuracy values
K, *N*	NiCr-NiAl (NiCr-Ni), *NiCrSi-NiSi*	IEC 60584 part 2	1	-40 ... +1000 °C	±1.5 °C or 0.0040 · | t |
			2	-40 ... +1200 °C	±2.5 °C or 0.0075 · | t |
		ASTM E230	Special	0 ... +1260 °C	±1.1 °C or ±0.4 %
			Standard	0 ... +1260 °C	±2.2 °C or ±0.75 %
J	Fe-CuNi	IEC 60584 part 2	1	-40 ... +750 °C	±1.5 °C or 0.0040 · | t |
			2	-40 ... +750 °C	±2.5 °C or 0.0075 · | t |
		ASTM E230	Special	0 ... +760 °C	±1.1 °C or ±0.4 %
			Standard	0 ... +760 °C	±2.2 °C or ±0.75 %
E	NiCr-CuNi	IEC 60584 part 2	1	-40 ... +800 °C	±1.5 °C or 0.0040 · | t |
			2	-40 ... +900 °C	±2.5 °C or 0.0075 · | t |
		ASTM E230	Special	0 ... +870 °C	±1.0 °C or ±0.4 %
			Standard	0 ... +870 °C	±1.7 °C or ±0.5 %
T	Cu-CuNi	IEC 60584 part 2	1	-40 ... +350 °C	±0.5 °C or 0.0040 · | t |
			2	-40 ... +350 °C	±1.0 °C or 0.0075 · | t |
			3	-200 ... +40 °C	±1.0 °C or 0.015 · | t |
		ASTM E230	Special	0 ... +370 °C	±0.5 °C or ±0.4 %
			Standard	-200… 0 °C	±1.0 °C or ±1.5 %
			Standard	0 ... +370 °C	±1.0 °C or ±0.75 %
R, *S*	Pt13%Rh-Pt, *Pt10%Rh-Pt*	IEC 60584 part 2	1	0 ... +1600 °C	±1.0 °C or ±[1 + 0.003 (t - 1100)] °C
			2	0 ... +1600 °C	±1.5 °C or ±0.0025 · | t |
		ASTM E230	Special	0 ... +1480 °C	±0.6 °C or ±0.1 %
			Standard	0 ... +1480 °C	±1.5 °C or ±0.25 %
B	Pt30%Rh-Pt6%Rh	IEC 60584 part 2	2	+600... +1700 °C	±0.0025 · | t |
			3	+600... +1700 °C	±4.0 °C or ±0.005 · | t |
		ASTM E230	Special	/	/
			Standard	+870... +1700 °C	±0.5 %

During the experimental campaign (mapping activity) carried out on Honeywell GT17 turbocharger the pre and post-compressor side temperature measurements were taken with Class A RTD sensors, all other measurements of the gas at temperatures below 200°C with Class B RTD sensors. Finally, pre- and post-turbine temperatures were measured with k-type thermocouples. The examples of calculation of the temperature measurement uncertainty are given below for the post-compressor pre- turbine temperatures measured with RTD and thermocouple respectively.

In the first example the measured post-compressor temperature is 150°C (mean arithmetic value of four separate measurements at various depths as per the SAE code of practise). The accuracy (error) of the used sensor is calculated as follows:

$$e_{T2s} = \pm(0.15 + 0.002\mathrm{t}) = \pm(0.15 + 0.002 * 150) = \pm 0.45°\mathrm{C}$$

Based on the above accuracy the uncertainty of the measurement is calculated as follows:

$$\delta T_{2s} = \pm\frac{e}{\sqrt{3}} = \pm\frac{0.45°\mathrm{C}}{\sqrt{3}} = \pm 0.26°\mathrm{C}$$

In the second example the pre-turbine temperature is 550°C (also arithmetic mean as above). The accuracy (error) of the used sensor is either 2.5°C or 0.75%*t whichever is higher. In this case the latter is the higher value:

$$e_{T3s} = \pm 0.75\% * 550°\mathrm{C} = \pm 4.13°\mathrm{C}$$

Based on the above accuracy the uncertainty of the measurement is calculated as follows:

$$\delta T_{3s} = \pm\frac{e}{\sqrt{3}} = \pm\frac{4.13°\mathrm{C}}{\sqrt{3}} = \pm 2.38°\mathrm{C}$$

When preparing for any experimental testing apart from understanding the differences in accuracy and temperature range limitations between PRTs and thermocouples it shall also be acknowledged the supplier recommendations regarding the installation of sensors. This is mainly related to the construction and operating principles of sensors. In simple words a thermocouple is a device made by two different wires joined at junction end which is immersed inside the environment which temperature is to be measured (Figure 5-3). Due to the temperature difference between junction end and tail end a voltage difference can be measured between the two thermo-elements (wire 1 and wire 2) at the tail end. Thus, the critical thing from the installation point of view is the placement of the junction end located at the end tip of the thermocouple's metal sheath.

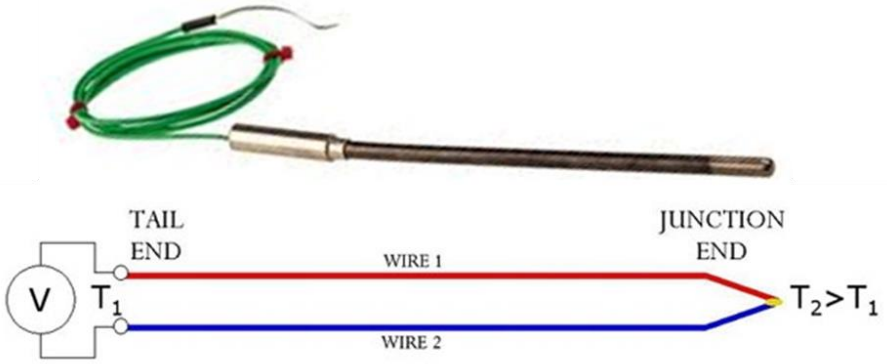

Figure 5-3. Typical k-type thermocouple

Resistance Temperature Detectors unlike thermocouples determine the temperature measuring the resistance of pure electrical wire. In RTD devices copper, nickel and platinum are the most widely used metals which have different resistance variations with respective to the temperature changes. That is called resistance-temperature characteristics. Regardless of the construction type (2-wire, 3-wire or 4-wire) the RTDs unlike thermocouples have a specific sensing length over which the value of resistance is integrated. As an example the photo below (Figure 5-4) shows the construction of the 3-wire Class B Pt100 (upper) and 4-wire Class 1/10DIN Pt100. The lower accuracy class device has a sensing length of 10mm whereas it's 20mm for the high accuracy device.

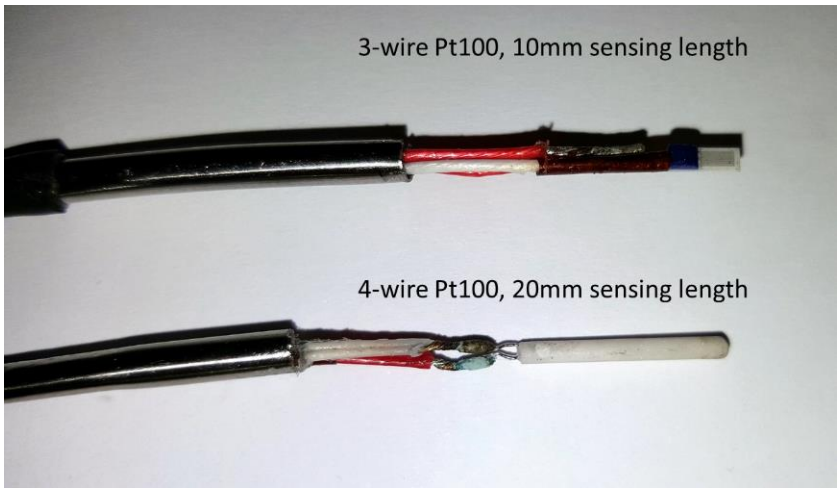

Figure 5-4. Various construction of Pt100

This information shall be taken into account when installing the sensors - the most correct temperature reading is made when the centre of the sensing coil is placed in the location where the temperature is to be measured. Another important aspect when using RTDs is the recommended immersion depth which informs how deeply the sensor shall be immersed in the environment to reach the thermal equilibrium. If this requirement is not followed the sensor loses its accuracy due to the conductive heat transfer along the metal stem (sheath). The recommended immersion depth for the RTDs shown in (Figure 5-4) above is 5cm and 15cm respectively. It can be imagined that the immersion depth of 15cm is rather unlikely to be kept at majority of turbocharger gas stands as the pipes are of lower diameter. In conclusion, in order to maintain the best accuracy of the temperature measurements the selection of the temperature sensor shall be made based on the operating temperature range, location of the sensing part of the device and it's recommended immersion depth (in case of RTDs).

5.1.3 Flow sensors

The turbocharger gas stand installed is equipped with several differential pressure type V-cone mass flow meters. These devices gained their popularity due to their robustness and high accuracy. Despite its popularity the device is not governed by any standards

like ISO 5167 that covers Venturi tubes, orifice plates and nozzles [104]. For this reason the V-cone meters are not manufactured to a specified tolerance and require individual calibration before use. McCrometer - the manufacturer of the V-cones installed at Bath University specifies the accuracy of the prime element as high as ±0.5% of flow rate reading. It is also highlighted that the level of accuracy is dependent to a degree on application parameters and secondary instrumentation (Siemens differential pressure sensor). The overall uncertainty of the mass flow measurement combines the following uncertainties:

- Uncertainty related with the creation of differential pressure by the V-cone prime element,
- Uncertainty of differential pressure measurement,
- Gas density uncertainty (temperature and pressure sensors located upstream of the V-cone meter).

5.1.4 Rotational speed sensor

The measurement of the rotational speed of the turbocharger shaft is made by speed sensor. Generally, the errors in the measurement of physical speed are fairly low – SAE standard recommends a maximum error of 0.5% of the reading value however it is common to have rotational speed meters with the error band of 0.2% [29]. Micro Epsilon DZ 135 eddy current sensor was used at the turbocharger test rig within the experimental campaign. It is characterised by the combined accuracy of 0.22361% for Full Scale Output (FSO). The given accuracy combines the errors of linearity (0.2%) and resolution (0.1%). The sensor's range is between 0 and 400.000 rpm. An error in the rotational speed measurement will indirectly affect the measurement of pressure ratio.

5.1.5 Compressor performance uncertainty

The turbocharger performance uncertainty analysis was carried out with the use of sensors as listed in Table 1 and for HTT GT17. Figure 5-5 and Figure 5-7 show the turbocharger compressor performance plots with the superimposed error bars on pressure ratio, corrected mass flow and efficiency.

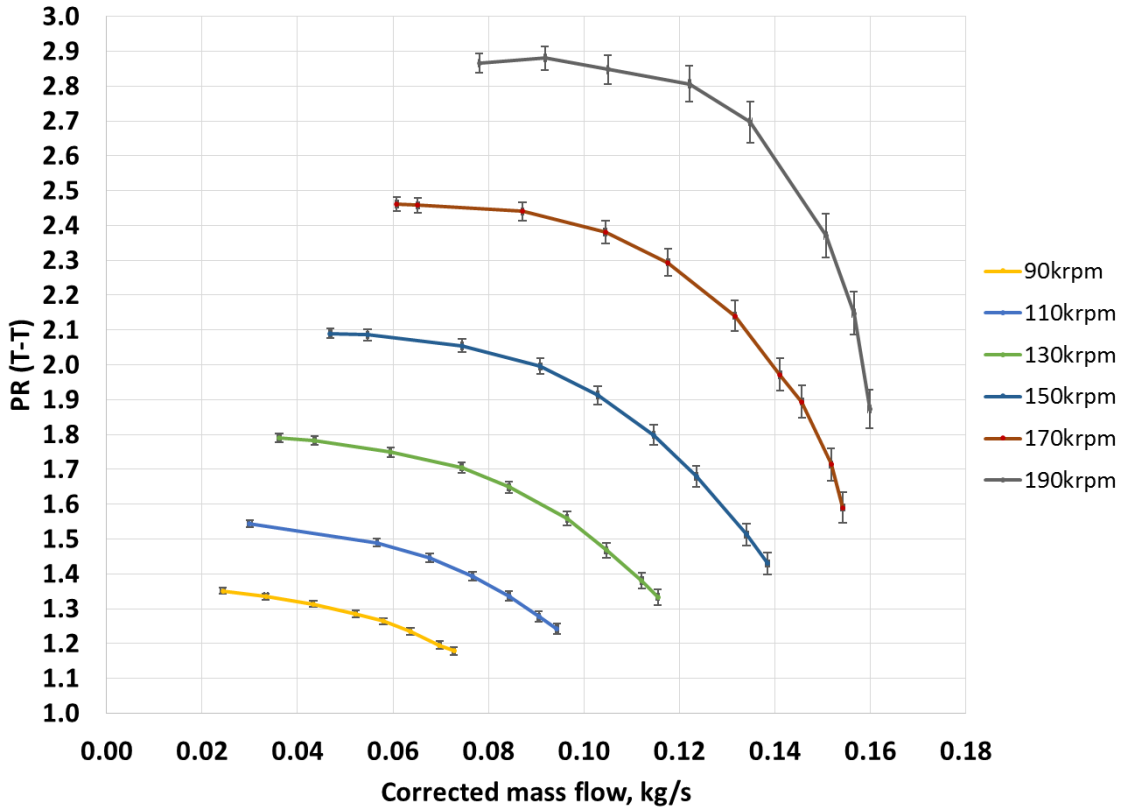

Figure 5-5. Uncertainty of the measured compressor performance map. Pressure ratio vs. corrected mass flow

In Figure 5-5 it can be noted that the uncertainty of pressure ratio increases with the rise of the turbocharger speed. Also, at the constant speed line δPR drops in the direction of lower mass flow rates. The uncertainty of the corrected mass flow is generally lower than the uncertainty of pressure ratio and rises in the low flow region of the map (Figure 5-6). The relative uncertainty shown in the figure is the ratio of calculated uncertainty of the corrected mass flow and calculated value of corrected mass flow. The increase of the relative uncertainty of the corrected mass flow is dominantly dependant on the relative uncertainty associated with the measurement of differential pressure across the V-cone mass flow meter. As the accuracy of the volumetric mass flow measurement is fixed across the range of measured flows and therefore measuring the low pressure drops results in the increase of the relative uncertainty.

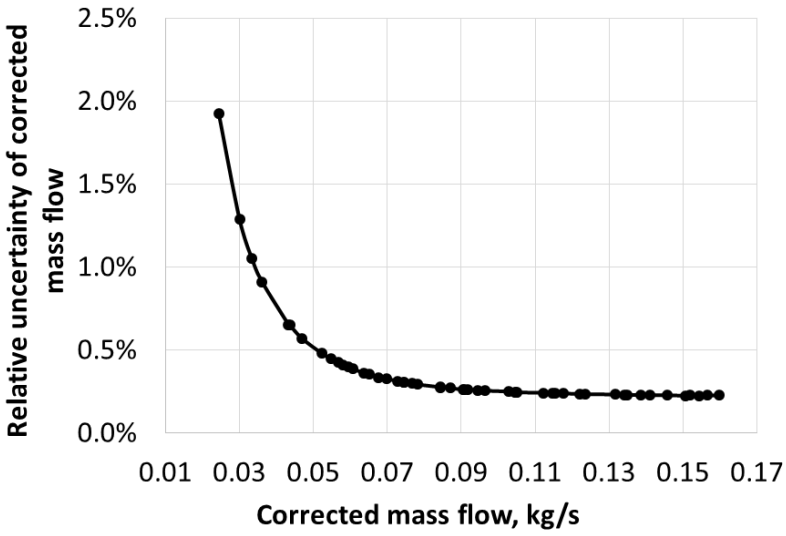

Figure 5-6. Relative uncertainty of the compressor mass flow vs. corrected mass flow

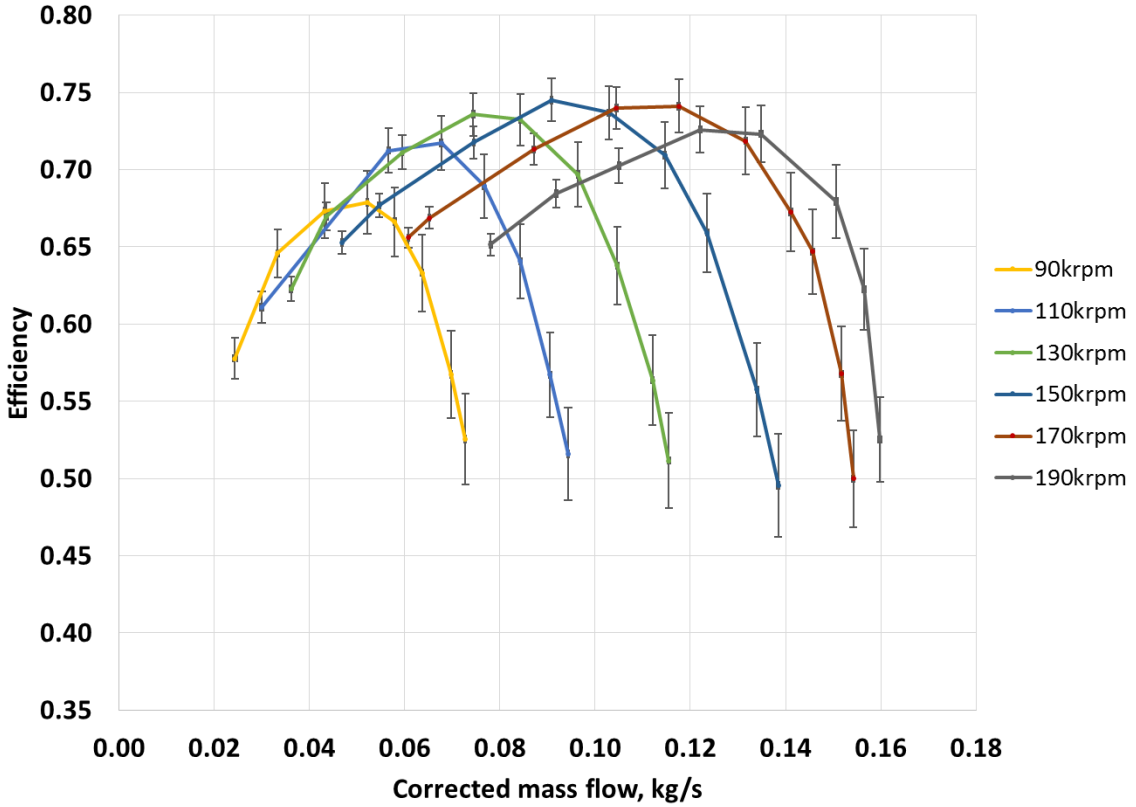

Figure 5-7. Uncertainty of the measured compressor performance map. Efficiency vs. corrected mass flow

The uncertainty of compressor efficiency rises towards the higher corrected mass flows at constant speed lines and slightly rises when the turbocharger speed is reduced.

In order to understand how the particular measurements affect the uncertainty of pressure ratio and efficiency across the map the total uncertainty of those parameters have been broken down to the associated measurement variables. In Figure 5-8 it is shown what the dominant measurement uncertainties are at the overall PR uncertainty and all tested turbocharger speeds. The integer numbers given in the x-axis are the operating

point numbers on the constant turbocharger speed line. The operating point number 1 denotes the highest mass flow point recorded; the operating points move towards surge with the increase of numbers on the x-axis. The last (highest) number given on the x-axis denotes the last stable operating point before the hard surge condition. The PR uncertainty percentage calculated at a given point (y-axis) is a sum of calculated measurement uncertainties therefore it always equals 1 (100%). Generally it can be concluded that the mass flow measurement and inlet static pressure uncertainties are two factors which affect the uncertainty of PR the most. The uncertainties of temperature and outlet pressure measurement affect the uncertainty of PR less significantly. When moving towards surge both the uncertainties of mass flow and post compressor temperature rise whereas the uncertainty associated with inlet static pressure drops. The uncertainty rise of post-compressor temperature can be justified relatively simply - the post-compressor gas temperature rises when operating near surge and at higher pressures whereas the accuracy of PRTs' is proportional to the measured temperature. To understand the uncertainty trends of the inlet static pressure and mass flow a bigger picture should be looked at. First of all the compressor pressure ratio is a function of total post-compressor pressure and total pre-compressor pressure of which the uncertainty of the former is dominant. An example of such dominancy at the highest tested speed is shown in Figure 5-9. Also, both the pre and post-compressor pressures are calculated differently – the total inlet pressure is a sum of static and dynamic pressures (Equation (*19*)). The dynamic pressure is a function linking density and velocity of the gas and therefore is directly linked with the gas mass flow through the continuity equation (Equation (*25*)). The total post-compressor pressure is a mass flow independent variable (Equation (*20*)).

Now, considering the compressor operating towards surge on the constant speed line an area of low mass flow rates and high post-compressor pressures is approached. As the static pressure barely changes, mass flow measurement is the dominant source of uncertainty. Both of these variables affect the uncertainty of the total inlet pressure and therefore the rise of the mass flow uncertainty fraction directly causes the drop of the static pre-compressor relative uncertainty.

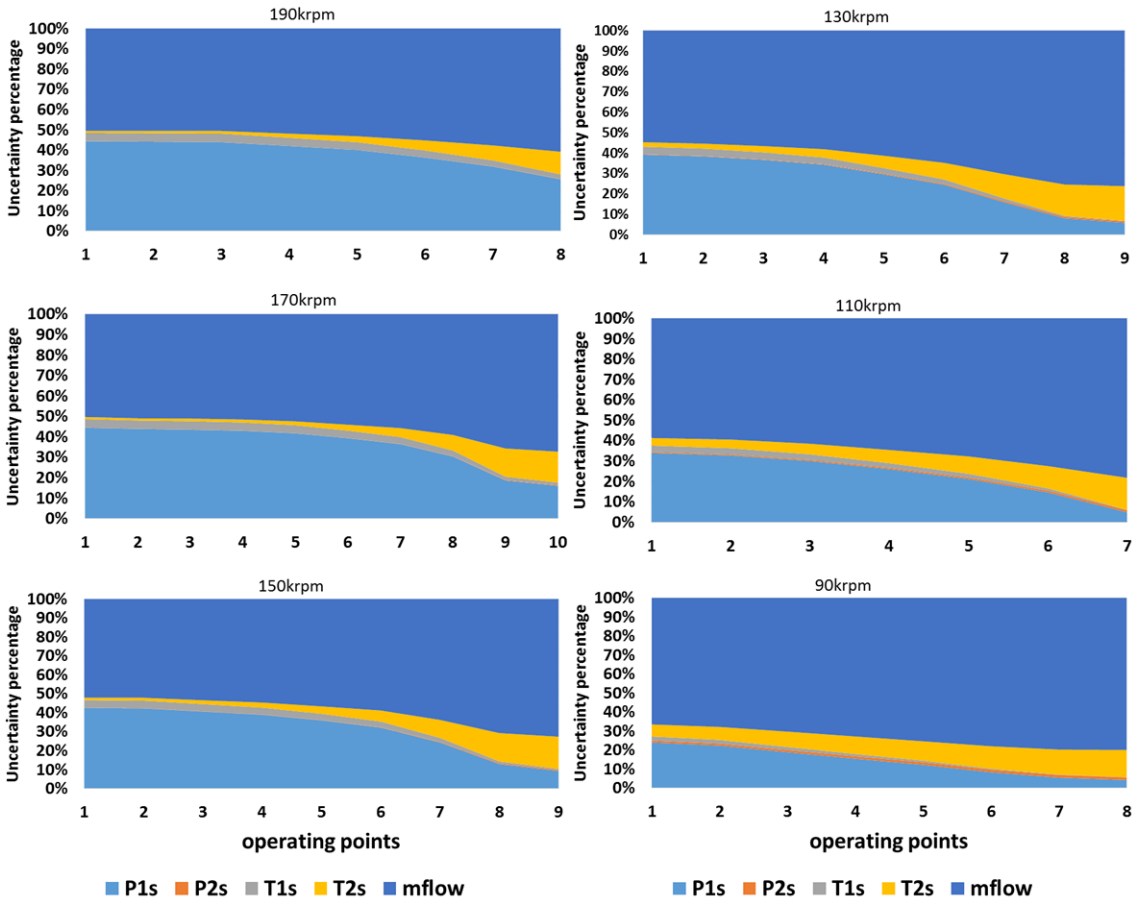

Figure 5-8. PR uncertainty at tested turbocharger speeds for the original instrumentation

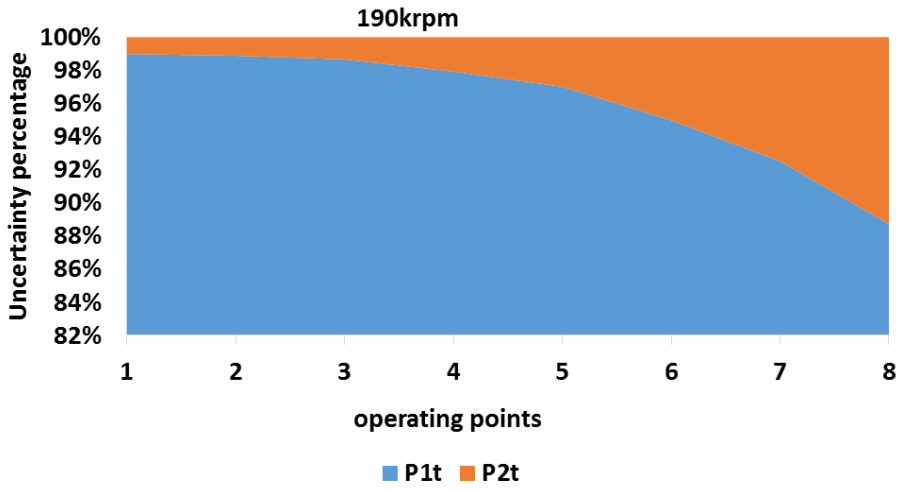

Figure 5-9. P1t and P2t uncertainty fractions in the overall uncertainty of pressure ratio

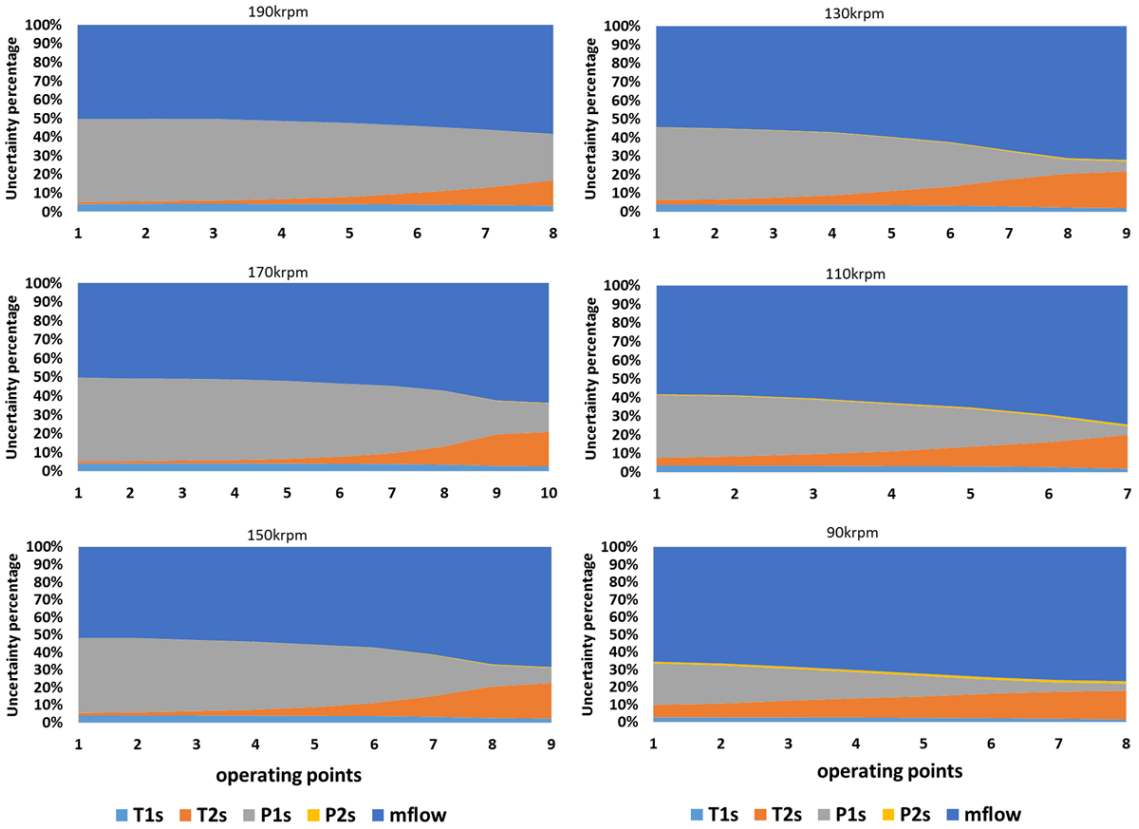

Figure 5-10. Efficiency uncertainty at tested turbocharger speeds uncertainty at tested turbocharger speeds for the original instrumentation

The uncertainty of compressor efficiency is also dominantly dependent on the uncertainty of the inlet static pressure and mass flow measurement (Figure 5-10). The temperature uncertainty is very low due to the high accuracy PRTs used at the test facility.

Analysing the existing gas stand instrumentation data (Table 1) it can be noticed that the easiest way of improving the accuracy of compressor map would be achieved by:

a) Selecting a lower range pressure sensor at the compressor entry. The existing wide range sensor has been chosen to measure the various pre-compressor pressures during the closed-loop operation. This is not required at standard mapping configuration where the compressor inlet pressure is usually near atmospheric pressure. As an example let's assume that the new sensor also reads the absolute pressure, has the same accuracy and covers the range between 0-120 kPa.

b) Selecting a lower range and higher accuracy pressure sensor measuring the gas pressure at the inlet to the V-cone mass flow meter (for density calculation). In this case let's assume the accuracy of the sensor to be increased from 0.25% to 0.08% and the range to be between 0-120 kPa absolute.

Changing the two pressure transducers as described above has caused the uncertainty of both pressure ratio and efficiency to drop as can be seen in Figure 5-11 and Figure 5-12.

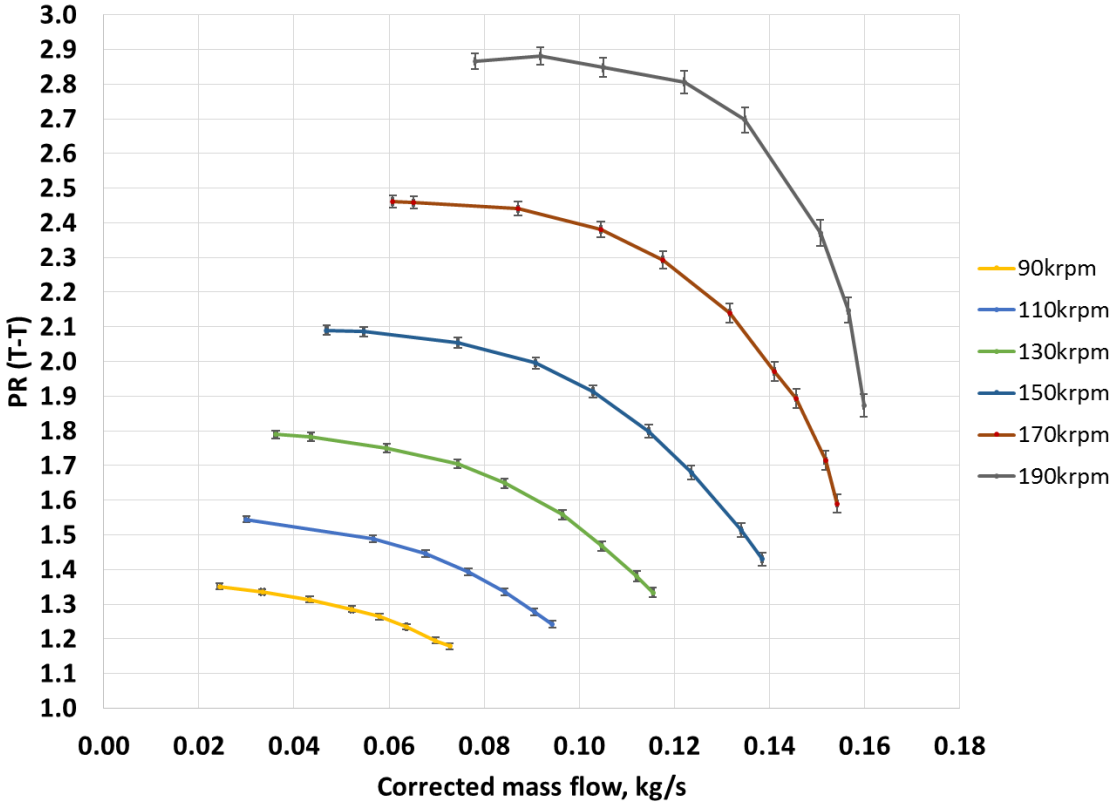

Figure 5-11. Uncertainty of the measured compressor performance map – corrected mass flow vs. PR based on the above instrumentation improvements

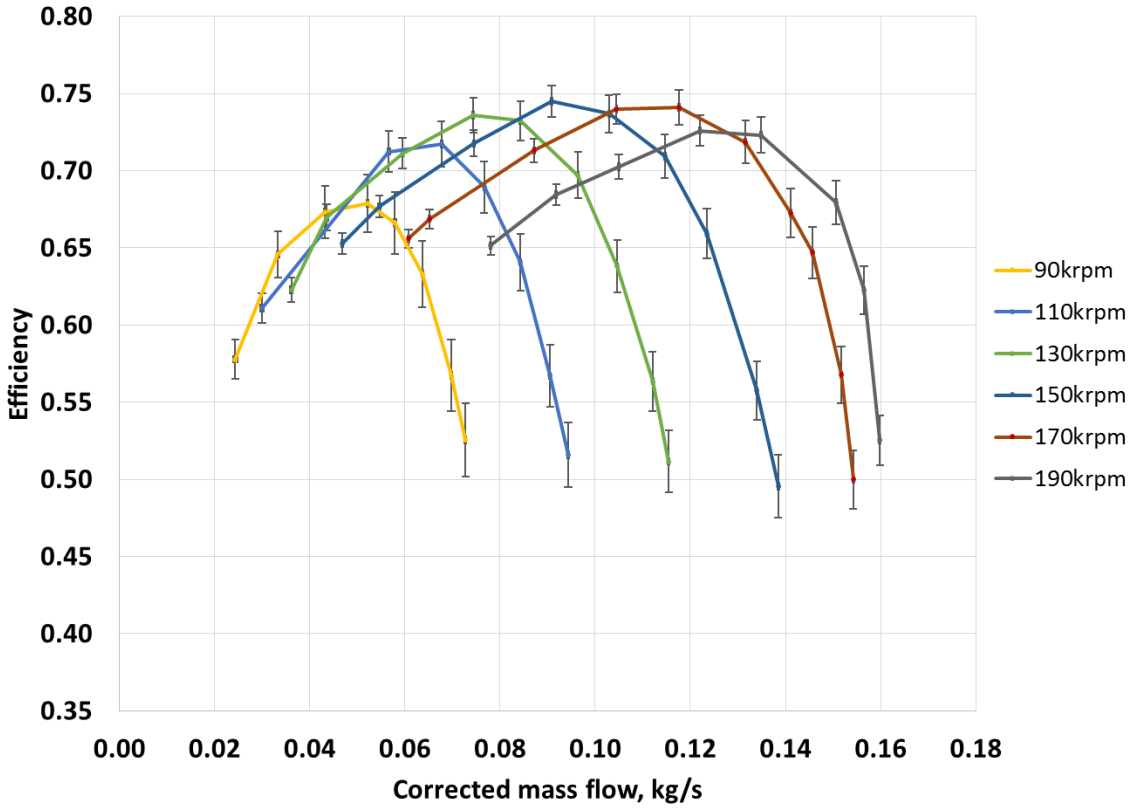

Figure 5-12. Uncertainty of the measured compressor performance map – corrected mass flow vs. efficiency based on the above instrumentation improvements

The reduction of the uncertainties associated with the static pre-compressor pressure and static pressure at the V-cone mass flow meter entry has also affected the respective fractions of all measurement uncertainties related to total-to-total compressor pressure ratio (Figure 5-13) and efficiency (Figure 5-14). Generally, despite the improvement in the accuracy of the gas density measurement and therefore reduction in the mass flow measurement uncertainty the latter still remained the dominant factor. However it can also be noticed that the post-compressor temperature now plays a bigger role in the overall PR and efficiency uncertainty.

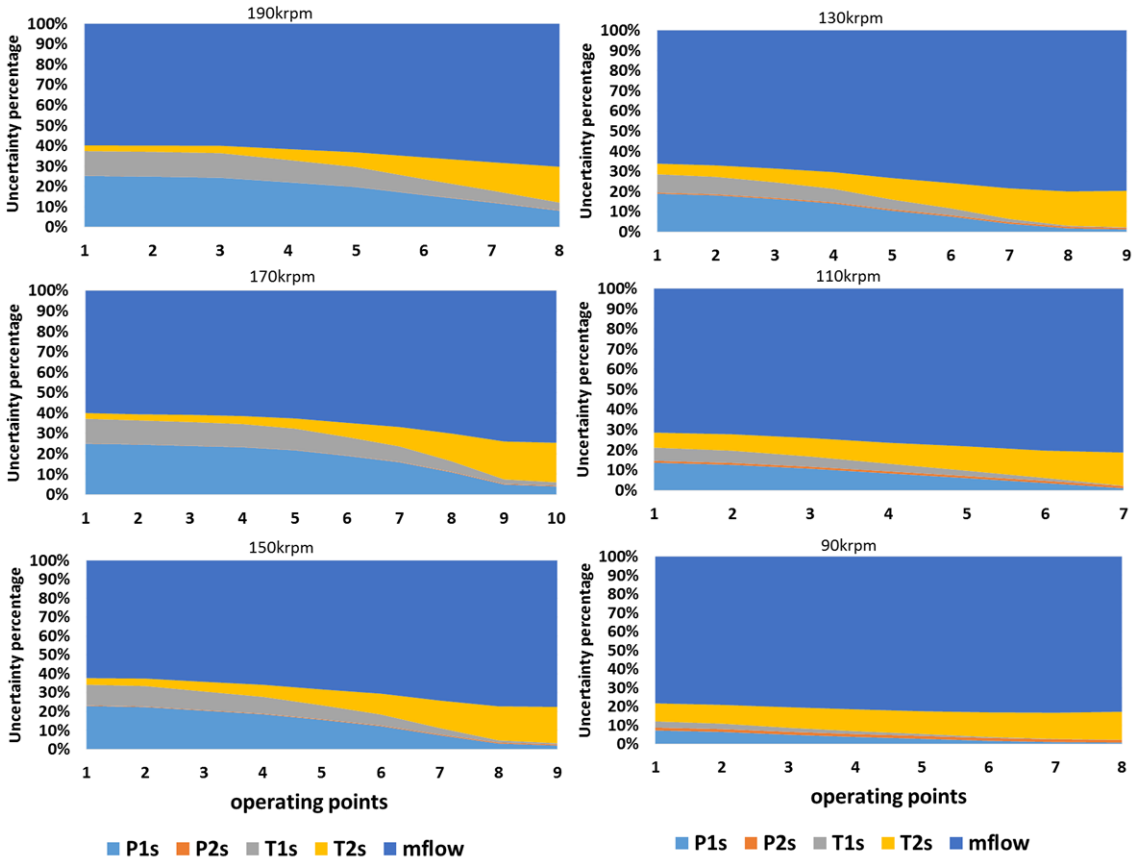

Figure 5-13. PR uncertainty at tested turbocharger speeds for the modified pressure transducers

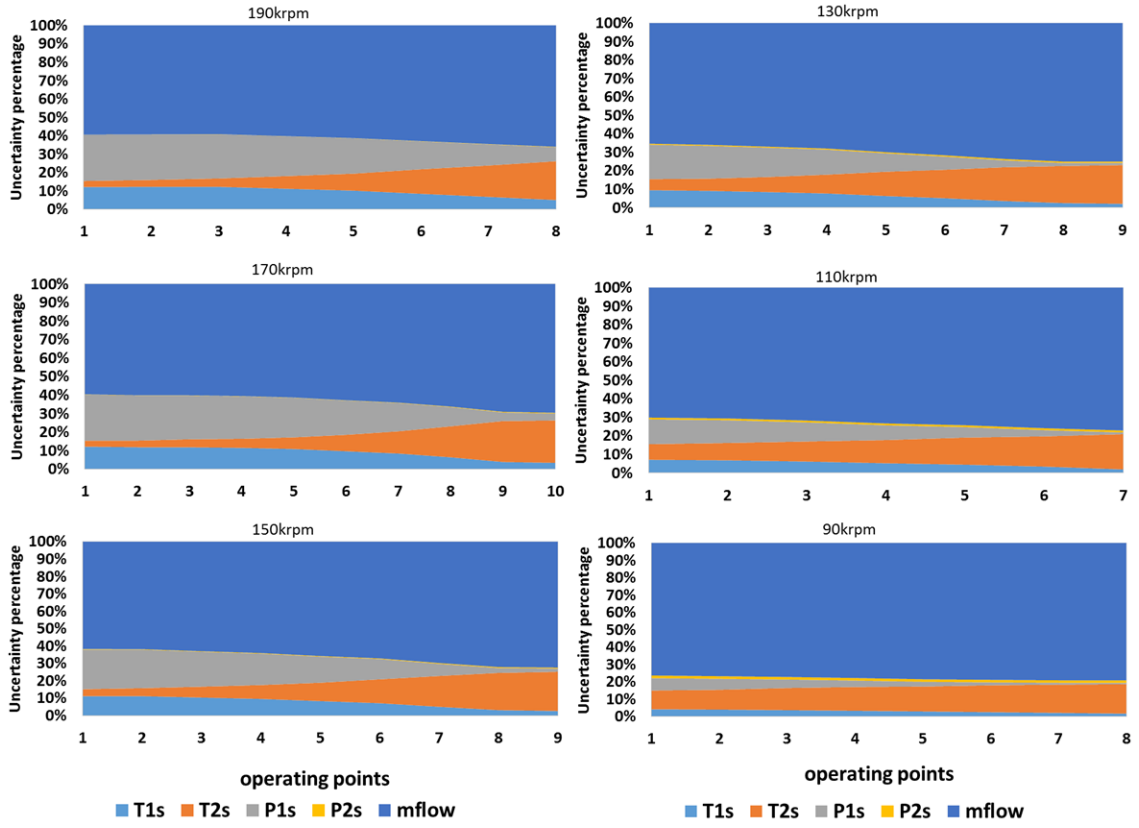

Figure 5-14. Efficiency uncertainty at tested turbocharger speeds uncertainty at tested turbocharger speeds for the original instrumentation

In the above two cases where the original instrumentation (case 1) and replacement pressure transducers (case 2) were used it may be slightly surprising that the temperature measurement is not a major player in the uncertainty of compressor efficiency. However this is easily justified by the fact that the heat transfer effects were not taken into account in this part of the analysis and because of the high accuracy PRT sensors used during the tests. So what would happen with the uncertainty of the compressor performance describing parameters if k-type thermocouples were used instead of the chosen PRTs at the pre- and post-compressor performance measurement locations? Such check was easily performed thanks to the excel spreadsheet that was developed for the purpose of the uncertainty analysis – the plots were updated automatically after the temperature sensor accuracies have been updated with those adequate for the k-type thermocouples. These are presented in Figure 5-15 and Figure 5-16 accordingly. It can be noted that replacement of the high accuracy PRTs with k-type thermocouples significantly affected both pressure ratio and efficiency. The uncertainties associated with the temperature measurement are also dominant over the static pressure and mass flow measurement uncertainties which is shown in Figure 5-17 and Figure 5-18.

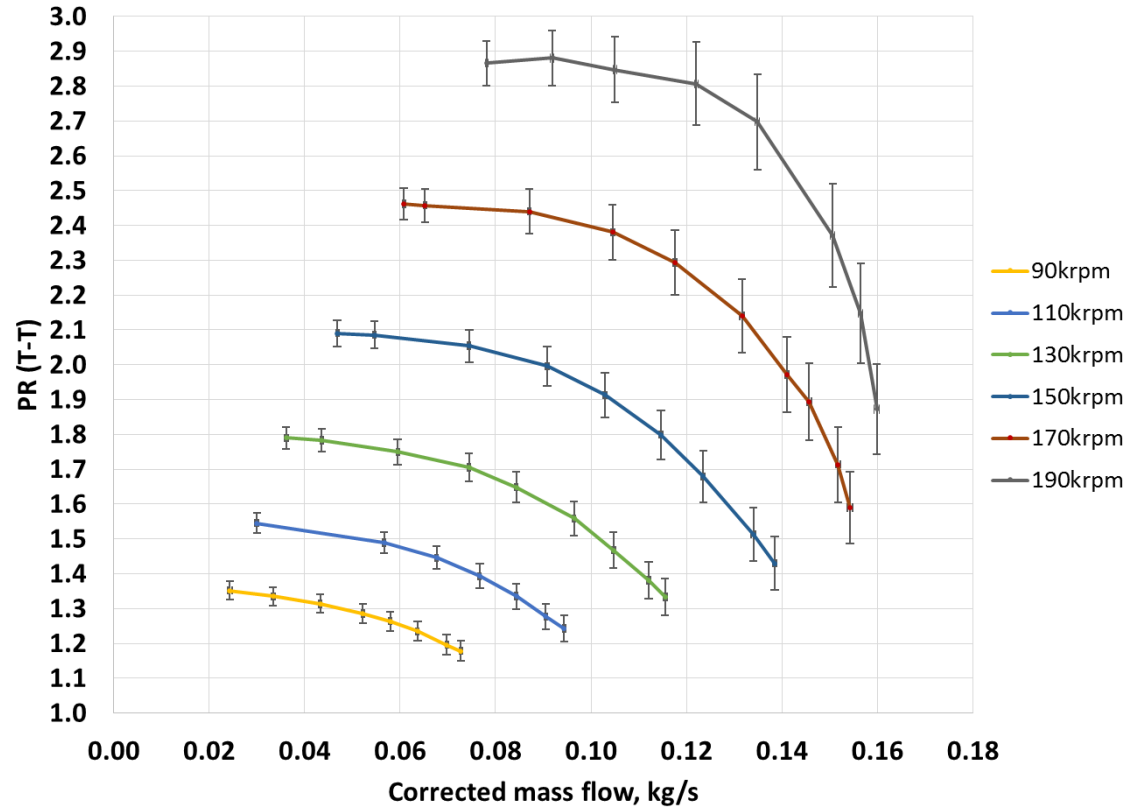

Figure 5-15. Uncertainty of the measured compressor performance map – corrected mass flow vs. PR based on the original instrumentation and thermocouples installed at pre and post-compressor performance measurement locations

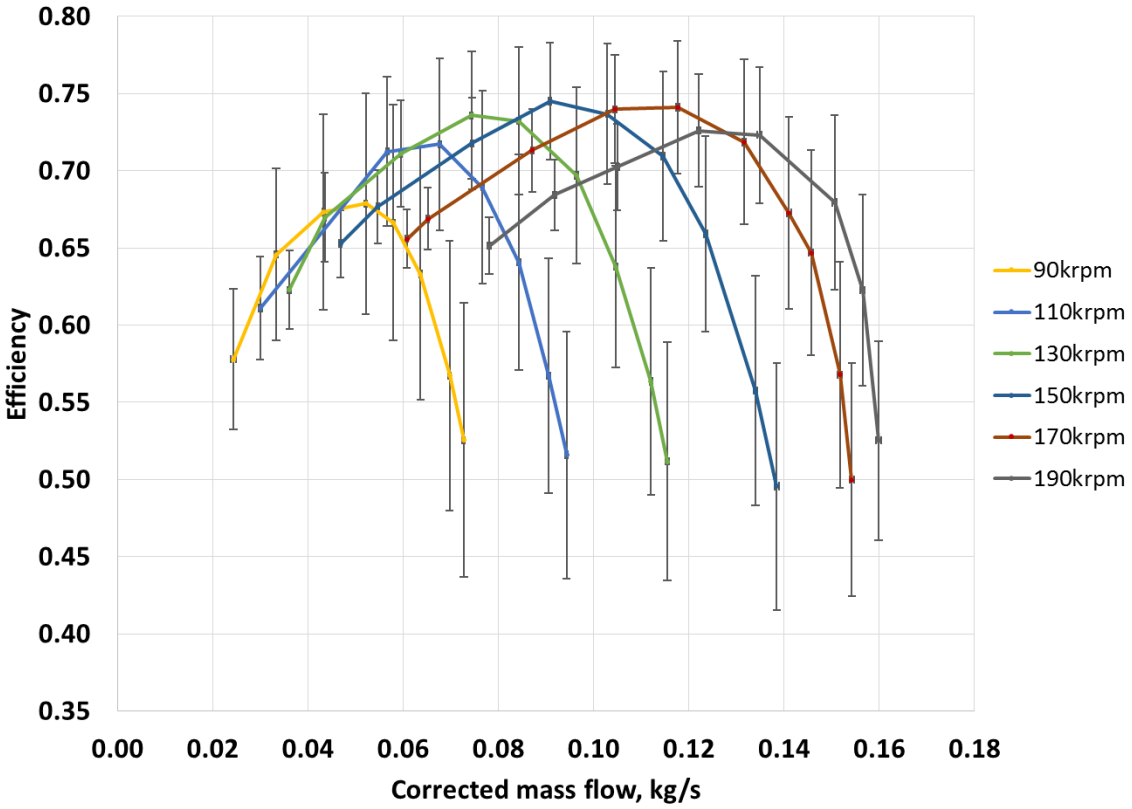

Figure 5-16. Uncertainty of the measured compressor performance map – corrected mass flow vs. efficiency based on the original instrumentation and thermocouples installed at pre and post-compressor performance measurement locations

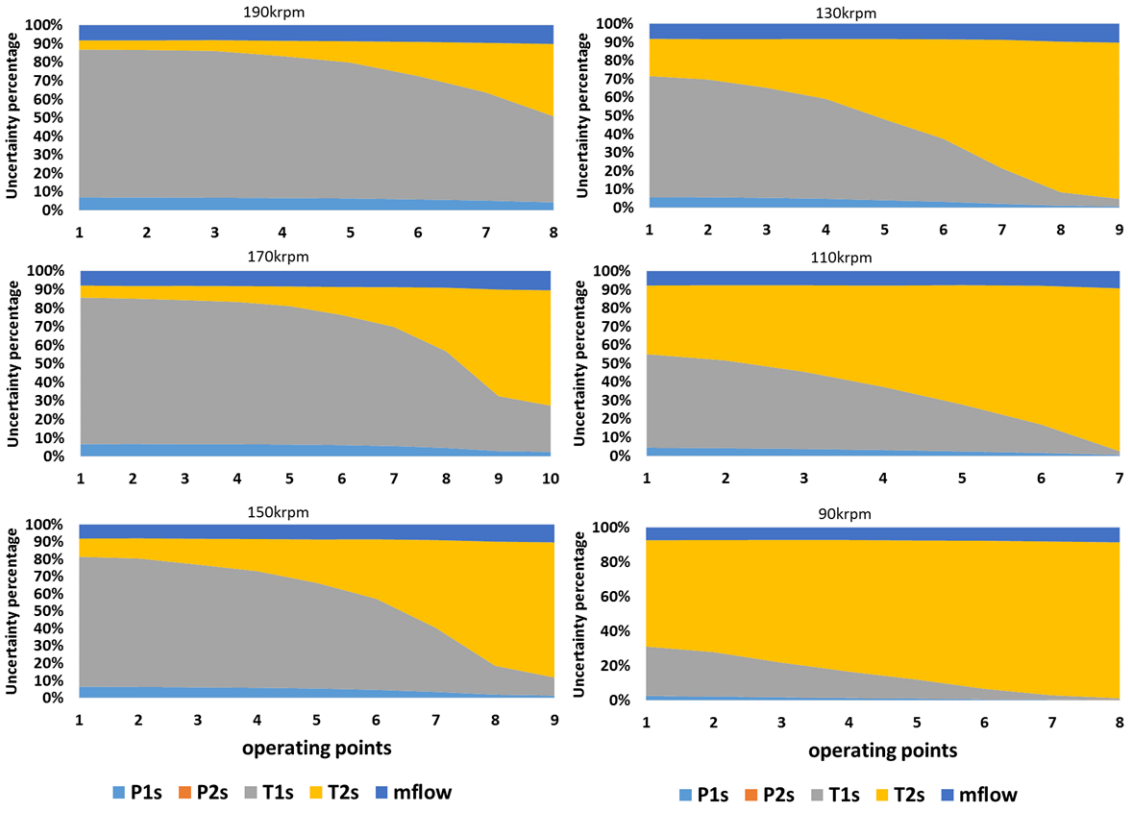

Figure 5-17. PR uncertainty at tested turbocharger speeds for the original instrumentation and thermocouples installed at pre and post-compressor performance measurement locations

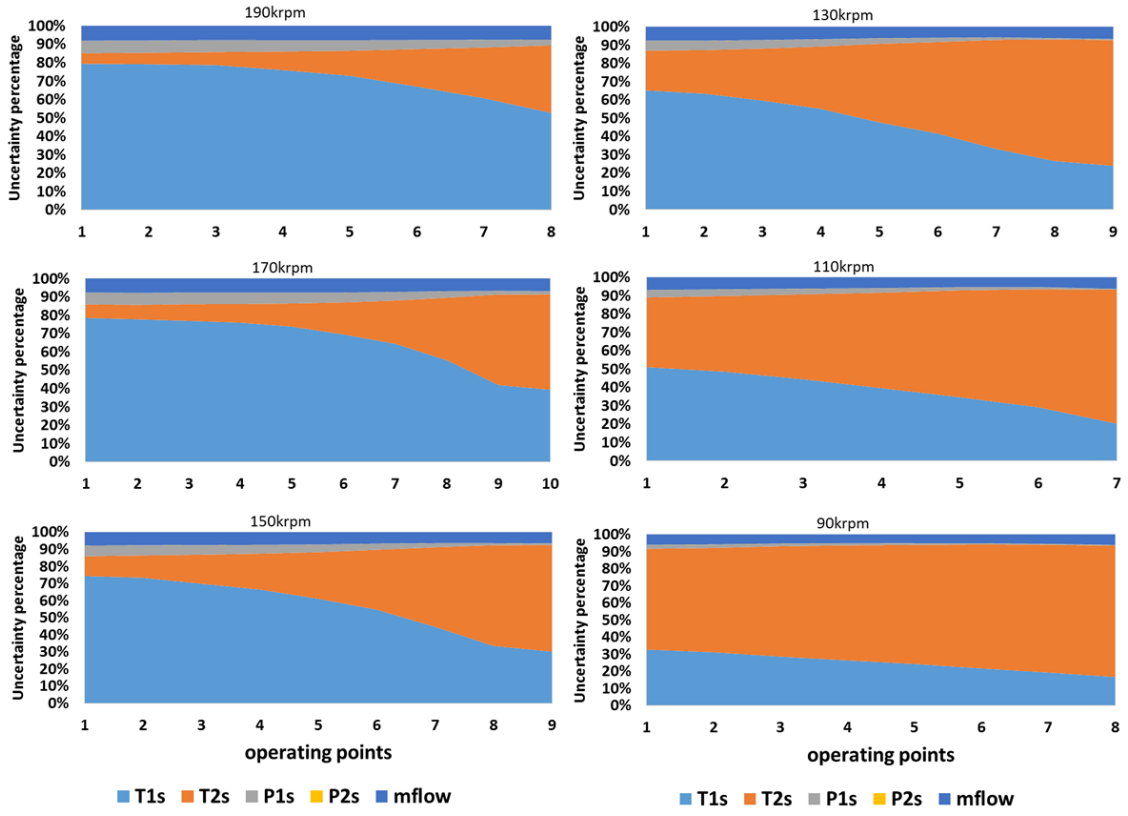

Figure 5-18. Efficiency uncertainty at tested turbocharger speeds for the original instrumentation and thermocouples installed at pre and post-compressor performance measurement locations

5.1.6 Turbine performance uncertainty

Similarly to the compressor also type-B uncertainty analysis for the turbine side has been carried out. There are two aspects that shall be looked at when analysing the uncertainty of turbine performance maps. First of all, the formulation of performance parameters which are calculated slightly differently than the compressor equivalents. Unlike the total-to-total pressure ratio used to characterise compressors, the turbine definition of expansion ratio is a function of total inlet pressure and static outlet pressure. The use of the static outlet pressure is due to the fact that the kinetic energy of the post turbine gas is wasted and therefore there is no need for the calculation of the dynamic pressure (based on the gas velocity). In theory, the efficiency of turbine can be calculated similarly to the compressor's, based on the temperature and pressure drop across the turbine as per the following equation (Equation (*61*)).

$$\eta_t = \frac{T_{3t} - T_{4s}}{T_{3t}[1 - (1/PR_t)^{\left(\frac{\gamma_t - 1}{\gamma_t}\right)}]} \quad (61)$$

However, the highly swirling nature of the post turbine flow disallows the precise temperature measurement. For this reason a different way of calculating the efficiency of the turbine is commonly used which links compressor power, friction losses (mechanical efficiency) and turbine related variables (Equation (*42*)). While the friction losses can be assumed as constant in a simplified approach the compressor power is a vital component which affects the overall uncertainty of the turbine efficiency. A second important aspect when comparing the uncertainty of turbine and compressor maps (next to the formulation of performance parameters) is the instrumentation difference. Looking at the instrumentation used on both sides of the turbocharger (Table 1) it is noted that on the turbine side k-type thermocouples are used instead of PRTs for the turbine temperature measurement. This is due to the high temperature of the gas flowing within the turbine which is beyond the capabilities of the platinum resistance thermometers. As the flow of the gas is measured upstream from the electric heaters - at low temperatures – PRTs can be used there. Apart from using the lower accuracy thermocouples also all the pressure transducers used on the turbine side are characterised by wider operating ranges – typically from 0 to 100 psi (both absolute and gauge types). The turbine performance charts with the superimposed uncertainty bars on the plotted parameters are shown in Figure 5-19 and Figure 5-20. The uncertainty associated with the turbine pressure ratio is dominantly dependent on the turbine total inlet pressure of which the highest uncertainty is linked with the measurement of the static inlet temperature (an example of a broken down uncertainty of turbine pressure ratio at the speed of 190 krpm is shown in Figure 5-21).

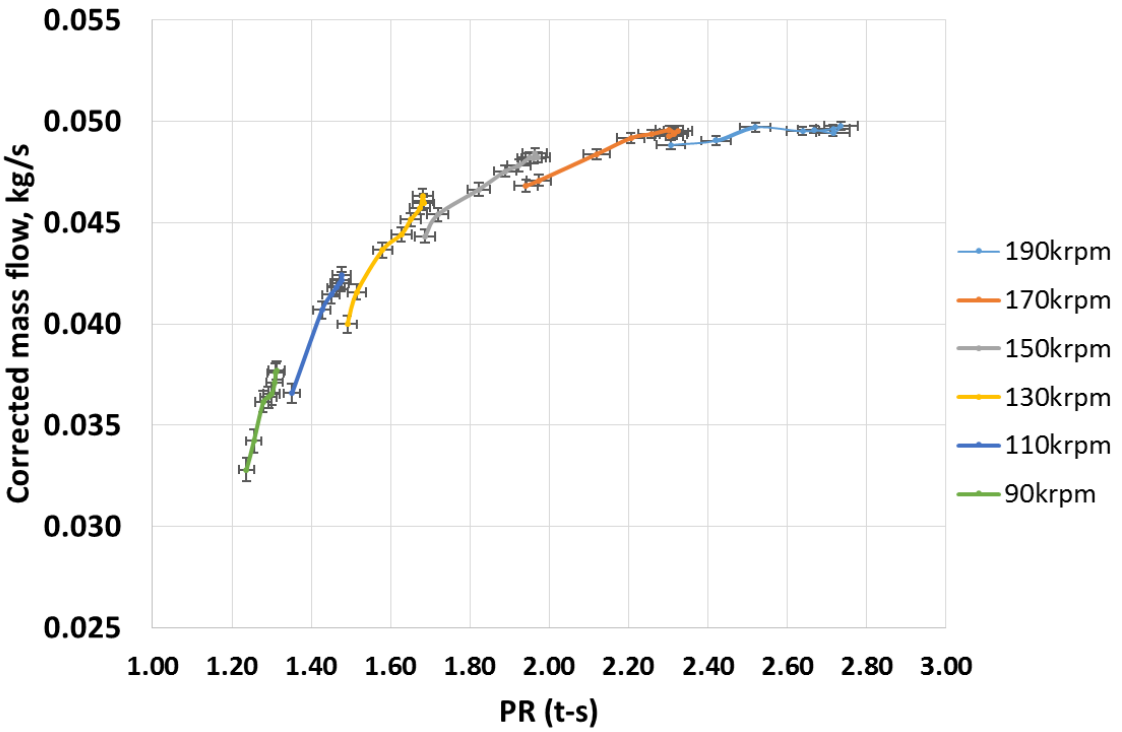

Figure 5-19. Uncertainty of the measured turbine performance map. Corrected mass flow vs. pressure ratio based on the original instrumentation

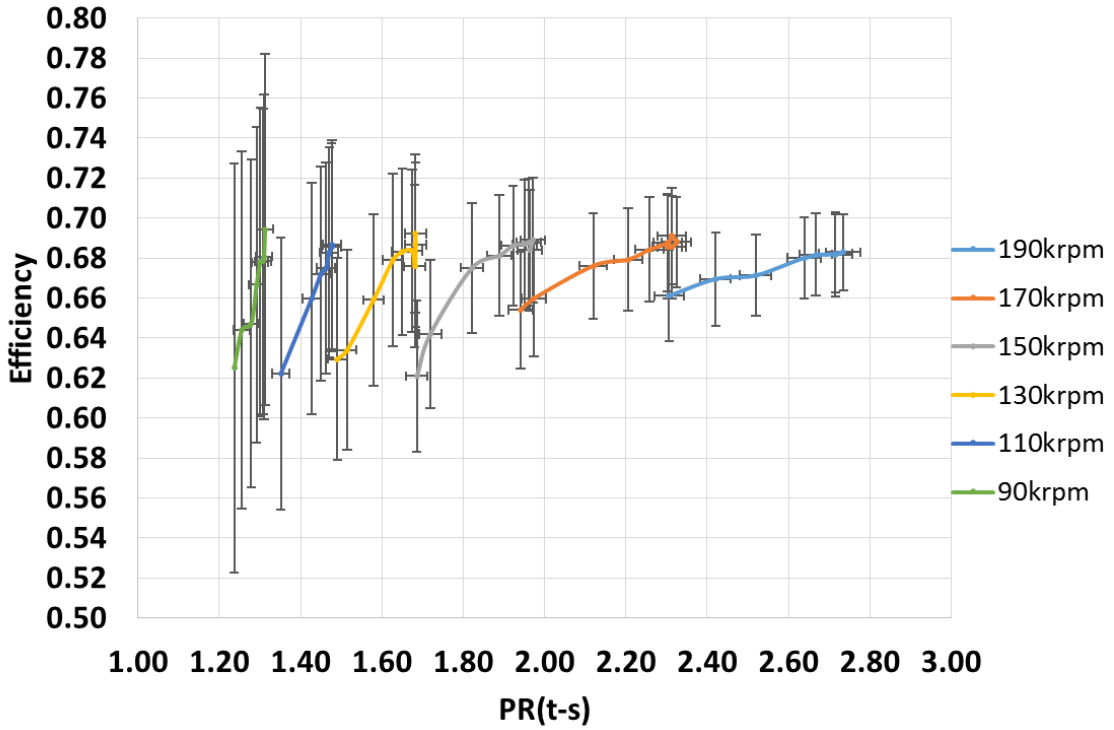

Figure 5-20. Uncertainty of the measured turbine performance map. Efficiency vs. pressure ratio based on the original instrumentation

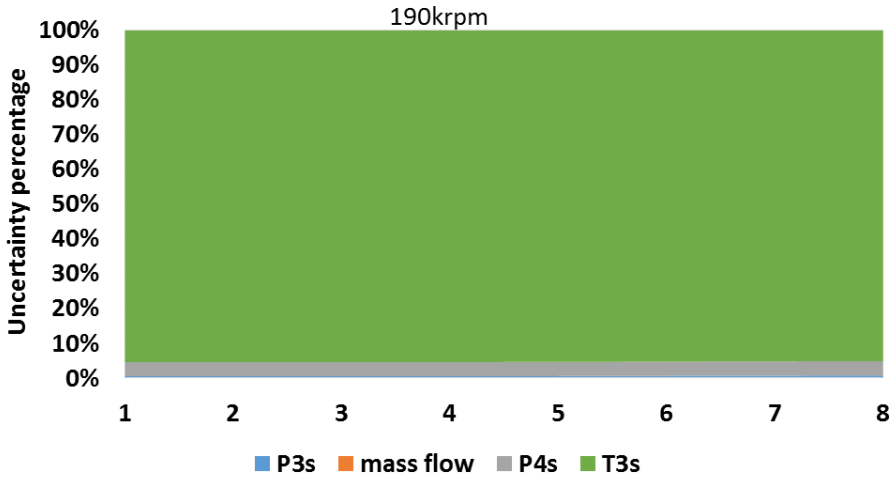

Figure 5-21. Turbine pressure ratio uncertainty fractions of the measured turbine performance map at 190 krpm.

The uncertainty of turbine efficiency is affected by greater number of variables, however the most important uncertainty factor is again turbine inlet temperature. Elimination or partial reduction of the turbine inlet temperature measurement uncertainty would significantly reduce both the pressure ratio and turbine efficiency uncertainty. In order to do so more accurate thermocouples can be selected. In this case using PRTs would not bring a significant benefit in terms of improved accuracy – only lower class PRTs (class B & C) are available on the market that can be operated at temperatures up to 600°C. Measuring a temperature of 500°C (turbine inlet temperature targeted at this mapping process) with a class B PRT is achieved with an accuracy of ±2.8°C (0.3+0.005*t) compared to ±3.75°C of k-type thermocouple (0.75%*t). The best improvements can be achieved with the platinum-rhodium thermocouples (r- or s-type) that have the accuracy of ±1.5°C when measuring the temperatures up to 600°C. However the accuracy improvement comes with the high cost – the platinum-rhodium thermocouples are about twenty times more expensive than k-type thermocouples [105]. Regardless of the opinion whether it is worth or not having the high accuracy thermocouples when testing automotive turbines, the figures below (show the uncertainty of the turbine with the platinum-rhodium thermocouples installed upstream from the turbine (no changes to other sensors).

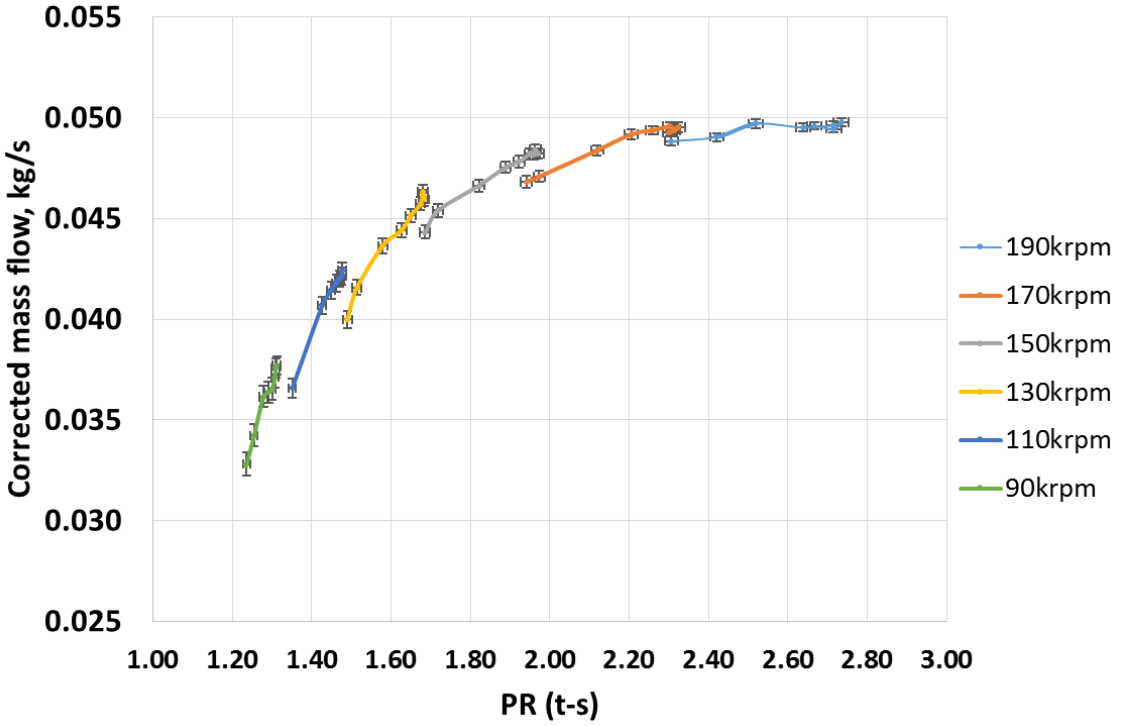

Figure 5-22. Uncertainty of the measured turbine performance map. Corrected mass flow vas pressure ratio based on r-type thermocouples installed pre-turbine and original instrumentation installed elsewhere

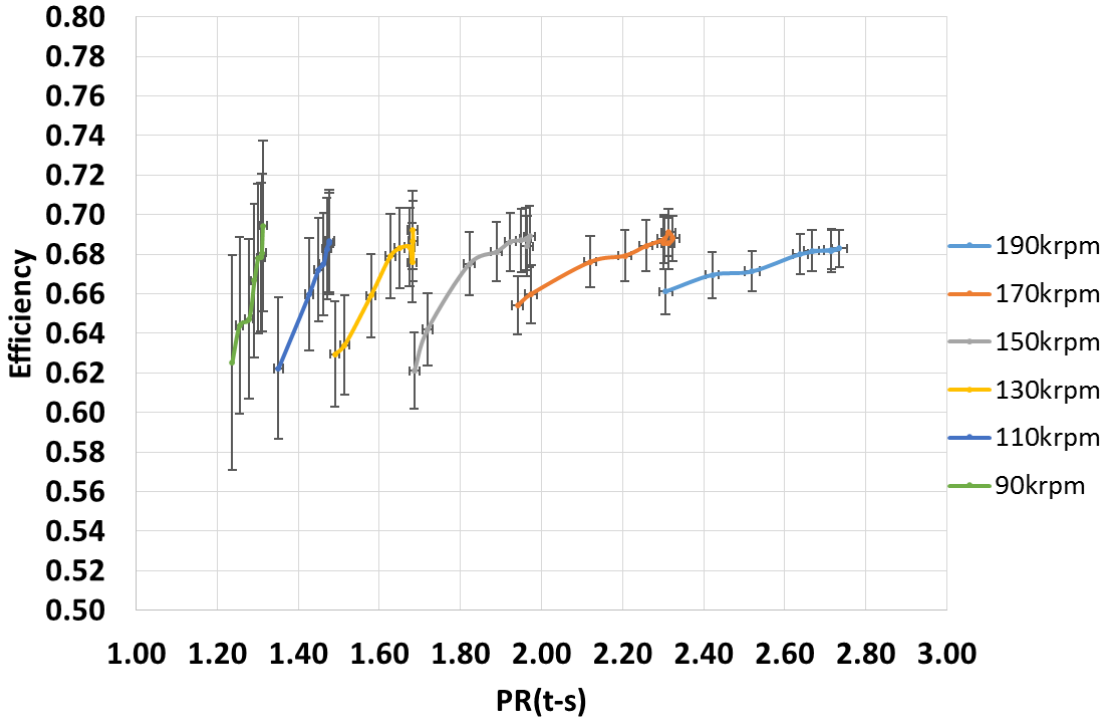

Figure 5-23. Uncertainty of the measured turbine performance map. Efficiency vs. pressure ratio based on r-type thermocouples installed pre-turbine and original instrumentation installed elsewhere

Finally, the uncertainty of the turbine corrected mass flow is in general fairly low across the turbine map and slightly rises towards the low mass flow region.

5.2 Heat transfer related uncertainty of turbocharger maps

For the purpose of reflecting real hot on-engine conditions, standard turbocharger maps are generated maintaining a fixed temperature at the turbine entry which is usually between 500-600°C (depending on the turbocharger manufacturer). The high temperature gradient between the gases flowing through the turbine and compressor is a mechanism driving the heat transfer between the two components. As a result, the compressor side measured temperatures (pre- and post-compressor) are affected which has a direct influence on the compressor efficiency. In other words, the compressor efficiency which by definition should determine the aerodynamic ability of the device to raise the pressure and temperature of the gas (in adiabatic conditions and as in Equation (*18*), no longer reflects such a case. Instead, the apparent efficiency (measured) combines both the work and heat related factors transferred to the gas. Thus, any compressor efficiency offset from its true (aerodynamic) value and due to the heat transfer shall be interpreted as an error. The turbine efficiency gets affected too as the calculation method (Equation (*42*)) involves the compressor power and that is affected by the temperature rise across the compressor. The compressor efficiency measurement error due to the heat transfer between the turbocharger components is especially important at the low turbocharger speeds because of the higher (than at high speeds) temperature differences between the turbine and compressor gases and the longer residency time of the gas passing through the compressor (more time to absorb heat). One of the ways to reduce the heat transfer effects during the turbocharger maps generation recommended by the SAE code of practise is to thermally clad the compressor housing. However, even this method is not efficient enough at very low turbocharger speeds where the heat transfer driving temperature gradients still exist. For this reason and due to other technical constraints, the turbocharger manufacturers provide the measured data (by means of the performance maps) only to a limited turbocharger speed beyond which the measurement data would be difficult to obtain and very uncertain due to the aforementioned heat transfer effects. This is a valid problem as in the real on-engine conditions the turbocharger operates in low turbocharger speeds for a considerably significant period of time. When simulating such low speeds at the engine development 1D codes - extrapolated data is used beyond the lowest turbocharger speed which itself brings a dosage of uncertainty onto the modelled turbocharger operating point. As an alternative to the extrapolated data, experimental mapping at low speeds is introduced. However, in order to assess the influence of the heat transfer effects on the measured compressor efficiency a separation of compressor work and heat to the compressed gas from the hot side of the turbocharger, the tests should be carried out in adiabatic conditions. This method has been pursued here in Bath and is discussed in the following subsection.

The problem of the separation of the heat transfer from the compressor efficiency has been widely investigated by many researchers. Generally, simple turbocharger models are seen as a weak link in the accuracy of the wave-action 1D engine simulation tools, and advanced models (but still simple in structure to allow efficient running within a full engine code) have been proposed to account for phenomena including heat transfer. These models are most often based on the assumption that the heat transfer inwards/outwards the compressor gas occurs only after compression process. A validity of such assumption has been investigated in a simple lumped capacitance thermal model of a turbocharger developed at University of Bath by Burke [2] supported by a three-dimensional CFD conjugate heat transfer simulations carried out by the author of this thesis. Finally, a validity check of a chosen literature based function linking the turbocharger operating point with the compressor and turbine powers and the estimated heat transferred to the compressor is also performed. The reason behind this exercise is to check if the real adiabatic turbocharger efficiencies can be found when mapping at low speeds and at standard hot gas conditions without the need for the separate adiabatic tests.

5.2.1 Low turbocharger speed data – a comparison between the data obtained experimentally and by map extrapolation

The lack of the steady-state test data in the low turbocharger speed region is an effect of the increasing measurement uncertainty caused by the heat transfer between the turbine and compressor. This can be overcome if the tests are carried out in adiabatic conditions (or as close to adiabatic as possible). In such situation the turbine inlet temperature is matched with the post-compressor temperature and oil temperature. As it can be imagined during the adiabatic mapping the turbine inlet temperature is a variable parameter that is much easier controlled on gas stands equipped with electrically regulated heaters and using air as the working medium (passing power to the flowing air) than on the ones that use natural gas burners and exhaust gases to drive the turbine. Another aspect that shall be considered when testing at low turbo speeds is the mechanical efficiency or in other words friction losses. These are substantially different if the temperature of the lubricating oil is low and that is due to the viscosity change. In the case of the incorrect measurement of the friction losses, turbine efficiency will be affected. Finally, testing at low turbo speeds means that both the low mass flow and low pressure will be measured and this may require an adequately lower range mass flow meters and pressure sensors. The turbocharger gas stand is equipped with both – power controlled electric heaters are various range mass flow meters which allow for the low speed mapping both at hot and adiabatic conditions. The target of this exercise was to compare the experimentally gained data at low turbocharger speeds and various thermal conditions

to understand how much the efficiency uncertainty can be caused by the heat transfer effects. Also, an extrapolation of the Wave encoded turbocharger compressor map has been performed in the low turbo speed region to see how accurate this technique is when compared against the experimental data. In order to answer all these questions the chosen turbocharger (HTT GT17) was mapped at three turbocharger speeds of 70, 50 and 30 krpm. First, the mapping process was carried out at hot conditions, feeding the turbine with the gas at constant temperature of 500°C while the oil temperature was kept constant at 90°C. Secondly, the turbine inlet temperature was matched with the compressor outlet temperature, whereas the oil temperature was still maintained at 90°C. This case would let the author understand how much heat is transferred to the compressor only from the hot lubrication fluid. In the last case the turbine inlet temperature was again matched with the compressor outlet temperature but the oil temperature was reduced to 60°C. The last case still does not reflect the fully adiabatic conditions across the tested speed lines, however the decision to maintain the oil temperature at 60°C was made to minimise the risks of turbocharger damage (due to low oil temperatures). Despite the above a couple of compressor operating points were managed to be obtained in adiabatic conditions (turbine inlet, compressor outlet and oil temperatures matched at 60°C). The extrapolation of data for the same turbocharger speeds as mentioned above was carried out in Ricardo Wave 1D engine simulation code and based on the original performance map. Due to this fact a comparison between the manufacturer's and Bath gas stand's obtained data is first presented (Figure 5-24 & Figure 5-25).

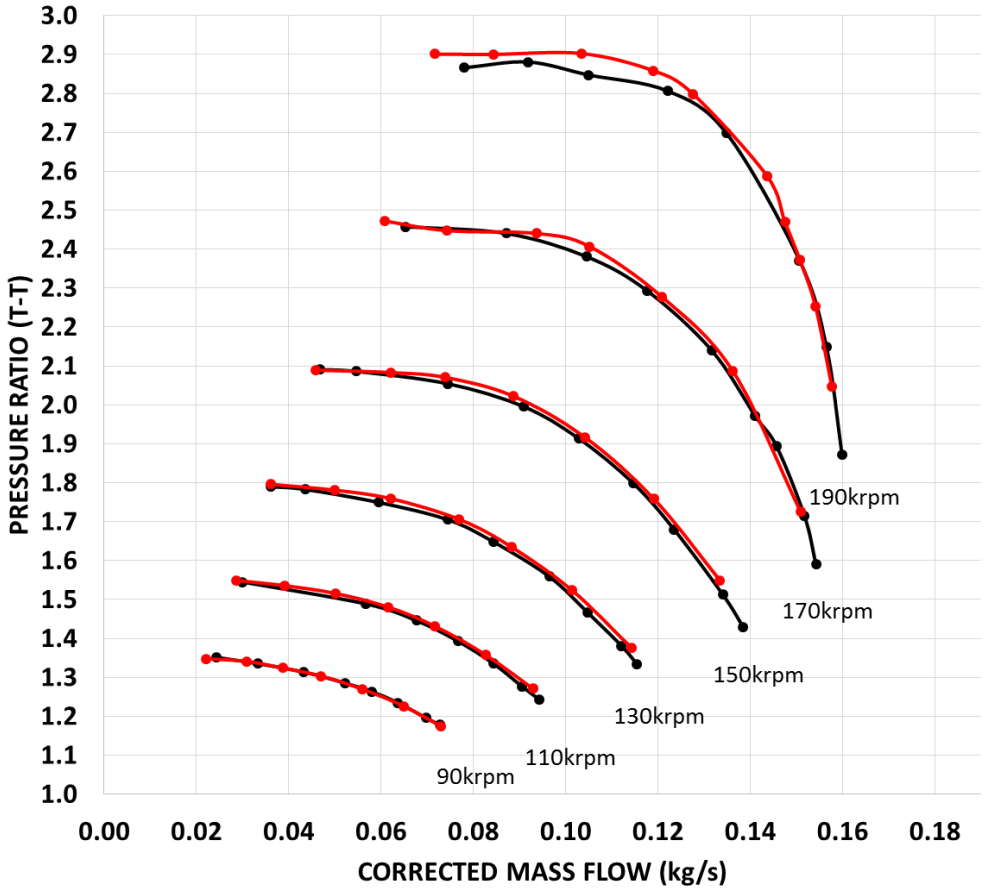

Figure 5-24. Compressor pressure ratio vs corrected mass flow generated on the manufacturer's gas stand (red solid lines) and Bath gas stand (black solid lines)

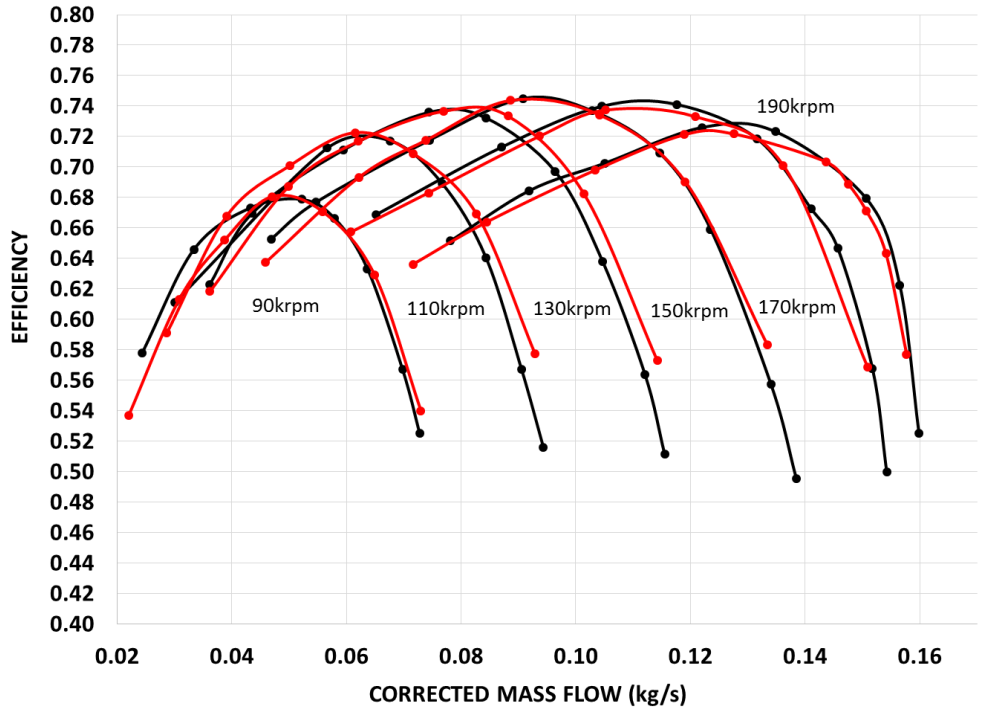

Figure 5-25. Compressor efficiency vs. corrected mass flow generated on the manufacturer's gas stand (red solid lines) and Bath gas stand (black solid lines)

The black solid lines on the above two figures indicated the data obtained on the gas stand in Bath whereas the red solid ones indicate the data obtained on HTT's gas stand. After comparing the two maps it can be concluded that a good match in terms of pressure ratio, corrected mass flow and efficiency was achieved between the above rigs. Thus, the extrapolation of data in the low speed region of any of these maps should provide very similar results.

Figure 5-26 shows the compressor performance lines drawn for the experimentally obtained data (black lines – hot conditions; red and purple lines - semi-adiabatic conditions with various oil temperatures as discussed above) and extrapolated data (green lines). There is only a very small and insignificant pressure ratio difference between all experimental cases, whereas the extrapolated lines indicate a significant over-prediction of pressure ratio for given corrected mass flows. The difference between the surge limits for the experimental and extrapolated data have not been investigated in detail. The offsets between all the considered cases are very clear (Figure 5-27). First, analysing the experimental data only it is noted that the heat transfer from the hotter side of the turbocharger (turbine and bearing housing) has a substantial effect on the efficiency of the compressor. The compressor efficiency measured at case one (hot turbine and oil) denoted by the black solid lines is clearly the lowest of all three. This is due to the fact that the total temperature difference across the compressor (compressor outlet total temperature minus inlet total temperature) is highly affected by the heat transfer. As a result, the compressor total temperature difference rises (mainly compressor outlet temperature). Increasing the value of the denominator in the compressor efficiency formula (Equation (*18*) causes the efficiency value to drop. The differences between the temperature gradient across the compressor for three experimental cases is shown in Figure 5-28. The other interesting thing to see based on the experimental efficiency comparison (Figure 5-27) is how the measured compressor efficiency is affected by the oil temperature. A reduction of the oil temperature by 30°C (from 90°C to 60°C) whilst maintaining the same turbine inlet condition (turbine inlet matched with compressor outlet temperature) has caused the efficiency to rise by up to about 6 percentage points at 70 krpm, 10 percentage points at 50 krpm and 12 percentage points at 30 krpm.

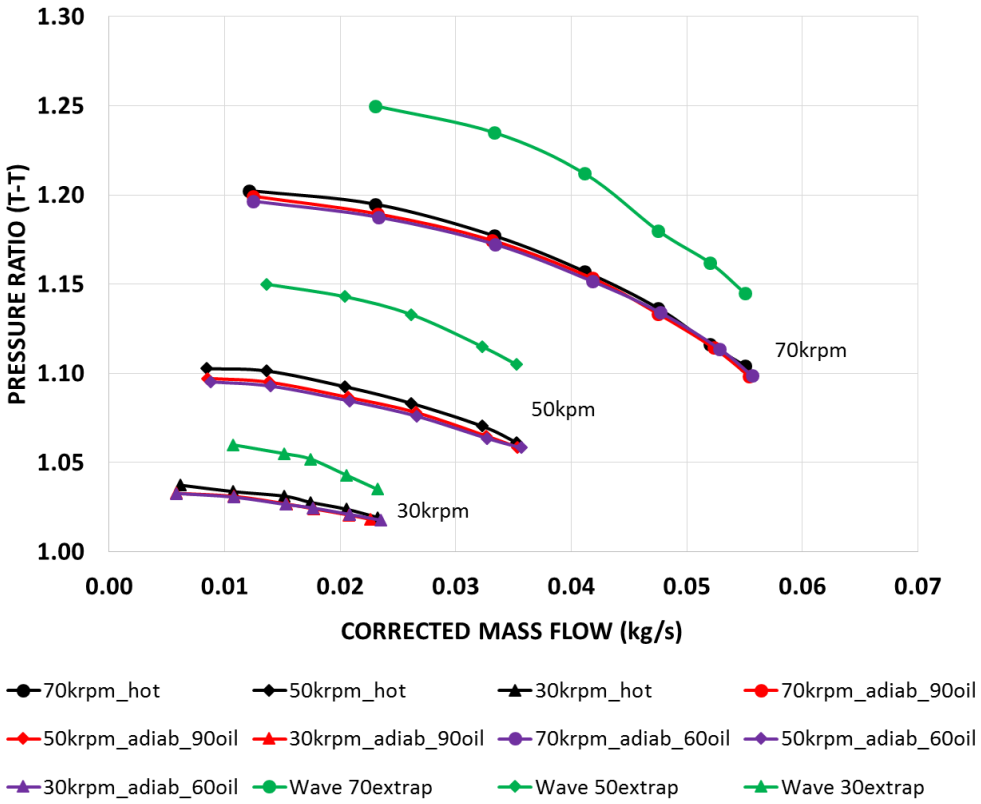

Figure 5-26. Compressor pressure ratio vs. corrected mass flow for the three measured cases and original map extrapolated data

Next, comparing the measured and extrapolated compressor efficiencies it can be concluded that under-predicted values of efficiency have been achieved at 70 krpm as a result of the original map extrapolation. The measured efficiency at case 3 at 70 krpm is already higher that the extrapolated one even despite the fact that still some heat is still transferred to the compressor gas from the hotter oil. It is difficult to judge the extrapolated efficiency values at 50 and 30 krpm, fully adiabatic tests are required to conclude on this.

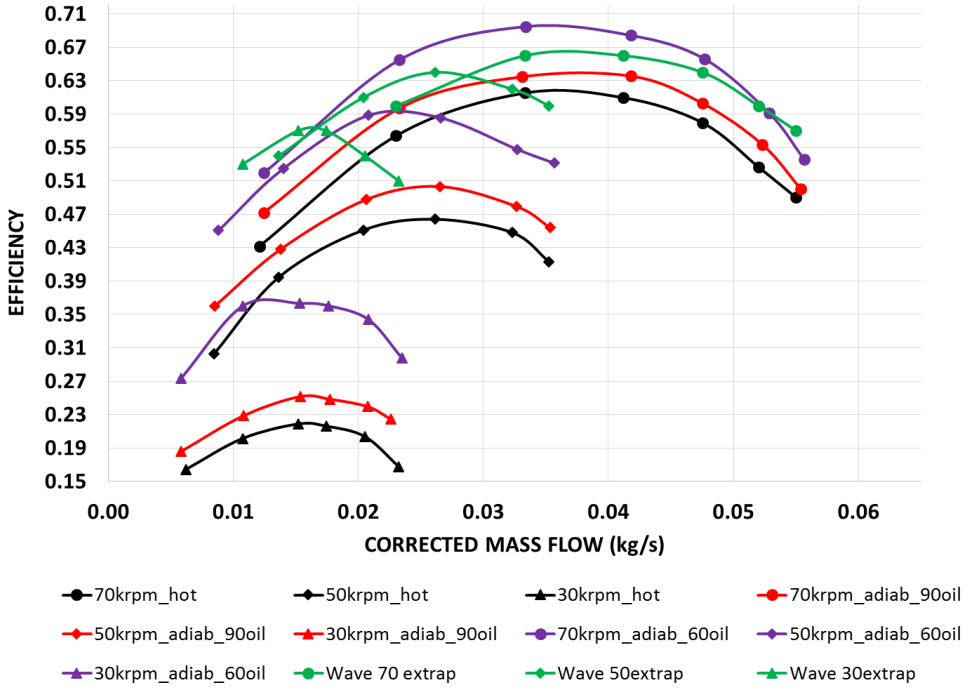

Figure 5-27. Compressor efficiency vs corrected mass flow for the three measured cases and original map extrapolated data

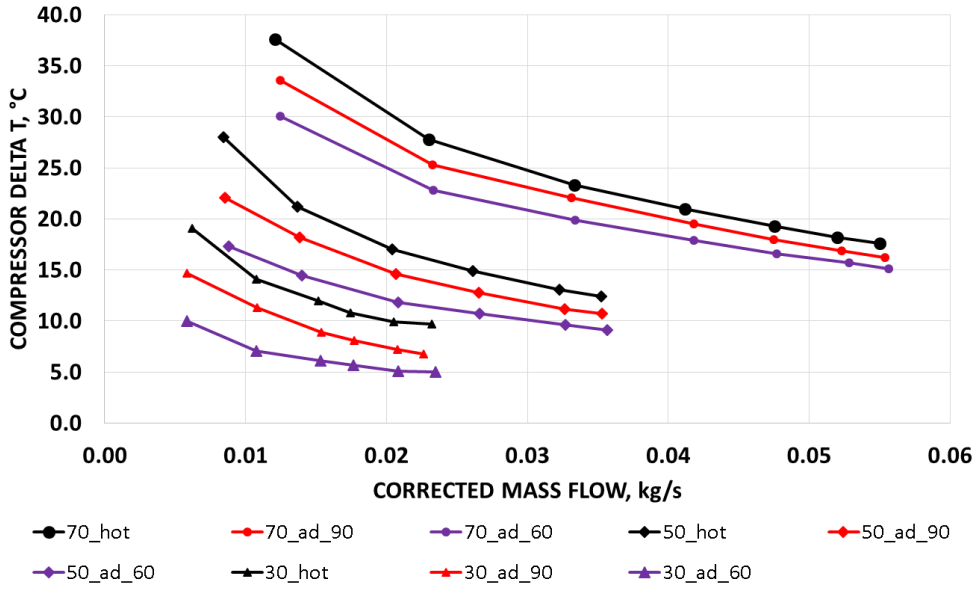

Figure 5-28. Temperature rise across the compressor at three tested experimental cases

Generally, based on the above data it can be concluded that generating the turbocharger adiabatic maps would increase the accuracy of any 1D simulation that currently uses the extrapolated data. Also, the heat transfer to the compressor gas from the hot turbo-charger side significantly affects the values of the measured efficiency.

5.2.2 3D CHT model of the turbocharger compressor

Introduction

The inaccuracies of the turbocharger performance maps caused by the heat transfer effects have been a motivation for the development of turbocharger models capable of separating work and heat transfer processes. The problem is shown below in Figure 5-29. Points 1 and 2 indicate the measured temperatures across the compressor which are used in the calculation of the compressor efficiency. However, in reality the work transfer happens only between points 1' and 2' whereas the heat transfer occurs between point 1 and 1' and between point 2' and 2. Failing to account for the heat transfer will lead to the efficiency error – the apparent efficiency (measured) will not reflect the work performed on the working gas but a sum of work and heat transfer.

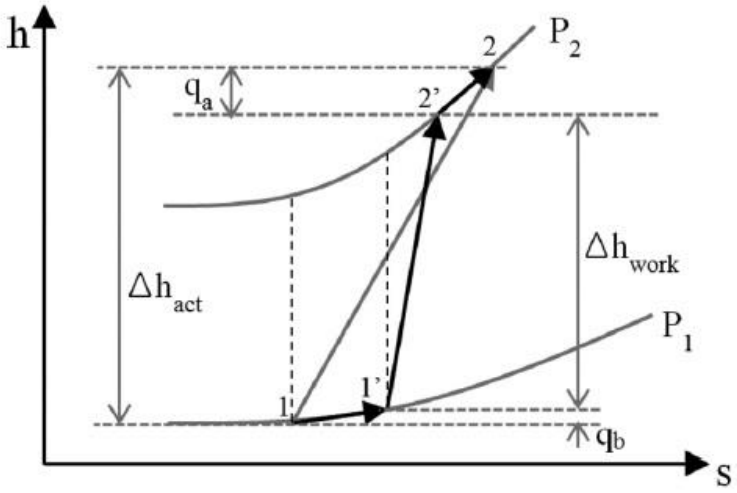

Figure 5-29. H-s compression chart [1]

Most of the existing models are based on the assumption that both the work transfer and heat transfer are independent. In other words and as can be seen in the figure above the compression and the expansion processes are assumed to occur adiabatically whereas the heat transfer to be isobaric and occur before or after the work transfer. Unlike many previous models that account for the heat transfer to happen only after the compression and before the expansion, a model developed at University of Bath by Burke [2] includes for the heat transfer between the compressor housing and fresh air both before and after compression. In general, the model is based on electrical analogy and originally formed by two nodes (Figure 5-30) corresponding to turbine and compressor housings. However, in order to include for the heat transfer both before and after compression a new variable (α_A) is introduced. This coefficient divides the total internal wetted area of the compressor into two: one area before compression and one are after it ($A_T = A_b + A_a = \alpha_A A_T + (1 - \alpha_A)A_T$). In such case the single compressor node has been split into two

nodes Figure 5-31. More details regarding the lumped capacitance model developed by Burke is given in two published papers [1, 2].

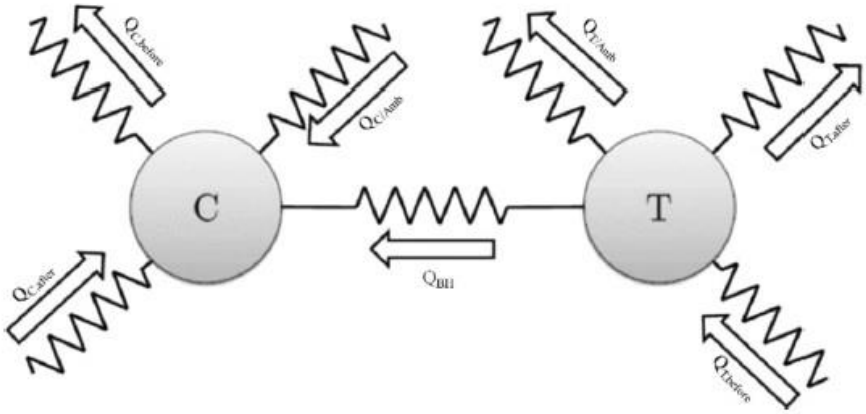

Figure 5-30. Two-node turbocharger model [2]

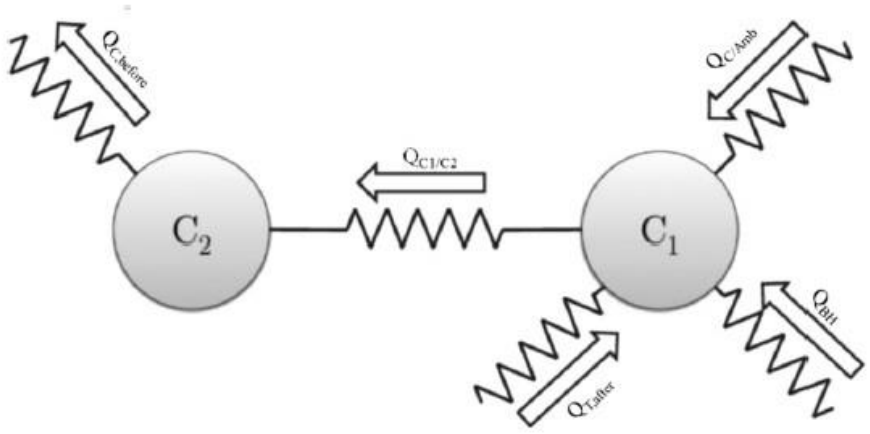

Figure 5-31. Two-node compressor model [2]

The investigation on the heat transfer between the turbocharger components carried out with the use of the above model was supported by a 3D conjugate heat transfer (CHT) model. The main aim behind performing the 3D simulations was to gain a detailed information regarding the complex heat flows in the compressor stage and feed the lumped capacitance model with values of heat transfer coefficients and α_A.

Model description and results

In general, CHT refers to situations in which multiple modes of heat transfer occur simultaneously and thus CHT analysis can accurately predict heat transfer by simultaneous solving all the relevant solid and flow field heat transfer processes. For this study a commercial code STAR CCM+ was used for all the calculations. The turbocharger utilised in this study was GT17 manufactured by HTT – the same turbo as used in the study of low

turbocharger speeds, surge and variable fluid properties. The 3D CHT model of the compressor and bearing housing was prepared based on the available CAD model and the following simplifications: turbine and shaft were not included in the simulations whereas the size and shape of the bearing housing was modified accordingly as shown in Figure 5-32.

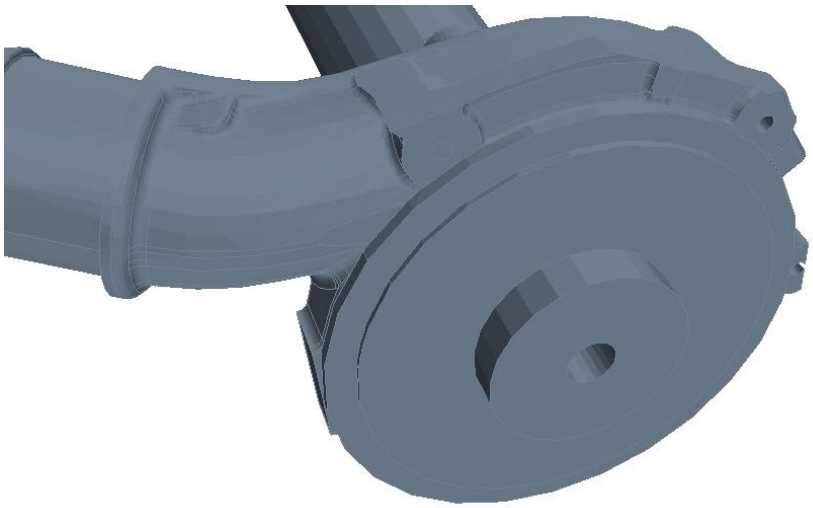

Figure 5-32. A view on the compressor back-plate and bearing housing of the CHT model

Three different scenarios were investigated within this study: for the first two, the convective heat transfer between the solid bodies and the internal working fluid as well as conduction within the solid bodies in contact were resolved. All the external boundaries of the model are set as adiabatic to block any heat transfer in the inbound and outbound directions. These two cases can therefore be considered to represent an externally insulated condition. In addition, in order to study the effects of α_A on the fluid compression and heat transfer, case 2 was set with some of the internal wetted surfaces as adiabatic walls. By doing so the pre-compression heat transfer between the compressor casing and working fluid has been eliminated (similar to setting $\alpha_A = 0$ in the lumped capacitance model). In the third case, the internal heat transfers were again modelled and external heat transfer was also modelled (compressor housing placed in a box of $1m^3$ filled with air as shown in Figure 5-33).

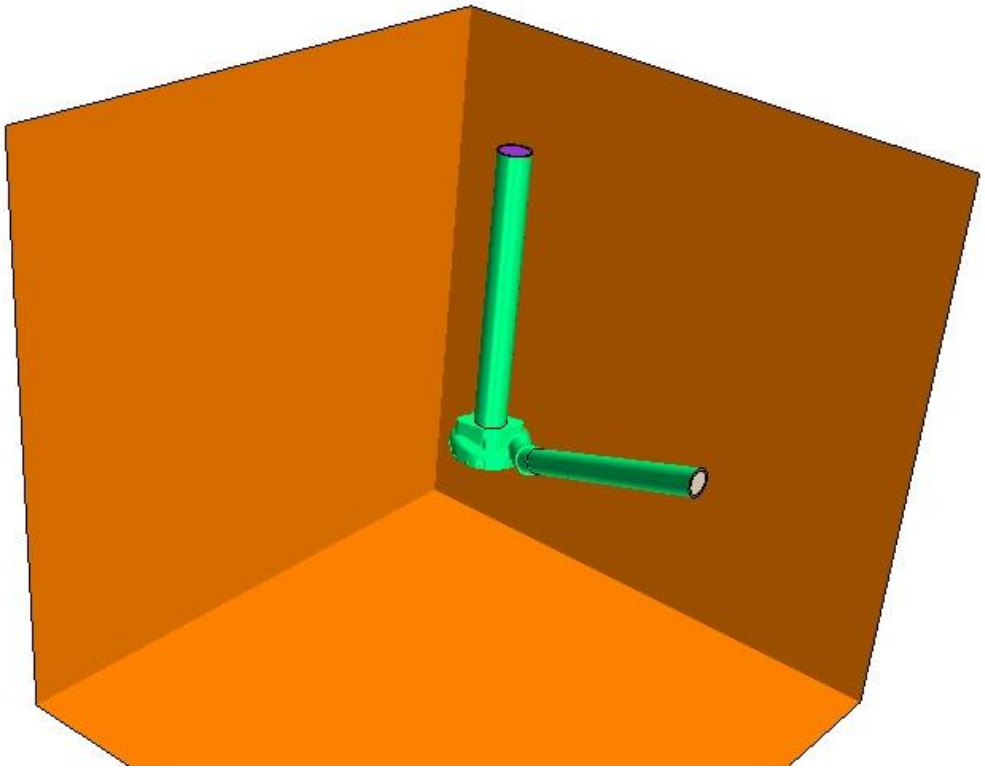

Figure 5-33. Geometry model of the third simulated scenario

The distribution of adiabatic and diabatic walls in cases 1-3 is shown in Figure 5-34. In all the simulated cases the conduction was resolved between the bearing housing, compressor case and inlet/outlet pipes. Radiation was excluded from consideration, whereas the summary of the convective flows is given in Table 5.

Table 5. Occurrence of the convective heat transfer within the simulated cased

	Pre-compression	Post-compression	To ambient air
Case 1	Yes	Yes	No
Case 2	No	Yes	No
Case 3	Yes	Yes	Yes

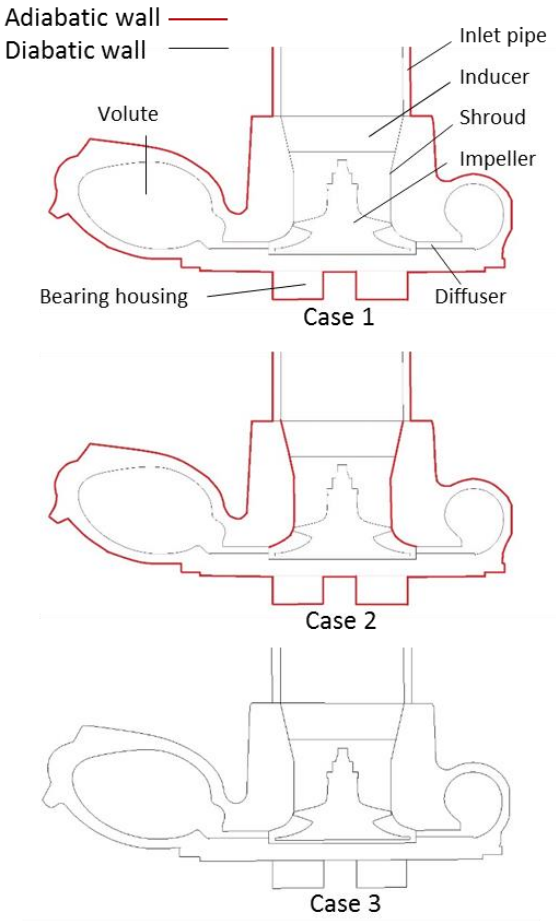

Figure 5-34. Cross-sections of the 3D CHT investigated cases

To resolve the heat transfers between the solid and fluid regions of the model material properties of aluminium were assigned to the compressor wheel and housing, cast iron to the bearing housing, and rubber to inlet and outlet pipes. The compressor working medium was air - an ideal gas. The movement of the impeller was modelled using the frozen rotor technique which generates constant rotational forces in the rotating domain to mimic the rotating effects but does not explicitly rotate the rotor domain thereby significantly reducing computational effort. The numerical mesh was generated from polyhedral elements and six layers of prism mesh on each side of the contact interface. This gives in approximation $2.45x10^6$ elements for cases 1 and 2 and $4.77x10^6$ elements for case 3. For the purpose of the turbulence modelling during the compression process Reynolds-averaged Navier–Stokes realizable k–e model has been chosen. Finally, the ambient air flow surrounding the compressor was assumed to be laminar. To resolve the compression of the flowing air the following boundary conditions have been chosen:

- Atmospheric pressure and static temperature at the fluid inlet boundary,
- Compressor impeller rotational speed,
- Air mass flow rate at the volute outlet,

- A fixed temperature set at the external surface of the bearing housing.

To understand the consequences of the various locations of thermal insulation for the heat paths within the compressor housing (as per the simulated models - Figure 5-34), an example of temperature contours is shown in Figure 5-35.

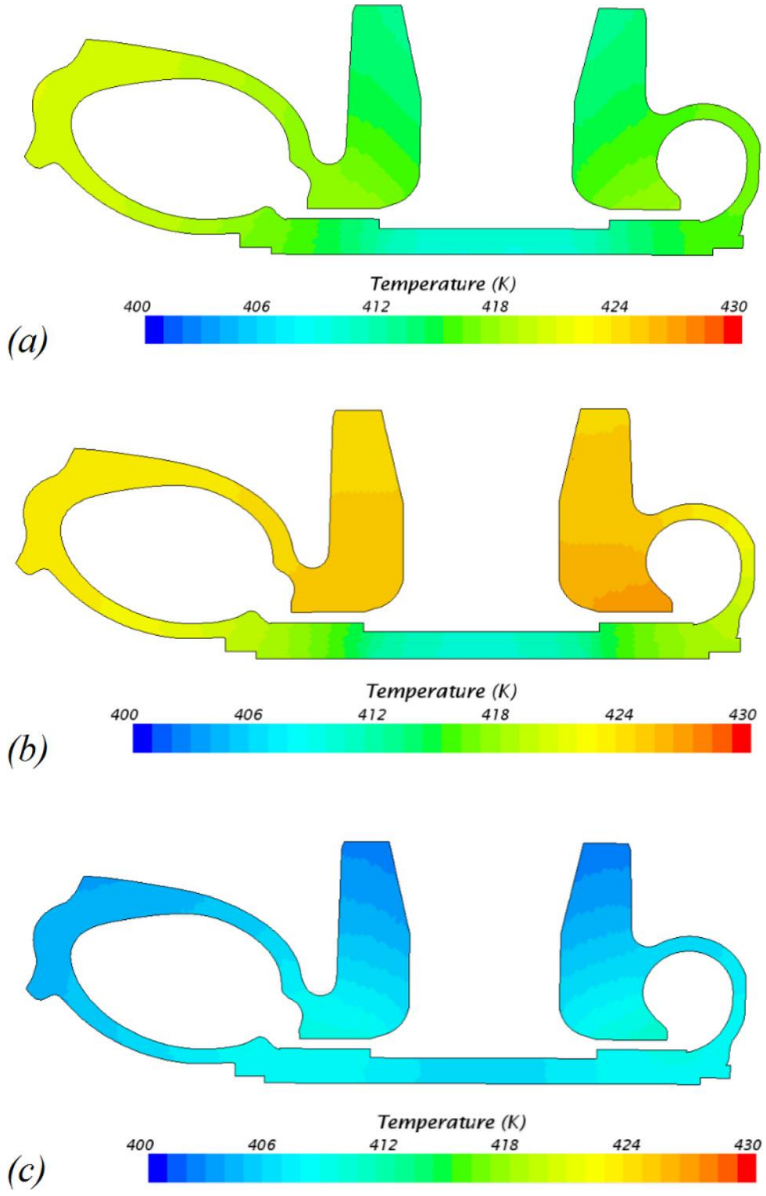

Figure 5-35. Compressor housing temperature contours for at three simulated cases – a) – case 1; b) – case 2; c) – case 3

The temperature contours shown above were obtained for the same compressor operating point and fixed temperature of the bearing housing. Comparing cases 1 and 2, the compressor housing temperature is 10–15K higher in case 2. This is caused by a greater accumulation of thermal energy as the heat path towards the gas is blocked at the inducer side and shroud surfaces. It is also interesting to note the high temperatures of the compressor housing in the region of the inducer in case 2 (with an adiabatic inducer and shroud). As this appears hotter than the compressor housing on the bearing housing

side, this suggests that this heat comes primarily from the compressed intake gases rather than being conducted round through the housing. For case 3, where external heat transfer is considered to the ambient, it is observed how the whole compressor case remains to a fairly constant temperature that is around 20K lower than predicted for the externally insulated case.

The area of the heat transfer modelling at the lumped capacitance model initially included four turbocharger speed lines, however this progressively has been reduced to two. It has been decided that the most interesting region would be the low and the high turbocharger speeds and therefore the analysis was made at 50 and 150 krpm. The calculations performed within the lumped capacitance model considered three various turbine inlet temperatures (100ºC, 300ºC and 500ºC) whereas α_A varied between 0 and 0.3. The lumped capacitance model was fed with the heat transfer coefficients achieved from the 3D CHT model to improve the prediction accuracy. As the result of the heat transfer model (lumped capacitance) simulations it can be concluded that the effect of the change of α_A predicted apparent compressor efficiency is negligible in the low speed region as opposed to the turbine inlet temperature change (Figure 5-36).

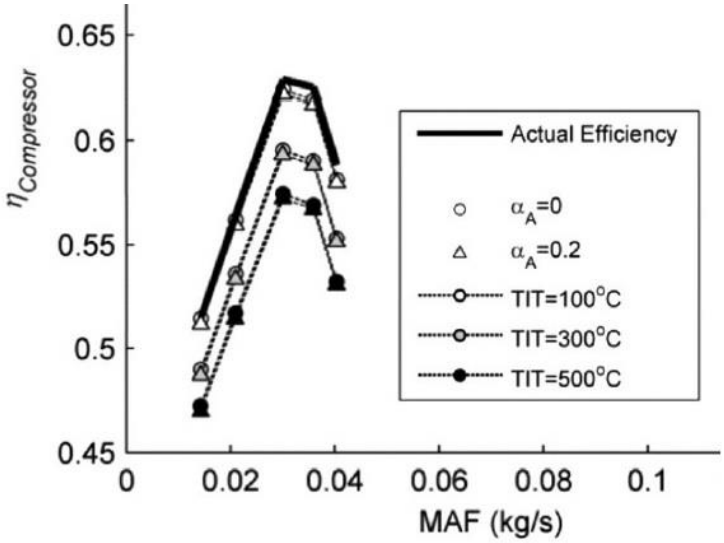

Figure 5-36. Compressor efficiency at 50 krpm for various turbine inlet temperatures and α_A [2]

At the high turbocharger speed of 150 krpm the influence of the turbine inlet temperature on the prediction of the compressor efficiency (Figure 5-37) is of a similar importance as the value of α_A (Figure 5-38).

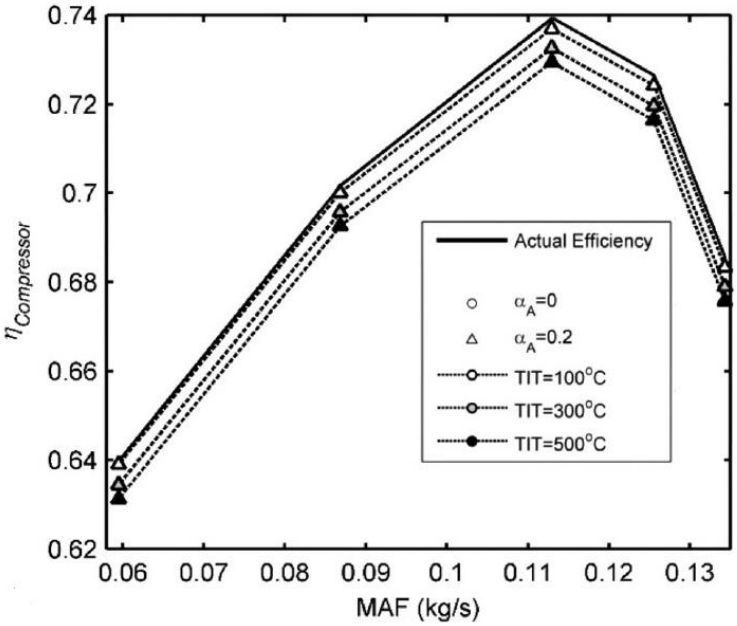

Figure 5-37. Compressor efficiency at 150 krpm at fixed value of α_A (0.2) and various turbine inlet temperatures [2]

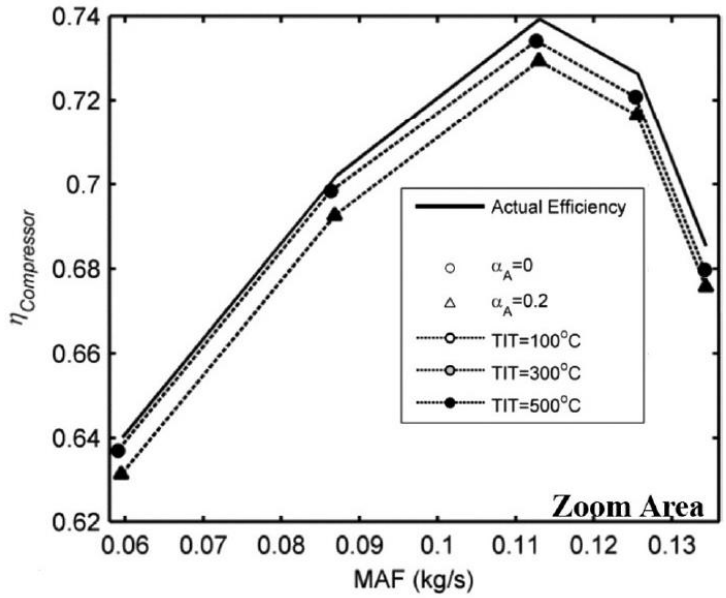

Figure 5-38. Compressor efficiency at 150 krpm at fixed turbine inlet temperature (TIT=500ºC) and various values of α_A [2]

5.2.3 Uncertainty of the compressor efficiency based on the heat transfer estimation method

Another example of work targeting the separation of heat and work transfer within the turbocharger compressor is the study carried out by Serano et al [35]. As a result of their testing campaign on two selected turbochargers a relation linking the measured turbine

enthalpy drop with the ratio of compressor enthalpy rise and heat passed to the compressed gas has been described (Figure 5-39).

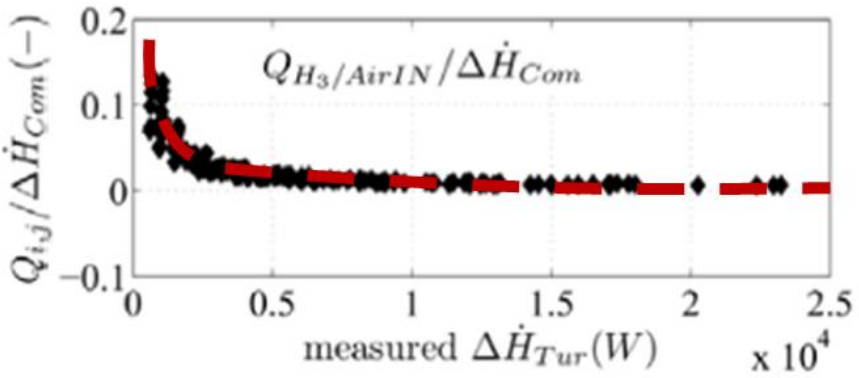

Figure 5-39. The ratio of compressor enthalpy rise and heat delivered to the compressor vs. turbine enthalpy drop [35].

The geometry comparison between the Serano's tested and Bath gas-stand tested turbocharger (Puma) is given in Table 6 and it can be concluded that a fairly similar size turbochargers were used.

Table 6. Comparison of tested turbochargers (Valencia vs. Bath)

	Turbocharger tested in Valencia	Puma turbocharger tested in Bath
Turbine Wheel Diameter	40mm	42.5mm
Compressor Wheel Diameter	54mm	49mm
VGT	Yes	Yes
Coolant circuit	Yes	No

Now, based on the above function the amount of the heat transferred to the compressor (and therefore the work related efficiency) can be found. For this reason the following calculations were carried out based on the steady-state gas stand data obtained in hot turbine inlet conditions (500ºC):

- Turbine enthalpy drop:

$$\Delta H_t = (T_{3t} - T_{4s})\dot{m}_t c_{p_{t,avg}} \quad (62)$$

- Compressor enthalpy rise (compressor power):

$$\Delta H_c = \dot{m}_c c_{p_{c,avg}} (T_{2t} - T_{1t}) \quad (63)$$

- Estimated heat transferred to the compressor, Q is based on the above calculations and function linking the compressor and turbine enthalpy and heat Q as shown in Figure 5-39.

It is known that the turbine enthalpy drop (turbine power) can also be calculated as a sum of compressor power and friction losses (Equation (*64*)).

$$\Delta H_t = \Delta H_c + P_f \tag{64}$$

Although the above method is preferable (no need to know the post-turbine temperature which is difficult to measure correctly due to flow fluctuations) it requires accurate measurement of the oil parameters (temperature drop, pressure for density calculation if volumetric flow is measured, oil flow). However as the oil parameters (oil pressure) were not measured throughout the experimental tests the first method (Equation (*62*)) of turbine enthalpy drop was used.

Once the estimated value of the heat absorbed by the compressor is calculated, the temperature rise across the compressor due to that heat transfer can be found as follows:

$$(T_{2t} - T_{1t}) = \frac{Q}{\dot{m}_c c_{p_{c,avg}}} \tag{65}$$

Assuming that all of the heat transfer happens post compression (which is a valid case in low turbocharger speeds as proven by the lumped capacitance model discussed in the preceding subsection of this thesis) the change of the compressor outlet total temperature T_{2t} is calculated from the above formula. This value shall be then understood as the uncertainty of the post-compressor temperature measurement due to the heat transfer effects.

Figure 5-40 shows the compressor efficiency measured at the low turbocharger speed region and for the experimental data obtained at hot test conditions (TIT = 500ºC). The superimposed error bars reflect the uncertainty of efficiency based on the Type-B uncertainty analysis (sensor accuracy sensitive only) for the sensors as given in Table 1.

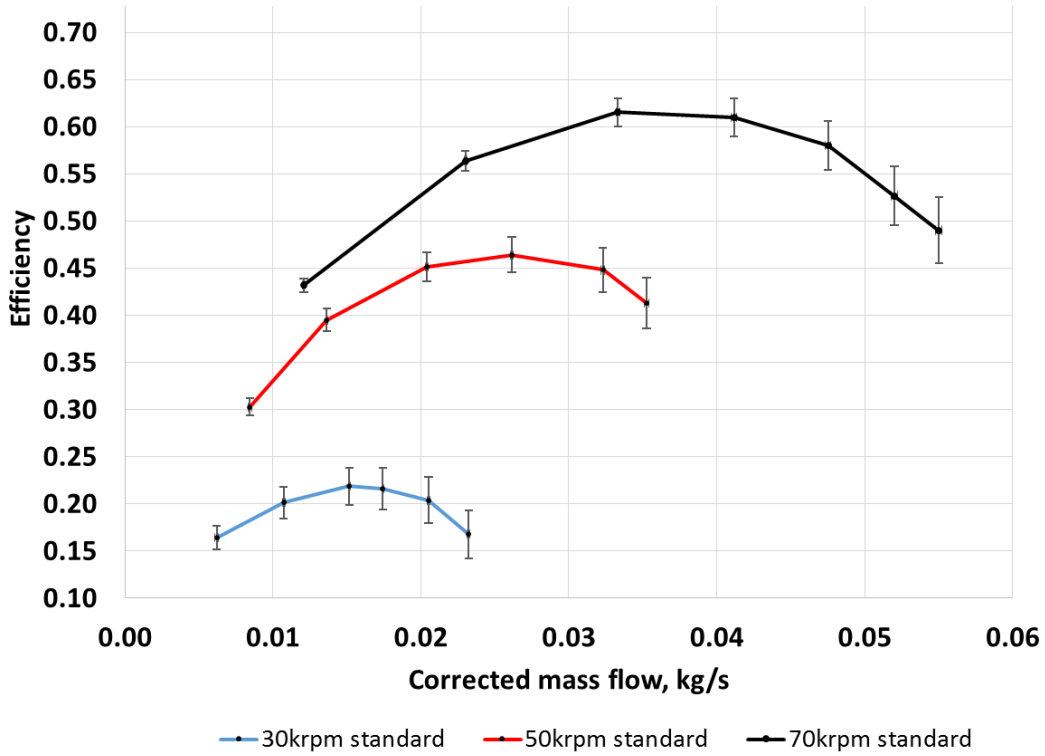

Figure 5-40. Uncertainty of the measured compressor efficiency based on the selected sensors

The uncertainty of the measured compressor efficiency due to the sensor accuracy and heat transfer effects (estimated heat) is plotted in Figure 5-41.

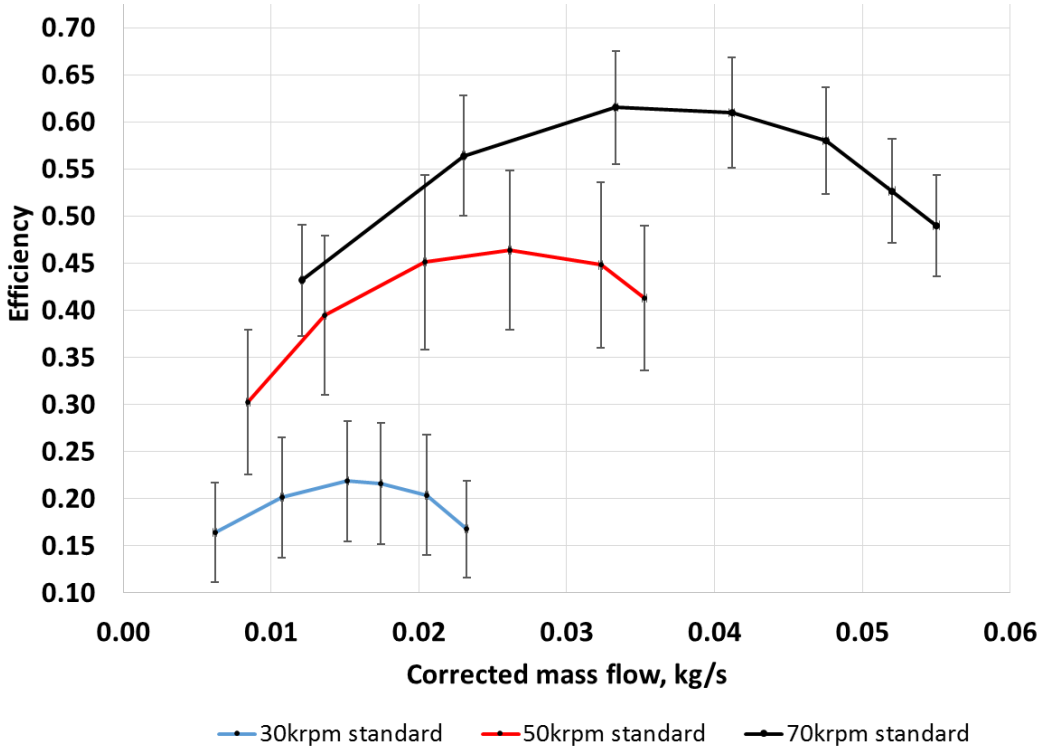

Figure 5-41. Uncertainty of the measured compressor efficiency based on the selected sensors and estimated heat transfer

Comparing the Figure 5-40 and Figure 5-41 it can be noted that in the low turbocharger speed region the estimated heat transfer from the hot side of the turbocharger is a dominant factor in the total uncertainty of the measured compressor efficiency which stays in agreement with the experimental tests (Section 5.2.1). However, the experimental tests carried out in hot and semi-adiabatic conditions have shown that the heat transfer related uncertainty rises when moving towards the lower speeds. This does not stay in agreement with Figure 5-41 which indicates the greater efficiency uncertainty at the speed of 50 krpm that at 30 krpm. The reason for this is probably the errors associated with the turbine power calculation.

6. Experimental surge measurement

The lack of the standardised definition of experimental surge onset is a serious issue. While turbocharger manufacturers keep their own surge metrics confidential, vehicle engineers struggle to compare compressor maps that come from various suppliers and are characterised by various surge limits. Moreover, it has been proven by some researchers (Section 3.3.3) that the surge limits established in steady-state conditions do not fit well with the limits that are valid under on-engine operation. Namely, the steady-state surge limits are most often too conservative for the latter where the turbocharger compressor can be pushed further towards the lower mass flow rates without experiencing surge. This makes the turbocharger-engine matching process inconvenient as it is lacking precision in predicting the full operating range of compressors in pulsating flow (on-engine conditions). As a result some compressor maps may be dropped out during the process due to the insufficient surge margin whereas they could actually make a better match. Therefore, to understand how the surge line is drawn during the steady-state mapping process, and how much surge lines can be offset if based on various metrics, the first phase of study is performed. It is carried out on a small turbocharger compressor (from gasoline 1.0l Fox engine) manufactured by Continental, addressed as Fox compressor here after. The author looks into various ways of measuring surge considering measurement of temperature and pressure. In parallel, various available surge metrics are to be compared. Next, based on the conclusions drawn from phase one, a comparison of steady-state gas stand surge is performed between two various compressor sizes – Fox compressor and a larger size compressor from diesel 2.2l Puma engine (manufactured by Honeywell Turbocharging Technologies), referred as Puma compressor hereinafter. Finally, a comparison between the surge development between steady-state gas stand and on-engine pulsating conditions takes place based on the Puma compressor testing campaign.

6.1 Experimental surge measurement methodology in steady-state gas stand conditions – Fox compressor

All tests included within this phase of the study were carried out on a steady-state turbocharger facility. The selected turbocharger came from a modern gasoline 1.0 litre engine and incorporated a fixed geometry radial turbine and radial compressor equipped with a blow-off valve. The turbocharger compressor impeller tip diameter was 42.3mm. Both the turbine wastegate and compressor blow-off valves were kept closed throughout the tests. Turbine inlet temperature was fixed at 600°C ± 2ºC whereas oil and bearing housing cooling water were kept at 90°C (at the outlet to the respective Regloplas units). The full layout of the gas stand and equipment used is presented in Figure 6-1.

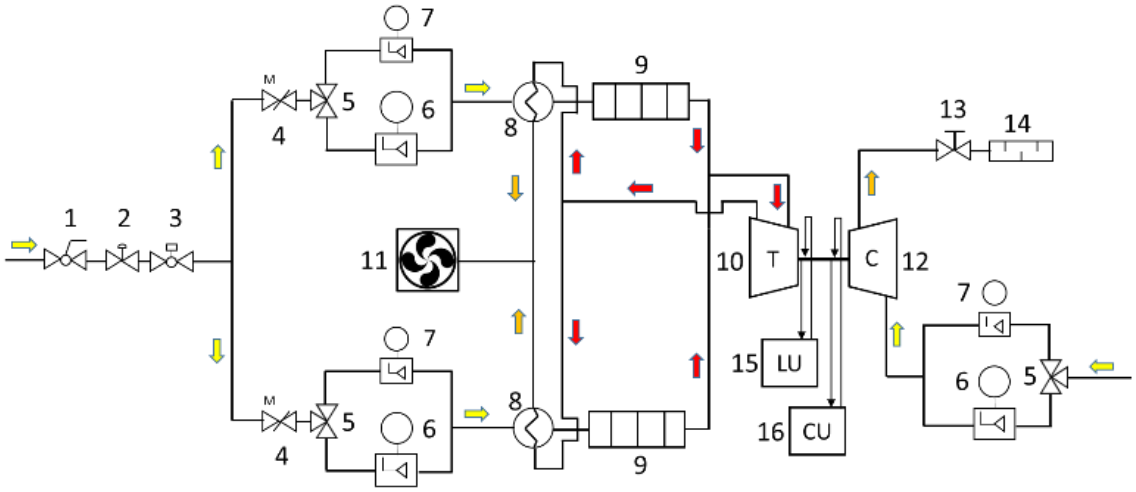

Number	Turbocharger gas stand equipment
1	Manual ball type shut off valve
2	SMC pneumatic pressure regulator
3	Ball type valve with Kinetrol electro-pneumatic positioner
4	Sierra CP motorized butterfly valve
5	Fiesto 3-way ball type valve
6	3" McCrometer V-cone mass flow meter with Siemens DSIII differential pressure transmitter
7	2" McCrometer V-cone mass flow meter with Siemens DSIII differential pressure transmitter
8	Bowman gas-to-gas heat exchanger
9	Axes Design variable power electric heater
10	Turbocharger turbine
11	Electrically controlled roof extraction fan
12	Turbocharger compressor
13	Motorized backpressure valve
14	In-line type performance silencer
15	Turbocharger lubrication unit c/w variable speed pump, electric heater, gas-to-water heat exchanger, pressure & temperature sensors
16	Turbocharger bearing housing cooling unit c/w electric heater, water-to-water heat exchanger, temperature sensors

Figure 6-1. Layout of turbocharger gas stand facility

The general mapping approach has been discussed in paragraph 4.2.1. The basic instrumentation of the gas stand is given in Table 1 whereas the surge detection oriented instrumentation schematic is shown in Figure 6-2 and the sensors used are listed in Table 7. Finally, a photograph of the turbocharger installed on the rig is shown in Figure 6-3.

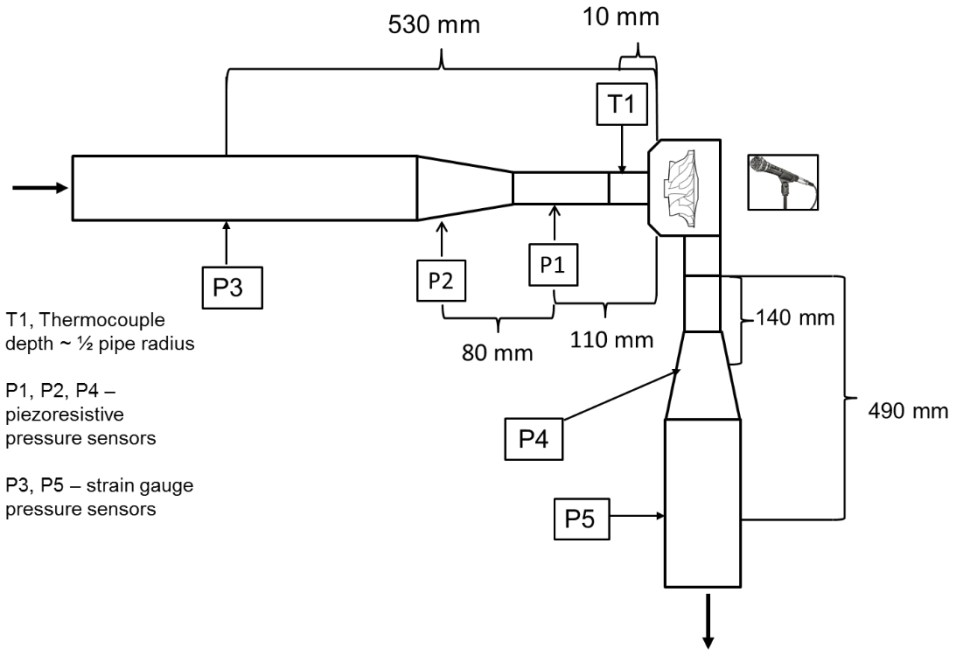

Figure 6-2. Schematic of the instrumentation used for the compressor surge study

Table 7. Gas stand surge detection instrumentation list

Sensor Symbol	Sensor Location	Measured Quantity	Sensor Model	Manufacturer	Sensor type	Accuracy	Operating Range
P1	Compressor Intake Pipework	static pressure	XCEL-100-50PSIA	Kulite	piezoresistive	0.10%	0-689.5kPa absolute
P2		static pressure	XCEL-100-50PSIA	Kulite	piezoresistive	0.10%	0-689.5kPa absolute
P3		static pressure	PX312-050AV	Omega	strain gauge	0.25%	0-344.7kPa absolute
P4	Compressor Outlet Pipework	static pressure	XCEL-100-50PSIA	Kulite	piezoresistive	0.10%	0-689.5kPa absolute
P5		static pressure	PX312-100GV	Omega	strain gauge	0.25%	0-689.5kPa above atm.
T1	Comp. Inducer Pipe	static temperature	1.5mm k-type	TC Direct	thermocouple	higher of 2.5K or 0.75%	(-50°C to 1100°C)
Microphone	Close from compressor	pressure	377C01microphone + 426B03 preamplifier	PCB	pre-polarized microphone	/	3Hz-100kHz

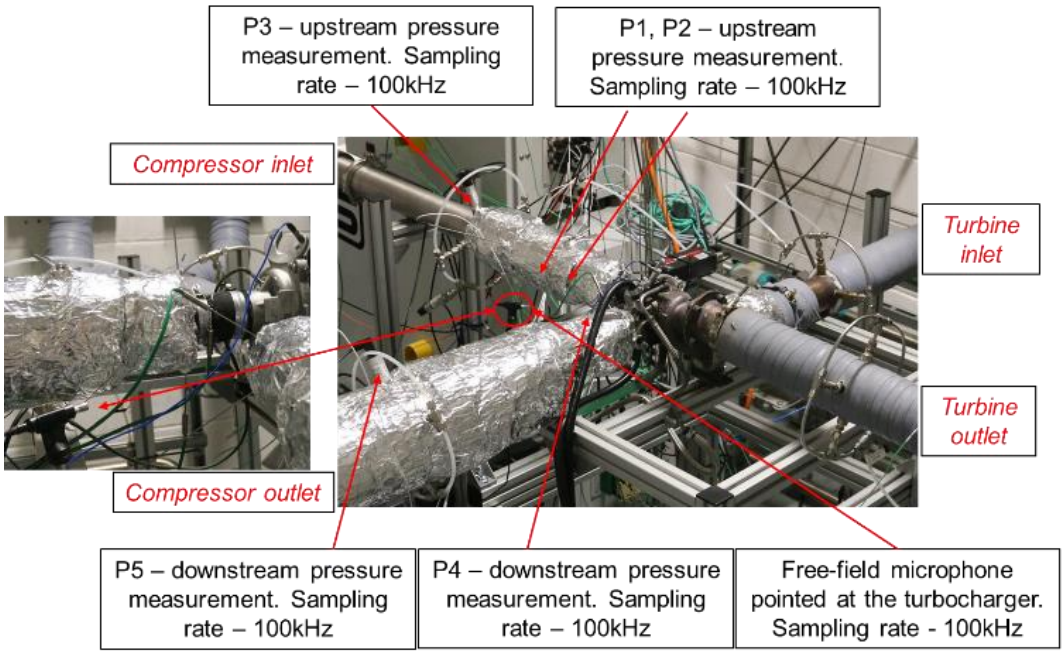

Figure 6-3. Fox turbocharger installed on the test rig with surge detection instrumentation indicated

Two types of pressure transducers were used in this investigation: Kulite miniature piezoresistive sensors (P1, P2, P4) and Omega silicon strain gauge (P3, P5), all connected to a Dewesoft Sirius data acquisition system. A free-field prepolarized PCB microphone (model 377C01) was placed 15cm from the compressor housing and pointed towards it. All pressure data was sampled at 100 kHz. The 1.5mm k-type thermocouple tip was placed 10mm from the compressor impeller at half of the inducer pipe radius (half the distance from centreline to ID at housing inlet). Figure 6-4 shows the performance map of the Fox compressor generated on the gas stand. As can be seen the data is recorded at seven constant corrected compressor speeds and various steady-state operating points at each compressor speed line. The compressor operating area for the surge study is bounded by two black solid and dashed lines. The left hand side solid black line denotes the hard surge condition that is judged by the rig operator based on the large post compressor pressure signal oscillations (live observation of FFT spikes of the post compressor pressure P5) and audible noise. Hard surge is approached slowly with gradual closure of the back-pressure valve. No ramp is set on the back-pressure valve response time to see if the hard surge point location is dependant on the dynamics of change of the operating condition. The right hand side dashed black line connects the points of the highest mass flow rate included in this analysis. There is no specific criterion for the selection of these however they are chosen in a region shortly before and when audible noise is noticed by the rig operator. Finally, the black dots placed between the black solid and dashed lines show the operating points of the compressor where data was recorded. The logging period at each operating point is ten seconds except for the hard surge points where it is reduced to two-three seconds to reduce the risk of potential mechanical damage. Both mass flow and pressure ratio have been normalised. This has been achieved by dividing the original corrected mass flow and pressure ratio values by a chosen fixed number.

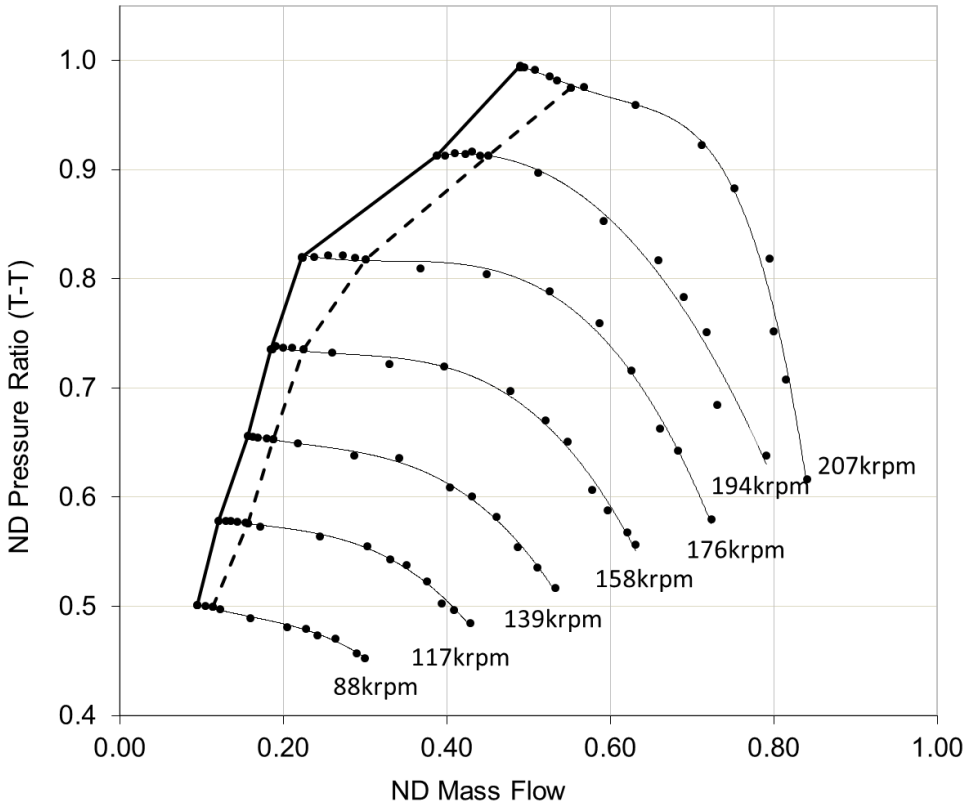

Figure 6-4. Turbocharger compressor map with the indicated region (bounded by solid and dashed lines) of data points for surge analysis.

6.2 Experimental surge measurement methodology in steady-state gas stand conditions – Puma turbocharger compressor.

Comparison of surge development at steady-state gas stand conditions for various size turbocharger compressors has been achieved by testing the Fox and Puma compressors. Table 8 provides details regarding both of the tested and compared turbochargers.

Table 8. List of tested turbochargers

Manufacturer	Engine platform and size	Compressor Impeller tip diameter	Compressor blow-off valve	Fuel type	Turbine geometry	Tested Turbine Inlet Temperature (TIT)	Water-cooled bearing housing
Continental	Fox 1.0l	42.3mm	YES	gasoline	fixed (wastegate)	600°C	YES
HTT	Puma 2.2l	49mm	NO	diesel	variable (VNT)	500°C	NO

The level of instrumentation used for surge detection on the Puma compressor was significantly reduced compared with the previously tested Fox compressor, as can be seen in Figure 6-5. Only post-compressor pressure is logged when testing the Puma turbo, using the same sensor as previously. The sampling frequency is 100 kHz, and the logging period at the steady-state operating points has been reduced (when compared with the Fox compressor) to five seconds in order to limit the size of the output data files. The turbine inlet temperature throughout the tests is kept at 500°C ± 2ºC. The Puma turbocharger installed on the gas stand is shown in Figure 6-5. The operating points that the

data was logged at are indicated in Figure 6-6. Again, these are the points bounded by solid and dashed black lines.

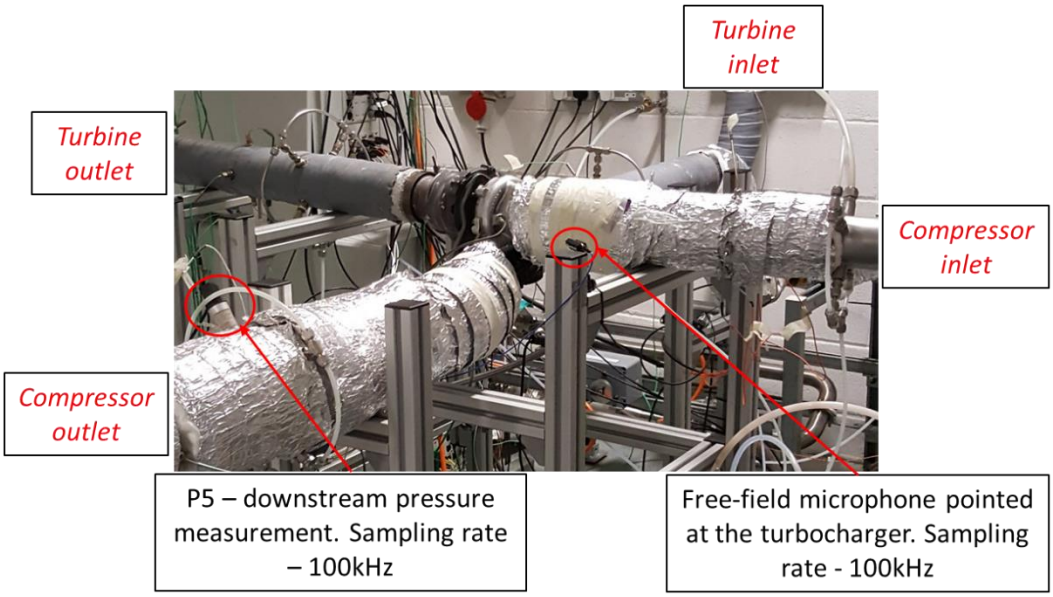

Figure 6-5. HTT Puma turbocharger installed on the test rig with the marked instrumentation for compressor surge study

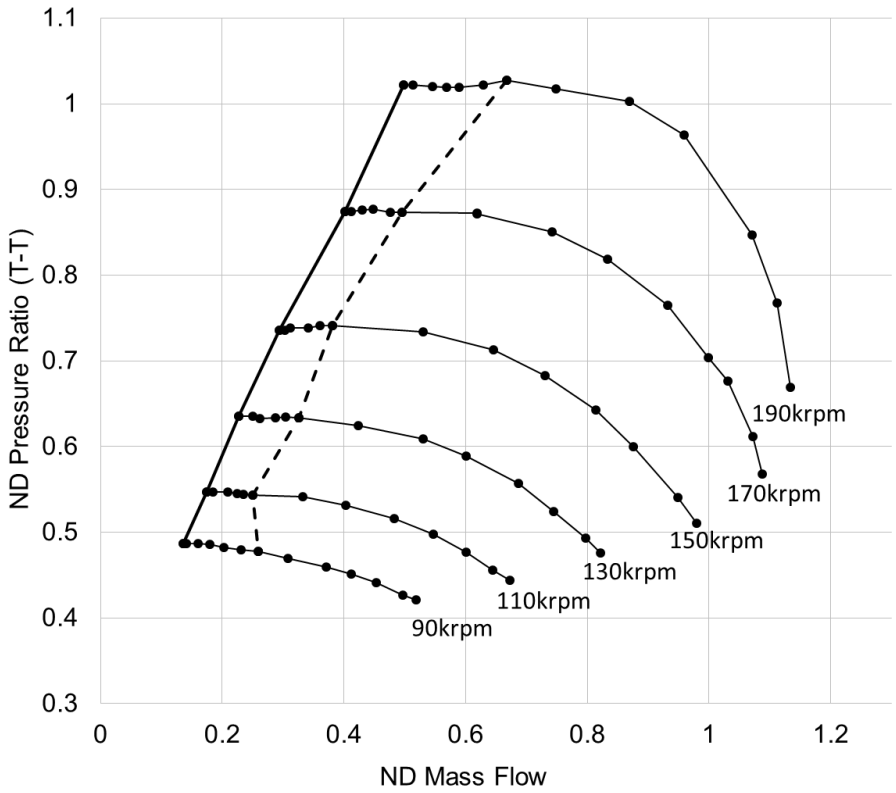

Figure 6-6. Puma turbocharger compressor map with the indicated region (bounded by solid and dashed lines) of data points for surge analysis

6.3 Experimental surge measurement methodology on-engine conditions

The last part of the study on surge has been carried out on an externally boosted engine dynamic test facility. The development of the test rig and most of the research carried out on it since the installation, have been a part of other student's PhD. Therefore detailed description of the equipment and instrumentation will not be reported within this thesis. The three major components of the rig are: a 2.2l Diesel Puma engine sitting on a dynamic test bed, a charge air conditioning boost rig capable of providing steady-state or transient boost to the engine intake manifold as an alternative to the turbocharger compressor (shown in Figure 6-7) and a gas stand-like piped and instrumented turbocharger (Figure 6-8).

Figure 6-7. Boost rig

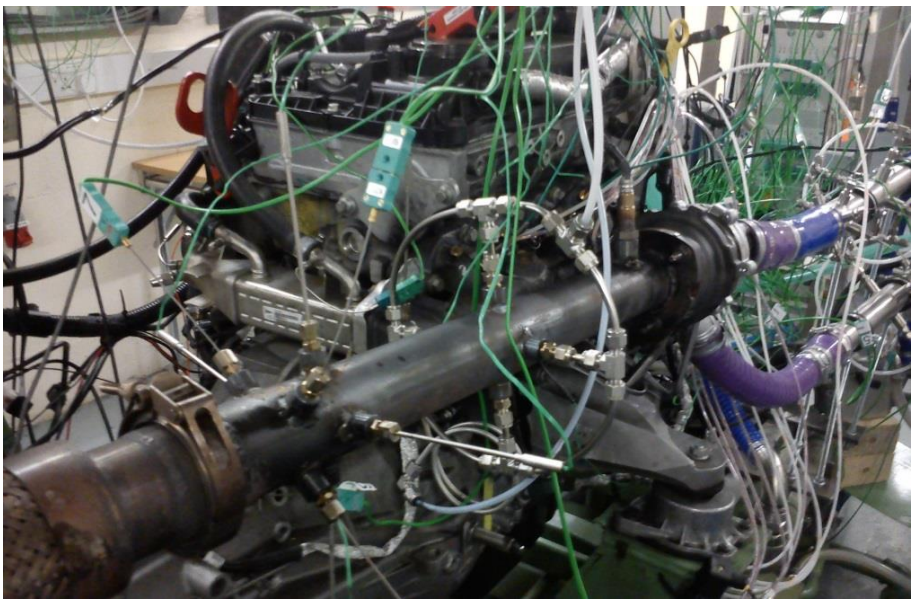

Figure 6-8. On-engine installed turbocharger

The detailed information regarding the rig operation and its instrumentation can be found in the reference [106]. Generally, the test rig allows for testing various turbochargers on the engine but without the engine-based constraints. The turbocharger compressor can either work in steady-state or pulsating conditions. In the former case the pipework located on the high pressure side of the compressor is disconnected from the engine intake manifold, air mass flow is controlled via a back-pressure valve, and the compressed air is discharged to ambient. Steady-state operation of the compressor is assumed despite the minor turbocharger speed oscillations due to the exhaust gas pulse arrival at the turbine entry. The speed fluctuation is minor because of the inertia of the turbocharger, and the compressor side performance parameters are calculated based on the averaged data. A schematic of this arrangement is shown in Figure 6-9. In order to control the compressor surge for a complete powertrain system, the boost rig has been connected with the compressor outlet ducts before connecting the intake manifold. The installation of a non-return valve downstream from the boost rig is required to avoid any back-flows. In this configuration (Figure 6-10) the external boost supply can increase the load on the compressor and reduce the mass flow simultaneously. Due to the boost pressure limits of the engine intake manifold, and to further control the compressor mass flow a compressor restricting flow (CMV) valve has been installed upstream from the compressor. In this configuration the turbocharger compressor can see the returning pressure waves (due to reflection from closed intake valves) and therefore operate in pulsating flow. The engine gas stand facility is arranged as shown in Figure 6-10.

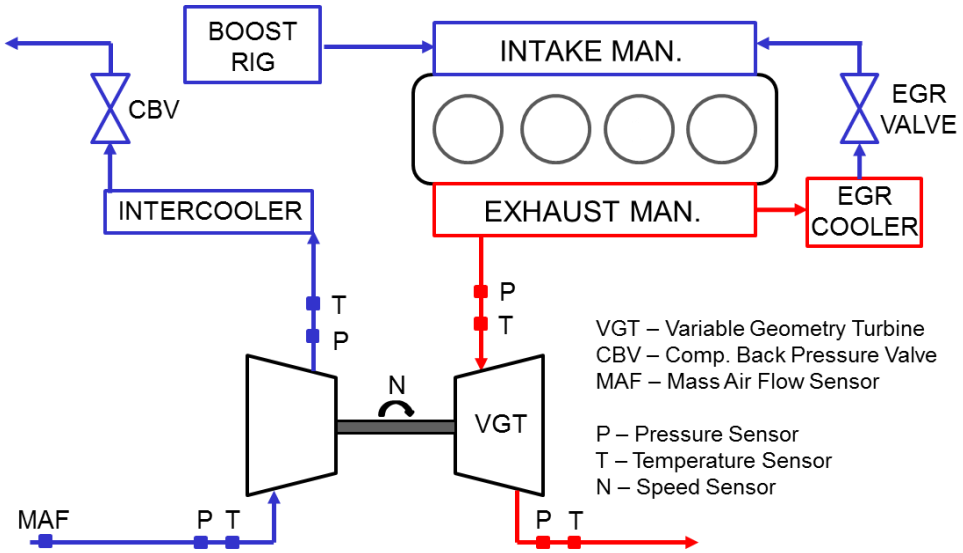

Figure 6-9. On-engine application with steady-state air flow through the compressor

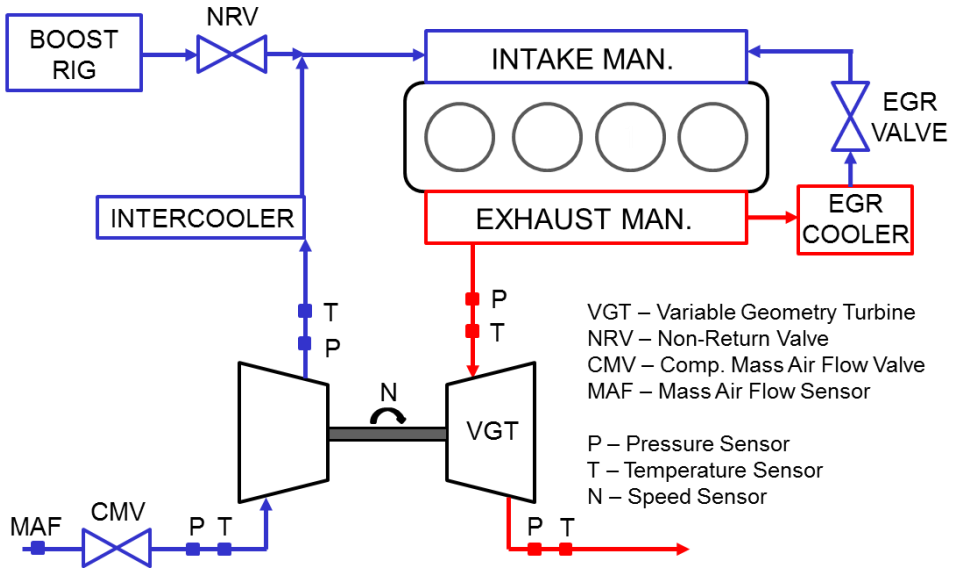

Figure 6-10. On-engine application with pulsating flow through the compressor

6.4 Experimental surge measurement results – Fox turbocharger

In the first part of the investigation on experimental surge measurement carried out at steady-state gas stand conditions and for the Fox compressor it was aimed to find the preferable measurement quantity and sensor location for surge measurement and compare various surge metrics. The preferable location was defined as the one where the measured quantities are able to indicate surge-related phenomena, and the magnitudes of the signal are as independent of the distance from the hardware as possible. Also, based on the behaviour of the measured quantities at surge it is sought for the potential of using those quantities in the process of defining the surge metric or even in the active process of surge mitigation.

6.4.1 Low frequency pressure data analysis

The first physical quantity that is analysed is pressure and it is measured at three different locations in the intake pipework and two locations in the post-compressor pipework. The raw data logged during the recording period is a function of measured quantity (pressure) and time. Examples of such data for two different compressor operating points at a sampling rate of 100 kHz is shown in Figure 6-11 and Figure 6-12.

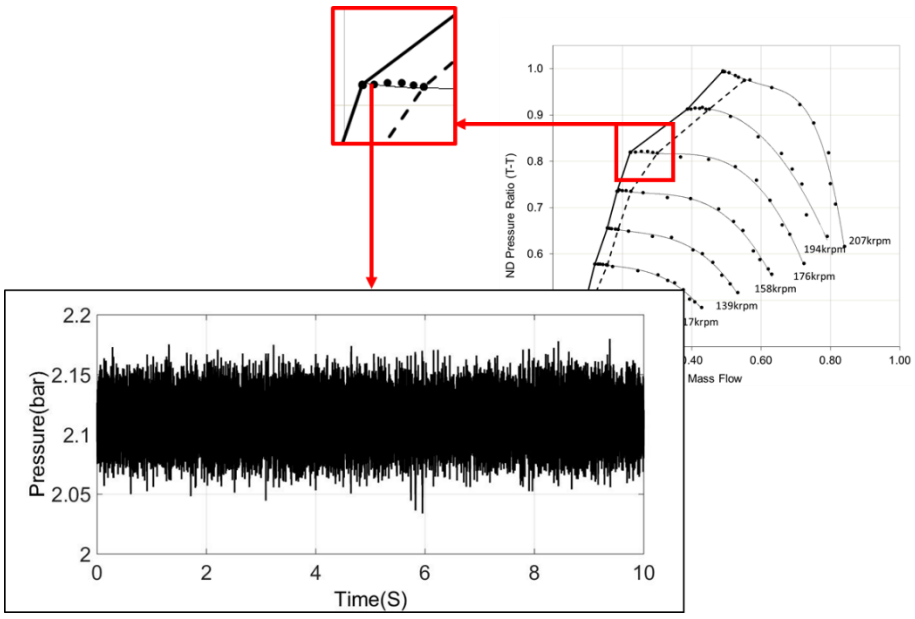

Figure 6-11. A plot of a post-compressor pressure recorded at 176 krpm at location P5 and at a selected operating point

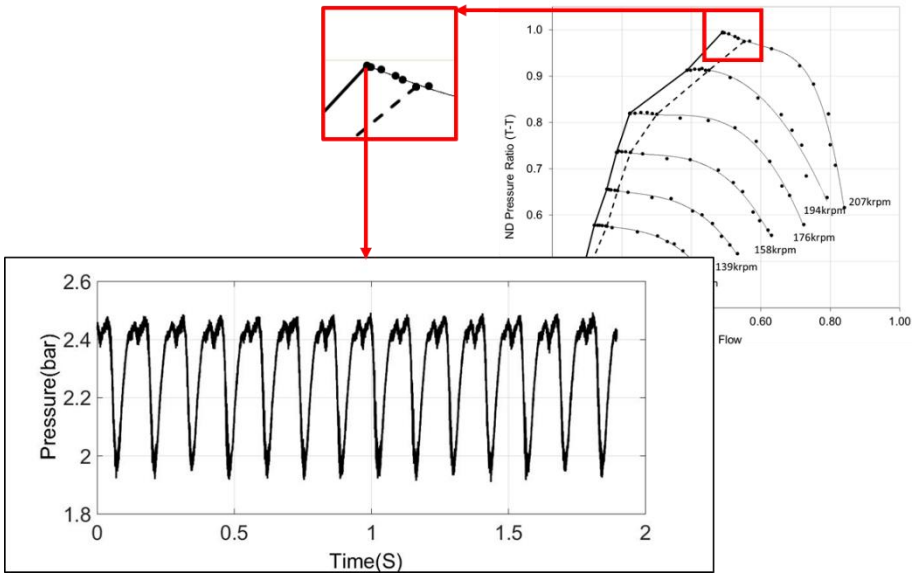

Figure 6-12. A plot of a post-compressor pressure recorded at 207 krpm at location P5 and at a selected operating point

An interpretation of the raw data (as above) which is rather a cloud of points is rather difficult or impossible without using any of the available signal processing algorithms. Therefore FT (Fourier Transform) has been used to convert the signal from its original

domain (time) to a representation in the frequency domain. Such a transformation was performed in the MATLAB R2014b environment with the use of the appropriate scripts. Based on a literature review and the objectives of this study there are two particular frequency windows (ranges) of most interest and these are as follows:

- A Low Frequency region (at 5-40 Hz) where mild surge and hard surge related pressure oscillations can be captured;
- A High Frequency region associated with the dynamics of the rotating turbomachinery, namely Blade Passing Frequency and its harmonics.

In order to eliminate the effects of amplitude leakage (as discussed above) the script was constructed as per the following diagram (Figure 6-13).

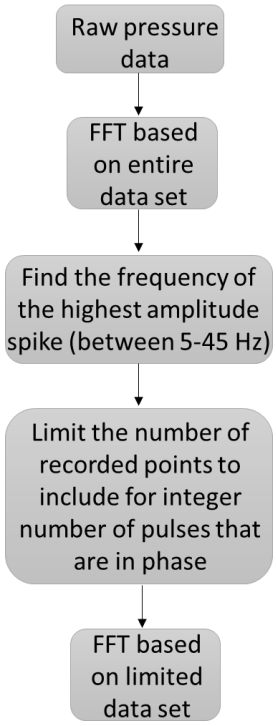

Figure 6-13. Logic of the MATLAB processing script

First, the comparison of the compressor inlet pressure (P1, P2, P3) has been performed by plotting the gathered data in the low frequency spectrum. The operating points within the selected range (as described in Section 6.1) are numbered starting at the highest mass flow rate whereas the last plotted point is the hard surge point. An example of the operating point numbering logic is shown in Figure 6-14.

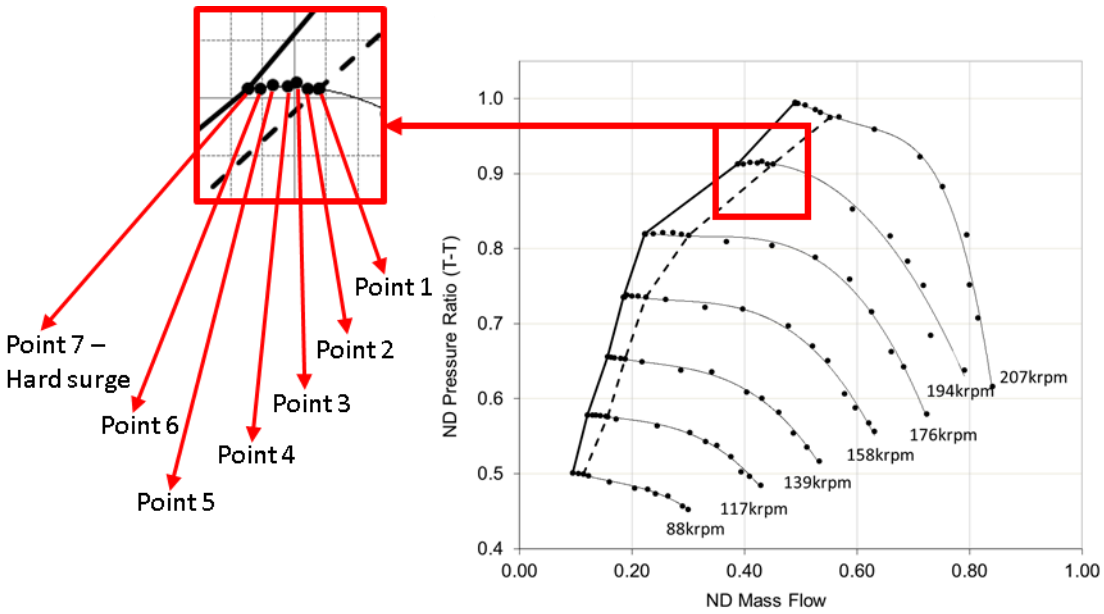

Figure 6-14. Surge study operating points at 194 krpm

The inlet pressure based FFT plots for three chosen speed lines of 207, 176 and 117 krpm are given in Figure 6-15 - Figure 6-17 (the remaining plots shown in Appendix C). It is worth mentioning that the Helmholtz (natural) frequency calculated for the current pipework layout of the gas stand following the method used by Dehner et al [42] is in the region of 20-26.5 Hz depending on the operating point (speed and PR and therefore outlet temperature and speed of sound at this temperature). The inlet pressure based FFT plots at the highest compressor speed of 207 krpm (Figure 6-15) show that for the first four tested points the flow is very stable and therefore the FFT magnitude is close to 0. At operating points 5 and 6 two peaks start to develop at frequencies of about 25 Hz and 50 Hz. At location P1 the dominant FFT peak occurs at the former frequency, however for locations P2 and P3 they occur at a frequency of about 50 Hz. The frequency of hard surge (point 7) and its harmonics is much lower than Helmholtz frequency as it is set by the plenum blowdown and refiling time [40]. Although the spikes of FFT magnitude related to the inlet pressure oscillations (due to hard surge) are captured at the same frequencies, it is noted that the values of FFT magnitude vary depending on the location of sensor.

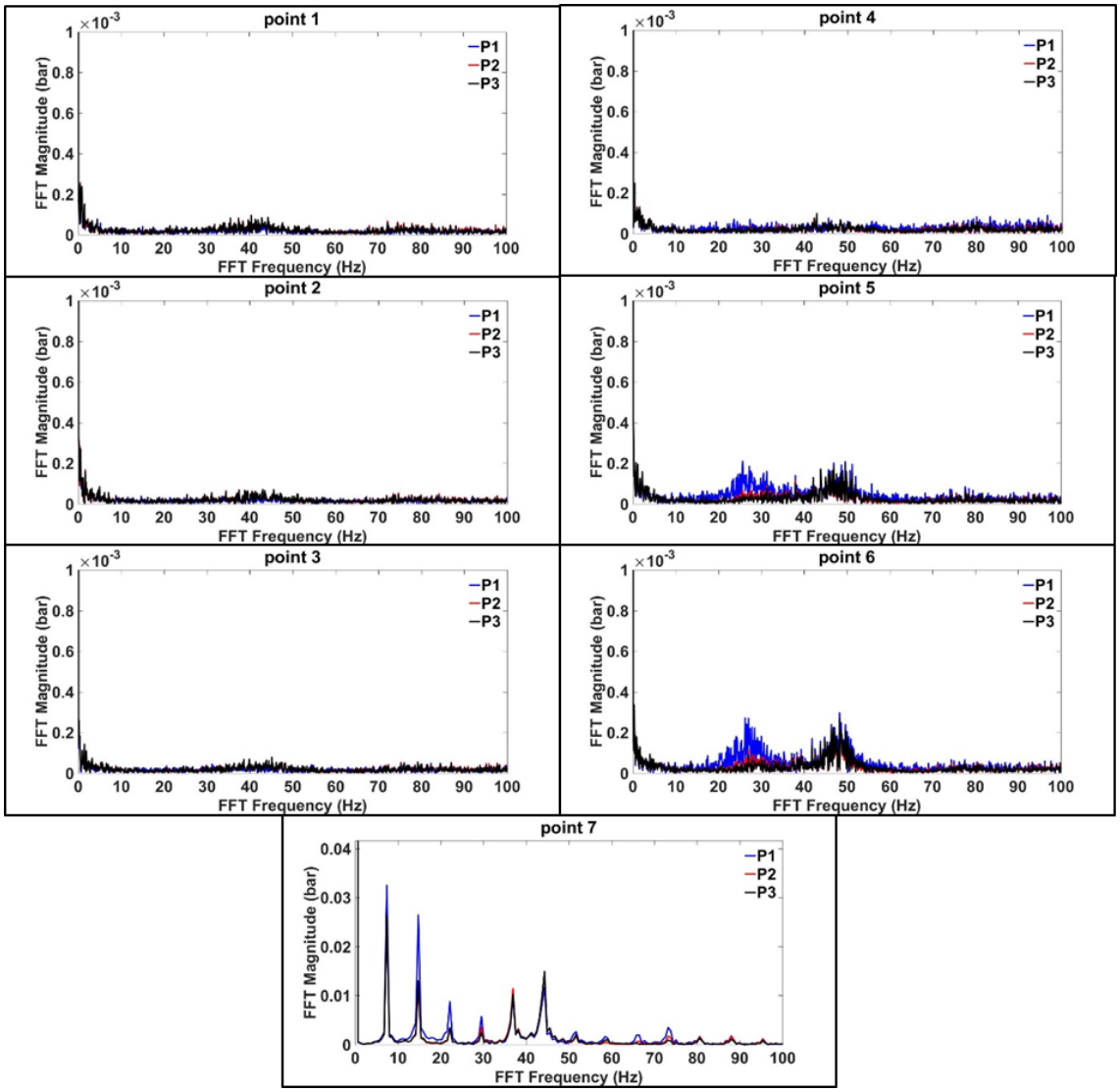

Figure 6-15. Inlet pressure based FFT plots of operating points at 207 krpm

For the next compressor speed of 176 krpm (Figure 6-16) the mild surge related FFT magnitude spike occurs at point 4 at a frequency of 25 Hz and then it diminishes at lower mass flow rates (operating point 5). This is the only tested case when the compressor comes out of mild surge and operates stably despite operating at a lower mass flow rate when compared to the preceding point. The situation happens in the region where there is no further increment of pressure ratio when moving to lower mass flow rates (i.e. the speed line is flat).

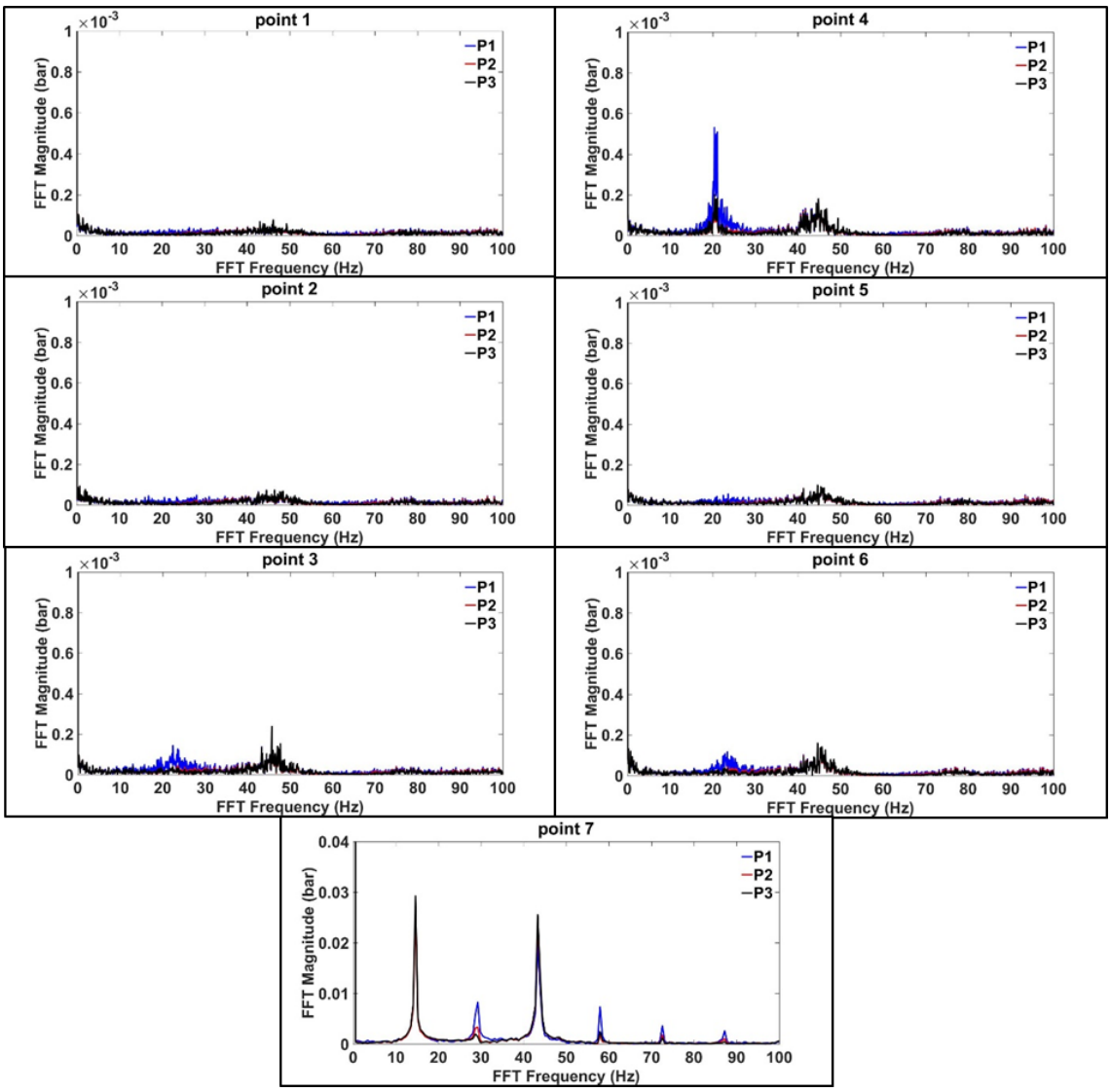

Figure 6-16. Inlet pressure based FFT plots of operating points at 176 krpm

Looking at the lower compressor speed line of 117 krpm it can be seen that there is very little warning in terms of the FFT magnitude rise during the operation in the mild surge region. The onset of hard surge is more sudden. At the hard surge condition at 117 krpm the FFT magnitude is higher at locations P2 and P3 and this is not in agreement with the trend observed at the highest speed line.

.

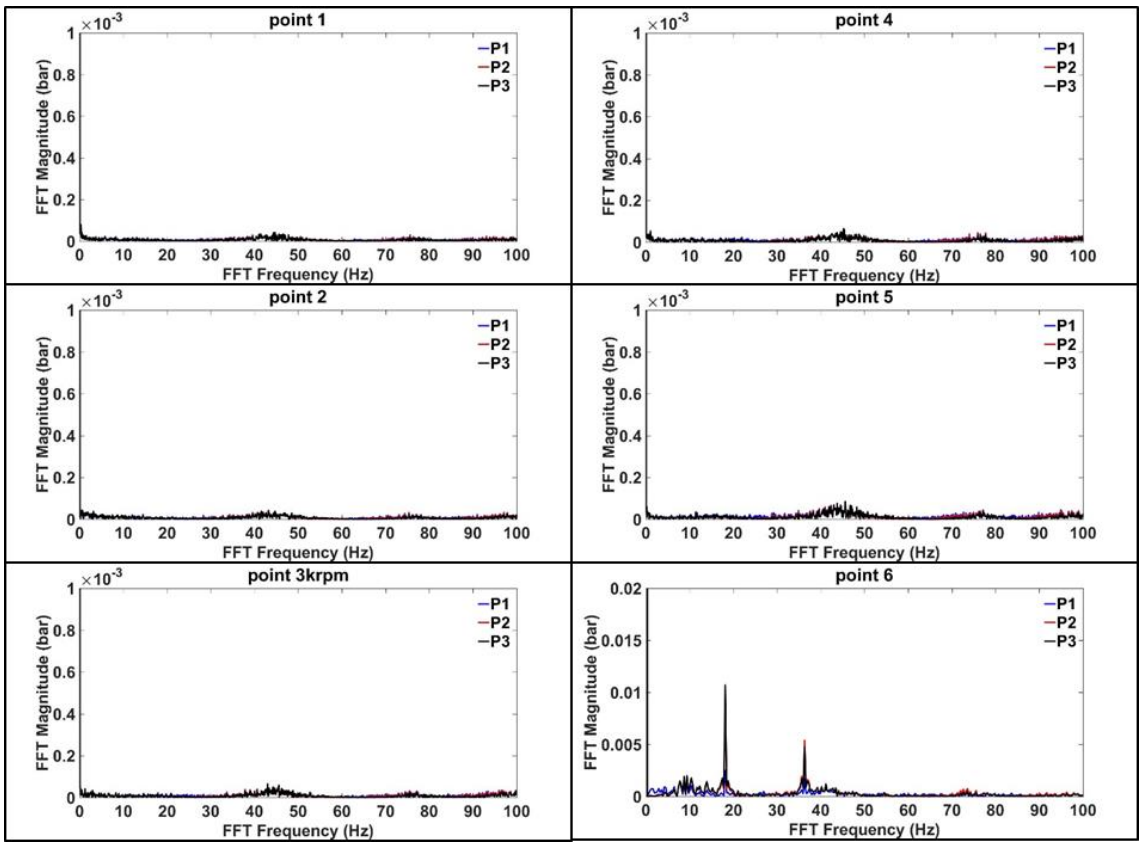

Figure 6-17. Inlet pressure based FFT plots of operating points at 117 krpm

Overall it is concluded that pre-compressor installed pressure sensors are capable of capturing the mild surge and hard surge related flow perturbations. However different FFT magnitudes of pressure have been noted at various locations, even those where pressure sensors of the same model and range were used (P1 and P2).

Next, the post compressor pressure based FFT plots for chosen tested compressor speed lines are shown in Figure 6-18 - Figure 6-20 (plots for the remaining speed lines in Appendix C).

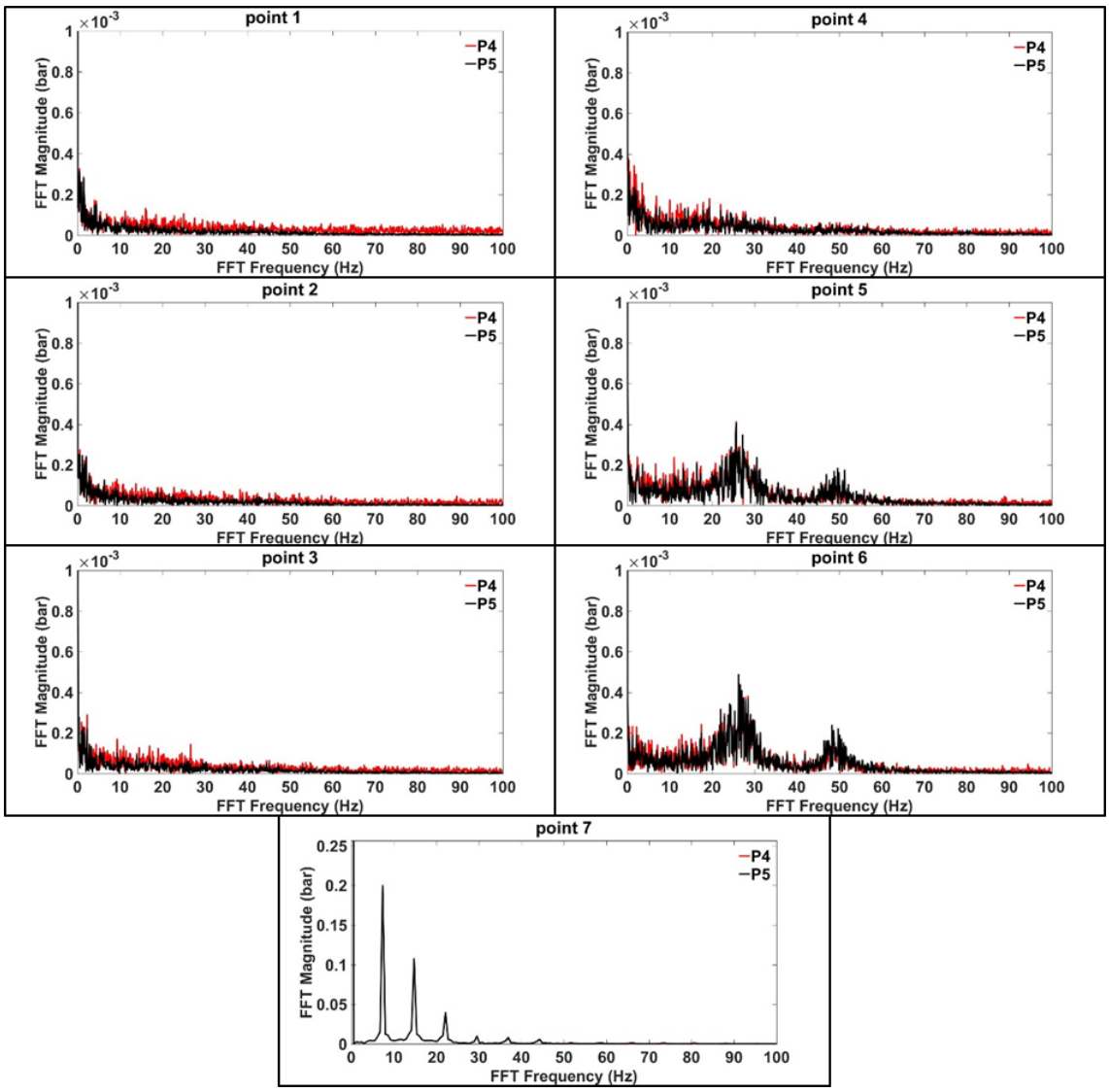

Figure 6-18. Post compressor pressure based FFT plots of operating points at 207 krpm

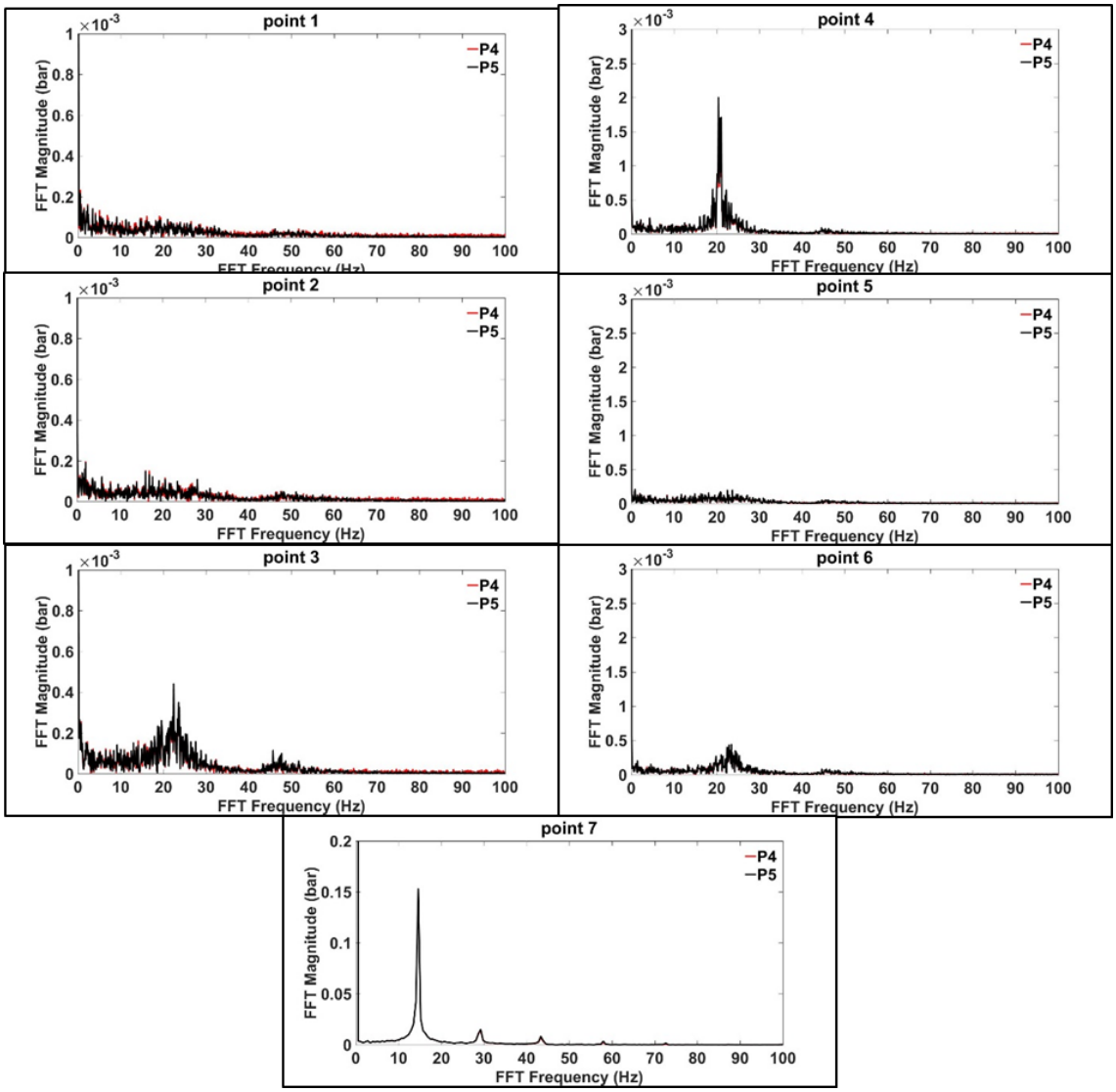

Figure 6-19. Post compressor pressure based FFT plots of operating points at 176 krpm

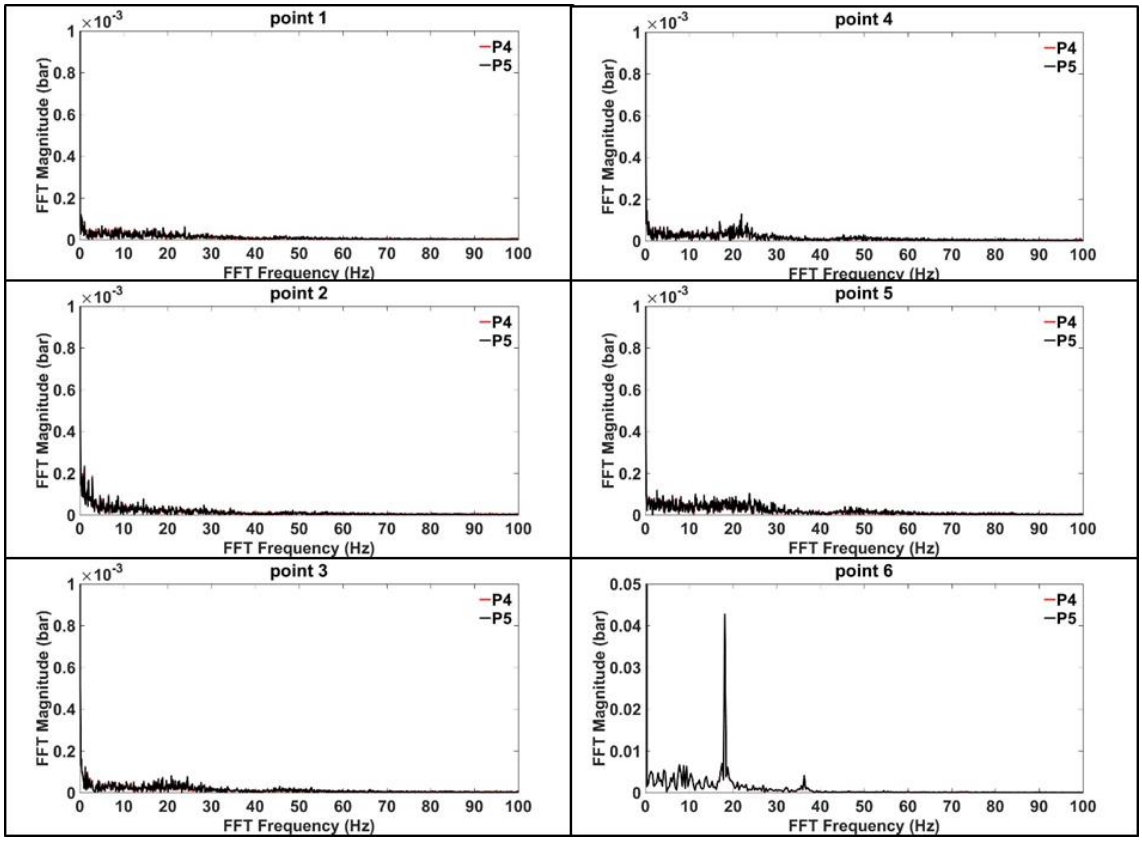

Figure 6-20. Post compressor pressure based FFT plots of operating points at 117 krpm

It is clear that FFT picked up by the downstream sensor locations are of a much higher magnitude than those at the upstream location. During hard surge the complete break-down in compression leads to flow reversal which encompasses all compressor components. The highest pressure oscillations are seen on the outlet side of the compressor and they weaken in magnitude as they progress back through the compressor (damping effect). From a surge indication point of view the important fact is that the magnitude of the FFT spikes do not vary between P4 and P5 at all tested conditions across all compressor speed lines. Due to this consistency one can conclude that post compressor pressure measurement can be more useful in setting compressor surge limits. That is, they offer more consistency across differing installations and thus, sensor positioning. Another positive conclusion drawn from this part of the analysis is that if an FFT magnitude limit is to be set for hard surge onset no extra high frequency instrumentation is required. In order to capture surge a sensor with a pressure frequency range between 5-30 Hz along with an acquisition system capable of sampling at a minimum of 60 Hz (i.e. twice as much as the FFT frequency spectrum) is required.

6.4.2 High frequency pressure data analysis

To investigate the possibility of using the blade passing frequency and its harmonics

as a potential indicator of near surge operation (as suggested by Boyce [20]) both microphone and post-compressor pressure sensors are used. To calculate the blade passing frequency the following formula is used:

$$BPF = N_{act} * f \tag{66}$$

where:

N_{act} – actual speed of the turbocharger, [rps]

f – number of full impeller blades, [-]

First, it is established whether all three sensors (P4, P5, and microphone) are capable of and effective in measuring BPF. For this purpose one random operating point (within the investigated region) is chosen from the selected operating range at the compressor speed of 117 krpm and compared by means of an FFT. BPF and its second and third harmonics can be observed in Figure 6-21. It can be noted that the sensor distance from the compressor is important when investigating the high frequency region. The FFT spikes of pressure data collected at P5 are of a much lower magnitude when compared with P4. The third harmonic of BPF cannot be determined for the P5 pressure sensor. Although BPF and its harmonics can be captured by both the microphone and P4 pressure transducer there are large discrepancies between the relative FFT magnitudes which is studied further.

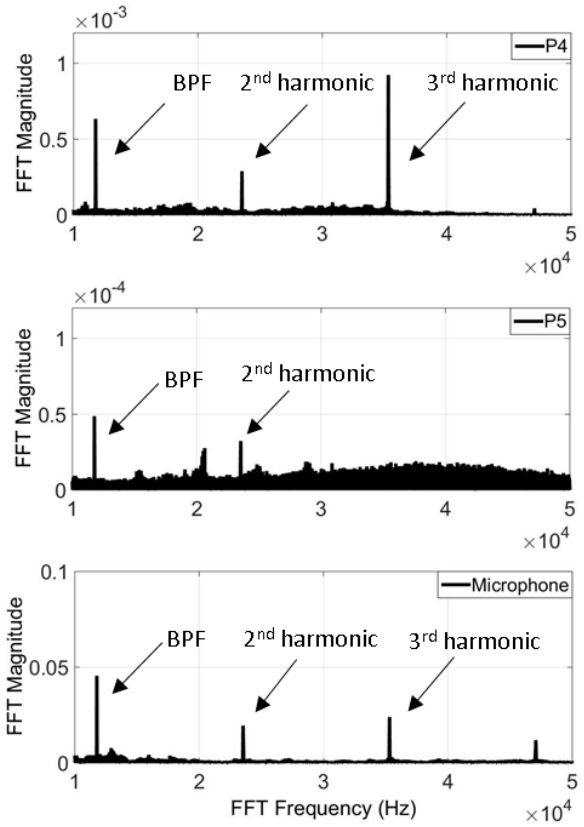

Figure 6-21. BPF and its second and third harmonics for the operating point at 117 krpm

In order to investigate the use of BPF measurement as an indicator of surge, all operating points at the two selected speed lines (158 krpm, 139 krpm) are looked at. The data is obtained for the microphone and the pressure sensor located at P4. Point 6 plotted in the figures below denotes the hard surge condition whereas point 1 is the operating point of the highest mass flow within the marked region on the compressor map. Referring to Boyce's statement [20] that: "in a limited number of tests it has been noted that when the second harmonic of the blade passing frequency reaches the same order of magnitude as the blade passing frequency, the unit is very close to surge" and based on Figure 6-22 & Figure 6-23 it can be concluded that the relative magnitude of BPF and its harmonics is sensor dependent. The FFT plot of the pressure levels recorded by microphone (Figure 6-22) at 158 krpm shows that at point 1 the second harmonic of the signal is higher than BPF whereas at location P4 this situation occurs at point 3. At 139 krpm the second harmonic of BPF does not reach the same FFT magnitude as the BPFs prior to hard surge for the microphone (Figure 6-23). This is contrary to the pressure data where the second harmonic of BPF reaches a larger magnitude of FFT than the BPF itself (point 3). For this reason it is shown that for this particular compressor no relation between BPF and surge development exists.

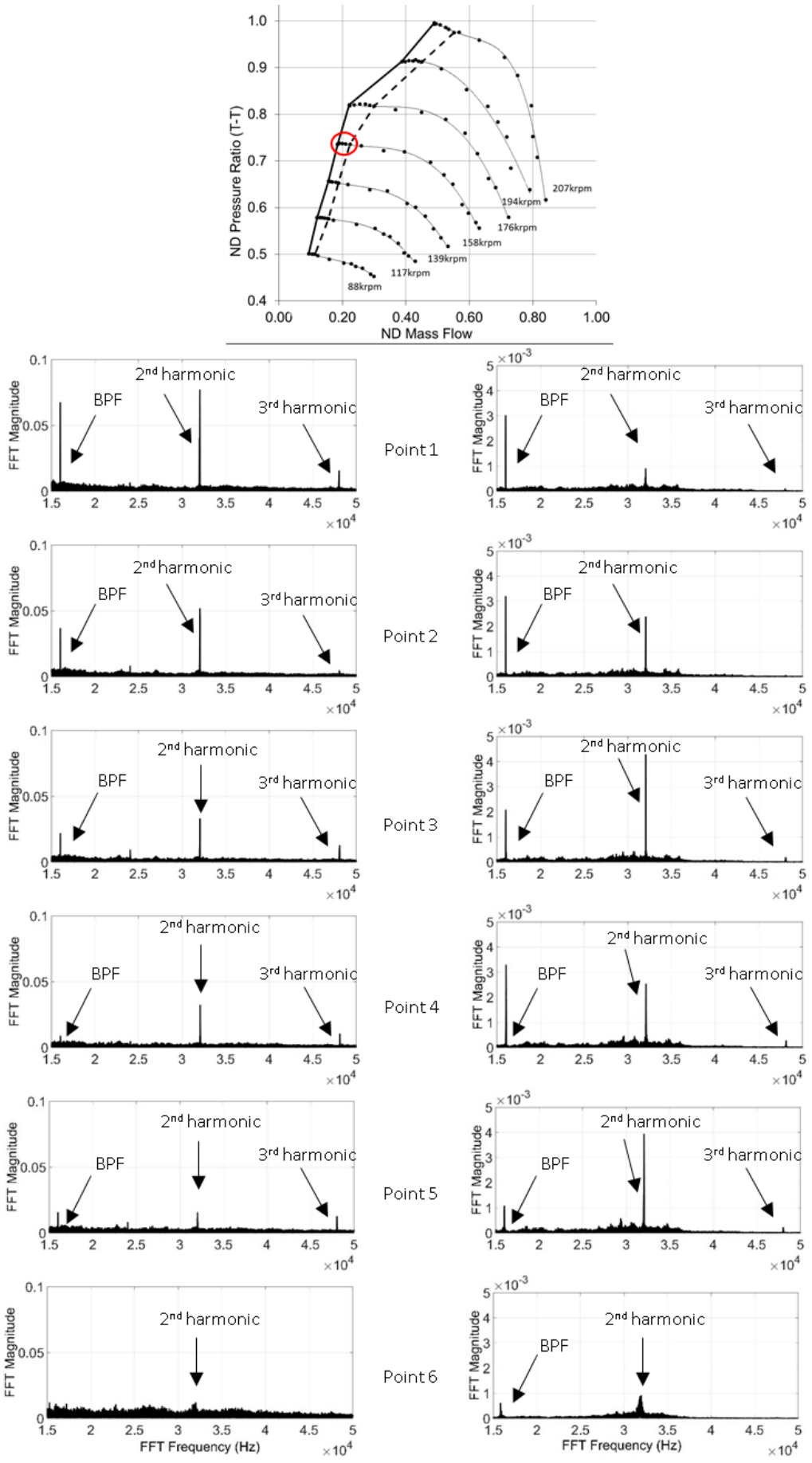

Figure 6-22. Microphone (left) and P4 (right) measured BPF and its second and third harmonics for the operating points at 158 krpm

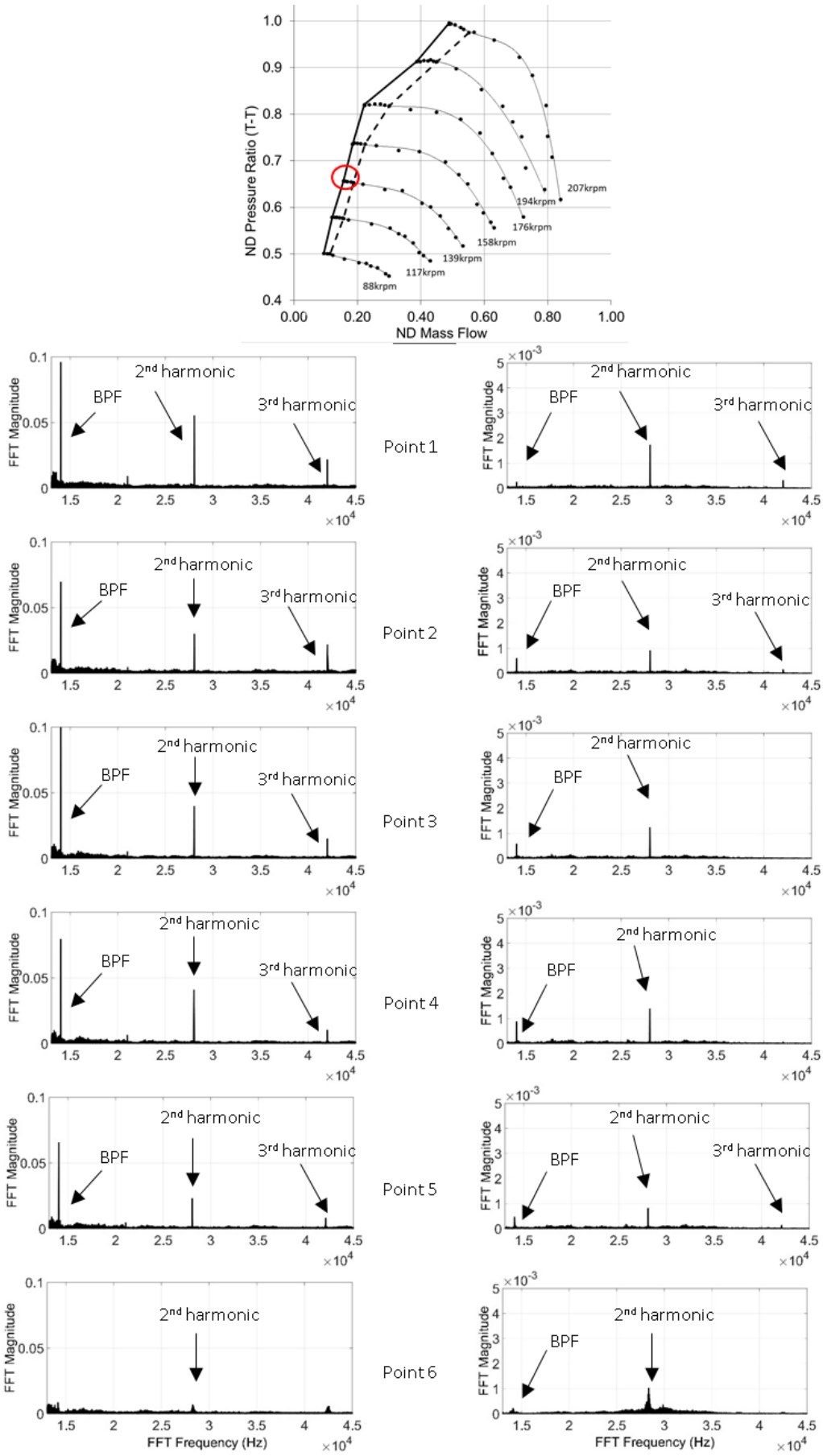

Figure 6-23. Microphone (left) and P4 (right) measured BPF and its second and third harmonics for the operating points at 139 krpm

6.4.3 Temperature data analysis

Inducer temperature rise at mild and hard surge conditions was also studied within this part of the work. This was captured by a 1.5mm k-type thermocouple located 10mm from the impeller eye and at half of the inducer radius. The selection of a widely available and inexpensive thermocouple was made purely due to its durability – a thin or exposed junction thermocouple breaking apart upstream of the compressor impeller is a potential blade damage risk. The question to be answered is whether a temperature sensor can be a useful tool from a surge prediction point of view when used in an algorithm for an active hard surge suppression technique. The temperature rise during a hard surge event recorded at a sampling frequency of 40Hz is shown in Figure 6-24.

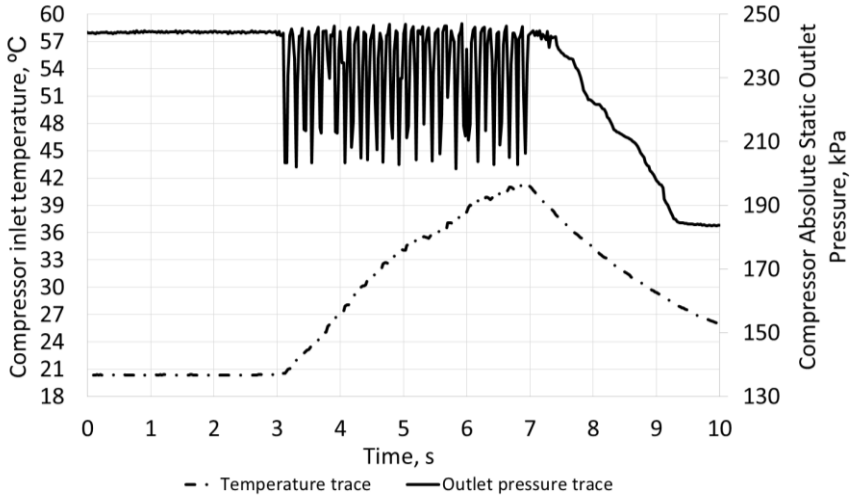

Figure 6-24. Hard surge event at a compressor speed of 207krpm

During the first three seconds of the event the compressor was in stable operation (no visible outlet pressure oscillations) and the temperature was constant. At the time when hard surge was triggered (between 3s and 7s of the event) the temperature gradually rose (by 21°C within 4s) until the compressor was driven out of surge (by opening the back pressure valve). It can be concluded that no indication of the coming hard surge can be picked up based on the temperature behaviour. Even though the temperature was quickly rising at hard surge it is not a valuable information to feed an active hard surge suppression system. Nevertheless, the question remains as to whether there is useful information regarding the temperature rise when only mild surge region is taken into account. Figure 6-25 below shows the temperature measured at every compressor speed line at the studied compressor operating points with the exception of the last hard surge points.

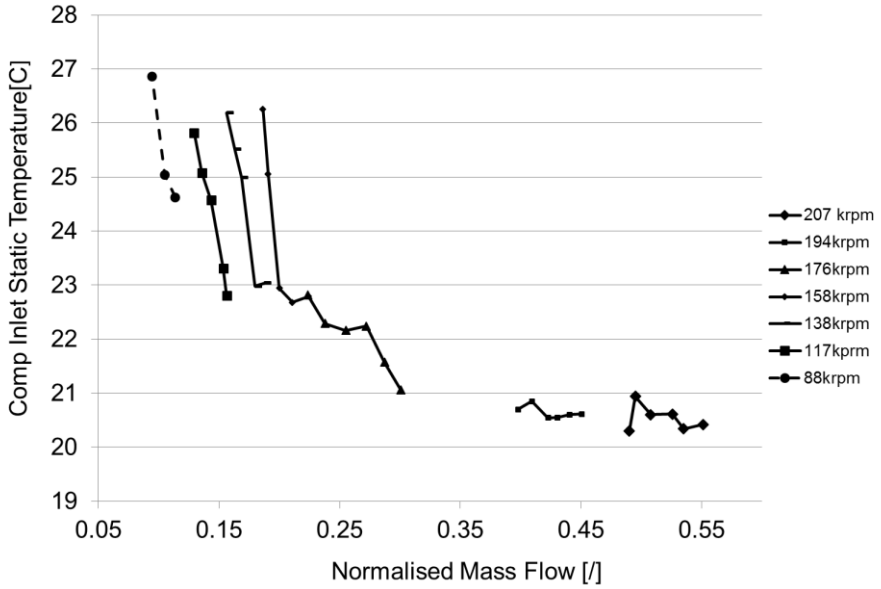

Figure 6-25. Mild surge temperature rise at operating points at various compressor speeds

It can be noted that at lower compressor speed lines (88 krpm – 158 krpm) the temperature measured at the last operating point (lowest mass flow) preceding hard surge is about 26-27°C with the clear temperature rise when moving towards the lower mass flow region. This is not the case for the highest two speed lines where the temperature within the entire studied operating range is fairly constant. In general the temperature measured in that particular location is affected by the mass flow recirculation however the temperature of the recirculation flow may be linked to other compressor size and speed dependent variables like Reynolds number. Perhaps even heat transfer from the hot turbine casing (at low turbocharger speeds) is the reason why the compressor inlet temperature (shortly before hard surge) is different at the various compressor speed lines. Overall it can be concluded that measurement of temperature near the compressor impeller has no use from the surge avoidance point of view, which is in agreement with the conclusions drawn by Andersen et al [75].

6.4.4 Surge metric comparison

In the earlier section of this thesis it was concluded that using a Fast Fourier Transform algorithm in the low frequency spectrum (5-40Hz) for the post-compressor pressure and sound analysis can be a successful method in the process of marking the onset of hard surge on steady-state test facilities. A simpler alternative also based on the post-compressor pressure and often used within the industry sets a limit on the amplitude of pressure oscillations. This can be achieved in several ways, for example:

- By a maximum fixed value of the peak-to-peak amplitude;
- By a maximum value of the peak-to-peak amplitude multiplied by other weighting factors (i.e. compressor size or speed multipliers);

- Using other maximum limits, expressed in terms of standard deviation (SD), coefficient of variation (CoV), etc.

The first two of the above mentioned industry surge metrics were plotted onto the investigated turbocharger compressor map generated at the University's flow rig (Figure 6-26).

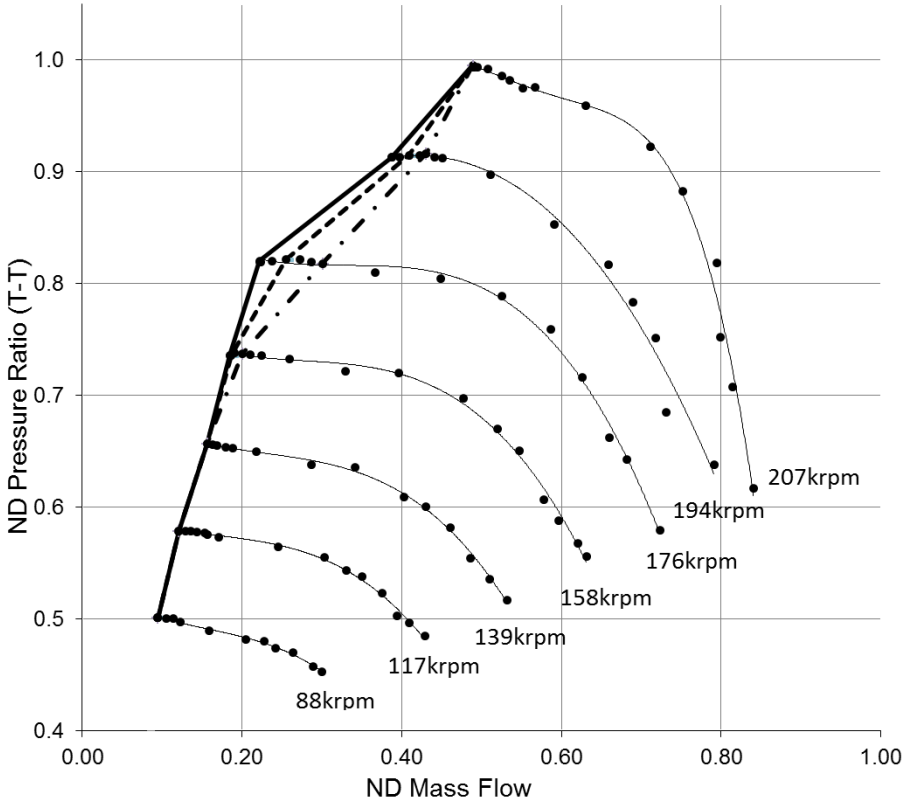

Figure 6-26. Compressor performance map with three surge lines based on various industry surge metrics

It can be noted that at the low compressor speed lines (88-139 krpm) as well as at the highest speed line (207 krpm) all three surge lines are marked at the same operating point. However, at three other speeds the surge lines are drawn at different compressor operating points. The surge limit marked by a dashed-dotted line and based on the fixed peak-to-peak amplitude of the post-compressor pressure reveals the onset of surge at the highest mass flows when compared with other surge lines. The dashed line marking the surge onset based on peak-to-peak amplitude and multiplied by other factors (taking into account compressor size and speed) lies closer to the solid black line denoting violent hard surge. To closer analyse the compressor speed line of 176 krpm (the greatest dislocation between surge lines on that speed line), the FFT algorithm was again applied to post-compressor pressure data (P4 and P5). The results are plotted in Figure 6-19 for the low frequency range. Again point 1 denotes the first selected operating point at the speed of 176 krpm whereas point 7 (hard surge) is the last point in the operating range. It can be noted that at this particular compressor speed the FFT plot shows no indication of surge at points 1 and 2. At point 3 there seems to be a spike growing at a frequency

of about 22 Hz which develops and is very clear at point 4. Further closing of the back-pressure valve and therefore reducing the mass flow through the compressor moves the operating point to point 5 where the FFT spike disappears. This means that the compressor comes out of surge despite the further mass flow reduction. This phenomenon is found to be repeatable at this particular speed line for this particular compressor. For other speed lines the low frequency FFT spike either takes place only at hard surge conditions (88 krpm, 117 krpm) or gradually develops when moving towards lower mass flow operating points. At the speed of 176 krpm the FFT spike is developing again at point 6 and reaches the highest magnitude at hard surge point (point 7). The FFT plot indicate the nature of the post-compressor pressure amplitude of oscillations. Looking back at Figure 6-26 it is noted that at the compressor speed of 176 krpm the dashed surge line is marked at point 4 where a clear FFT low frequency spike was observed. This means that at this particular point the chosen surge onset criterion was reached. However the second surge line drawn in Figure 6-26 (dashed-dotted) is marked at point 1 despite the fact that no indication of a low frequency spike is indicated on the FFT plot. This suggests that the amplitude of the post-compressor pressure that triggered the surge limit must have been of a higher frequency that the typical surge frequency of 5-25 Hz. At the sampling frequency of 100 kHz (chosen for this study) the available FFT frequency spectrum is in a range between 0-50.000 Hz (i.e. half of the sampling rate). Figure 6-27 shows the FFT magnitude of the P5 post-compressor pressure signal over the selected frequency spectrum (0-10.000 Hz).

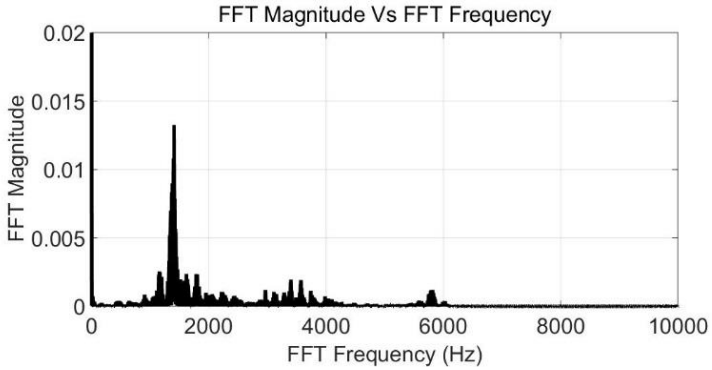

Figure 6-27. FFT magnitude of P5 post compressor pressure recorded at point 1 at 176 krpm over the selected frequency spectrum

The visible peak observed around 1500Hz is the reason why the surge onset metric was reached and therefore it can be concluded that if targeting a low frequency hard surge measurement an appropriate sampling rate or data filtering should be applied.

6.5 Experimental surge measurement results – Puma compressor

Following the surge study carried out on a small size compressor (Fox) it was decided to look at surge development for the larger size Puma compressor by means of

low frequency FFT plots based on the post-compressor pressure at location P5. The motivation was to check if the observations that were made for the Fox compressor also apply to Puma compressor. The performance maps generated for both compared compressors at steady-state gas stand conditions are shown in Figure 6-28. The Fox compressor map is drawn in red whereas the Puma compressor in black. It is clear that the maps are very different in terms of the map width, surge margin, choke line location etc. The Fox turbocharger compressor is a smaller size unit therefore the surge line is located in the region of lower mass flow rates (for similar speed lines) and the map is narrower (the choke line is similarly at lower mass flow rates). The surge development comparison is based on the post-compressor pressure data and for the operating points marked on both maps between the solid surge lines and superimposed dashed lines.

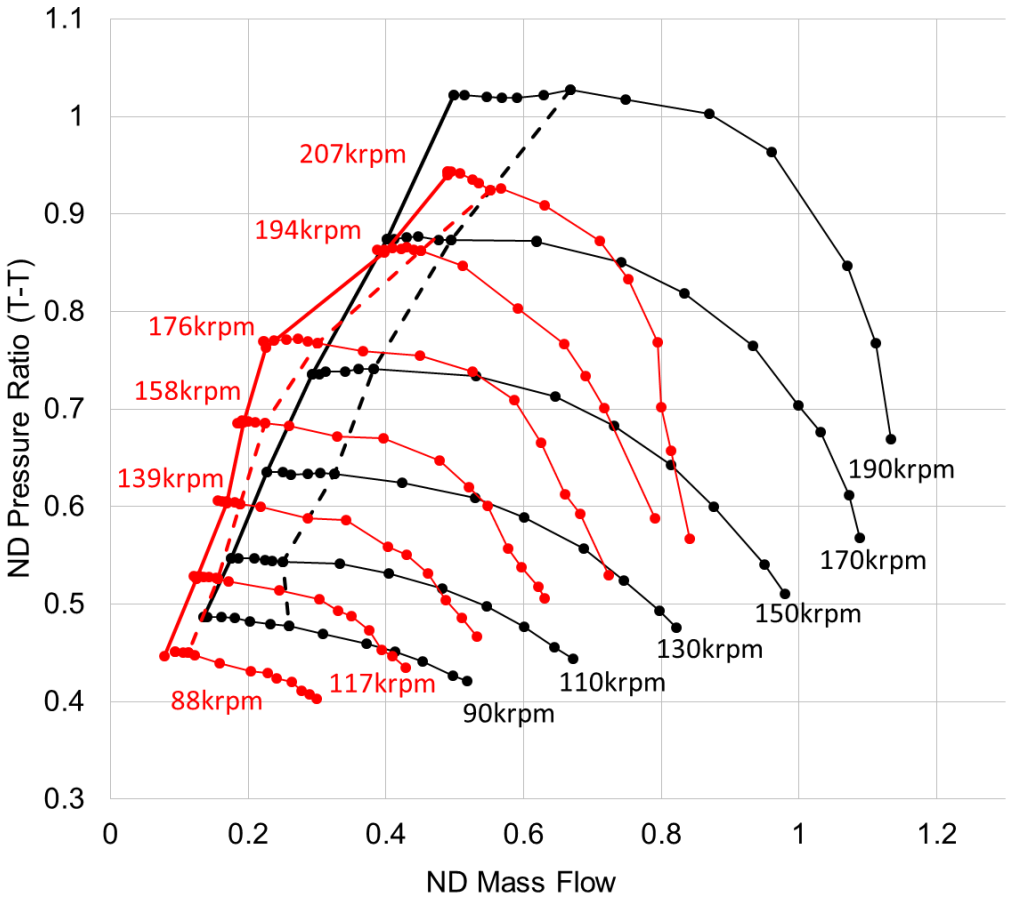

Figure 6-28. Performance maps of tested compressors (Fox – red lines, Puma – black lines)

The post-compressor pressure based FFT plots for the Puma compressor are shown in Figure 6-29 and Figure 6-30 (plots for the remaining speed lines are shown in Appendix D). At the highest speed line of 190 krpm (Figure 6-29) a visible FFT spike appears at operating points 2 and 3 and this later diminishes. Also the magnitude of the spike is much lower (several times) than the magnitude of the spike at hard surge condition. At the low speed of 110 krpm there is hardly any indication of surge at operating points

preceding the hard surge point (no visible FFT spikes in the low frequency region). Overall it can be concluded that the development of pressure oscillations (captured by FFT) at operating points preceding hard surge is rather less significantly linked to mild surge and that this compressor comes into surge rather rapidly.

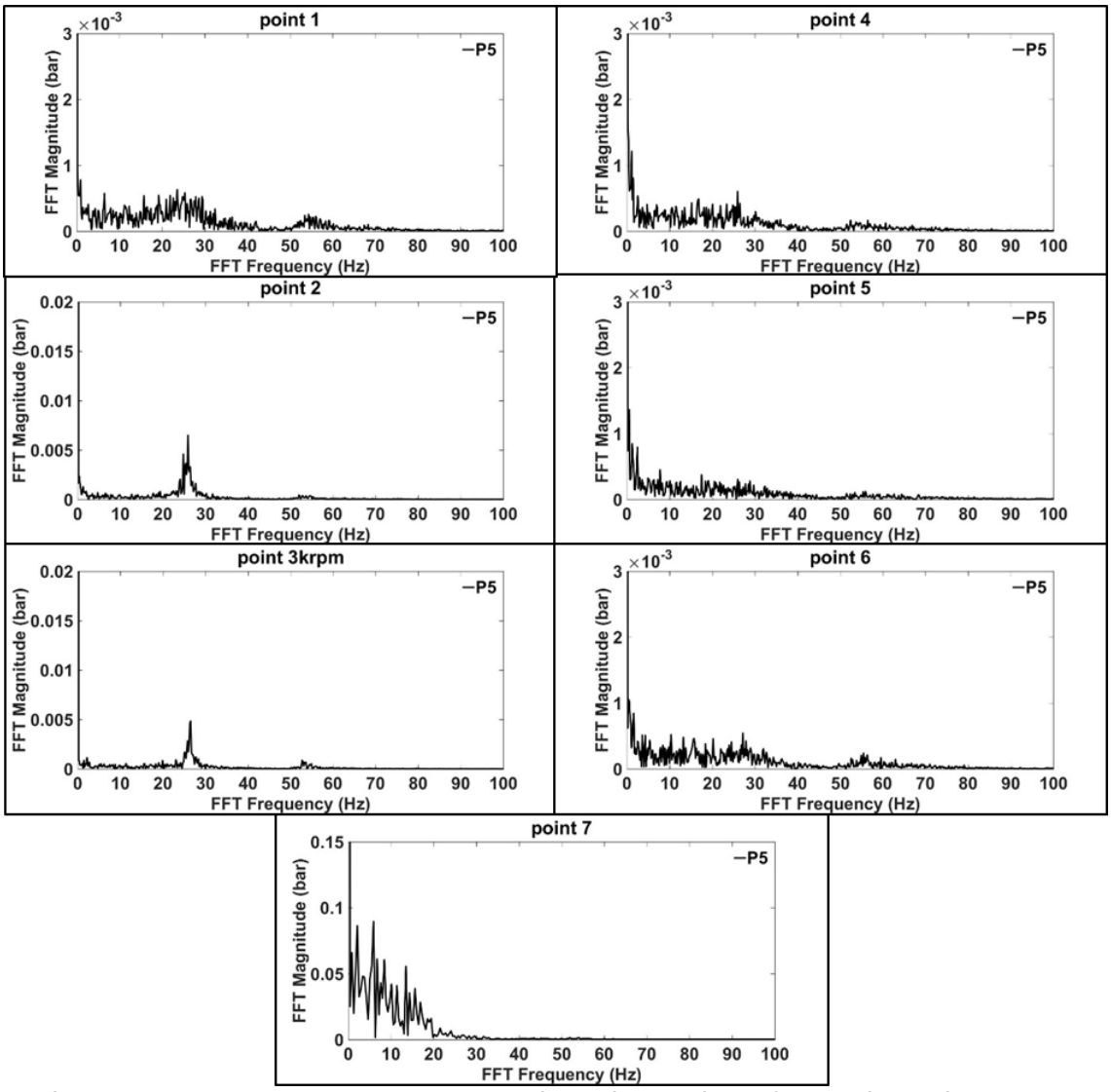

Figure 6-29. Post-compressor pressure based FFT plots of operating points at 190 krpm

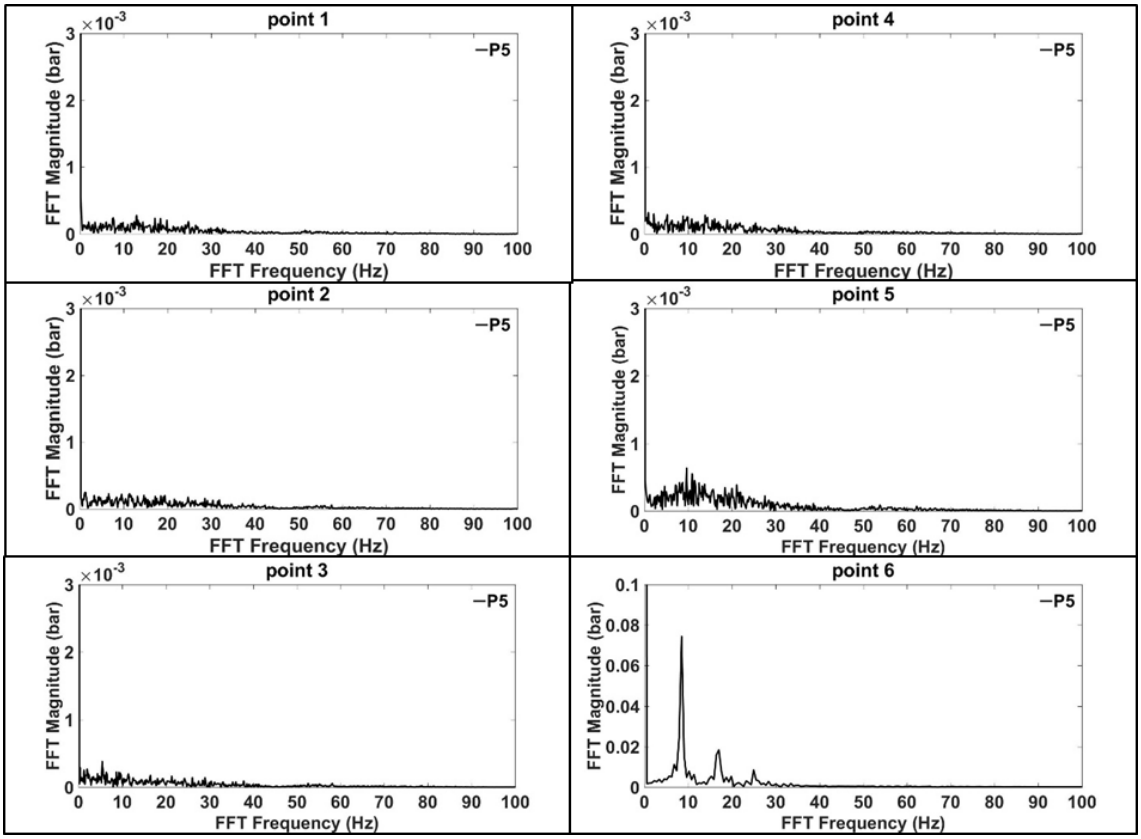

Figure 6-30. Post-compressor pressure based FFT plots of operating points at 110 krpm

6.6 Experimental surge measurement results – steady-state vs pulsating flow - Puma turbocharger

The last piece of work during the experimental surge measurement study was the comparison of the steady-state gas stand and pulsating on-engine flow surge development for the Puma compressor. While more detail can be found in a published paper [3] the most important findings are given below. Due to the on-engine turbocharger operation limitations only four speed lines can be compared and these are 150 krpm, 130 krpm, 110 krpm and 90 krpm, as shown in Figure 52. The first investigation is regarding the location of the hard surge line. It has been suggested by industry and proven by Galindo [79] that a compressor operating on-engine may have a greater surge margin when compared to its operation at steady-state conditions. This behavior has been confirmed also by comparing the surge margins observed for the Puma turbocharger operating on the steady-state gas stand (schematic of the rig as shown in Figure 6-1) and in the pulsating flow engine gas stand conditions (schematic of the rig as shown in Figure 6-10).

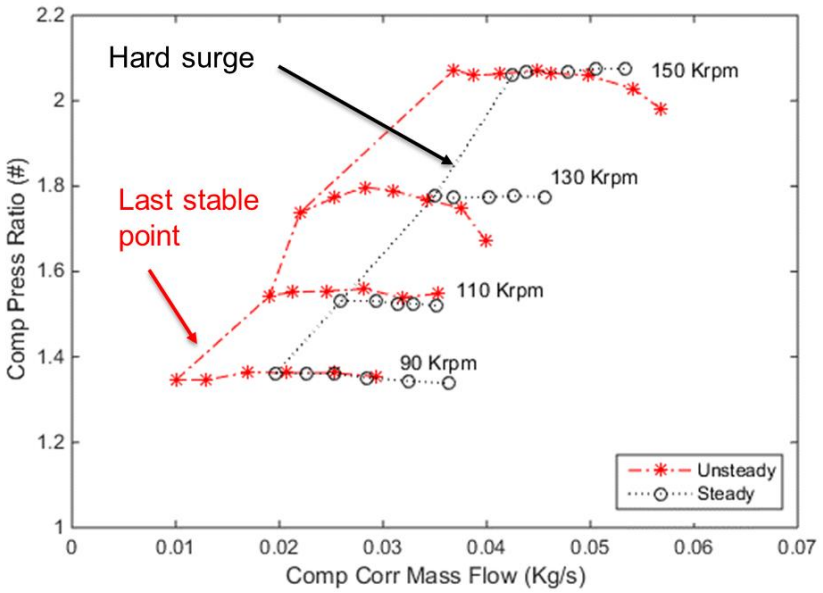

Figure 6-31. Surge margin comparison between steady-state and pulsating flow conditions – Puma compressor

Another interesting finding is that when operating a compressor on-engine and towards the hard surge condition the increase of the pressure fluctuation/oscillation seems to be more gradual than that in steady-state conditions (Figure 6-32). In other words, more of a surge-like behaviour build up is observed which is positive from the surge detection and mitigation point of view.

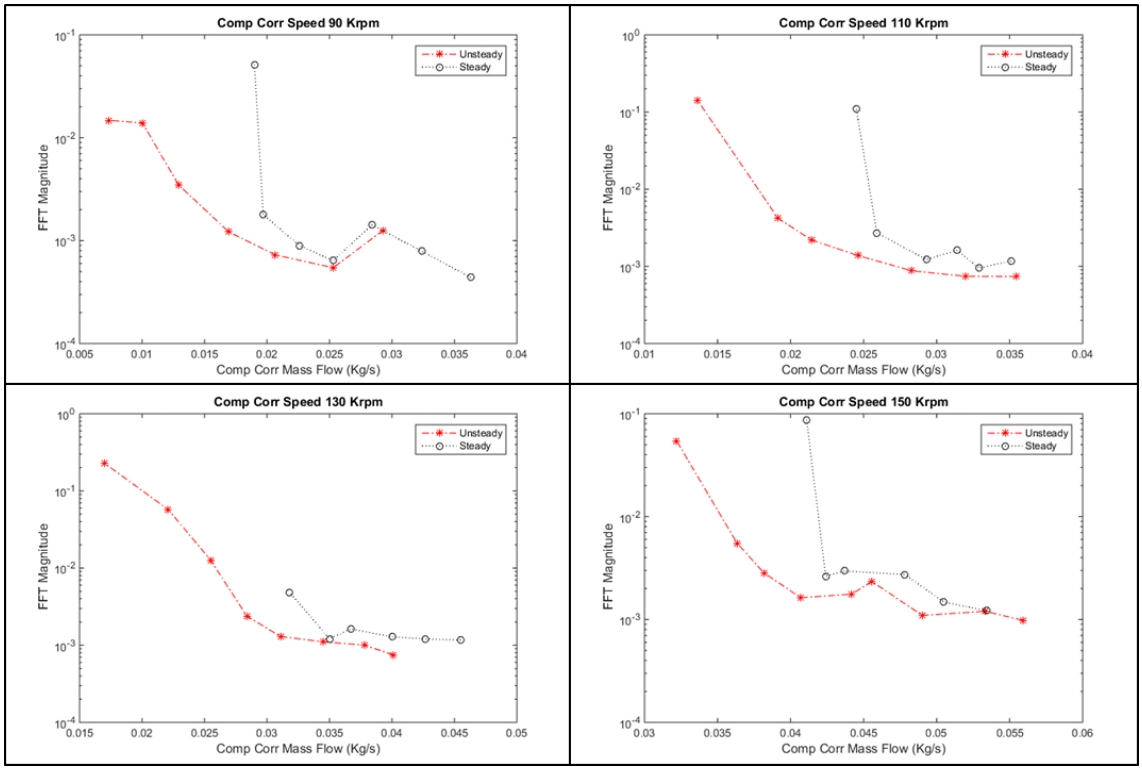

Figure 6-32. Surge development comparison between steady-state and pulsating flow conditions – Puma compressor

Finally, the FFT spike associated with the motion of the intake valves has been noted when operating the compressor on-engine in pulsating flow conditions. This is shown in Figure 6-33. Therefore it is important to monitor this frequency if a FFT of post-compressor pressure is to be used as surge indicator.

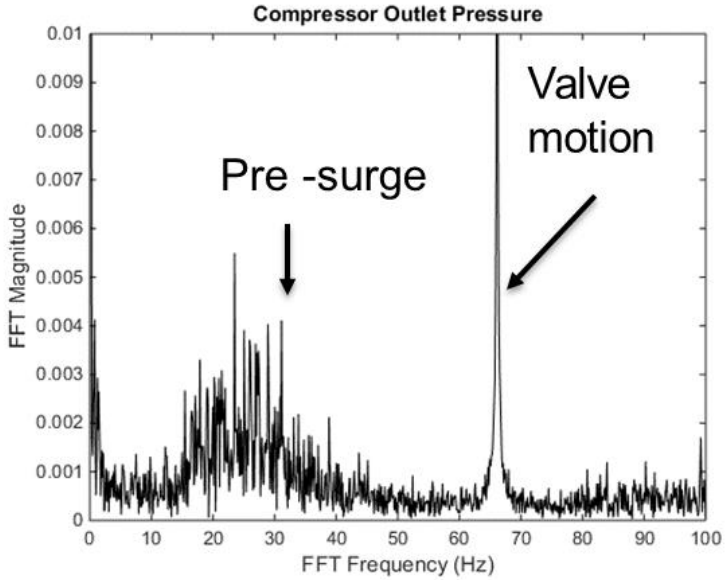

Figure 6-33. FFT plot of post-compressor pressure at operating point preceding hard surge at 150 krpm, showing the frequency spike associated with the motion of the intake valves

7. Turbocharger compressor performance with substitute gas

The effects of the substitute gas on the turbocharger compressor performance is studied experimentally and numerically by means of 3D CFD simulations. Both experimental tests and simulations take into account homogeneous and non-homogeneous mixtures of various concentrations of CO2 and air as well as extreme cases of pure air and pure CO2. Selection of the CO2 is motivated by the fact that it is an important component of the exhaust gas contributing to the greenhouse effect and it is also characterised by significantly different properties than air - individual gas constant and ratio of specific heats. The case of the homogeneous gas mapping considers a situation when the mixture of air and exhaust gas arriving at the compressor inlet is very well mixed and uniform in terms of local concentration of components. Looking from the point of view of LP EGR systems this can be achieved if there is sufficient pipework length between the EGR valve and compressors. Otherwise – the non-homogeneous mixture of gases enters the compressor. In this investigation compressor performance change due to variable fluid properties is studied (homogeneous gas). Also, the non-homogeneous gas and EGR valve study allow to look further at more complex system configurations.

7.1 Homogeneous substitute gas – experimental approach

All the experimental tests included in this investigation were carried out on a steady state turbocharger gas stand. The selected turbocharger was a 2.2l diesel VGT also used within other chapters of this thesis (hence more technical details regarding the hardware can be found in Chapter 4 and 5). Throughout the tests the turbine inlet temperature was fixed at 500°C whereas the variable vanes were locked at fixed position. The schematic and the photo of the compressor closed-loop rig is shown in Figure 7-1 and in Figure 7-2 respectively.

The experimental tests included generating five compressor performance maps – each for a different working fluid. These were:

1. Pure air,
2. Mixture of 3% CO2 and 97% air by mass;
3. Mixture of 5% CO2 and 95% air by mass;
4. Mixture of 10% CO2 and 90% air by mass;
5. Pure CO2.

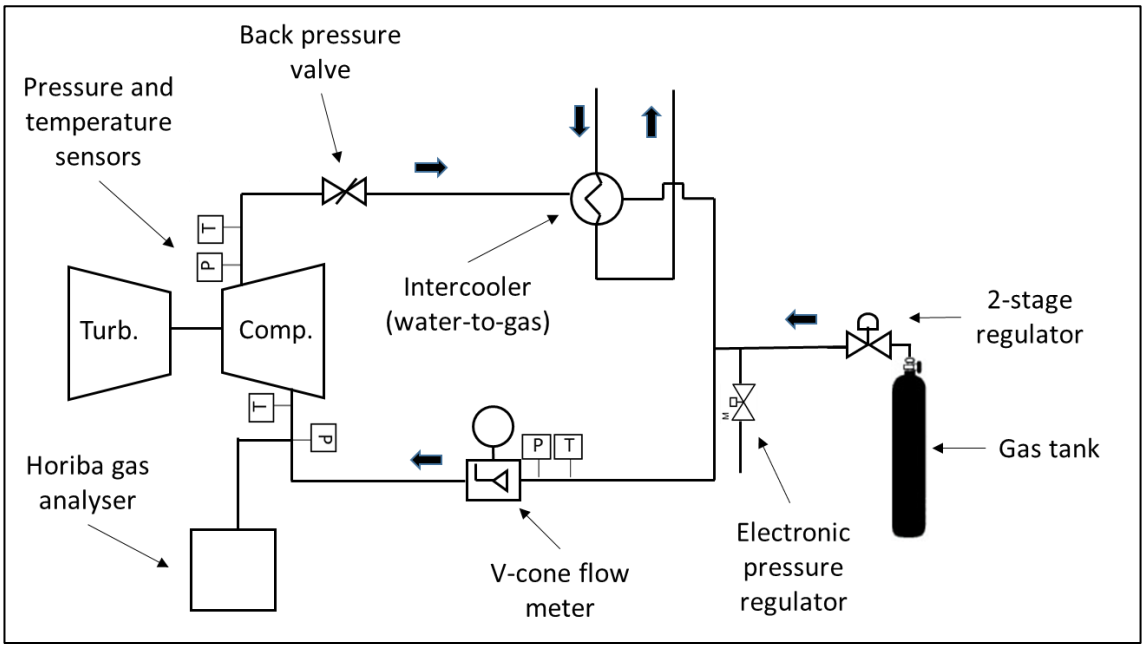

Figure 7-1. Schematic of the closed-loop compressor mode

Figure 7-2. Photo of the turbocharger gas stand in closed-loop compressor mode

All the maps were measured using the closed-loop compressor operation - the first map was produced for air that was drawn from the test cell, in contrary to other four cases where gas was delivered from a bottle (Figure 7-1). Delivering the already pre-mixed substitute gas (at required proportions) from pressurised bottles eliminated the requirements for any mixing tanks and other equipment that would be necessary for the on-site preparation of mixtures. As there was a minor leak discovered within the closed-loop, the gas pressure at any point in the loop was kept above the atmospheric pressure (to avoid suction of ambient air into the loop and changing the mixture concentrations). The

control of the pressure level at the compressor entry was achieved via a motorised electronic regulator. The concentration of the CO2 in the closed-loop was monitored by continuous sampling of a portion of gas by Horiba MEXA 7000 gas analyser. The mass of the gas passing through the compressor was measured by the V-cone mass flow meter.

7.2 Non-homogeneous substitute gas – experimental approach

The set of non-homogeneous tests was also carried out using the same turbocharger hardware and at a fixed turbine inlet temperature of at 500°C. However the flow rig layout has been significantly modified – some hardware and instrumentation has been added as shown in Figure 7-3. The control over the mass flow of the mixture of gases passing through the compressor was again achieved via the back-pressure valve, however after the compression process the gas was discharged outside the test cell via the extract system driven by the roof-mounted fan. The introduction of the non-homogeneous gas at the compressor entry was realised by injecting various mixtures of CO2 and air into one of the four passages of the inlet pipe (pipe bolted to the compressor housing on its upstream side) as shown in Figure 7-4.

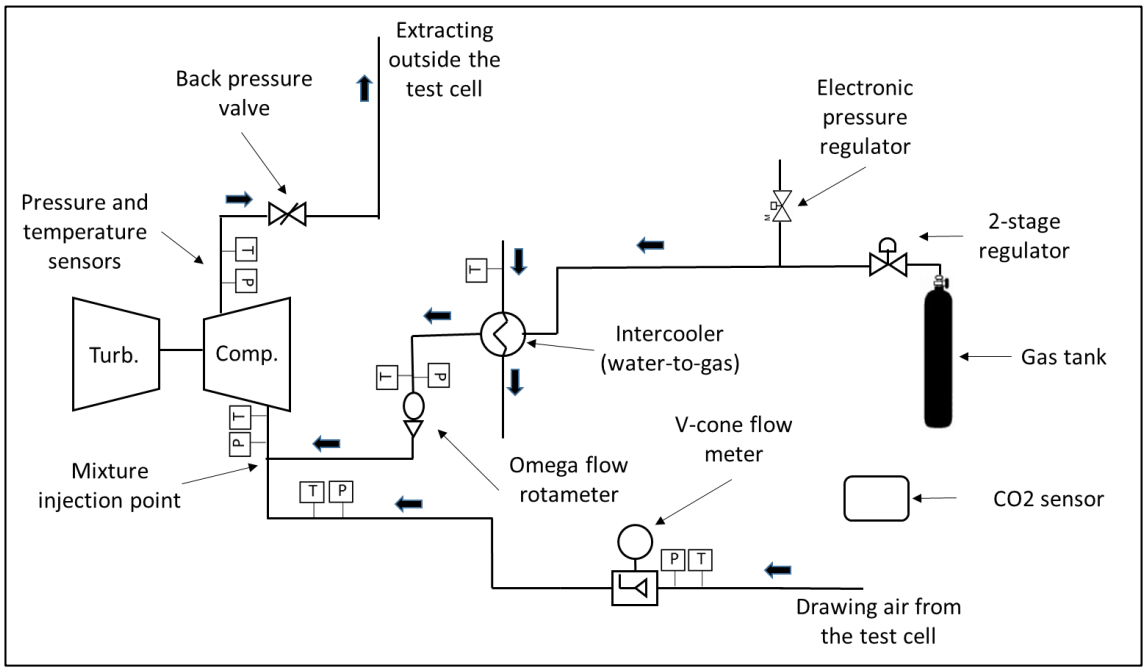

Figure 7-3. Test cell layout for the non-homogeneous gas mapping

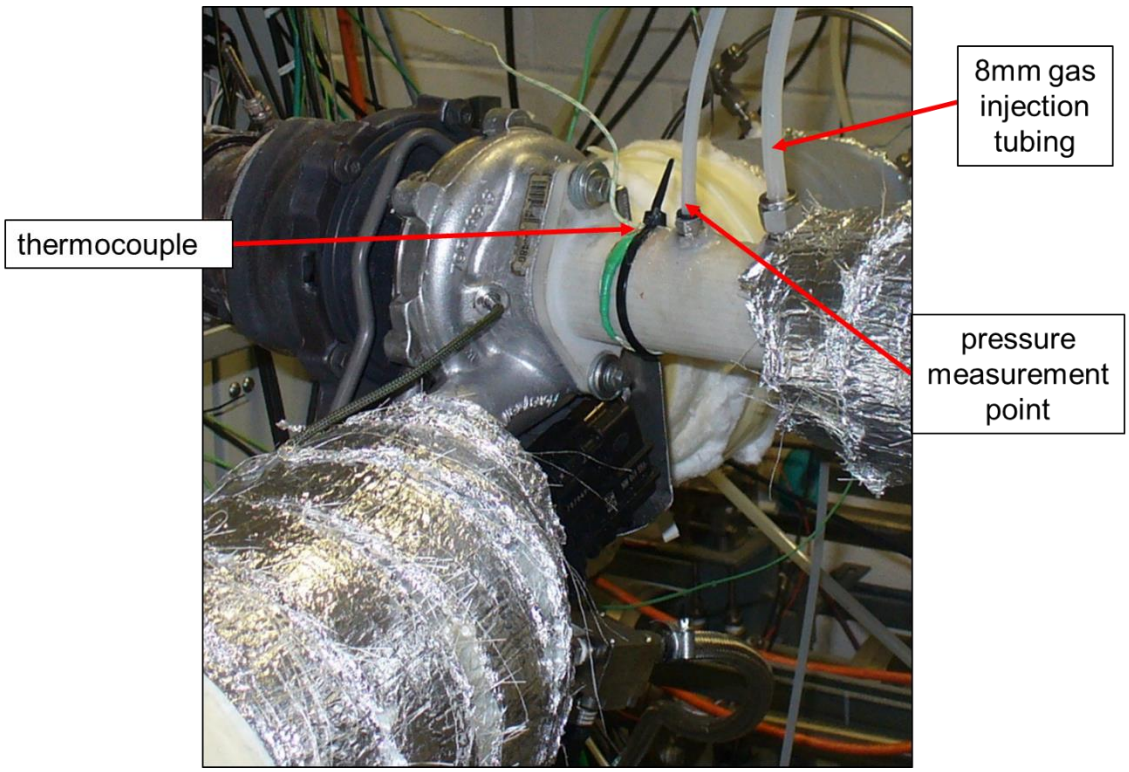

Figure 7-4. Non-homogeneous mapping – view of the inlet pipe

The injection gas was delivered from the bottle tank via a 8mm plastic tube. The actual mass flow rate was measured by Omega FLMR-14050BR in-line rotameter and controlled by the electronic pressure regulator. As the rotameter was originally calibrated for air, the following formulas were used to determine the density correction factors:

- pressure correction factor (f_1)

$$f_1 = \sqrt{\frac{101.35kPa + measured\ static\ gauge\ pressure}{790.83kPa}} \tag{67}$$

- temperature correction factor (f_2)

$$f_2 = \sqrt{\frac{530}{460 + measured\ temperature\ (Fahrenheit)}} \tag{68}$$

- specific gravity correction factor (f_3)

$$f_3 = \sqrt{\frac{1}{SG_{mix}}} \tag{69}$$

where:

$$SG_{co2} = \frac{\rho_{mix}}{\rho_{air}} \tag{70}$$

Opening the manual valve fitted on the bottle containing highly compressed gas (up to 200bar) resulted in a large pressure drop through the valve and this caused the temperature drop even below zero degrees Celsius. Therefore to control the temperature of the injection gas a small water-to-air heat exchanger has been used which allowed to maintain a similar temperature of gas at all four passages of the inlet pipe. On the other hand the temperature on the injection gas could be raised above the mean temperature of the gas at the compressor inlet and therefore the effects of the hot streams were evaluated. There were three cases of the injection methods tested within this study as shown in Figure 7-5 - Figure 7-7. It was targeted to select the least intrusive injection location/method in terms of aerodynamic effects. For this reason the third case of gas injection was selected. For the safety of the gas stand operator there was a CO2 sensor fitted to measure the actual concentration of CO2 inside the test cell.

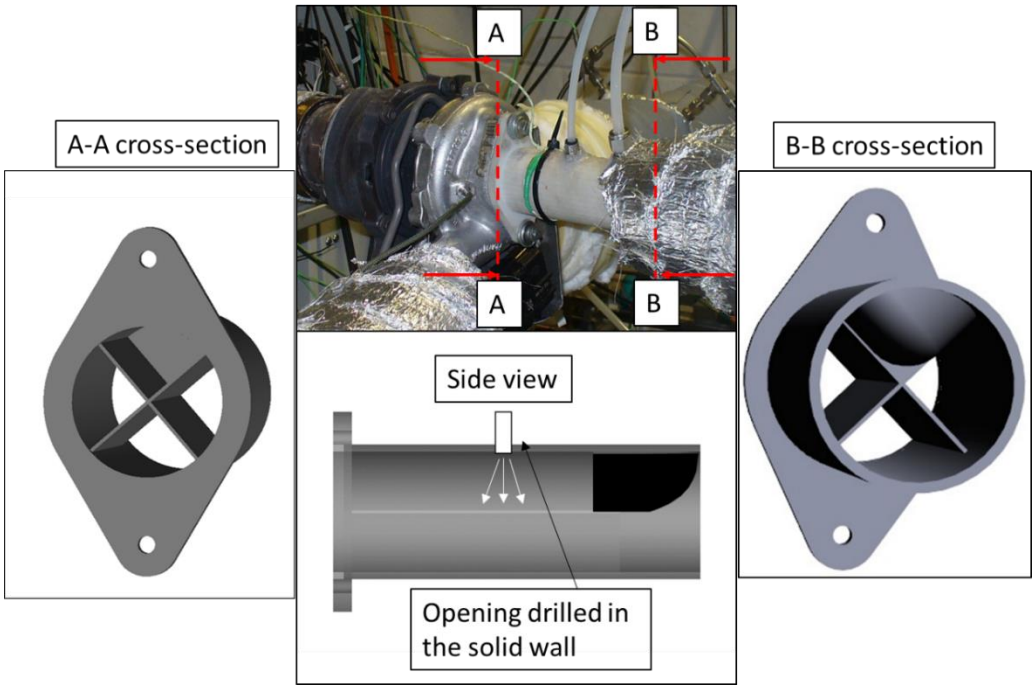

Figure 7-5. Non-homogeneous mapping – 1st injection location

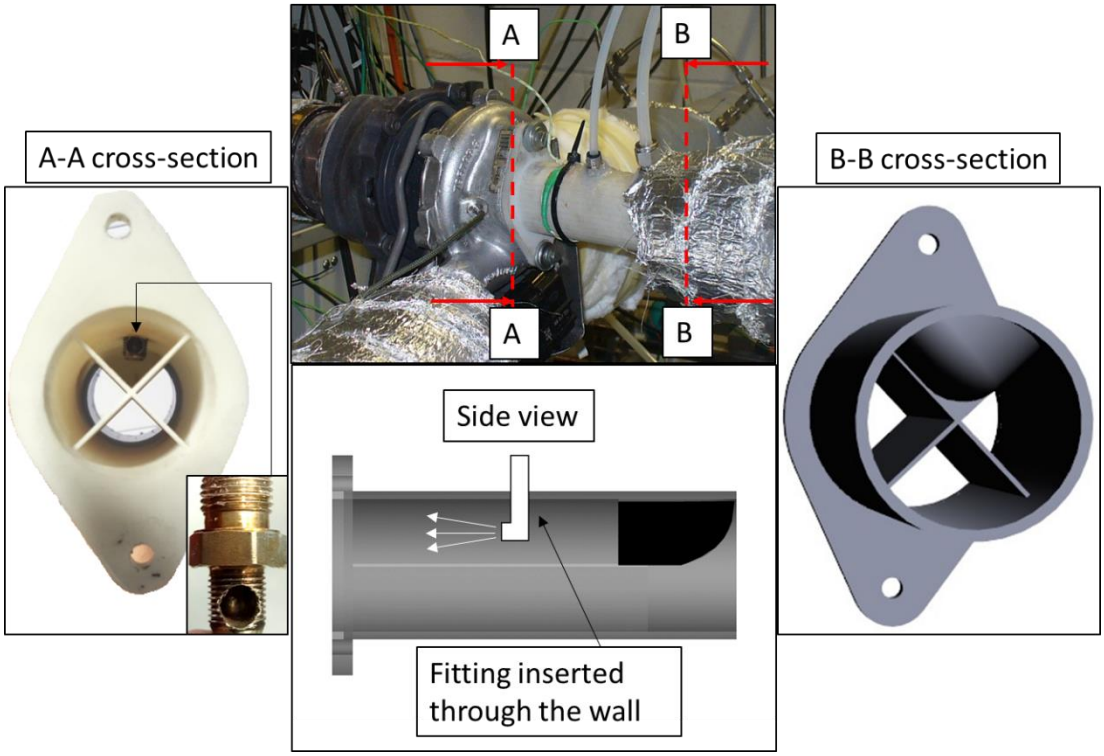

Figure 7-6. Non-homogeneous mapping – 2nd injection location

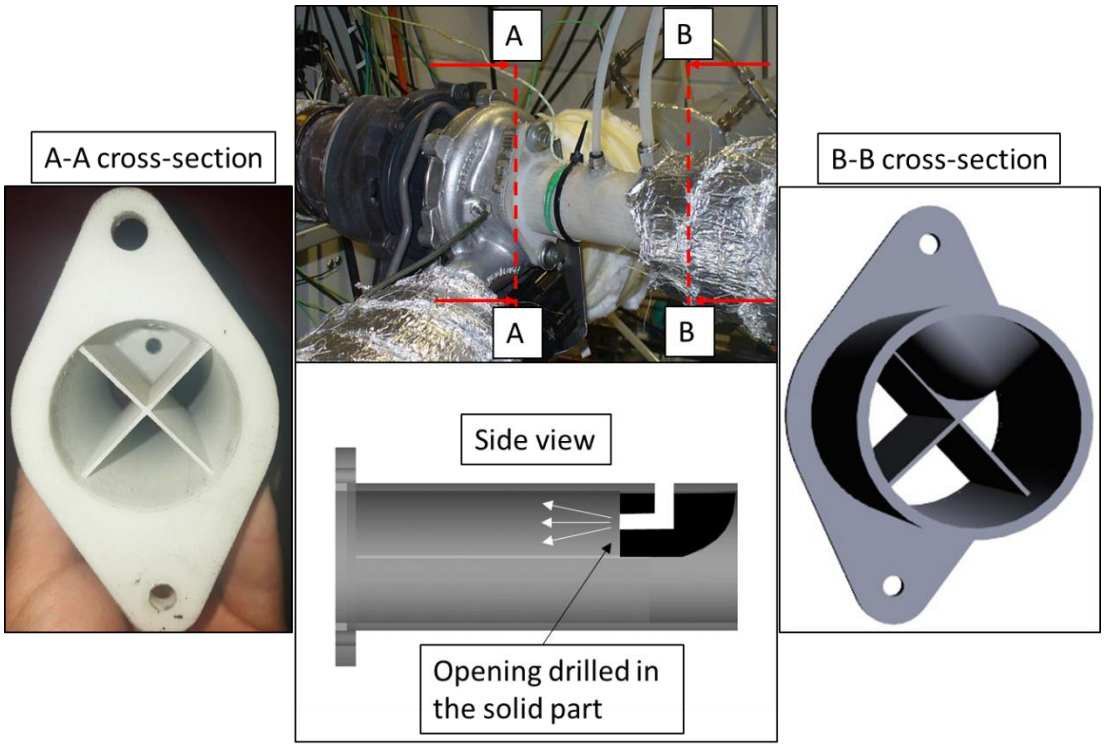

Figure 7-7. Non-homogeneous mapping – 3rd injection location

7.3 Numerical approach

Computational fluid dynamics has been for years an important element in the design and manufacture process in the automotive industry [107]. It is currently the most common tool to design and analyse all types of turbomachinery [108]. In this investigation it is

used in order to check the validity of the experimentally gathered data and for the numerical prediction of the fluid flows for the selected turbocharger compressor. A commercially available CFD code (Star CCM+) has been used for this study. The code is based on the finite volume method (FVM) which is a method for representing and evaluating partial differential equations in the form of algebraic equations.

a) Mathematical representation of fluid flows

CFD is based on the governing equations of fluid dynamics where the following physical laws are adopted. Mass conservation for the fluid (matter may neither be created or destroyed); Newton's second law (the rate of change of momentum equals the sum of forces acting on the fluid); first law of thermodynamics (the rate of change of energy equals the sum of rate of heat addition and work done on the fluid). For the fluids these fluid laws can be expressed as below:

Continuity equation (The balance of mass through a control volume):

$$\frac{\partial \rho}{\partial t} + \nabla \cdot (\rho \boldsymbol{V}) = 0, \tag{71}$$

Momentum equation (The time rate of change of linear momentum is equal to the resultant force acting on the continuum):

$$\frac{\partial (\rho \boldsymbol{V})}{\partial t} + \nabla \cdot (\rho \boldsymbol{V} \otimes \boldsymbol{V}) = \nabla \cdot \boldsymbol{\sigma} + \boldsymbol{f_b}, \tag{72}$$

The stress tensor $\boldsymbol{\sigma}$ (sum of normal stresses and shear stresses) is written as below:

$$\boldsymbol{\sigma} = -p\boldsymbol{I} + \boldsymbol{T}, \tag{73}$$

Where:

p – pressure, $\boldsymbol{I}$ – identity matrix, $\boldsymbol{T}$ – viscous stress tensor

Energy equation (The rate of change of energy equals the sum of rate of heat addition and work done on the fluid)

$$\frac{\partial (\rho E)}{\partial t} + \nabla \cdot (\rho E \boldsymbol{V}) = \boldsymbol{f_b} \cdot \boldsymbol{V} + \nabla \cdot (\boldsymbol{V} \cdot \boldsymbol{\sigma}) - \nabla \cdot \dot{q} + S_{E,} \tag{74}$$

b) Turbulence modelling

Turbulent flow is a flow regime that is characterised by chaotic changes in pressure and flow velocity. The onset of turbulence depends on the ratio of inertia force to viscous force (indicated by Reynolds number). At high Reynolds number, the inertia forces are large to amplify the disturbances and the transition to turbulence occurs. As the appearance of the turbulence eddies occurs over a wide range of length scales, solving such flows would require very large computing meshes. Instead, turbulence models are introduced which decompose the Navier-Stokes equations for the instantaneous velocity and pressure fields into a mean value and fluctuating component. This process of averaging brings the original Navier-Stokes equations to the form of Reynolds-Averaged Navier-

Stokes equations. The resulting equations for the mean quantities are identical to the original except that an additional term now appears in the momentum transport equation. This new term is called Reynolds stress tensor $\boldsymbol{T_t}$. There are several techniques to model the Reynolds stress tensor of which the most popular are: Eddy Viscosity Models (EVM's) and Reynolds Stress Transport (RST) models. Eddy viscosity models use the concept of turbulent viscosity μ_t to model the Reynolds stress tensor as a function of mean flow quantities:

$$\boldsymbol{T_t} = 2\mu_t \boldsymbol{S} - \frac{\mathbf{2}}{\mathbf{3}}(\mu_t \nabla \cdot \boldsymbol{V} + \rho\kappa)\boldsymbol{I}, \tag{75}$$

Where $\boldsymbol{S}$ is the strain tensor:

$$\boldsymbol{S} = \frac{1}{2}(\nabla \boldsymbol{V} + \nabla \boldsymbol{V}^T), \tag{76}$$

and κ is the turbulent kinetic energy. Eddy viscosity models solve additional transport equations for scalar quantities that enable turbulent viscosity to be derived by linking it to the turbulent kinetic energy k and turbulent dissipation rate ε (equation (*77*).

$$\mu_t = C_\mu \rho \frac{\kappa^2}{\varepsilon} \tag{77}$$

In this study a Realizable Two-Layer K-Epsilon turbulence model has been used. This approach combines the Realizable K-Epsilon model with two-layer approach. The turbulent dissipation rate is resolved here as proposed by Shih et al [109], turbulent kinetic energy as by Jones and Launder [110]. Finally, a critical coefficient of the model, C_μ, is expressed as a function of mean flow and turbulence properties, rather than assumed to be constant as in the standard model. The two-layer approach, is an alternative to the low-Reynolds number approach that allows the K-Epsilon model to be applied in the viscous sublayer. In this approach, the computation is divided into two layers. In the layer next to the wall, the turbulent dissipation rate and the turbulent viscosity are specified as functions of wall distance. The values of ε specified in the near-wall layer are blended smoothly with the values computed from solving the transport equation far from the wall. The formula for the turbulent kinetic energy is solved in the entire flow [111].

c) Geometry

The first step in any CFD analyses is the creation and definition of geometry of the flow region. In case of turbomachinery simulations most often a 3D CAD model of the turbocharger hardware is imported into a dedicated CFD software where it is processed according to the requirements. The CAD model of the turbocharger used in this investigation is shown in Figure 7-8.

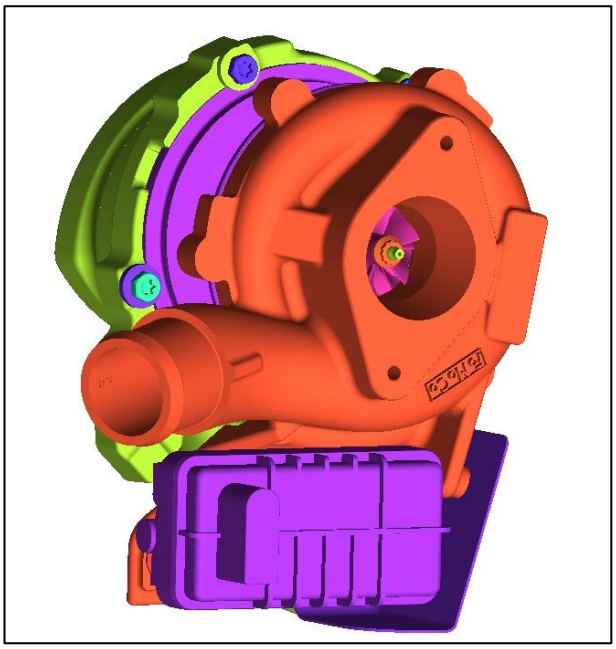

Figure 7-8. CAD model of the selected HTT turbocharger

The target of the CFD simulations in this investigation is the prediction of the fluid flows throughout the compressor. No heat transfer between the working gas and compressor housing is to be taken into account (adiabatic conditions). For this reason only internal (fluid) volume of the compressor is required. Some simplifications are made to the compressor wheel and back plate to allow for easier mesh generation and maintain its integrity. The compressor inlet pipe has been equally divided for four passages to enable for non-homogeneous gas introduction. The domain outlet plane has been created at a distance of 100mm from the volute outlet plane. The CFD geometry model is presented in Figure 7-9 and Figure 7-10.

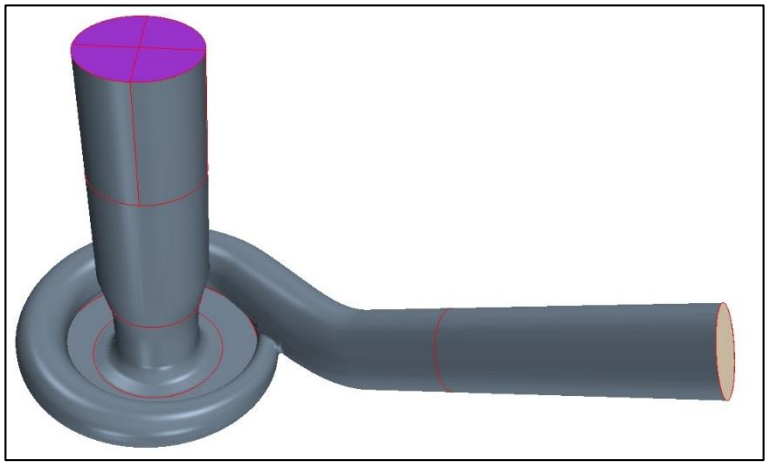

Figure 7-9. Geometry model of the turbocharger compressor

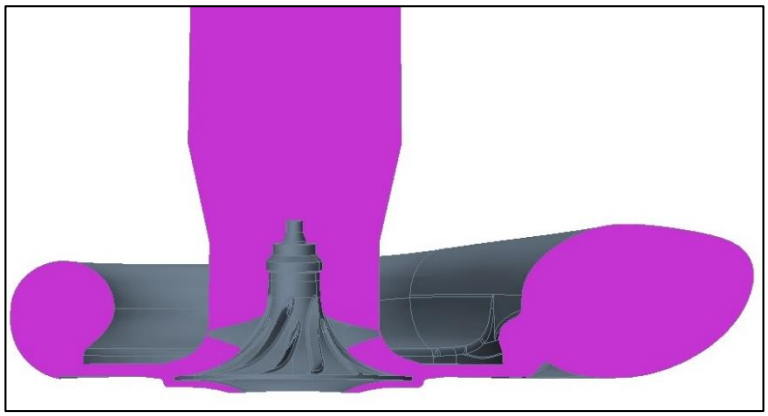

Figure 7-10. Cross section view of the geometry model

d) Computational mesh

Mesh generation is a second step in the process of solving a problem with the use of CFD. It is required that the domain of the flow is divided into smaller non-overlapping subdomains in order to solve the flow physics within the geometry that has been created. The fluid flows described in every mesh cell are solved numerically so the flow properties such as pressure, temperature, velocity etc. are determined. The total number of cells used in the computational grid is 6,197,436. The core of the mesh is built of polyhedral elements. On every surface where fluid domain is bounded by solid region there is additional four layers of prism elements for more accurate boundary layer representation. The size of mesh elements varies within the model, generally the smallest elements are generated in the impeller section – between the shroud and impeller blades, near blades and wheel hub. An example of the impeller grid is shown in Figure 7-11 - Figure 7-13.

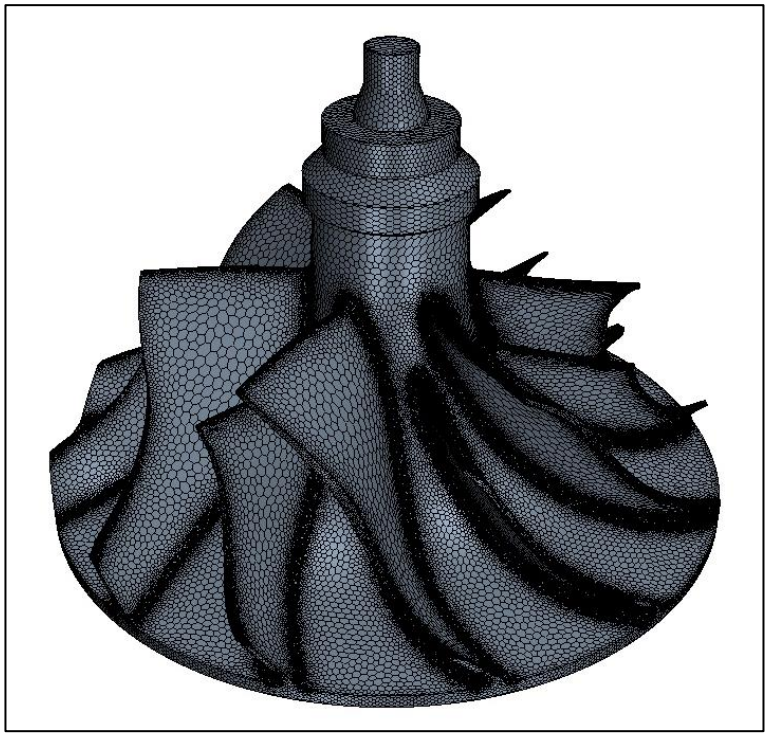

Figure 7-11. Impeller grid

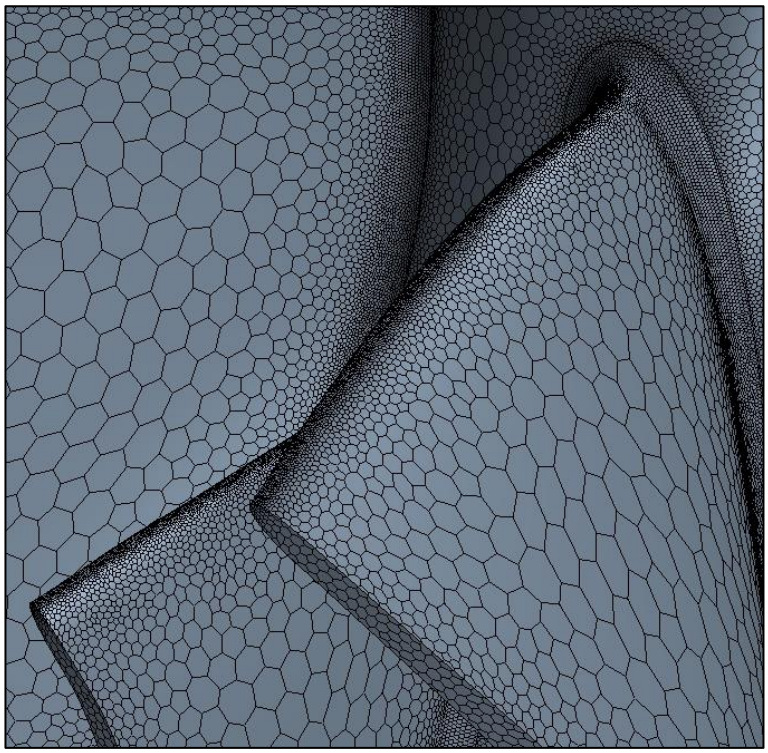

Figure 7-12. Grid on the impeller blades

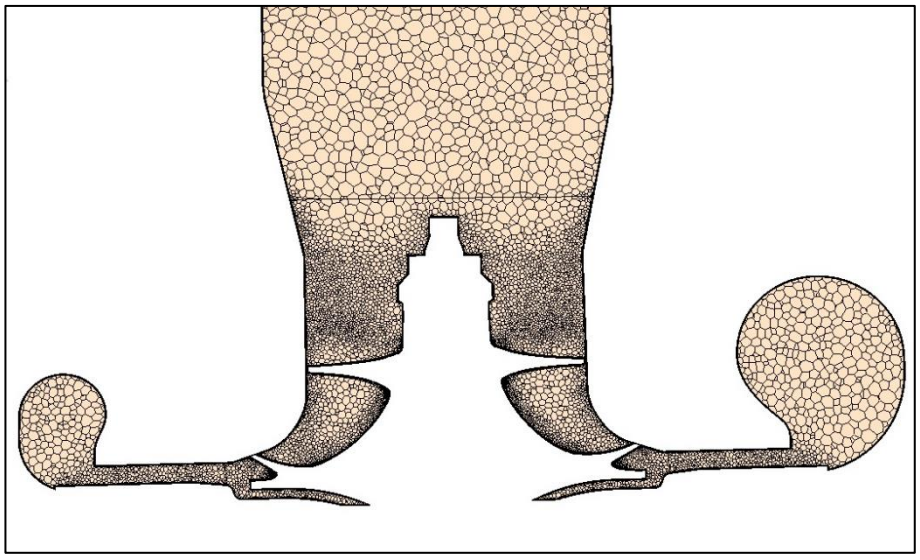

Figure 7-13. Cross-section view of the grid

e) Formulation of physics, modelling approach and set up of boundary conditions

Next step in the process of preparation of CFD simulation is formulation of physics to describe the occurring phenomena. In this case the following selections are made at the setup stage:

- Three-dimensional model
- Steady state simulation type (based on Frozen Rotor technique)
- Ideal gas model (compressible gas)
- Turbulent flow with RANS based Realizable K-Epsilon model with two-layer approach

- One-phase model: single component gas (for pure air or pure CO2 simulation) or multi component and non-reactive gas (for simulating mixtures of air and CO2)
- Coupled flow and energy model

Modelling of the motion of the turbomachinery component was performed by using the Moving Reference Frame approach. For the analysis of turbomachinery flows, moving reference frames can be used for two types of steady-state simulation: frozen rotor and mixing plane. In a frozen rotor simulation which is chosen for this investigation, a rotating reference frame at a speed of interest was applied to the region of mesh containing the impeller. The only stationary wall within this region was the compressor shroud. The remainder of the model mesh was static.

The setup of boundary conditions is in other words a process of constraining the model – it is decided what the physical bounds of the model and particular domains are, available information is given to mimic the real physical representation of the fluid flow. Based on the above a strategy for obtaining solution is espoused. For this case four different boundary types were chosen:

- Wall type boundary condition – on every external surface of the model, all impeller wheel surfaces and surfaces between inlet gas passages. All the mentioned surfaces set adiabatic borders between the fluid and solid domains, no-slip condition specifies the fluid velocity at the wall boundary to equal zero.
- Stagnation Inlet (Total Inlet) boundary condition – on the model's inlet plane and at normal direction (flow perpendicular to the inlet plane). Total inlet pressure was set as normal atmospheric pressure at a value of 101,325kPa, inlet total temperature at a value of 25°C. For the multi component gas cases – mixtures of air and CO2, the concentrations were specified by providing the mass fractions.
- Mass Flow Inlet boundary condition – applied on the model's outlet plane and in the negative direction. Therefore the flow of the gas is given the right (outbound direction). The value of the mass flow was a variable input provided based on the experimentally gathered data.
- Interface boundary condition. Baffle interface type was set between passages in the compressor inlet pipe, whereas Internal interface type was set between all fluid domains.

The combination of the above boundary conditions together with the speed of rotation allowed for simulation of the compressor operation – outlet static/total pressure and temperature were the outputs and therefore parameters like total-to-total pressure ratio, compressor efficiency could be calculated.

7.4 Homogeneous substitute gas – experimental results

Before the collected data is presented it is important to give more details on the formulation of compressor efficiency. SAE's standards [25, 112] define compressor efficiency as a ratio of isentropic enthalpy rise across compressor stage through compressor pressure ratio to the actual enthalpy rise across the compressor stage. This relationship is commonly recognised as in Equation (*78*).

$$\eta_c = \frac{T_{1t}(PR^{\left(\frac{\gamma-1}{\gamma}\right)}-1)}{T_{2t}-T_{1t}}, \tag{78}$$

Although it is known that for an ideal gas γ is a temperature dependent variable and that it progressively changes along the compression process the γ used in Equation (*78*) is a constant as it refers to isentropic outlet temperature (Equation **Error! Reference source not found.**)).

$$T_{2is} = T_{1s}(\frac{P_{2s}}{P_{1s}})^{\left(\frac{\gamma-1}{\gamma}\right)}, \tag{79}$$

Alternatively, the International Council on Combustion Engines (CIMAC), allows for calculating an average γ [113] based on the inlet and outlet temperatures (Equation (34)).

The formulation of γ in the calculation on compressor efficiency is expected to be an important factor when dealing with pure CO2 as the rate of its change with temperature is significantly higher than for air (Figure 7-14).

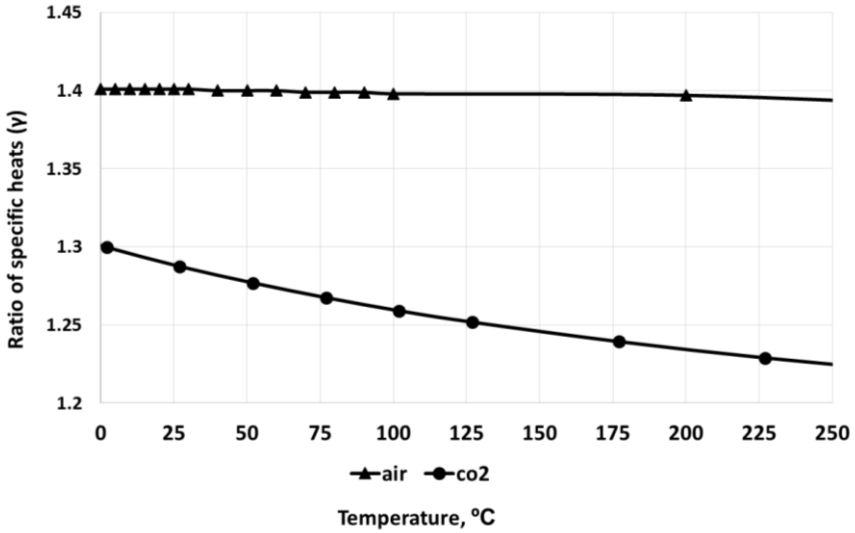

Figure 7-14. Ratio of specific heats as a function of temperature

Having noticed this important disadvantage of assuming constant specific heat during thermodynamic evolution Serrano et al [114] developed an iterative method for calculating the isentropic outlet temperature of dry air that takes into account the variations in specific heat during the isentropic process. However in this paper compressor efficiency is calculated based on two cases – constant γ (specified at reference condition), and average γ_{ave} as suggested in [113]. For the first tested working medium – air, the non-

dimensional mass flow parameter (NDMP) and speed parameter (NDSP) are calculated as in Equation (*80*) and (*81*) respectively. Both equations are simplified versions of equations (*7*) and (*8*) – all compressor geometry/size terms are dropped as this investigations only includes one selected compressor.

$$NDMP = \frac{\dot{m}_c \sqrt{\frac{RT_{01}}{\gamma}}}{P_{01}}, \tag{80}$$

$$NDSP = \frac{N_{act}}{\sqrt{(RT_{01}\gamma)}}, \tag{81}$$

Efficiency of the compressor is calculated as per Equation (18) and (78) - for two different γ values. In the first case it is calculated based on the arithmetic average at compressor inlet and outlet temperatures whereas in the second case it is a fixed value and equals 1.401 (reference temperature - 25°C). The comparison of compressor efficiencies based on various γ formulations is presented in Figure 7-15 and Figure 7-16. For better understanding of the non-dimensional speed parameter values plotted above performance lines the highest value of 17.4 corresponds to the corrected speed of 190krpm whereas the lowest value of 8.2 corresponds to 90 krpm. The speed increment between every next speed line is 20 krpm.

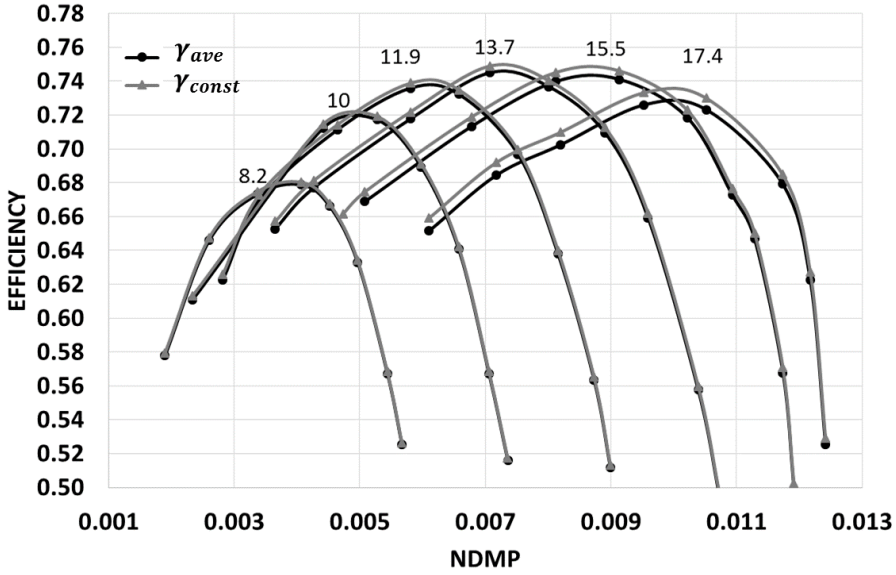

Figure 7-15. Efficiency vs. NDMP for constant and average ratios of specific heats.

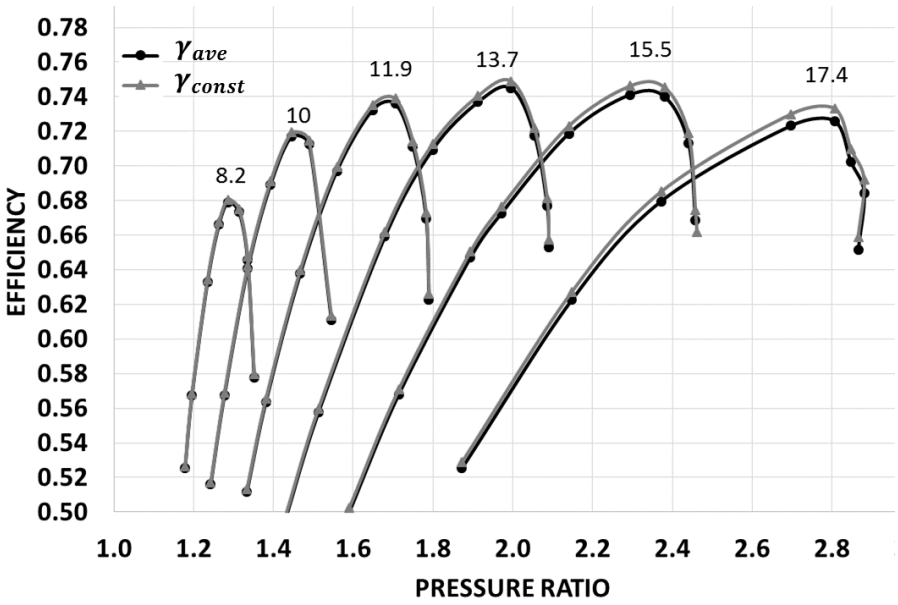

Figure 7-16. Efficiency vs. pressure ratio for constant and average ratios of specific heats.

It can be noted that the highest differences between the two compared efficiencies are in the high speed and high pressure ratio region of the map - where the highest compressor outlet temperatures occur. However these are still relatively small due to the low temperature dependency of γ. As the average value of γ seem to be more appropriate for the representation of compression process it is used to correct the flow and speed for the remaining gas mixtures. The comparison of performance maps for air and CO2 is carried out in stages. The first three selected CO2-air mixtures containing 3%, 5%, 10% of CO2 by mass respectively are to represent real achievable concentrations of CO2 at LP EGR operation. The data obtained for pure CO2 is an extreme case that perhaps will never find particular use in the automotive turbocharging but surely can contribute to other applications like semi-closed and closed gas turbine engines.

When calculating γ for mixtures the following formulas are used:

$$\gamma_{mix} = \frac{c_{p,mix}}{c_{p,mix} - R_{mix}}, \tag{82}$$

$$c_{p,mix} = w * c_{p,air} + (1 - w) * c_{p,CO2}, \tag{83}$$

$$c_{p,CO2} = (22.26 + 5.981e^{-2}T_1 - 3.501e^{-5}{T_1}^2 + 7.469e^{-9}T_1^3)/\, M_{CO2}, \tag{84}$$

$$R_{mix} = \frac{R_u}{M_{mix}}, \tag{85}$$

$$M_{mix} = y * M_{air} + (1 - y) * M_{CO2}, \tag{86}$$

Figure 7-17 - Figure 7-19 show the compressor non-dimensional performance maps generated for air and three CO2-air mixtures. It can be concluded that no significant performance change can be spotted between the maps (no substantial change either in surge and choke limits has been observed nor clear degradation or rise of pressure ratio and efficiency.

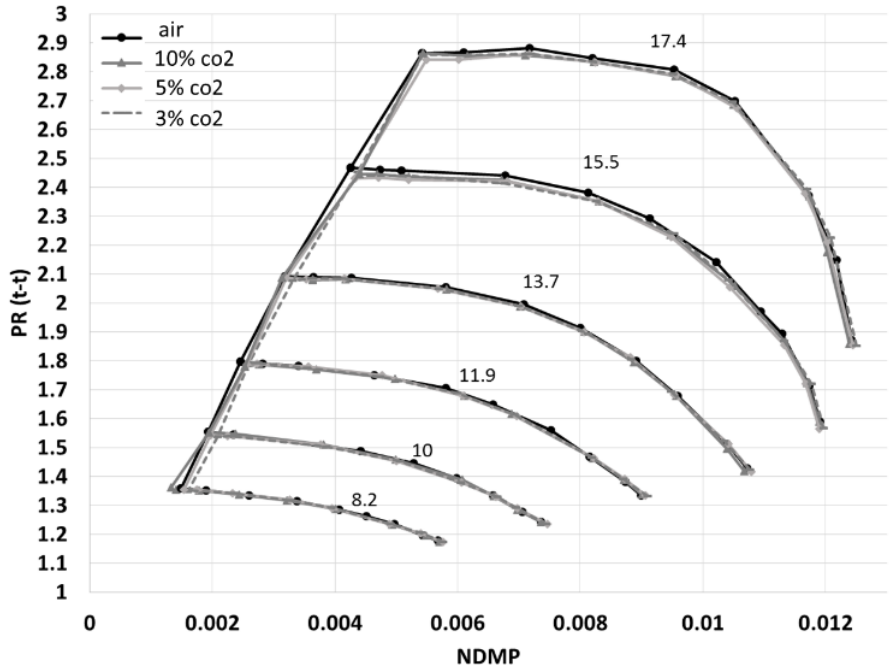

Figure 7-17. Pressure ratio vs. NDMP for various mixture concentrations

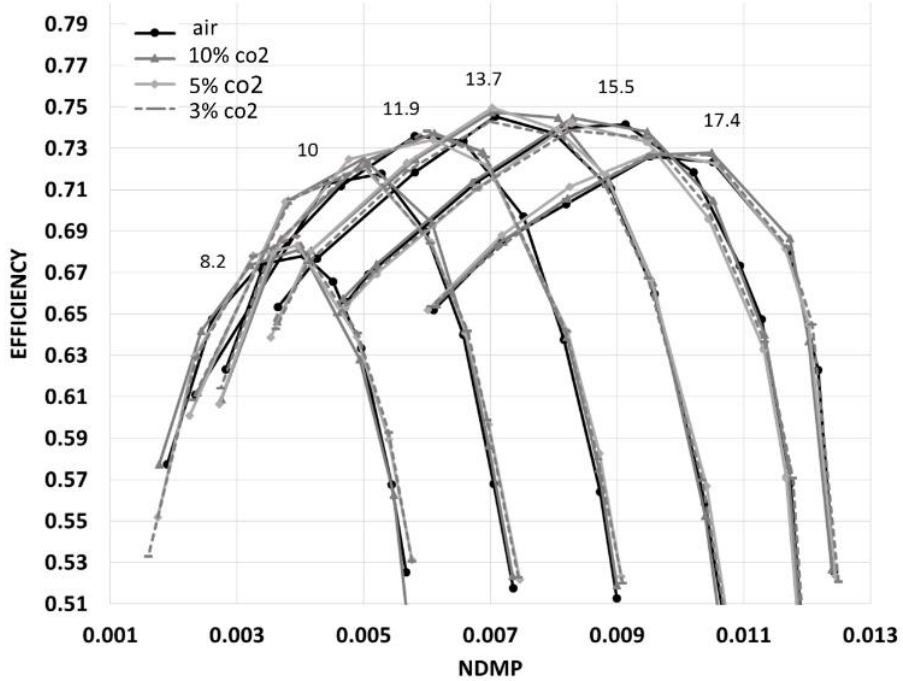

Figure 7-18. Efficiency vs. NDMP for various mixture concentrations

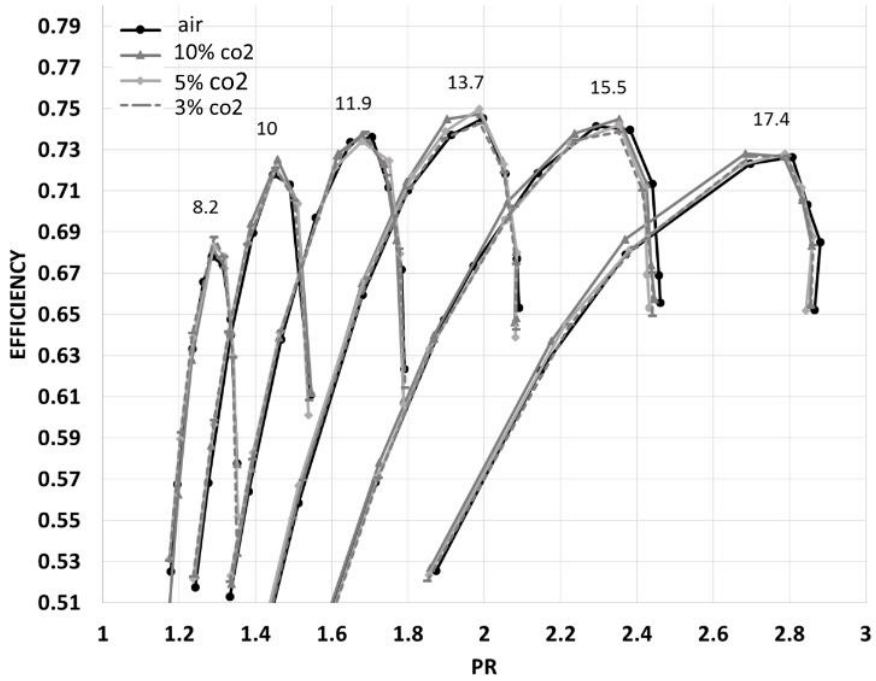

Figure 7-19. Efficiency vs. pressure ratio for various mixture concentrations

Now, when comparing the extreme cases of air and pure CO2, a clear PR difference is noted between the two (Figure 7-20). Also, for the CO2 case the surge line has moved to higher mass flows proportionally to the compressor speed. Finally, at the region of high mass flow and at two highest speeds the air and CO2 performance lines cross each other (different choke limits).

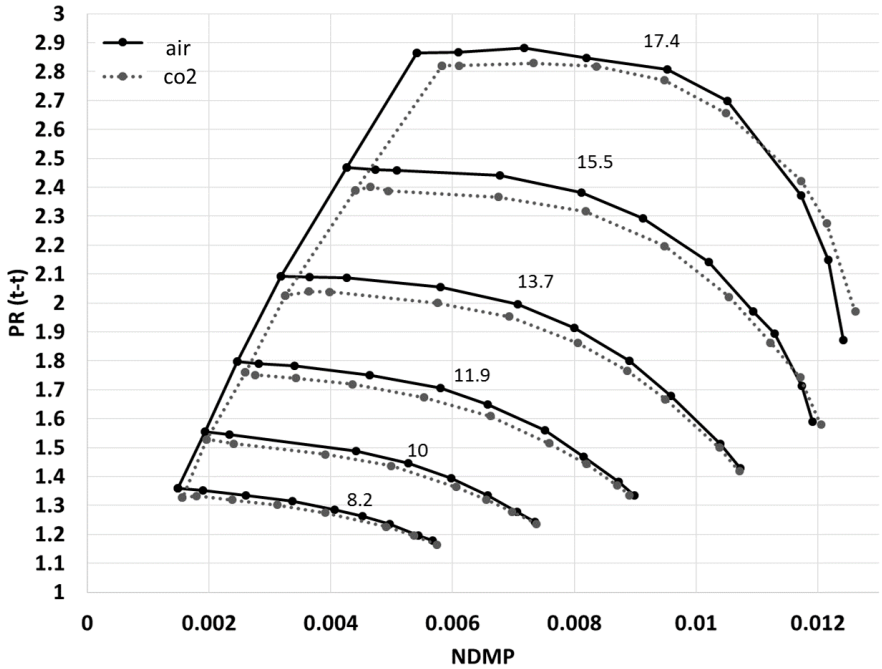

Figure 7-20. Pressure ratio vs. NDMP for air and CO2

Comparison of efficiencies (Figure 7-21) calculated based on average γ shows that at higher speed lines operation with CO2 is more efficient however the efficiency benefit

reduces when moving towards lower speed lines. Finally, at the lowest speed line the efficiency of operation with CO2 is lower than with air. This trend is similar for the case where efficiencies are calculated for the inlet temperature based λ (Figure 7-22). For the latter case also a larger offset is noted between the high speed efficiency lines and a closer match at the lowest speed line.

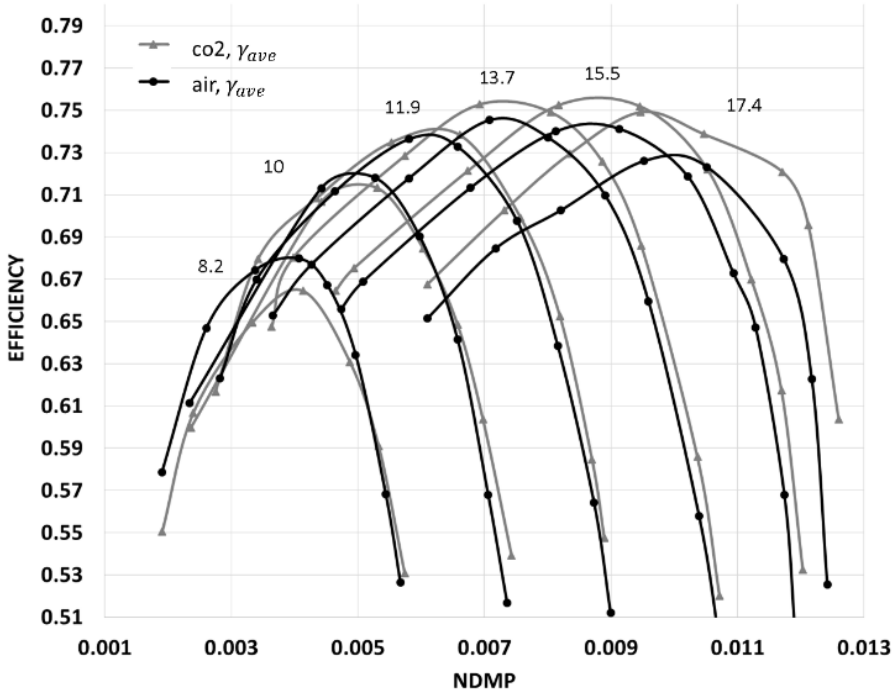

Figure 7-21. Efficiency vs. pressure ratio for air and CO2 based on average γ

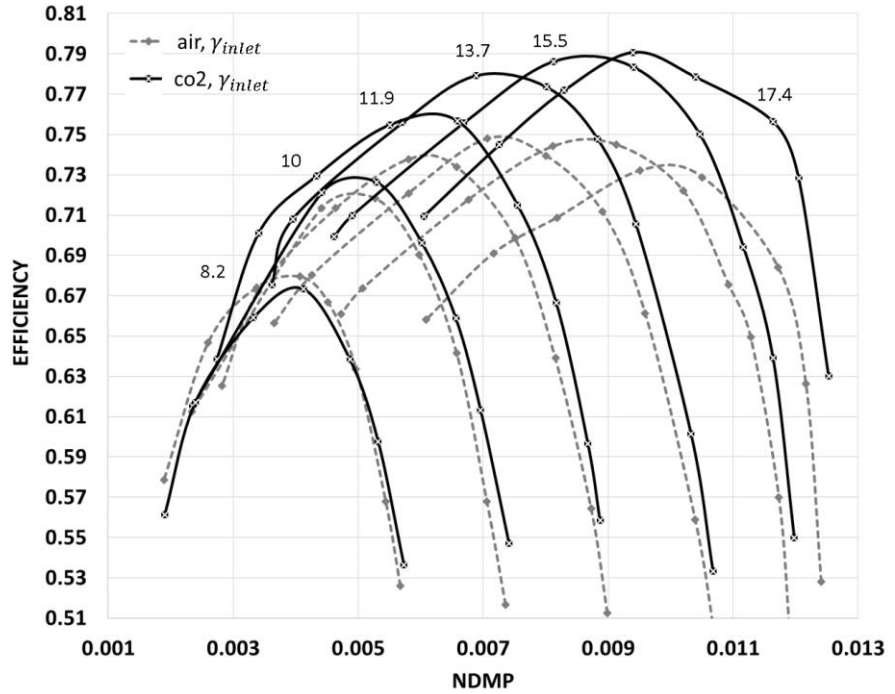

Figure 7-22. Efficiency vs. NDMP for air and CO2 based on inlet γ

The performance difference between the cases of pure air and pure CO2 are due to the different γ which itself is a criterion in the dimensional analysis. Therefore seeing the need for further performance map correction method when operating with substitute gas Roberts and Sjolander [98] proposed one which is based on the following technique. First, compressor corrected efficiency with substitute gas is found (Equation (*87*)). Next, pressure ratio at the same operating point is calculated (Equation (*88*)).

$$\frac{1-\eta_A}{1-\eta_B} = \left(\frac{\gamma_A}{\gamma_B}\right)^{0.8}, \tag{87}$$

$$PR_B = \left[\frac{\gamma_B-1}{\gamma_A-1}\left(\frac{\eta_B}{\eta_A}\right)\left(PR_A^{\gamma_A-\frac{1}{\gamma_A}}-1\right)+1\right]^{\gamma_B/(\gamma_B-1)}, \tag{88}$$

In order to check the validity of the above correction procedure for the data obtained during this test campaign the predicted compressor efficiency values (as Equation (*87*) were compared with the experimentally obtained data. It can be noted that poor match between the measured and predicted efficiencies is obtained (Figure 7-23) if n exponent equals 0.8. The curves of measured and predicted efficiency are fairly close only at the non-dimensional speed parameter of 11.9. It can also be noted that the efficiency is over-predicted at the two lowest speed lines and generally under-predicted along other speed lines. For this reason it can be concluded that the n exponent used in the efficiency correction formula is a variable rather than a fixed value as suggested by Roberts and Sjolander. It is suspected that this is caused due to the lack of thermal insulation and therefore the heat transfer between the turbomachinery components (from the hot turbine towards the compressor in the low turbocharger speeds and in the opposite direction at high turbocharger speeds). An important fact is that air and CO2 have different specific heats. In the simplest definition, specific heat is the amount of heat per unit mass required to raise the temperature by one degree Celsius. The fact that it is lower for CO2 means that less energy need to be delivered or rejected to heat it up or cool it down. The other important fact noted during the testing campaign is that the actual speed of the turbocharger was very different when operated with air and CO2 (at same non-dimensional speed) and therefore the compressor outlet temperatures were higher when operated with air. The rise of the compressor outlet temperature due to heat transfer when operated with CO2 was more significant as the turbocharger rotated slower (longer residency time) so more heat was passed to the flowing gas. The rise of the compressor outlet temperature directly influenced the efficiency drop so it was reasonable to see the compressor efficiency higher when operated with air rather than CO2. On the other end of the map, at the highest turbocharger speeds, the higher efficiencies are noted for compressor that operated with CO2. Appreciating that the heat was transferred in the

opposite direction – from the hot compressor gas towards the cooler bearing housing (conduction) and ambient (convection) and also that due to the lower specific heat for CO2, it was reasonable to expect the higher drops of the compressor outlet temperatures and therefore higher measured efficiency when operated with CO2.

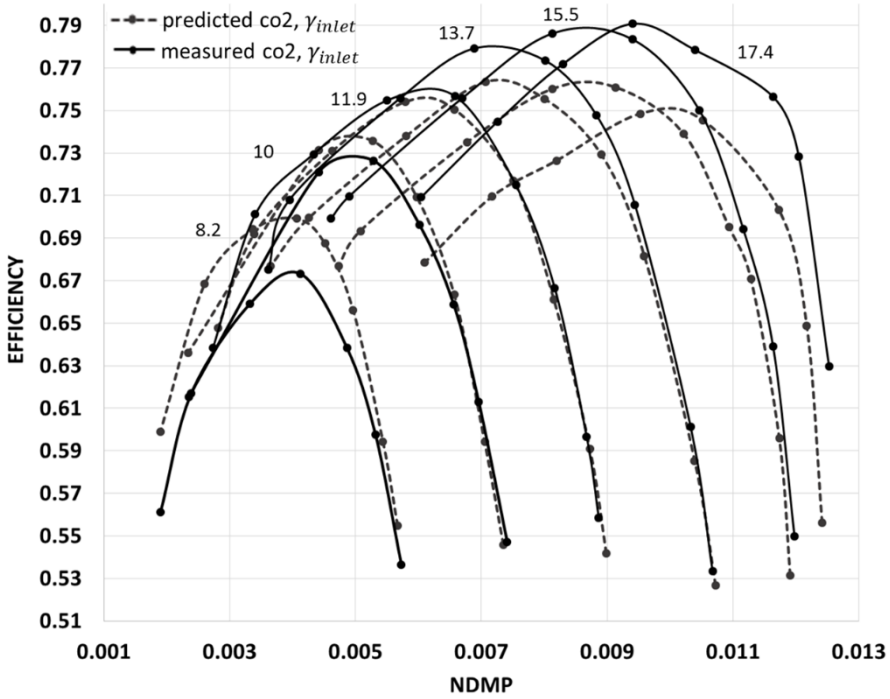

Figure 7-23. Efficiency vs. NDMP for measured and predicted CO2, n exponent = 0.8

Much better correlation (Figure 7-24) is achieved if n exponent is found as a result of linear function in which the argument is the non-dimensional speed parameter.

$$n = 0.27214*NDSP - 2.22889 \quad (89)$$

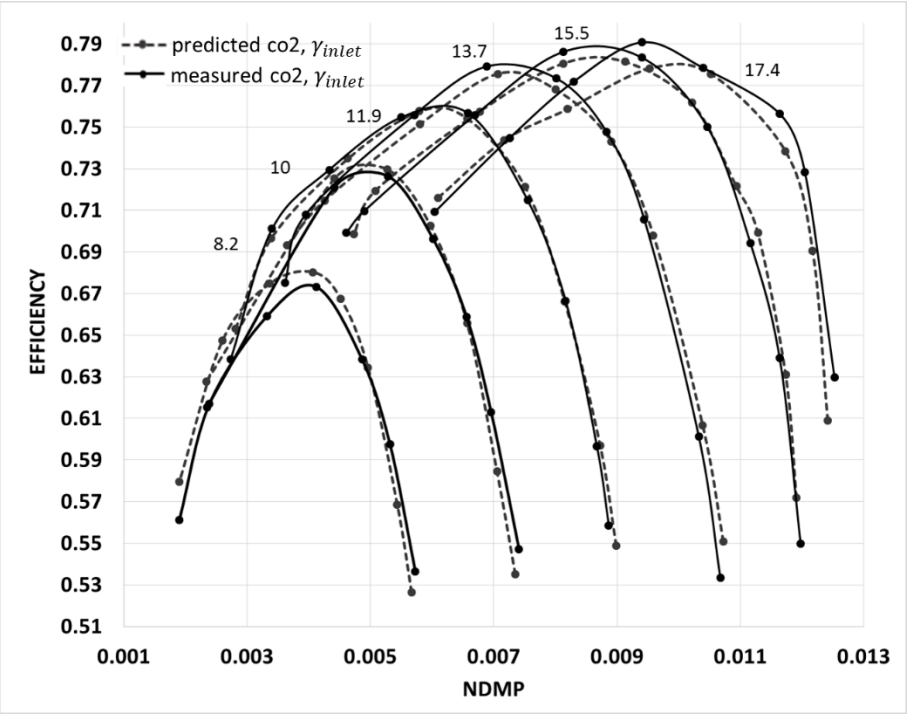

Figure 7-24. Efficiency vs. NDMP for measured and predicted CO2, n exponent as a function of NDSP

7.5 Non-homogenous substitute gas – experimental results

As performance is expressed by the efficiency, pressure ratio and mass flow (either corrected mass flow or non-dimensional mass flow) it is worth explaining how these parameters were measured for the non-homogenous condition. Both pressure ratio and efficiency related measurements (compressor inlet and outlet pressure and temperatures) were measured at standard gas stand measurement points. This means that both inlet pressure and temperature measurement locations were upstream from the injection point. For this reason it was important to inject the substitute gas at a similar temperature as the air drawn from the test cell. Otherwise as a consequence of a higher temperature of the injected gas a rise of the mean temperature of the compressed mixture and therefore also the rise of the outlet temperature would be seen. An increment of the compressor outlet temperature would lead to the isentropic efficiency reduction if both inlet temperature and pressure ratio were kept fixed (as per Equation (*78*)). The change of the mean static pressure as a result of gas injection has been considered as insignificant.

When moving from the homogeneous gas tests to non-homogeneous mixtures a smaller diameter new intake pipe radially divided for four passages has been introduced. The injection was realised as described in Section 7.2. It has been expected that these modifications could have an effect on the compressor performance. The effects from the former modification (introduction of section divider) are shown in Figure 7-25 - Figure 7-27. It can be noted that the new radially divided intake pipe causes some efficiency and pressure ratio degradation especially in the region of low mass flow and high pressure

flows. For this reason the results obtained in this section shall not be directly compared with the former case of homogeneous gases that has been described in paragraph 7.4.

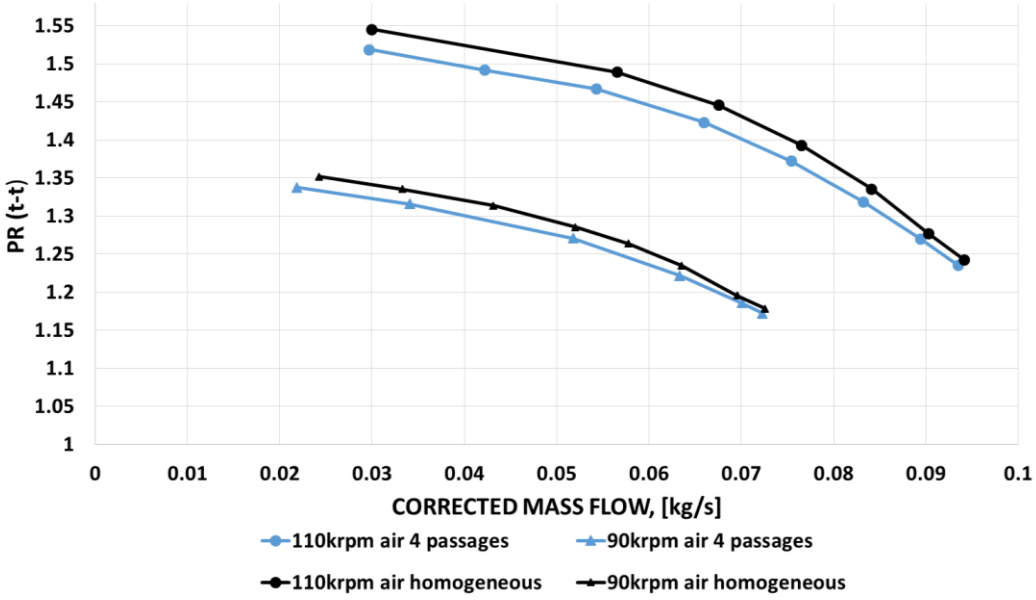

Figure 7-25. Pressure ratio vs. corrected mass flow for two intake pipes arrangements used during homogeneous and non-homogeneous tests

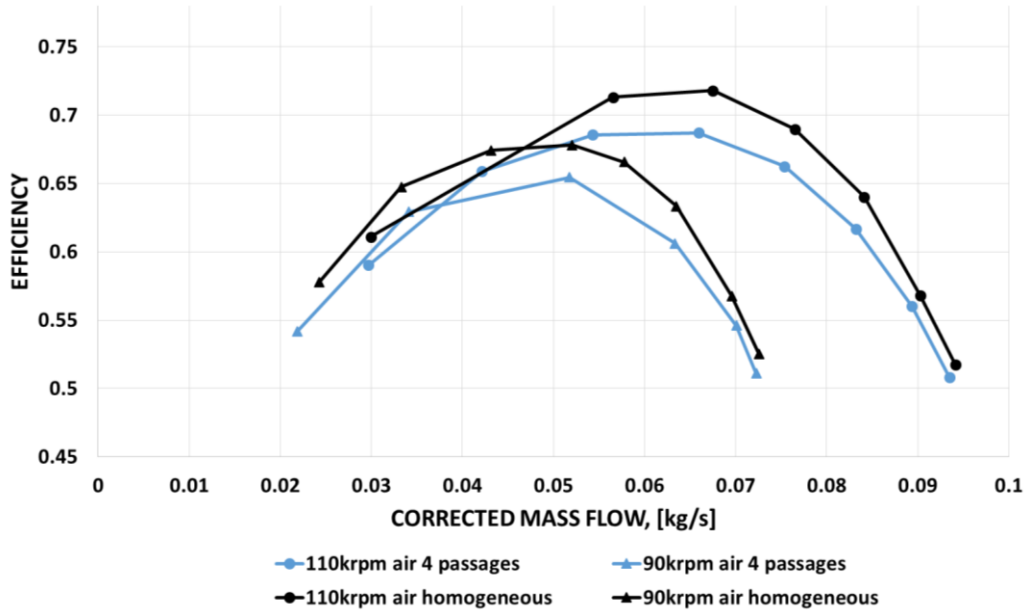

Figure 7-26. Efficiency vs. corrected mass flow for two intake pipes arrangements used during homogeneous and non-homogeneous tests

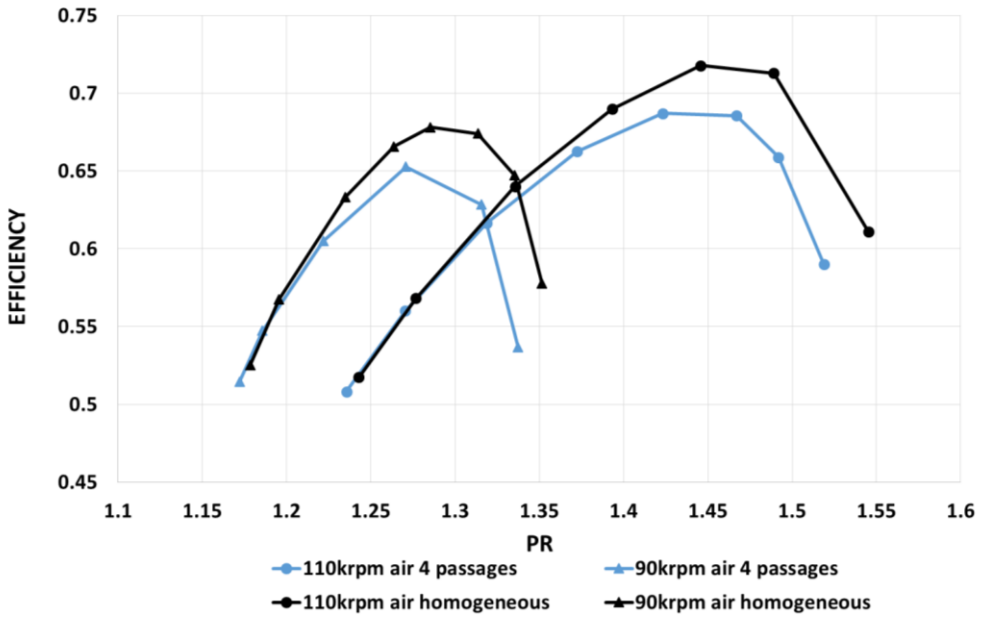

Figure 7-27. Efficiency vs. pressure ratio for two intake pipes arrangements used during homogeneous and non-homogeneous tests

To measure the effects caused by the gas injection (or non-homogeneous injection) two compressor speed lines were measured for two different cases. The main limitation allowing for mapping only two speed lines was the maximum achievable air flow during the injection. Mapping of higher speed lines could not be achieved without significant equipment upgrades (pressure regulators, tubing, fittings). In order to allow for comparing the homogeneous and non-homogeneous cases, the sector divided intake pipe has been installed with all passages open to the flowing air (Figure 7-28). No injection was performed at this point and therefore the flow at the compressor entry was considered to be homogeneous. Thus, this cases was further used to represent the homogeneous case conditions. Next, the injection was realised in the second case and as shown in Figure 7-7. The injected gas was air at a targeted quarter of the total air mass reaching the compressor entry. In this way, if any performance change was discovered it was most likely to be a result of an aerodynamic perturbation caused by the injection method.

Figure 7-28. Radially divided intake pipe

It shall be noted that after the non-homogeneous mixture test campaign the measurement discrepancy between the Omega rotameter (used for the injection flow measurement) and V-cone mass flow has been noticed. Such observation has been made when both mass flow meters were installed in series and measured the same amount of the flowing air mass. Here, since the V-cone measurement was the more reliable device, a correction function was identified to match the readings from both mass flow meters. However, as a consequence of the inaccurate Omega rotameter mass flow measurement during the tests, the targeted mass flow proportions between the sectors of fresh air and injected gas were unbalanced. In fact, the above issue caused the injected mass of air to vary from 15 to 25% at the higher speed of 110 krpm and from 16 to 30% at 90 krpm (the target value of the injected mass was 25%). The figures plotted below compare the compressor pressure ratio and efficiency achieved for the case of homogeneously distributed air (blue lines) and the case where injection was realised into one of the passages (orange lines).

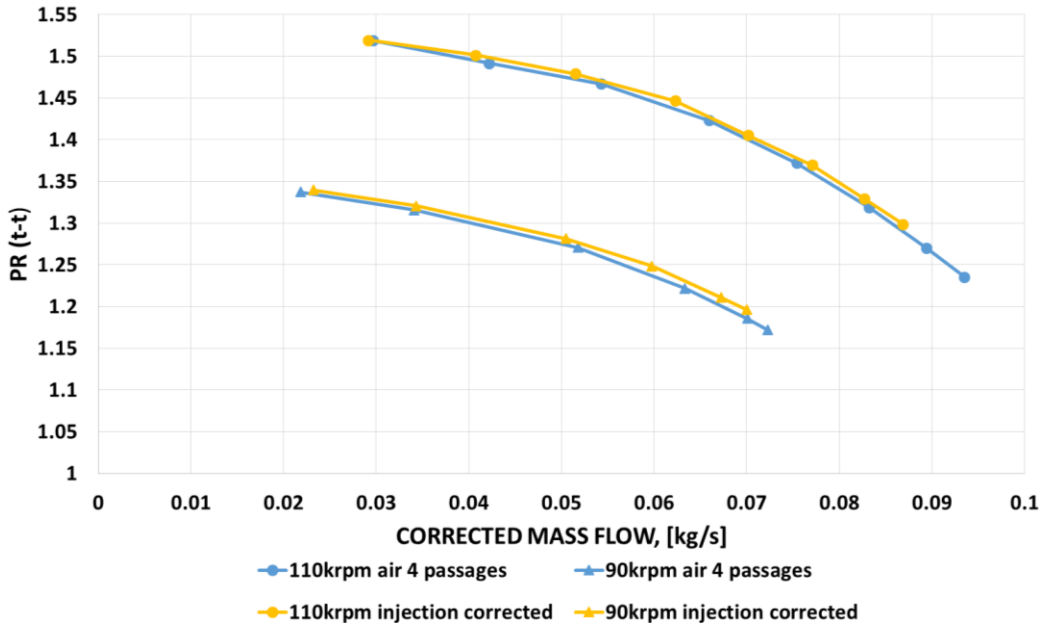

Figure 7-29. Pressure ratio vs. corrected mass flow for homogeneously and non-homogeneously injected air

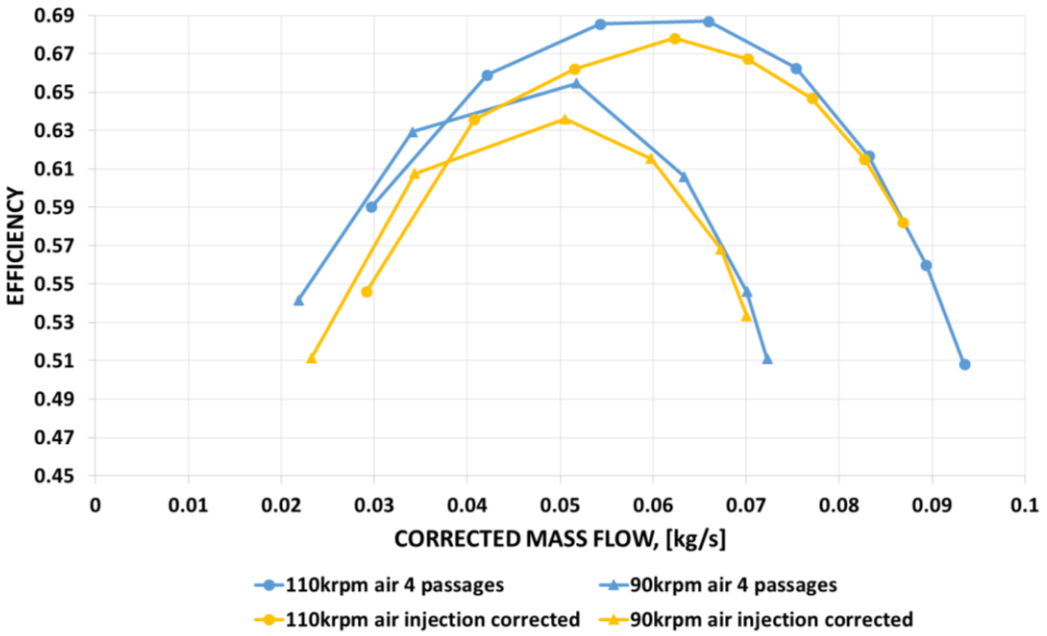

Figure 7-30. Efficiency vs. corrected mass flow for homogeneously and non-homogeneously injected air

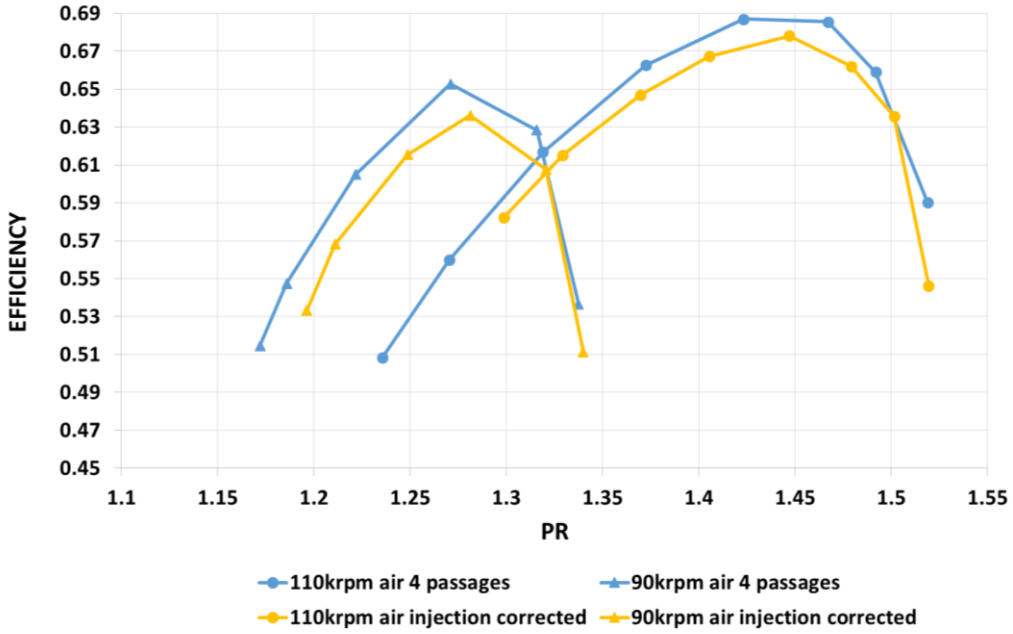

Figure 7-31. Efficiency vs. pressure ratio for homogeneously and non-homogeneously injected air

It can be noted (Figure 7-29) that the compressor pressure ratio does not vary between both considered cases however the efficiency drop of up to two percentage points is present if gas is introduced non-homogeneously (Figure 7-30, Figure 7-31). Based on the presented data it is suspected that this difference is a result of the unbalanced mass flow and the unbalanced velocity within the sectors caused by the jet stream injection. To compare the compressor performance for the cases of injection of various compositions of mixtures (air, a mixture of 20%CO2 and 80% air and a mixture of 40% CO2 and 60% air by mass) Figure 7-32 - Figure 7-34 are introduced.

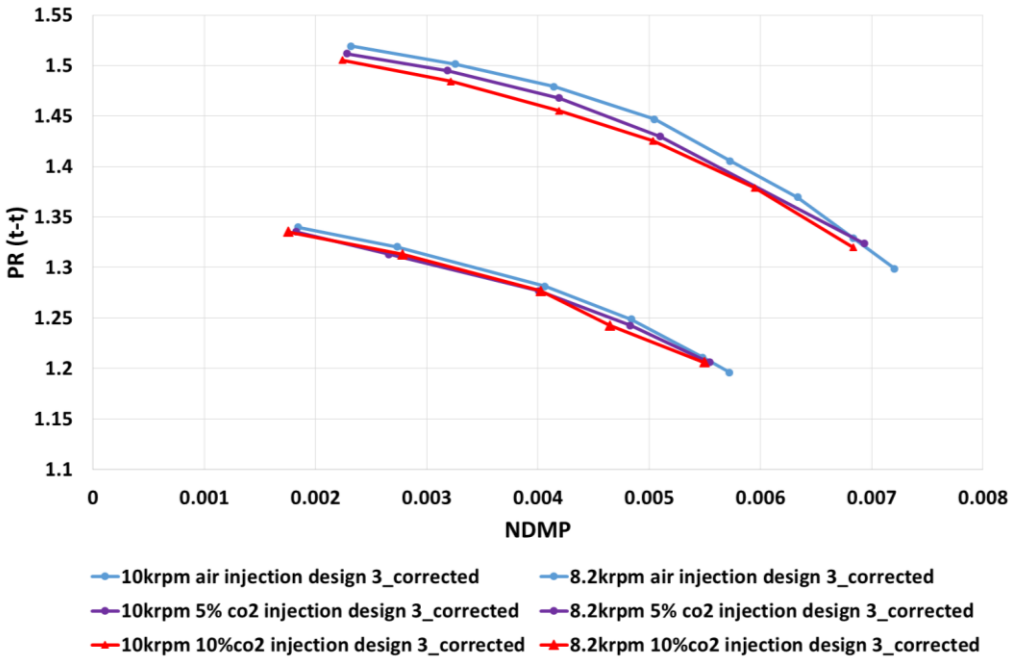

Figure 7-32. Pressure ratio vs. NDMP for various injected mixtures

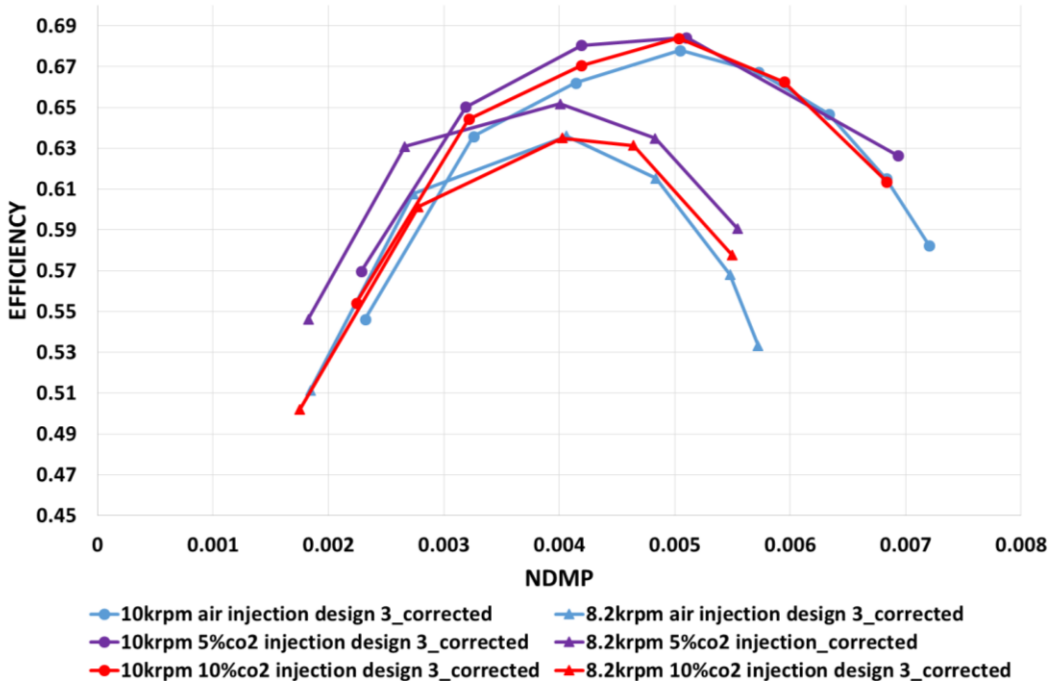

Figure 7-33. Efficiency vs. NDMP for various injected mixtures

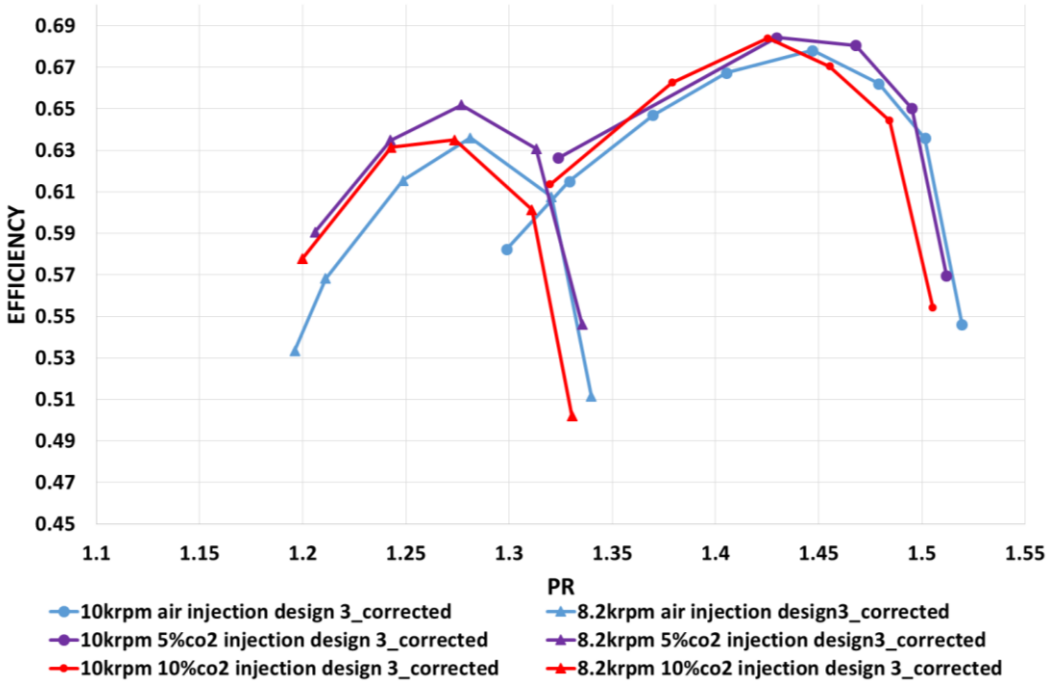

Figure 7-34. Efficiency vs. pressure ratio for various injected mixtures

Again, the reader is reminded that the mass ratio of the injected mixture and air drawn from the test cell has not been kept fixed at 25% due to the rotameter mass flow data correction. For the case where a mixture of 20% CO2 and 80% air was injected into the passage, the total mass ratio between the injected mixture and the mass of air in the other three passages varied between 15 and 21%. For the case where the mixture of 40% CO2 and 60% air the total mass ratio varied between 13 and 21%. In both situations the injected mass of the mixture of gases was always below the targeted value. Despite

this fact the overall mass of the injected CO2 was increased in the second case due the higher concentration of CO2 in bottle tank. Analysing Figure 7-32 it can be concluded that a minor pressure ratio degradation as well as a change in the choke flow is present if CO2 is introduced in the injected gas. A similar trend was observed in the homogeneous mixture tests. An interpretation of the efficiency change is more difficult (Figure 7-33, Figure 7-34). When only comparing the cases where air and 5% CO2 (averaged over total mass) is injected an efficiency rise is achieved for the latter. However this is different to the injection of the mixture containing higher concentration of CO2 (10% overaged over total mass). Analysing this case has highlighted a higher compressor outlet temperature which surely influenced the efficiency. The rise of the post compressor temperature might have been a result of the heat transfer from the turbine or an insufficient period to reach the thermal stability before the data was recorded.

The last objective of the non-homogeneous testing was to investigate the uncertainty of the compressor efficiency due to the so called hot strands of EGR gas. Such hot exhaust flows can occur in LP EGR systems despite the utilisation of EGR coolers. If the high temperature of the exhaust gas that mixes with the fresh air upstream of the compressor is unaccounted for then the both the corrected mass flow and corrected speed of the turbocharger are calculated incorrectly (both parameters are corrected for the compressor inlet temperature – Equation (16).

In this exercise two cases were compared:

1. Injected air at the temperature of 25°C
2. Injected air at the temperature of 55°C

In both cases the injection of air was realised into one of the four passages, whereas the temperature of air in the other three passages was maintained at 25°C. The injection temperature of 55°C was achieved with the use of the water-to-gas heat exchanger (heating liquid (water) was pumped at 90°C) as shown in Figure 7-35.

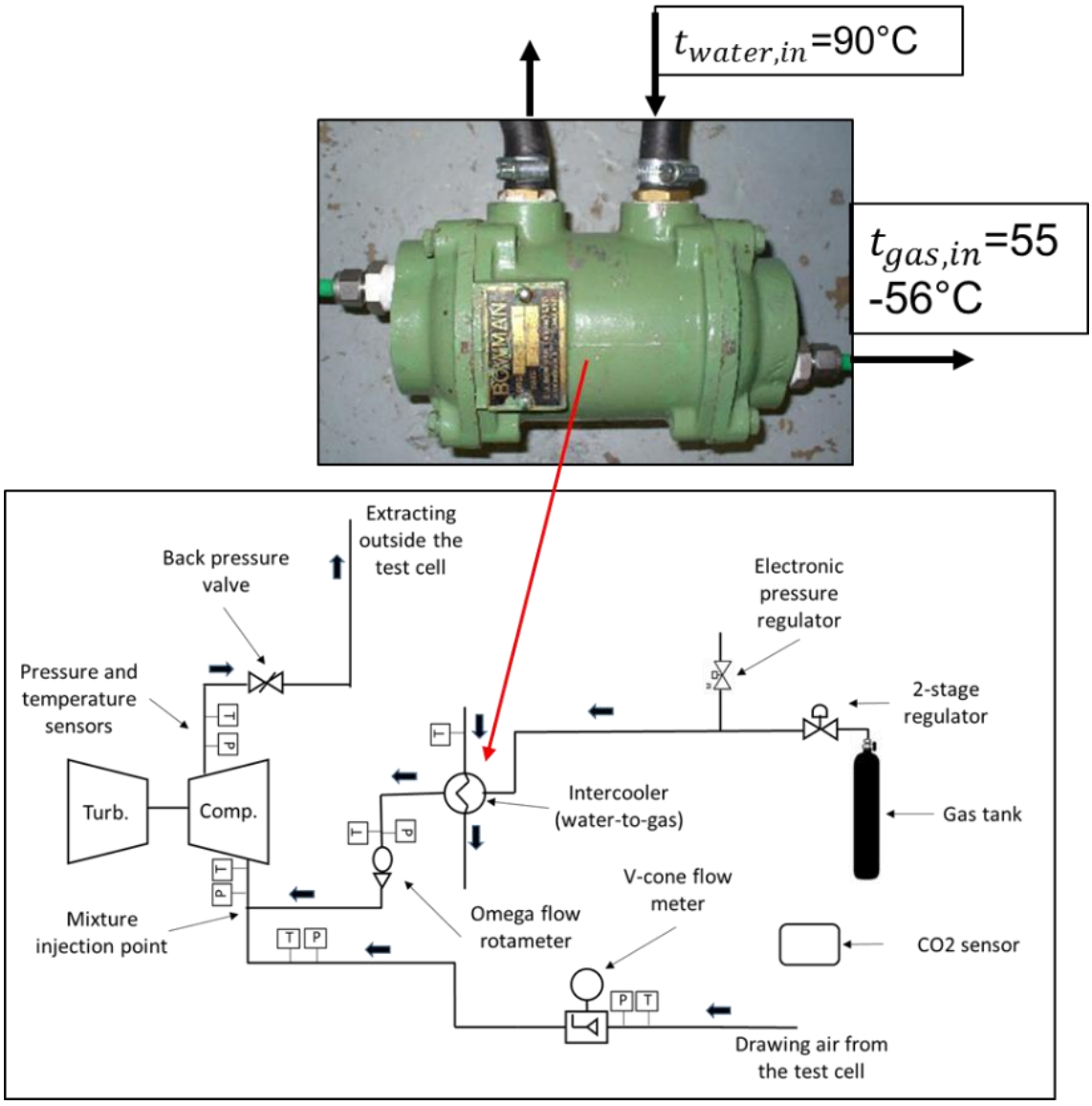

Figure 7-35. High temperature injection study

As achieved can be seen in the Figure 7-36 there is no difference in the pressure ratio between both tested cases. The efficiency curves are plotted in Figure 7-37, it can be noted that the highest efficiency is marked with the black solid line and it refers to the air injected gas at the temperature of 25°C. The efficiency is calculated for the temperatures measured at the gas stand standard measurement locations. The efficiency marked with the magenta line is the case of the injection of air at 55°C (gas within the other three passages is at the temperature of about 25°C). Efficiency is calculated the same way as the previous case therefore the efficiency drop is due to the outlet temperature rise (and unaccounted higher temperature at the compressor entry). The orange line reflects the case where the inlet temperature that is used in the efficiency calculation is a mass weighted average of injected air and air drawn from the test cell. As all three plotted efficiency lines are offset quite significantly it is concluded that when mixing the gases of various temperatures it is important to measure or calculate the temperature of such

mixtures otherwise errors are introduced which include the error in calculated efficiency and corrected speed of the turbocharger.

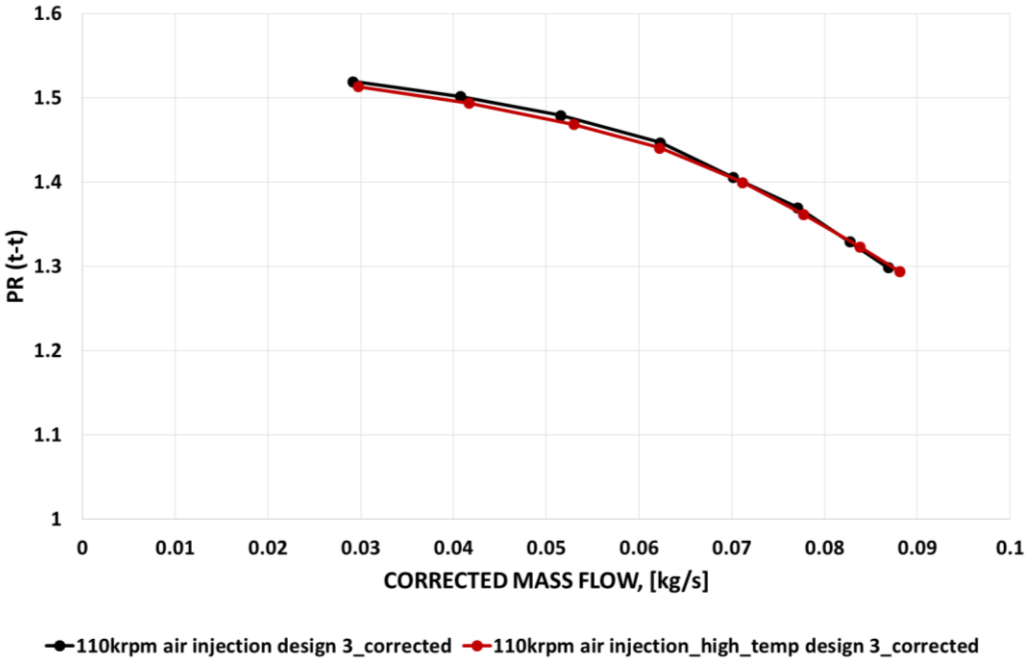

Figure 7-36. Pressure ratio vs. corrected mass flow for various temperatures of the injected air

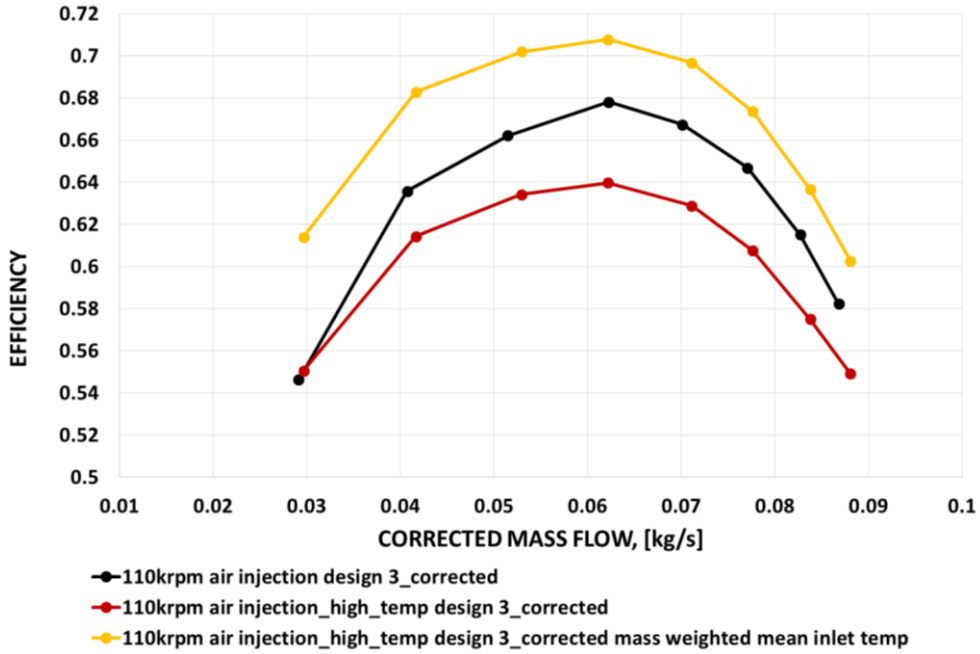

Figure 7-37. Efficiency vs. corrected mass flow for various temperatures of the injected air

7.6 Substitute gas – CFD results

The main intended outputs from the CFD simulations were:

- A comparison of compressor performance with homogeneous and non-homogeneous mixtures, independent of heat transfer.
- A validity check of the performance correction method proposed by Roberts and Sjolander.

The comparison of the experimentally measured and CFD predicted data achieved for air (the working medium) is presented in Figure 7-38 - Figure 7-40.

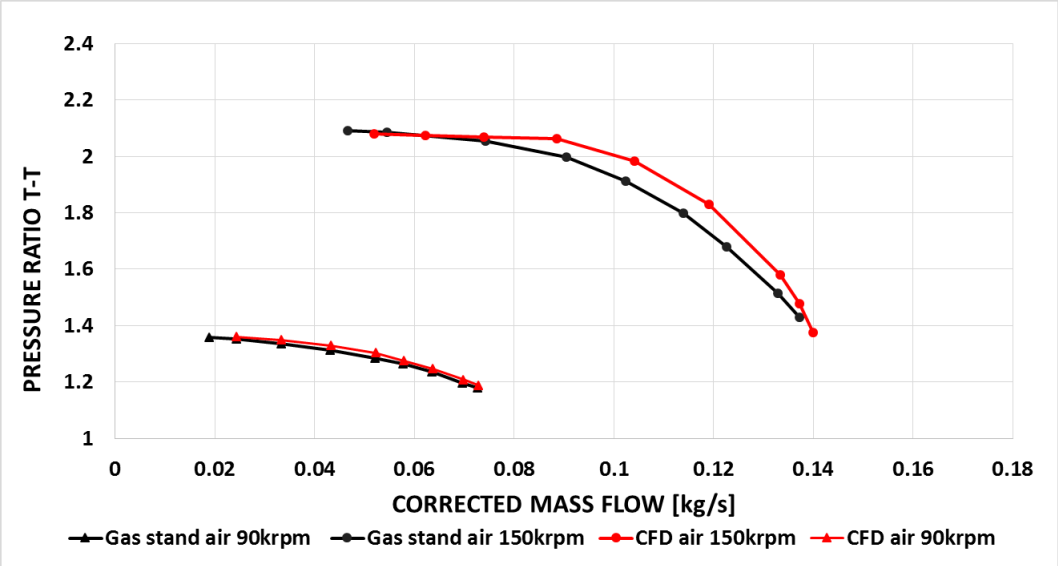

Figure 7-38. Gas stand measured and CFD predicted compressor operating points – plot 1

Overall very good fidelity between the measured and predicted pressure ratio is achieved at the lower corrected speed of 90 krpm. At the higher corrected speed of 150 krpm there is a small over-prediction of CFD in the region of higher mass flow rate. However, this difference reduces when moving towards the lower mass flow region of the speed line (Figure 7-38). There was no intention to find the surge line using CFD, the simulations were carried out (in the direction of low mass flow rates) until instabilities were picked up during the calculations.

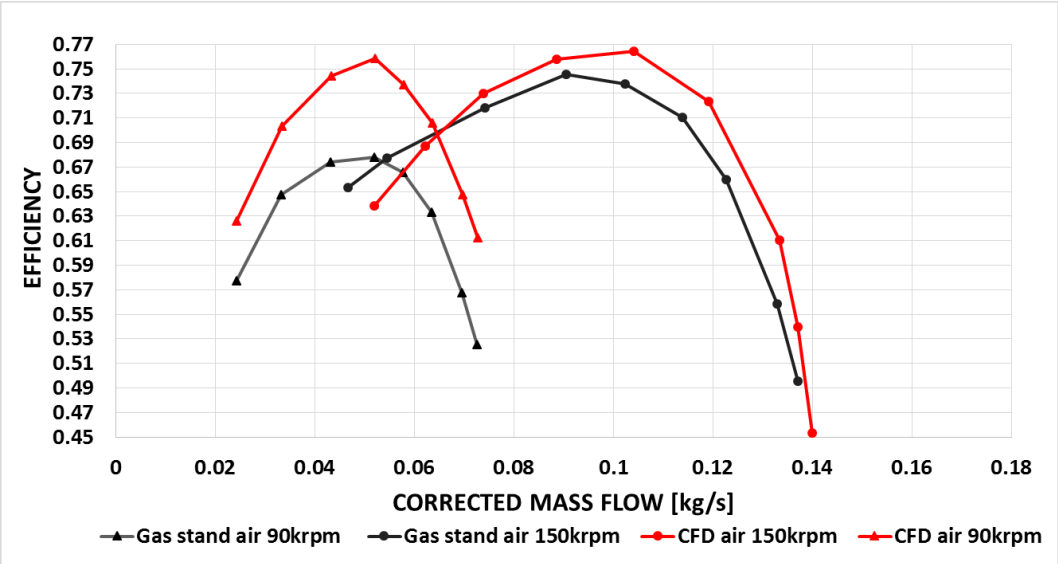

Figure 7-39. Gas stand measured and CFD predicted compressor operating points – plot 2

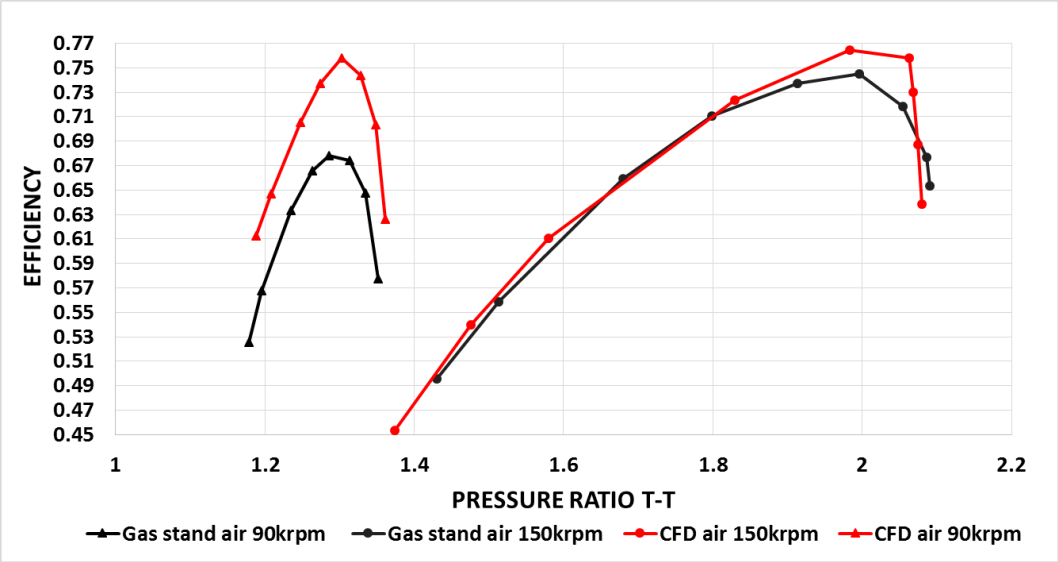

Figure 7-40. Gas stand measured and CFD predicted compressor operating points – plot 3

The CFD efficiency over-prediction (when compared with experiments) observed in Figure 7-39 and Figure 7-40 is as a result of adiabatic simulations (no conductive heat transfer from bearing housing and turbine, no convective gains or losses). In other words, the adiabatic CFD model relates to a case where the compressor is perfectly insulated whereas the experiments were carried out on the uninsulated turbocharger. In such a case at low turbocharger speeds the heat is transferred from the hot turbine and bearing housing into the gas passing through the compressor – the compressor outlet temperature rises and therefore the measured efficiency drops. At the higher speed line the offset between the measured and predicted efficiencies is smaller – the heat transfer between the turbine and the gas passing through the compressor is reduced (shorter residency of the gas, generally higher outlet gas temperature and therefore increased convection

losses). The heat transfer independent CFD analysis is promising from an efficiency comparison point of view when operating with substitute gas. The experiments carried out on the uninsulated turbomachinery showed that the efficiency of the compressor was higher when operated with CO2 at high non-dimensional speeds. That offset was smaller in the region of moderate non-dimensional speeds, whereas the efficiency of compressor operating with air was higher than for CO2 at the lowest non-dimensional compressor speeds (Figure 7-21 & Figure 7-22). This was not in the agreement with the findings that Roberts and Sjolander observed (efficiency for pure CO2 consistently higher than with air) however their compressor was insulated throughout the tests therefore much less exposed to heat transfer gains/losses. Now, comparing the results of the CFD simulations performed for homogeneous mixtures of gases - pure air and pure CO2 (Figure 7-41), it can be observed that:

- Similarly to experiments there is a pressure ratio drop/degradation when operating with CO2,
- The speed lines drawn for two tested gases cross each other indicating different choke flows,

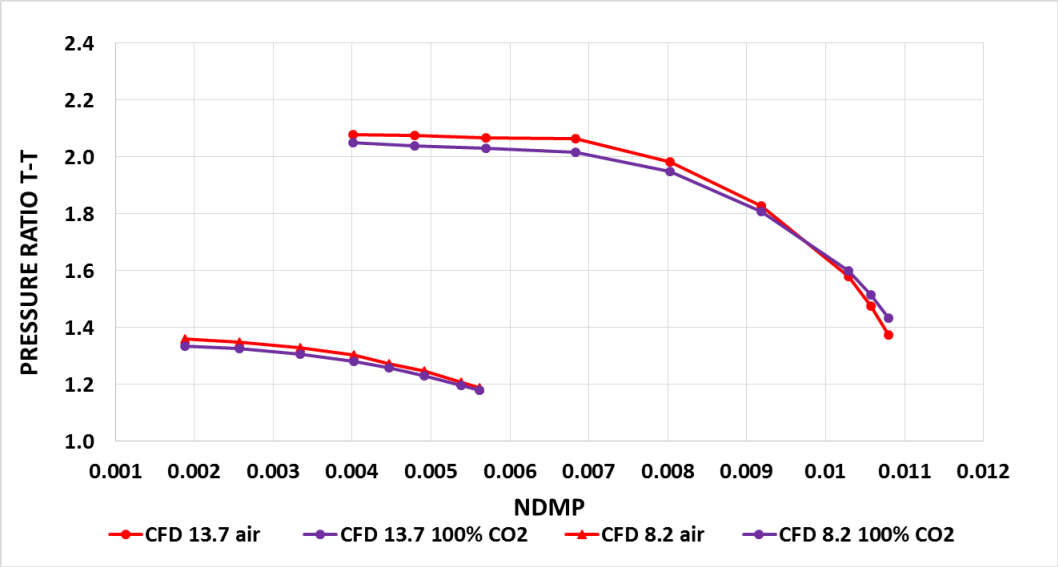

Figure 7-41. CFD calculated compressor performance with air and pure CO2 – plot 1

The efficiency comparison (Figure 7-42 & Figure 7-43) shows higher efficiencies with CO2 and assuming negligible effects from the Reynolds number change this is the effect of different ratio of specific heats. The trends are consistent with those observed by Roberts and Sjolander.

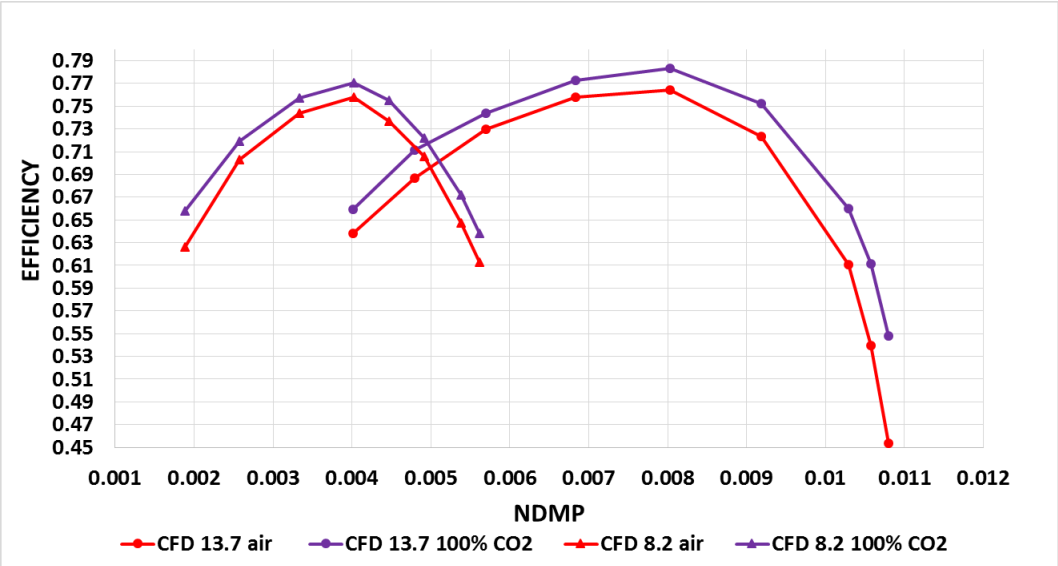

Figure 7-42. CFD calculated compressor performance with air and pure CO2 – plot 2

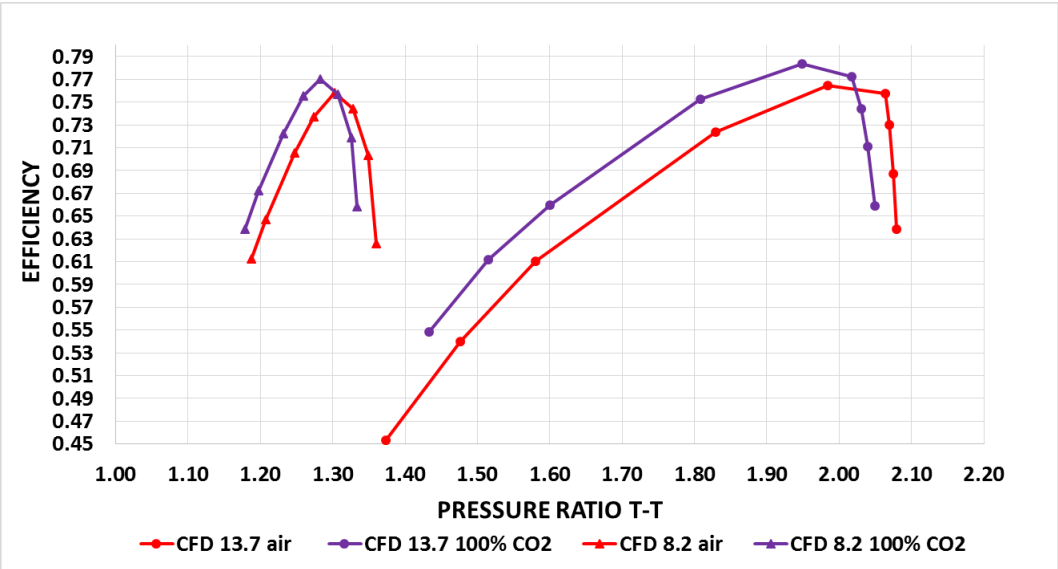

Figure 7-43. CFD calculated compressor performance with air and pure CO2 – plot 3

Using the data obtained when the compressor was operated with air (red solid lines) and substituting them into correction formulas (Equation (*87*), Equation (*88*)), the predicted compressor performance lines with pure CO2 are achieved (solid orange lines - Figure 7-44 - Figure 7-46). If these lines are now compared with the CFD predicted pressure ratio and efficiency with CO2 (purple solid lines) it can be concluded that good match has been achieved. The exception is the efficiency predicted at high flows at higher non-dimensional speed (Figure 7-45). Improving this can be achieved by taking into account that the choking occurs at different values for different working fluids (more details in [98]).

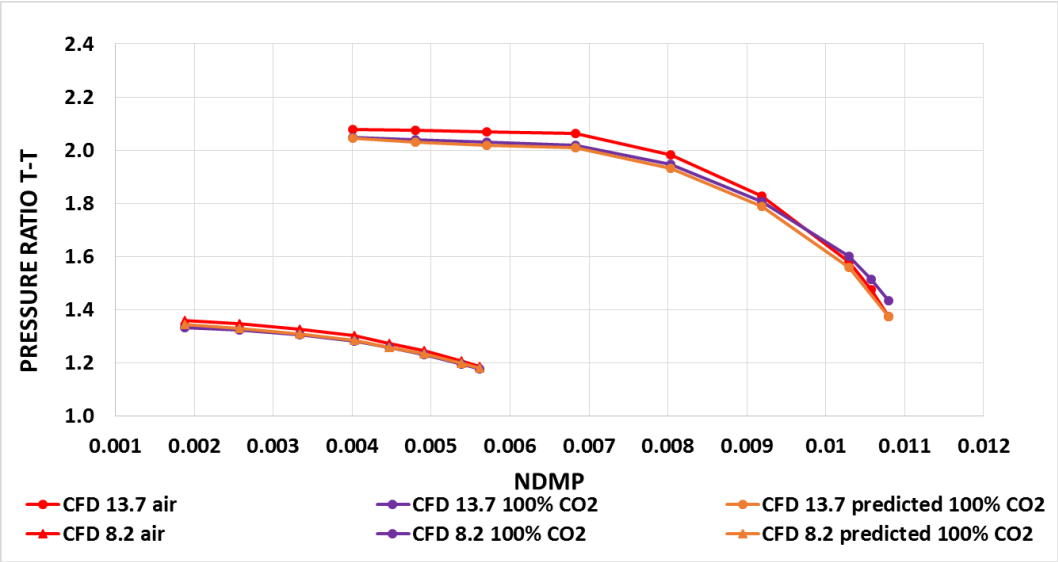

Figure 7-44. Pressure ratio vs. NDMP for air, CO2 (both CFD) and predicted for CO2

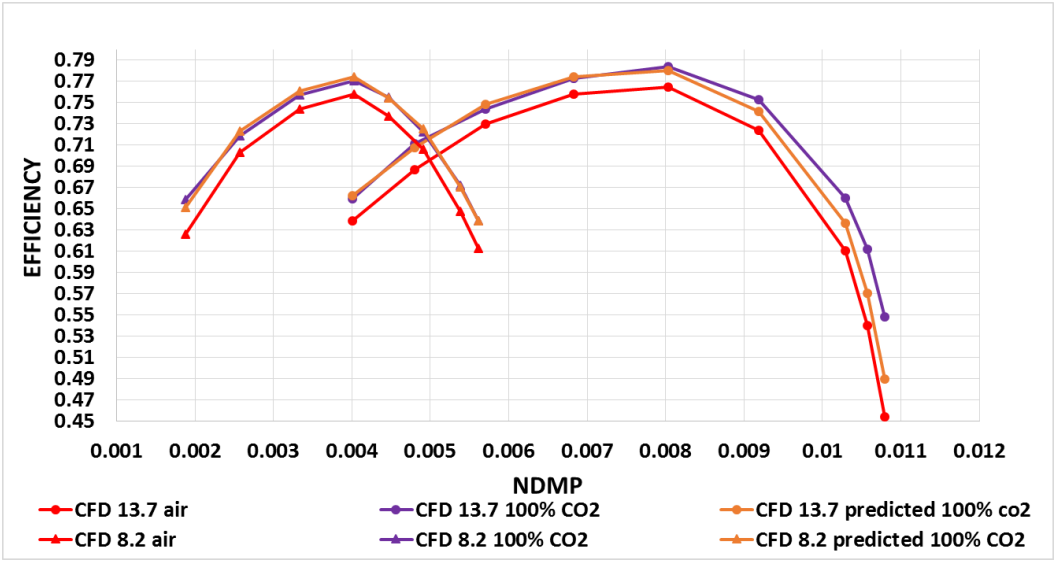

Figure 7-45. Efficiency vs. NDMP for air, CO2 (both CFD) and predicted for CO2 – plot 1

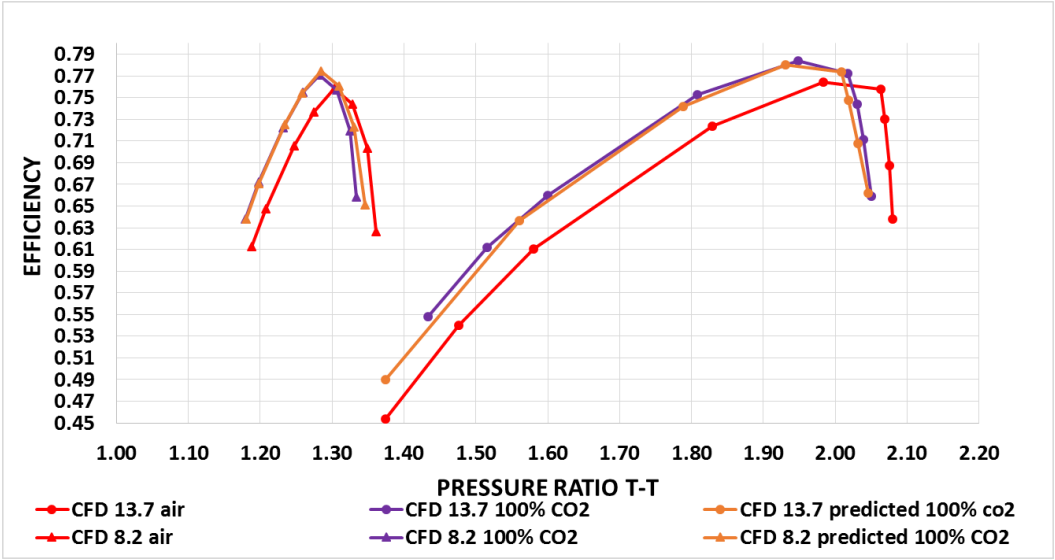

Figure 7-46. Efficiency vs. Pressure ratio for air, CO2 (both CFD) and predicted for CO2 – plot 2

Overall, based on the experiments and CFD calculations run for the homogeneous gases it can be concluded that the method proposed by Roberts and Sjolander for correcting compressor efficiency and pressure ratio when operating with CO2 works well and is applicable for the heat transfer independent performance maps. The efficiency predicted for CO2 did not match with the experimental measurements as the compressor was un-insulated in the testing campaign. The efficiency correction is improved if the n exponent varies with the speed of the turbocharger (in fact, it is heat transfer dependent however the rate of the heat transfer changes with the speed of the turbocharger).

The second question that could not be clearly answered based on the experiments is whether the non-homogeneous introduction of mixture of gases into the compressor changed the compressor performance compared to the homogeneous introduction of mixture of gases. As mentioned before, in the CFD model four equally divided passages with the infinitesimally thin walls between one another were introduced. Changing the fractions of gases in the mixture was applied at the model inlet planes (where also temperature, pressure, direction of the flow was given). The CFD calculations were carried out against the experiments were the injection of mixture of gases was realised into one of the passages whereas air was drawn through the other passages. The case under consideration is the non-homogeneous introduction of mixture of CO2 (10% of the overall mass of the gases at the compressor entry) and air (90% of the overall mass of the gases at the compressor entry). The mixture of CO2 and air was introduced into one of the passages and the overall mass fractions of the mixtures were distributed as shown in Figure 7-47.

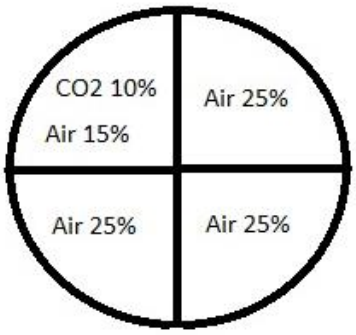

Figure 7-47. Overall mass fractions distribution at the model inlet plane

The non-homogeneous introduction of the gas at the compressor entry is shown in Figure 7-48.

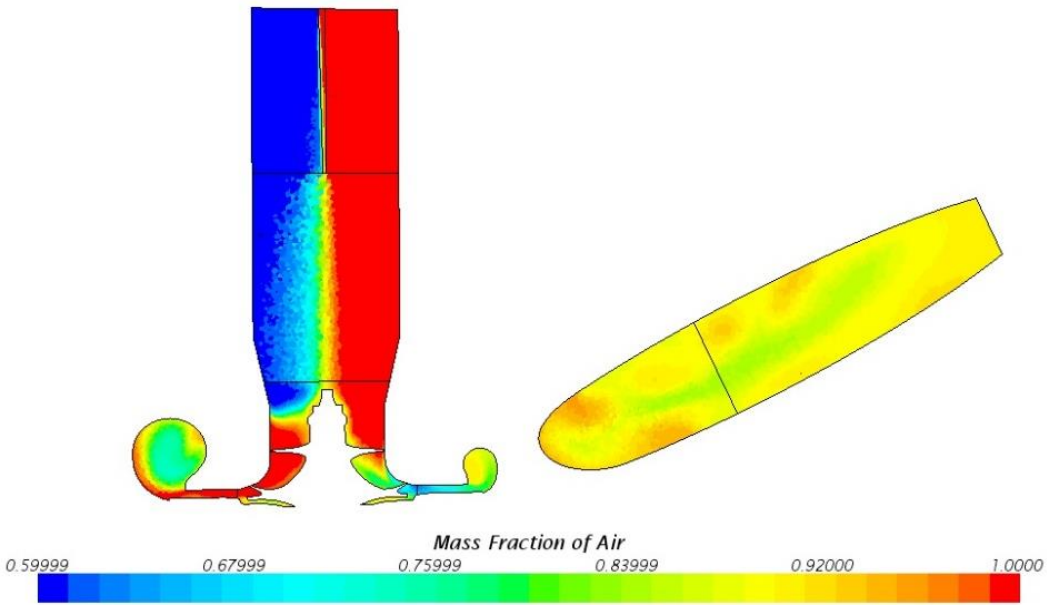

Figure 7-48. CFD model cross section – distribution of air

To compare the performance of the compressor due to the homogeneous and non-homogeneous gas introduction the following three plots are given.

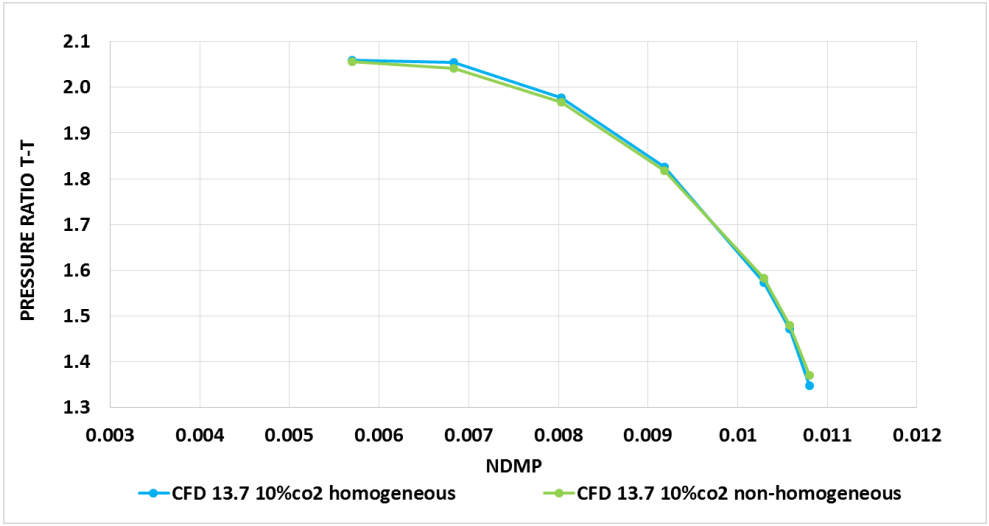

Figure 7-49. Compressor performance for homogeneous vs non-homogeneous gas introduction at the non-dimensional speed of 13.7 – plot 1

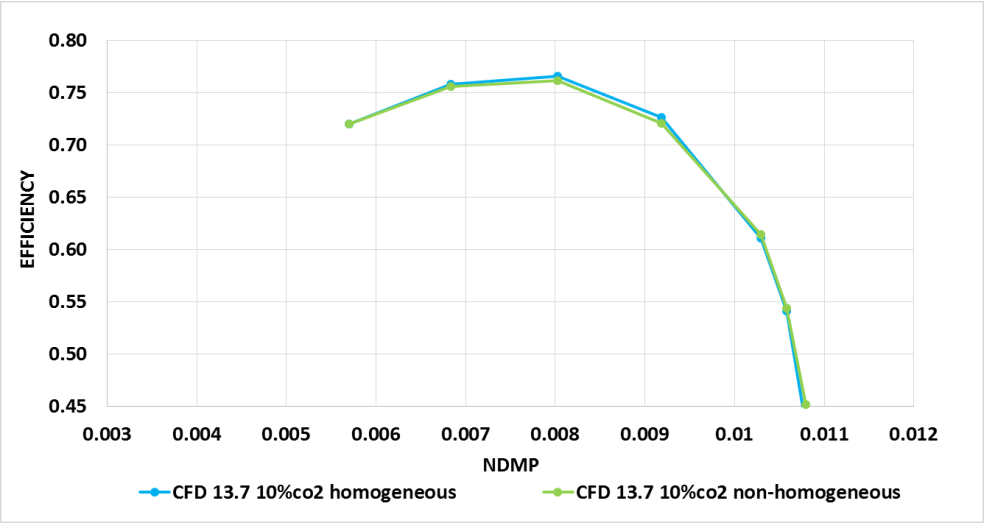

Figure 7-50. Compressor performance for homogeneous vs non-homogeneous gas introduction at the non-dimensional speed of 13.7 – plot 2

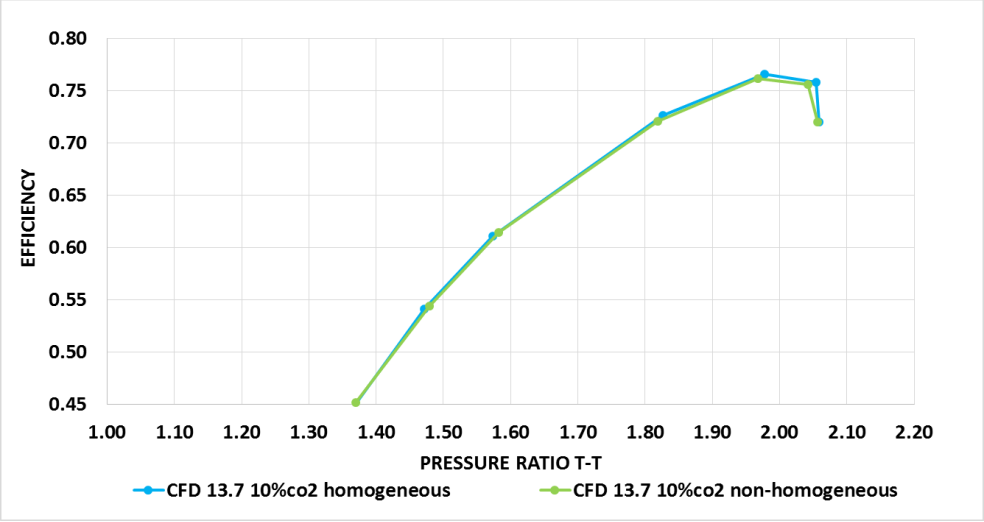

Figure 7-51. Compressor performance for homogeneous vs non-homogeneous gas introduction at the non-dimensional speed of 13.7 – plot 3

It is very clear that there is no significant compressor performance change at the given gas concentration at this compressor speed line.

7.7 Aerodynamic effects of the compressor intake duct combined with an EGR mixing valve

Apart from the study on the effects of fluid properties on the turbocharger compressor performance (homogeneous and non-homogeneous mixtures at the compressor inlet) a selected industrially available mixing valve has been investigated in various compressor gas delivery configurations. The purpose of this work is to understand how the tested configurations affect the performance of the turbocharger compressor. Throughout the undertaken tests, cold air was used for both mixed streams therefore the resultant compressor performance changes are due to the occurring aerodynamic processes.

7.7.1 Introduction and procedures

This experimental investigation focuses on various effects of LP EGR system arrangements on the turbocharger compressor performance. The LP EGR mixing valve (also known as LP EGR combination valve) is a valve that mixes two streams of gases – an exhaust gas and fresh air prior to the compressor entry (Figure 7-52). The photo of the valve used in this study is shown in Figure 7-53.

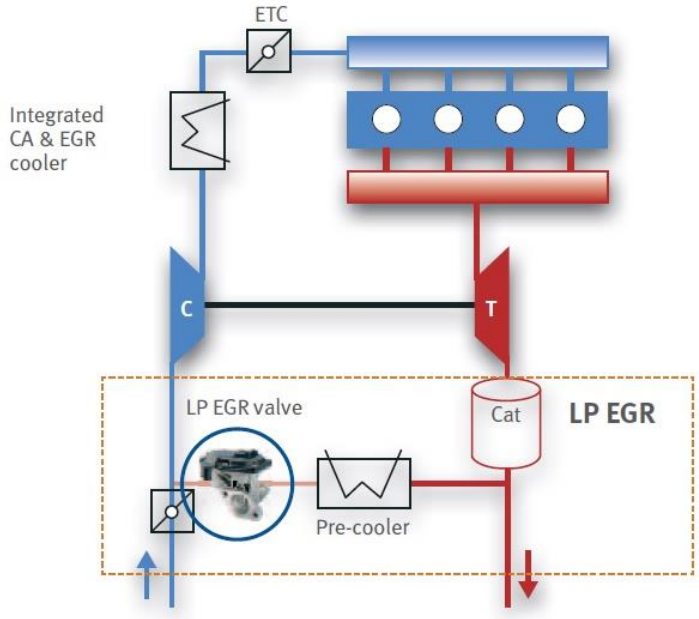

Figure 7-52. Typical location of LP EGR valve on a petrol engine [8]

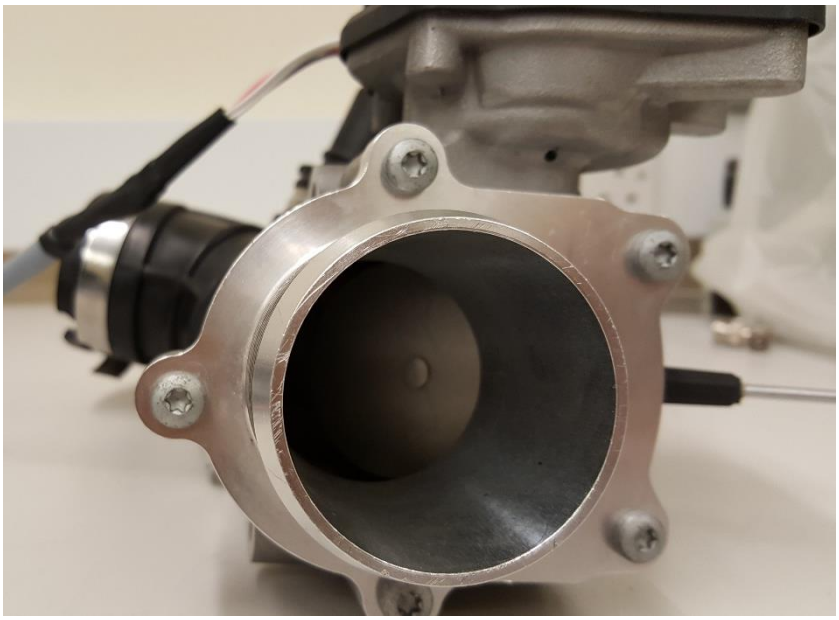

Figure 7-53. EGR mixing valve used in the study

Due to the packaging constraints very often compressor intake systems are equipped with a bend located prior to compressor entry. For the same reason, in this particular

configuration a 90 degree bend is fitted downstream from the valve and prior to the compressor inducer. Additionally, in order to improve the surge margin of the compressor, a fixed geometry inlet guide vane (IGV) has been fitted directly after the EGR valve. The tested turbocharger was manufactured by Honeywell Turbo Technologies (HTT) and it works on small, downsized diesel engines. There were five different cases mapped in order to distinguish between the aerodynamic effects of the 90 degree bend, IGV and the mixing valve respectively. Four of these cases included different geometry configurations (Figure 7-54 - Figure 7-57) whereas the last case tested included various valve openings. All the mapping work was performed in the cold flow turbine conditions, both the turbine and compressor were insulated as much as possible to reduce the heat transfer effects on the compressor efficiency. The compressor surge onset was judged by the rig operator based on the audible noise and oscillations of the pressure signal. The thermal stability between the subsequent operating points was gained between five and twelve minutes (depending on the turbocharger speed), oil temperature was maintained at a temperature range between 70°C and 80°C. Finally, the maximum tolerance for the turbocharger speed oscillations was ±200 rpm. The comparison begun with generating the compressor performance map for the first case (Figure 7-54), which comprised the straight inlet duct upstream from the compressor inlet. This case reflects a typical industrial gas stand arrangement for the compressor mapping activities. For this reason, the compressor performance characteristic generated for the “straight duct” case was treated as a baseline and then compared with all other cases.

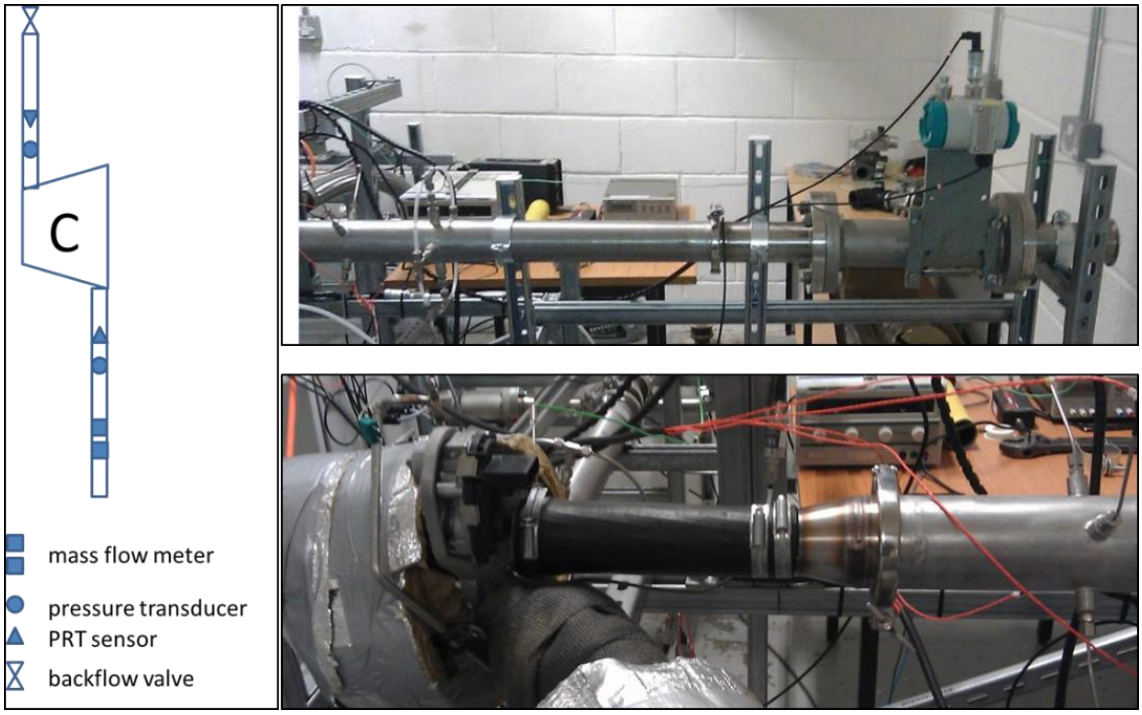

Figure 7-54. “Straight inlet duct” configuration

The complexity of the model was increased in the second case (Figure 7-55) where a 90 degree bend and a mixing valve were added. In this case the valve was fully shut (on the “exhaust” gas leg) during the mapping process therefore its effect on the map was expected to be negligible.

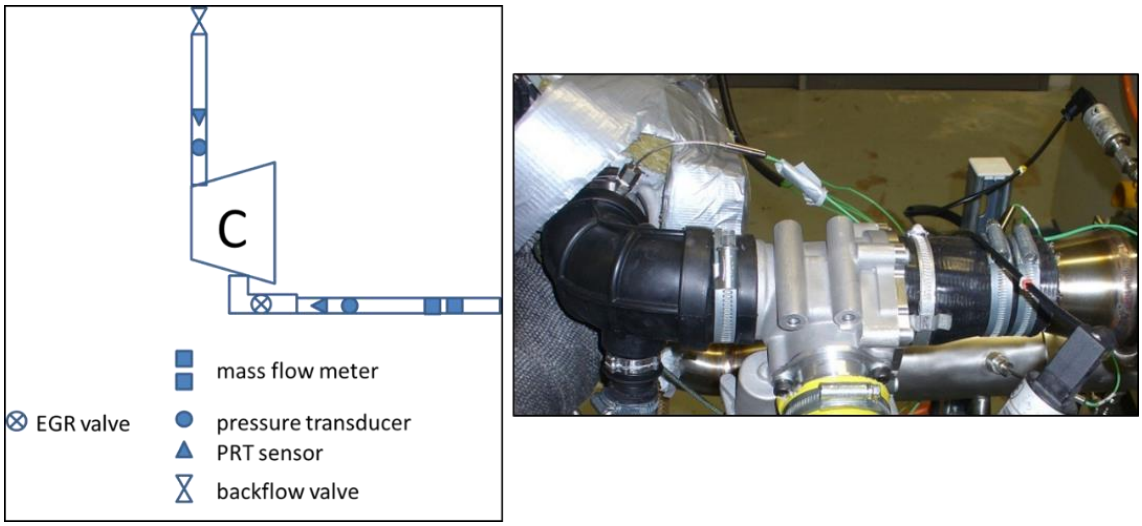

Figure 7-55. “90 degree bend” configuration

In order to increase the surge margin an IGV has been added in the case 3 (Figure 7-56). The IGV’s vanes are distributed circumferentially and create positive swirl (same direction of rotation as the compressor’s impeller). For more details of operation of such devices the author sends the reader to the “Off-design surge suppression and performance enhancement methods” section contained within the literature review of this report.

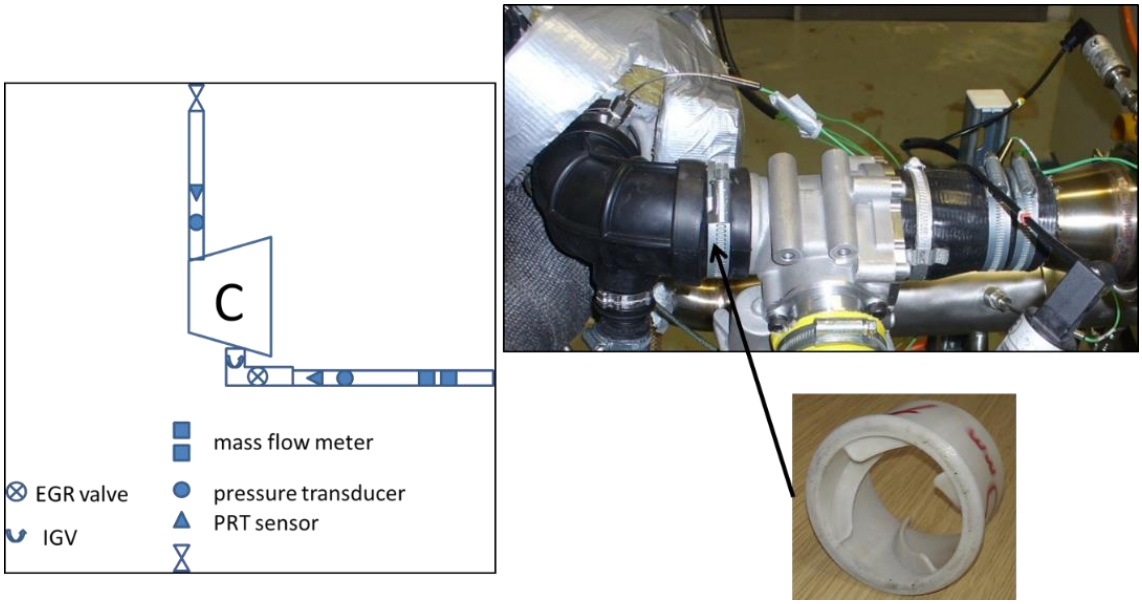

Figure 7-56. “90 degree bend + IGV” configuration

Finally, in the last two cases the mixing valve was partially open (Figure 7-57) to introduce the mixing of the two air flows. These two cases reflect the operation of LP EGR valve where the compressor fresh air drawn via the intake duct is mixed with the cooled

EGR flow re-directed towards the valve from downstream of the turbine. Surely, the composition of gases within the mixture would be different in the real case scenario (exhaust gas) but as mentioned before only aerodynamic effects are of interest in this exercise. In these two cases the valve was set open to maintain the specific ratios of the secondary corrected EGR mass flow rate and total corrected mass flow flowing through the compressor. These were 10% and 30% respectively.

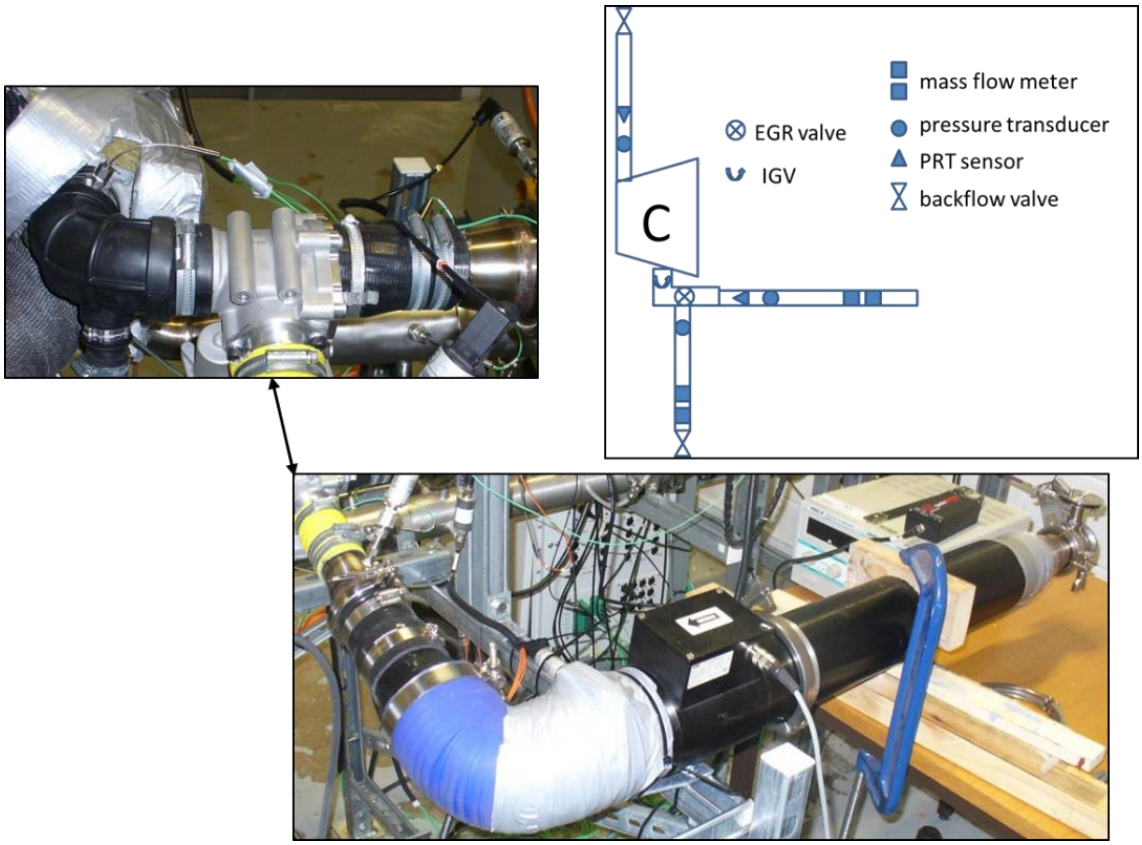

Figure 7-57. “90 degree bend + IGV + EGR” configuration

In order to maintain the required ratios of both main and secondary flows at a constant value, manual adjustment of the mixing valve and an automatic adjustment of the butterfly valve fitted on the secondary flow branch were required. The secondary EGR mass flow rate was measured by an ABB Sensyflow mass flow meter and corrected to the inlet temperature and pressure.

7.7.2 Results

The first pair of the compared compressor maps were those generated for the “straight inlet” and “90 degree bend” configurations (Figure 7-58, Figure 7-59, Figure 7-60). Surprisingly, the configuration comprising the 90° bend turned out to be more beneficial on the left hand side of the map – due to a greater surge margin (Figure 7-58) despite the efficiency drop (Figure 7-59, Figure 7-60). The number of efficiency lines has been reduced to avoid the overpopulation of plots (all lines shown similar trends).

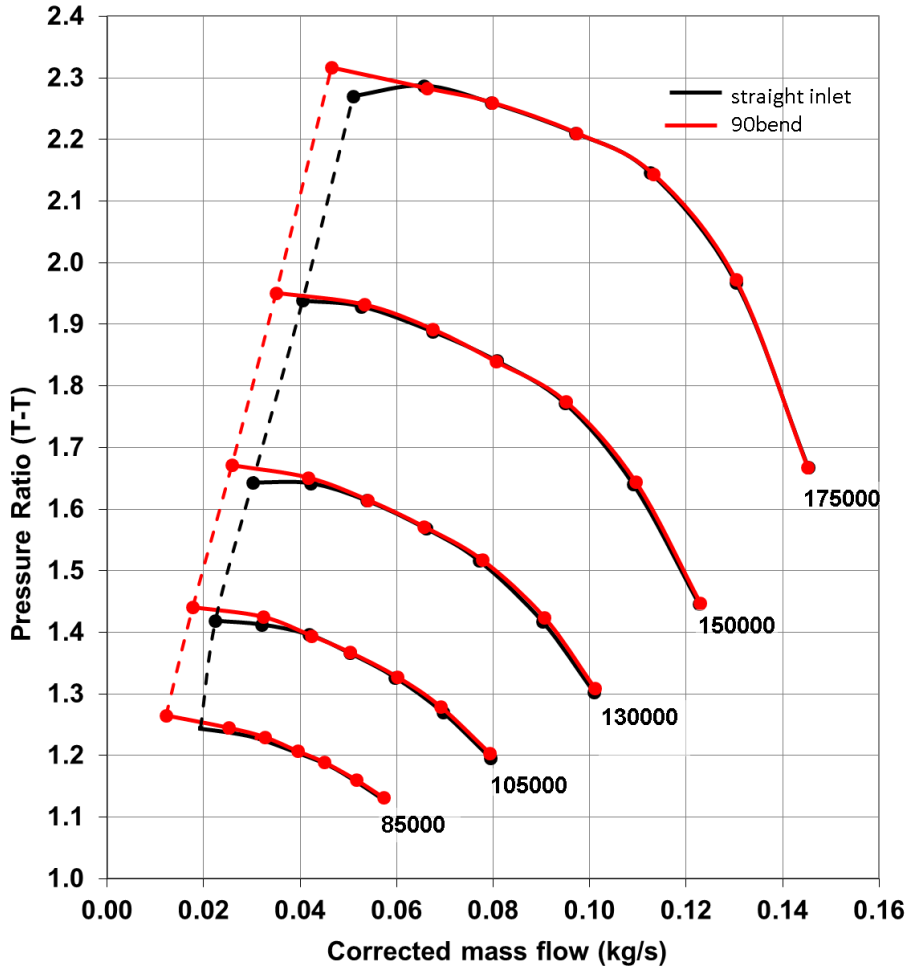

Figure 7-58. Pressure ratio vs. corrected mass flow for “Straight inlet” and “90 degree bend” configurations

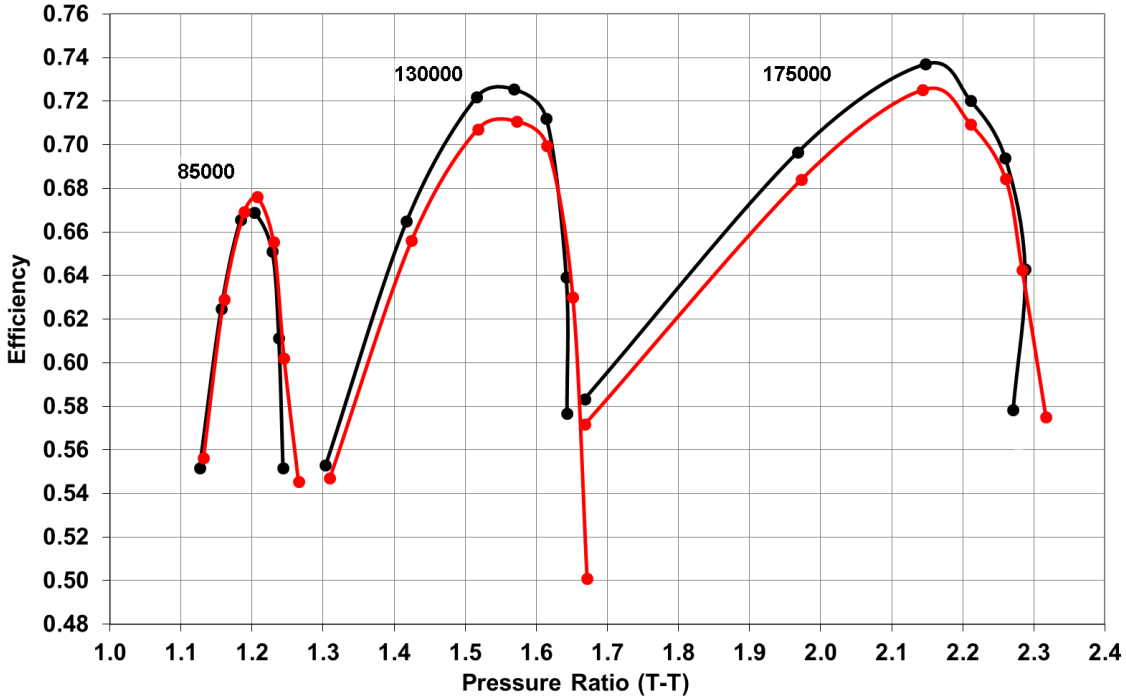

Figure 7-59. Efficiency vs. pressure ratio for “Straight inlet” and “90 degree bend” configurations

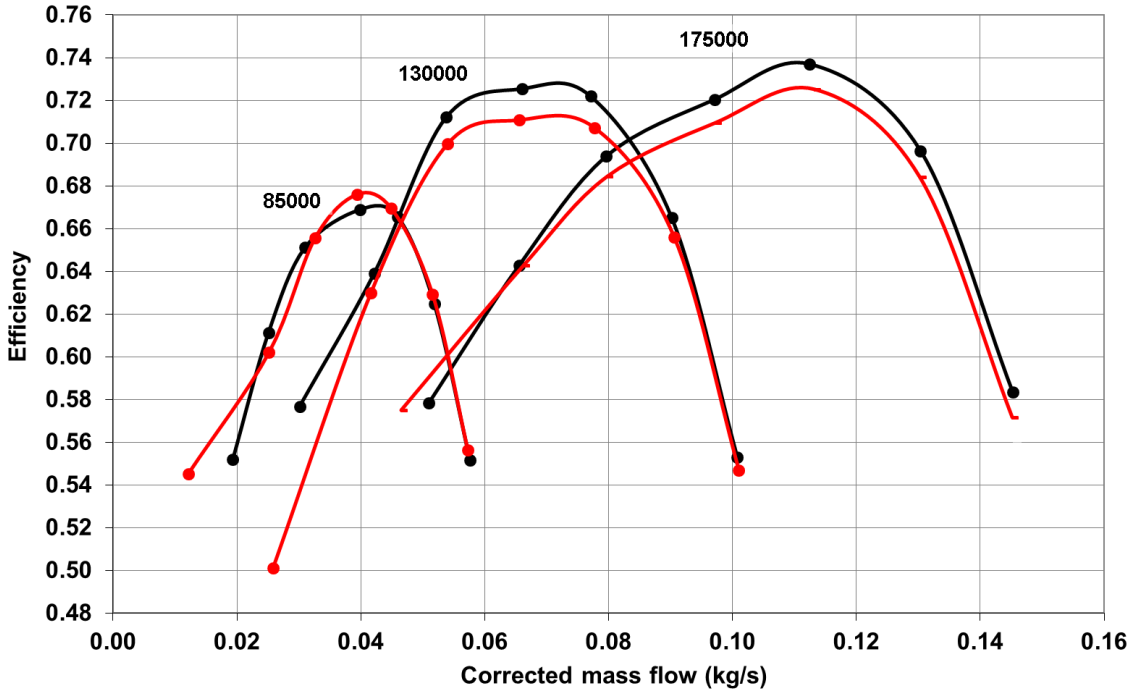

Figure 7-60. Efficiency vs. corrected mass flow for “Straight inlet” and “90 degree bend” configurations

The greater surge margin observed for the “90 degree bend” configuration is surprising as the results obtained here in this exercise do not comply with the trends found in the literature. However, it has to be noted that replacement of the part of the straight section by 90 degree bend is not the only geometrical/aerodynamic difference between both considered cases (fully shut mixing valve included only in the “90 degree bend” configuration). This would suggest that the effect of the surge margin increment for the latter case resulted from a combination of the valve and 90 degree bend. The next step in the investigation study was adding a production swirl conditioner by fitting it at the outlet part of the mixing valve, prior to 90 degree bend. The compressor performance map generated for this case revealed slightly larger surge margin at a turbo speed of 130 krpm and above (Figure 7-61). At speeds lower than 130 krpm there is no significant difference in the surge margin for the compared cases. Another consequence resulting from the installation of the pre-swirl device is that at all tested speeds a degradation of pressure ratio at the right hand side of the map. In other words, the width of the map with acceptable values of efficiency has been narrowed (Figure 7-61, Figure 7-62 and Figure 7-63).

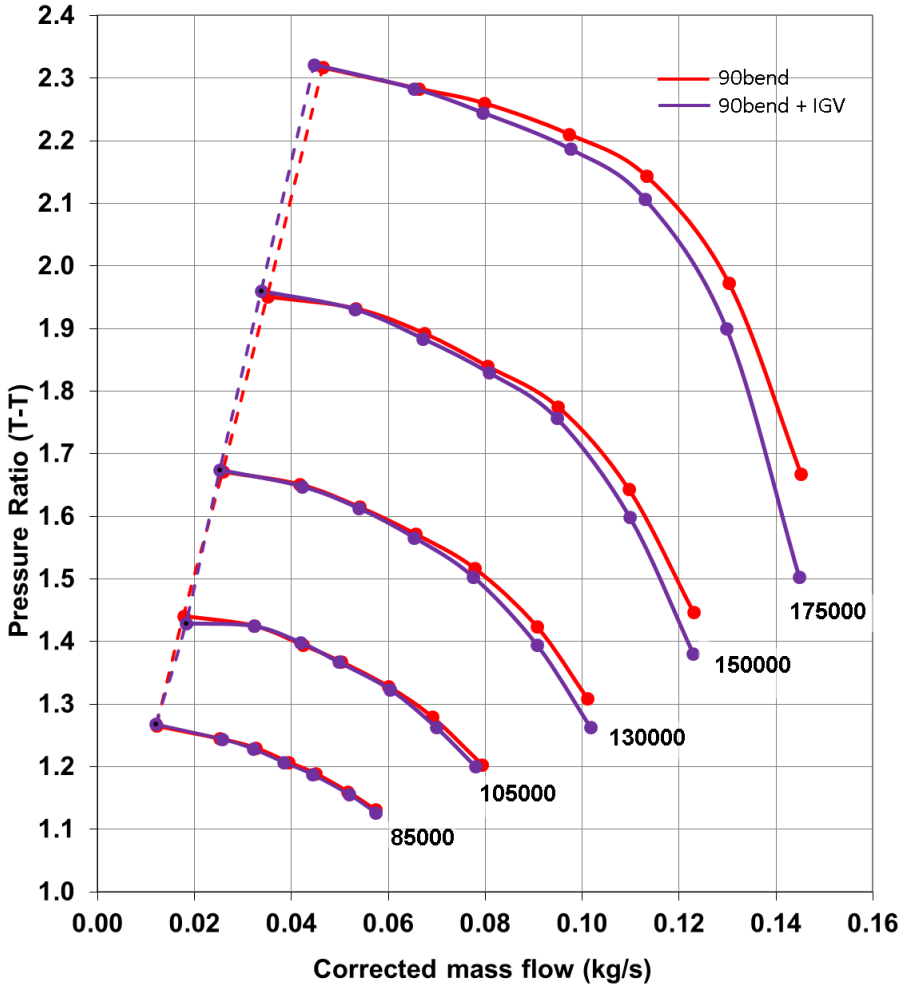

Figure 7-61. Pressure ratio vs corrected mass flow for “90 degree bend” and “90 degree bend + IGV” configurations

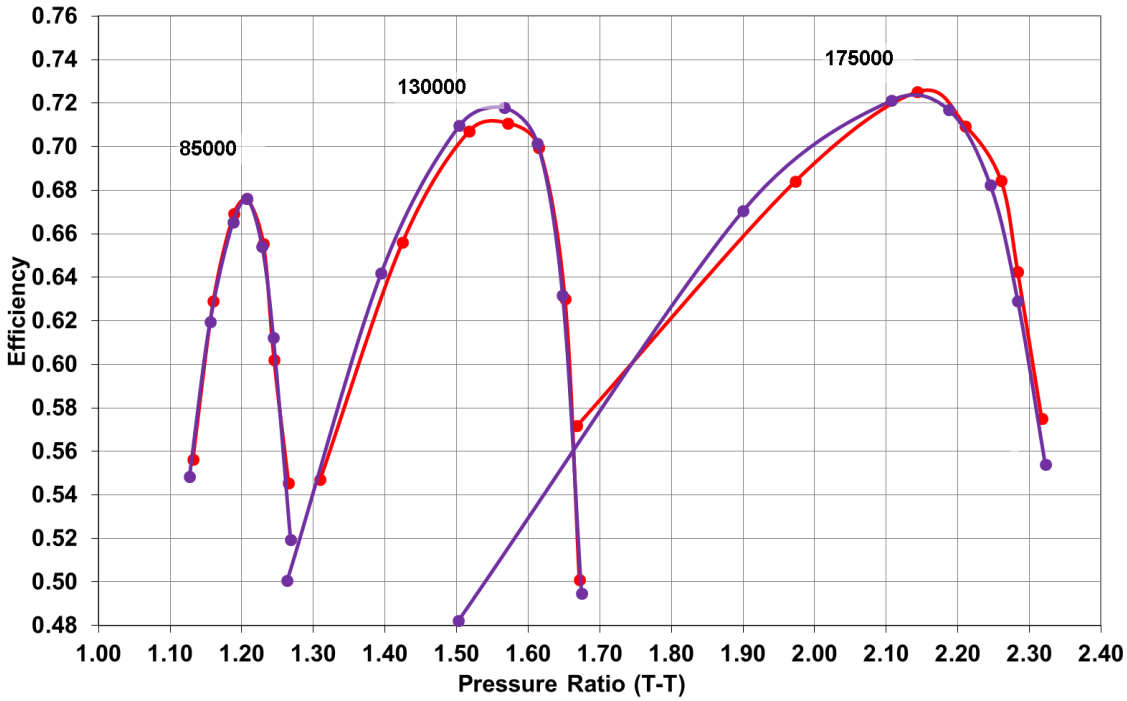

Figure 7-62. Efficiency vs. pressure ratio for “90 degree bend” and “90 degree bend + IGV” configurations

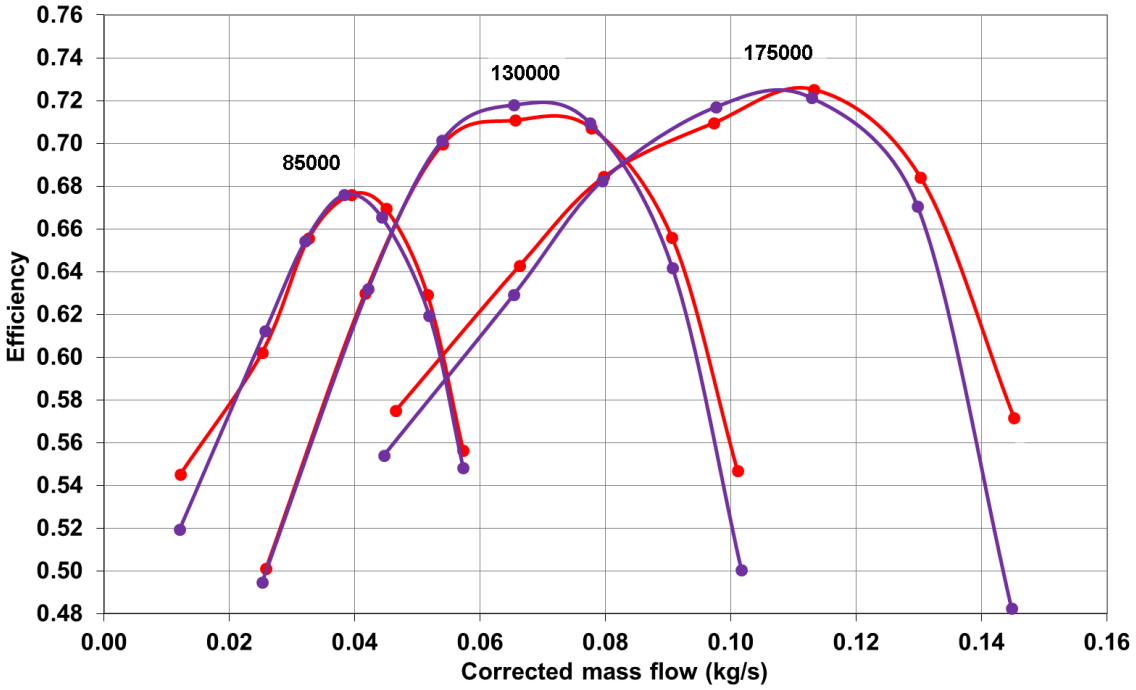

Figure 7-63. Efficiency vs. corrected mass flow for “90 degree bend” and “90 degree bend + IGV” configurations

The last objective in this mapping exercise was to compare the compressor performance maps obtained at various openings of the EGR valve (and therefore various rates of the mass flow rate of the mixed gas streams). To do so, two additional cases were investigated. The gate of the valve was fixed at a certain position during the mapping of each case - the corrected mass flow throughout the EGR valve equalled 10% and 30% of the total corrected mass flow throughout the compressor, respectively. In this way the real magnitude of the EGR flow could be targeted. The results show no negative effects of the surge onset caused by various openings of the valve – all three generated surge lines overlap (Figure 7-64). However, opening of the EGR valve has a detrimental effect on total-total pressure ratio. The wider the opening the larger degradation of the pressure ratio. This is very important from the turbocharger – engine matching perspective as the degradation of the pressure ratio badly affects the efficiency (Figure 7-65) of the compression process and narrows the operating range.

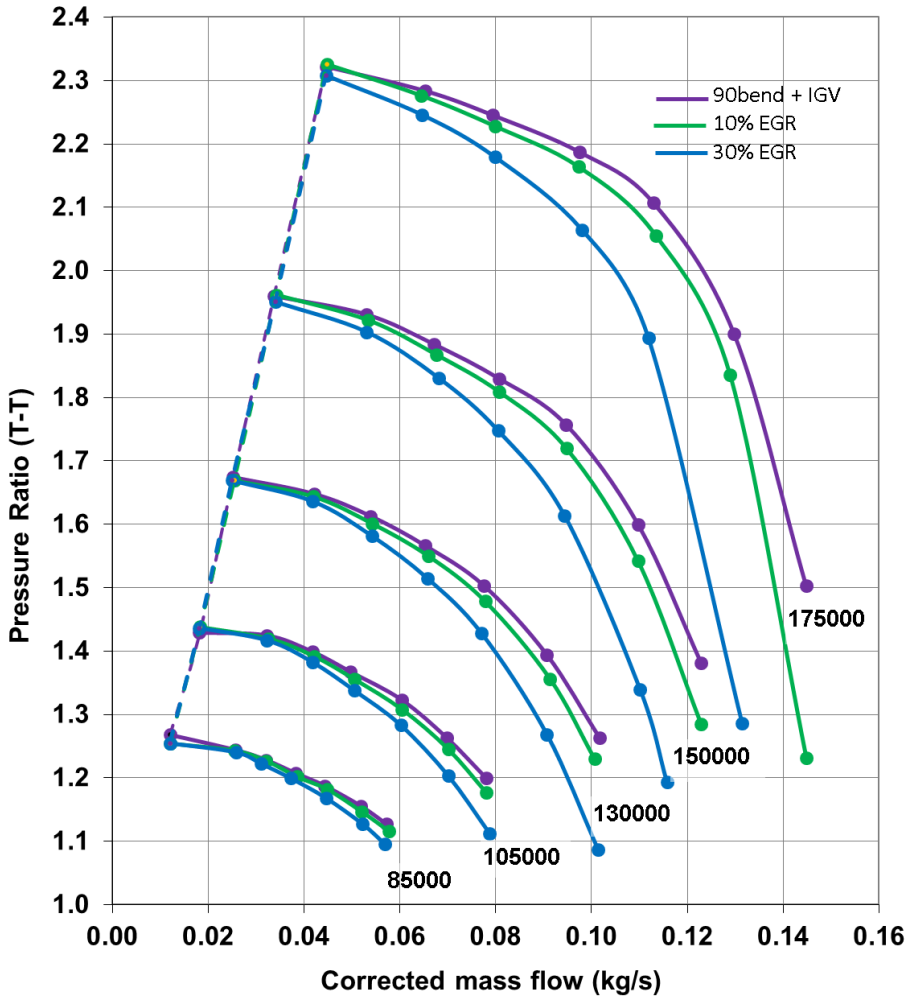

Figure 7-64. Pressure ratio vs. corrected mass flow for “90 degree bend + IGV”, “10% EGR” and “30% EGR” configurations

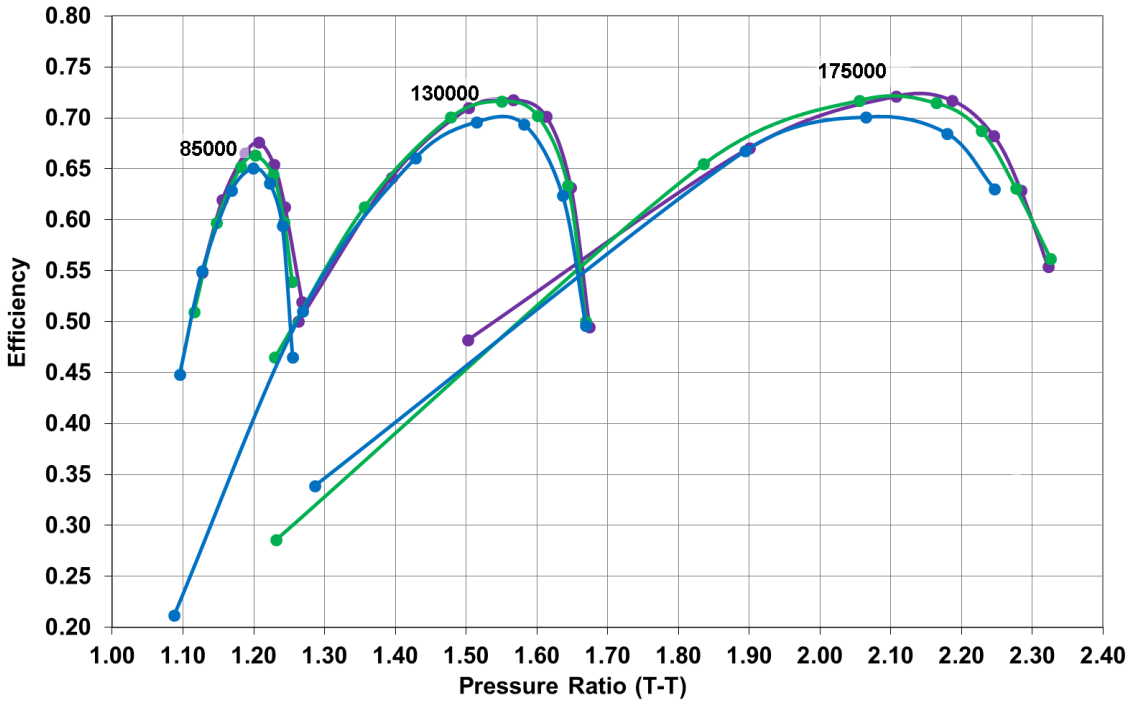

Figure 7-65. Efficiency vs pressure ratio for “90 degree bend + IGV”, “10% EGR” and “30% EGR” configurations

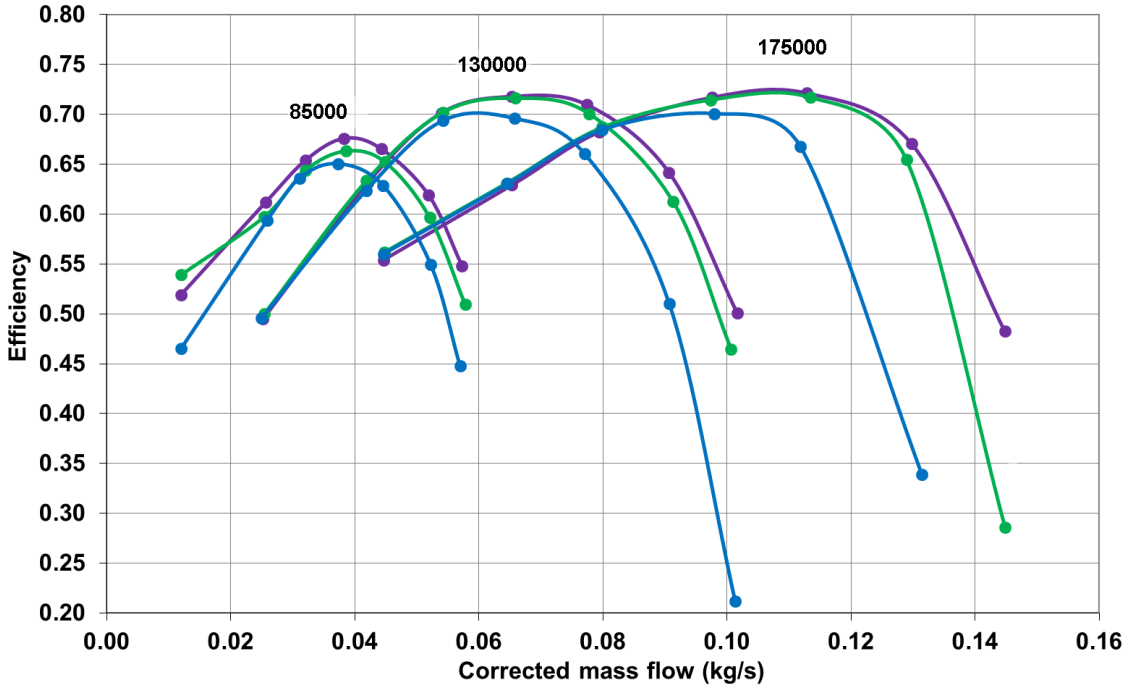

Figure 7-66. Efficiency vs. corrected mass flow vs for “90 degree bend + IGV”, “10% EGR” and “30% EGR” configurations

8. Summary and conclusions

Driven by the thesis objectives the following work has been accomplished:

- The development of a steady-state flow turbocharger gas stand.

  The author has made a significant contribution towards the design, installation and controllability of the rig and made sure it complied with the relevant SAE and ASME codes of practise. For the purpose of the experimental surge investigation the rig has been instrumented accordingly. Closed-loop compressor module has been developed in order to investigate on the effects of variable fluid properties on the turbocharger compressor performance (homogeneous mixtures). The rig was also modified accordingly to allow for the injection of mixtures prior to the compressor entry (non-homogenous gas) and study of various combinations of compressor intake pipes and EGR valve.

- Uncertainty analysis of a generated turbocharger performance map.

  This part of work has been performed in two stages. Stage 1 included the type-B uncertainty analysis and was based on single-sample measurements and sensor accuracy whereas in the second part of an investigation heat transfer effects on the performance uncertainty has been carried out. Also, as a part of the turbocharger heat transfer model development 3D CHT simulations have been performed.

- Experimental study of the surge development.

  In the first phase of the investigation based on the small size compressor, the analysis of the pressure data obtained at various locations (pre- and post-compressor), and temperature at the compressor entry was performed, along with the comparison of the available surge metrics. In the second phase of the study the surge development was compared for two compressors (different size) tested at steady-state conditions plus a comparison of surge development in steady-state and pulsating flow (on engine gas stand) conditions (same compressor).

- Experimental and numerical study of variable fluid properties on the turbocharger compressor performance.

  Three various composition air-CO2 mixtures along with pure air and pure CO2 were included in the investigation. Cases of homogeneous and non-homogeneous gas distribution at the compressor entry were taken into account. Also, the effects of the hot EGR strands on the compressor performance were looked at. Finally, experimental investigation of the developed flow regimes (resulting from a number of intake duct and EGR valve combinations) on the turbocharger compressor performance was conducted.

The overall conclusions are listed based on the three core parts of the thesis, namely the uncertainty analysis of the turbocharger performance map, compressor surge development study and investigation of variable fluid properties and developed flow fields on the compressor performance map.

1. Uncertainty analysis of the turbocharger performance map.

The assessment of the quality of the generated turbocharger performance maps was performed to answer the two leading questions. Namely, what is the uncertainty of the calculated performance parameters for both the turbine and compressor based on the chosen sensors? What is the heat transfer effect on the uncertainty of the compressor performance? Although both of the above closely address the uncertainty of turbocharger performance maps yet they are very different in terms of the approach. While the first method is based on the assumption of perfect sensor installation (no random or systematic errors considered) and only looks into a propagation of measurement errors, the second one, in fact, informs about the weaknesses of the current way of experimental characterisation of turbocharger performance (measured efficiency based on the work and heat transfer). The device error based uncertainty analysis was conducted for the following performance parameters: turbocharger corrected speed; corrected mass flow, pressure ratio, and efficiency for both compressor and turbine. Additionally, in order to find the dominant sources of pressure ratio and efficiency uncertainties, the latter two were broken down to the relevant measured quantities.

The uncertainty of the turbocharger corrected speed is affected by two variables and these are the speed measurement error and uncertainty of the temperature measurement. The uncertainty of the rotational speed measurement is very important as it indirectly affects the measurement of pressure ratio and compressor efficiency. However, the modern speed sensor kits used in the turbocharger industry offer measurements of high accuracy (if correctly installed) and therefore this uncertainty is not of a primary concern.

The uncertainty of the mass flow measurements was generally low (high certainty) on both the compressor and turbine side of the turbocharger, slightly dropping in the region of low mass flows (higher uncertainty of differential pressure measurement). The uncertainty of the turbine mass flow measurement was a little higher than the uncertainty of the compressor mass flow measurement mainly due to the higher uncertainty of pressure measurement used for the density calculation (wide range pressure transducers used on the turbine side).

The uncertainty of the compressor pressure ratio (total-to-total) has been shown to rise towards the region of high flows and low pressure ratios (on constant speed lines). This

is due the higher uncertainty of the low pressure measurements. The rise of the uncertainty of pressure ratio at higher speed lines is caused by the rising uncertainty of the post-compressor total pressure. The uncertainty of the turbine pressure ratio is dominantly dependent on the turbine total inlet pressure of which the highest uncertainty is linked with the measurement of the static inlet temperature.

Compressor and turbine efficiencies are parameters which combine the greatest number of variables and as a result of error propagation these are the least certain out of all the considered performance parameters. In fact, the uncertainty of the turbine efficiency is dependent on the uncertainty associated with the turbine inlet temperature and turbine pressure ratio but also on the measurements carried out on the compressor side (variables that are used for the calculation of the compressor efficiency). For this reason the uncertainty of the turbine efficiency is always considerably higher than the uncertainty of the compressor efficiency.

Having studied the consequences of using the selected sensors on the uncertainty of the turbocharger performance parameters also a couple of other scenarios were tested in the attempt of the uncertainty reduction. Using a lower range pressure transducer on the pre-compressor side of the turbo combined with a more accurate and lower range pressure transducer at the compressor V-cone entry has resulted in a considerable decrease of pressure ratio and efficiency uncertainty. Also, some improvement (uncertainty drop) can be achieved if more accurate thermocouples are installed at the turbine inlet.

Completing the conclusions made for the device error based uncertainty analysis it is worth to list some of the useful observations the author made during the study of the measurement standards and sensor accuracy determination:

- The specified accuracy of PRT sensor can only be achieved if sensor is immersed at the recommended depth (to reach thermal equilibrium). Otherwise the accuracy of measurement is degraded. This makes some of the highest class PRTs inadequate for certain applications.
- For the most accurate temperature measurement the construction of PRT sensor (sensing length) should be taken into account.
- Any heat transfer towards the tail end of the thermocouple should be avoided as the temperature determination is dependent on the voltage difference between the junction and tale ends of the device.
- Comparing the accuracies of pressure transducers may sometimes be difficult. This is because the relevant industry standard allows for various methods to combine the hysteresis, non-linearity and non-repeatability errors.

The second part of the turbocharger performance uncertainty study was devoted to the heat transfer effects. The reader was made aware that the current method for the com-

pressor efficiency measurement does not separate the occurring work and heat transfers. As a result, in the low turbocharger speed region, the measured compressor efficiency is significantly lower that the real (aerodynamic or actual) efficiency. The experimental study of the uncertainty of the compressor efficiency have been pursued by generating compressor performance maps in various thermal conditions (hot and two semi-adiabatic cases). It has been found (by comparing the hot and semi-adiabatic test data) that the uncertainty of the measured compressor efficiency rose with the decreasing speed of the turbocharger – the temperature gradient between the turbine and compressor gases was rising as well as the residence time of the compressor gas (more time for the cooler gas to absorb heat). The tests carried out at two different temperatures of the oil (60°C and 90°C) whilst matching the pre-turbine and post-compressor temperatures have shown that the heat fluxes from the lubricating fluid towards the compressor gas are significantly affecting the measured compressor efficiency. Comparing the experimentally obtained data (low turbocharger speed) with the extrapolated data (using the original manufacturer performance map) it has been observed that the extrapolated values of the compressor pressure ratio were higher than those approached experimentally. At 70 krpm the extrapolated value of the compressor efficiency was lower than the measured counterpart. At 50 and 30 krpm it was difficult to compare the extrapolated and experimental efficiency due to the test limitations (full adiabatic conditions were not achieved at 50 and 30 krpm). The main conclusion from this part of work is that generation of adiabatic maps is a successful method for the separation of heat and work components in the measured efficiency. However, the adiabatic tests are challenging due to the requirements of the low mass flow measurements and turbine inlet and oil temperature.

As an alternative to the adiabatic mapping, turbocharger heat transfer models have been developed by a number of researchers. These models are in fact trained by the turbocharger maps obtained in hot and adiabatic conditions – once developed they can be used, among others, also for obtaining the real (work related) compressor efficiency. One of such turbocharger heat transfer models (lumped capacitance thermal node model) created at the University of Bath have been used in the investigation of the effects of the assumption of pre- and post-compression heat transfer occurrence. 3D conjugate heat transfer model was built by the author of this thesis to help to understand the complexity of the heat flows within the turbocharger compressor and estimate the appropriate values of heat transfer and pre-compression coefficients (required by the lumped capacitance model). As a result of thermal node model simulations it has been found that assuming the post-compression occurrence of the heat transfer is a valid assumption in the low turbocharger speeds. However, at the speed of 150 kprm it was important to

specify a realistic value of the pre-compression coefficient to achieve more accurate values of the predicted compressor efficiency.

The final part of work included the study of the literature available function used for the estimation of heat transfer towards the compressor gas. As a result of this work, compressor efficiency uncertainty was calculated. Despite the limitations regarding the friction loss calculation it has been proven that the heat transfer related effects are the dominant source of uncertainty in the measurement of compressor efficiency which stayed in agreement with the experimental findings.

2. Compressor surge development study

Understanding the performance of the turbocharger compressor also includes knowing its operational limits. Surge is an important, low mass flow operation limitation of the compressor. The study of its development has been conducted experimentally and in two stages that targeted several objections. In the first phase of the study based on the small size Fox compressor, pressure (measured at various pre- and post-compressor locations) and temperature data (measured at the half of the inducer pipe diameter) was used in the analysis that sought for finding the preferable quantity and location for the surge onset identification. The next aim of this phase of the study was the comparison of the available surge metrics, performed to understand the offsets between the surge lines drawn on the compressor performance map. Finally, blade passing frequency and its harmonics were investigated as a possible indicator of surge onset.

Analysis of the temperature data recorded at various turbocharger speeds have shown that temperature measured at the compressor entry was capable of capturing the recirculation of air (back-flows) in the mild surge region of the map. However, the rate of change of the measured temperature was different across the turbocharger speeds (larger steps in temperature rise at low speeds and smaller steps at high speeds). This inconsistency has disqualified the inducer temperature measurement as an indicator of the surge onset. At hard surge condition the temperature measurement offered a much slower response when compared with any pressure signal (much quicker reaction resulting with signal oscillations).

Comparison of pressure data was carried with the use of the Fast Fourier algorithm allowing to distinguish the signal frequencies associated with the mild and hard surge conditions. At mild surge the frequency spectrum plots indicated FFT magnitude spikes in the region of about 15-25Hz which relates to the natural (Helmholtz) frequency of the used piping system. The hard surge related FFT spikes usually occurred at lower frequencies (5-15Hz). It has been concluded that post-compressor pressure measurement has been chosen as a preferable location for indication of mild and hard surge as it offered the best consistency across the tested speed lines. The consistency was judged

by comparing the FFT magnitudes and raw signals – these were much less dependent of the distance from the compressor for the case of the post compressor located sensors. The use of the FFT magnitude of the pressure signal was also investigated as a potential way for setting the surge metrics as an alternative to the amplitude of the raw pressure signal. It has been shown that when operating in surge it was possible to transfer the amplitude of the raw pressure signal into the frequency spectrum without any leaks to the neighbouring frequencies. In order to do so the dominant surge frequency was found and followed by an appropriate reduction of the data range - only pulses that stay in-phase can be transferred to frequency spectrum without any magnitude leaks.

The comparison of two available surge metrics and data obtained in hard surge condition have shown that different surge lines have been drawn on the compressor performance map. The biggest offsets between the three surge lines were noted in the region where the development of mild surge related peaks was clear (medium and high turbo speeds). All three surge lines collapsed at the low turbocharger speeds where mild surge build-up was non-existent and hard surge occurred suddenly.

Finally, investigation of the blade passing frequency and its harmonics was carried out with the use of high frequency pressure sensors and microphone. If has been shown that with the increasing distance from the compressor the quality of the measured data dropped (high-frequency waves were diminished). Also, it has been proven that Boyce's [82] observation regarding the proximity of hard surge occurrence with blade passing frequency and its second harmonic was not in agreement with data captured by the pressure sensor and microphone (inconsistent results at various operating points)

In the second phase of the experimental surge study the Fox compressor (phase 1) was compared with the Puma compressor (larger size) to look at the surge development variability. Moreover, a comparison of the steady-state and pulsating flow surge development (judged by FFT) was carried out based on the Puma compressor. It was noted that the surge development was similar for both steady-state flow tested turbochargers – sudden occurrence of hard surge at the low turbocharger speeds and more of a warning at high speeds.

Operating compressor on the engine gas stand in pulsating conditions provided a larger surge margin when compared with the steady-state flow conditions. This is in agreement with the work presented by other researchers. Moreover, comparison of the FFT magnitudes of the pressure signals captured in steady-state and pulsating conditions has indicated a more gradual rise is of the latter case and that offers more potential for using it in the active process of surge mitigation. At last, the intake valve motion related frequency spikes were distinguished when testing in the pulsating conditions – in some cases (low cylinder engines and low engine speeds) these may interfere with the mild surge frequencies.

3. Investigation of the effects of variable fluid properties and developed flow fields on the compressor performance map.

The analysis of the compressor performance with substitute gas has indicated the need for using the non-dimensional performance parameters (non-dimensional speed and non-dimensional mass flow).

As a result of the experimental study (closed-loop mapping) of the homogeneous gases (thoroughly mixed) several performance maps have been generated. Correcting those maps with the individual gas constant and ratio of specific heats has proven to be successful for the mixtures containing the low concentrations of CO2 (3%, 5% and 10% of CO2 by mass in the CO2-air mixture). However, the compressor performance map obtained for the pure CO2 has revealed significant offsets in pressure ratio, efficiency, surge and choke flow locations. In the attempt of the efficiency and pressure ratio correction a method proposed by Roberts and Sjolander has been followed. As a result of such, a poor match between the measured and predicted values of compressor efficiency were achieved. Better ones were obtained if the n exponent used a speed dependant variable (linear dependency) rather than a proposed fixed number of 0.8. This observation has suggested that the measurement of compressor efficiency was affected by the heat transfer between the uninsulated turbomachinery components. Unfortunately, due to the time limitations this allegation has not been proven experimentally.

Seeing this as a big disadvantage a series of adiabatic CFD simulations have been performed. These simulations have shown that for the case of pure CO2 at the considered non-dimensional speeds a reasonable match between the simulated and predicted values of efficiency and pressure ratio were achieved (using the above mentioned corrections).

Finally, it has been highlighted that for ideal gases a rate of change of ratio of specific heats due to temperature rise is much higher for CO2 than for air and therefore the current efficiency calculation (based on fixed γ) may introduce significant uncertainties.

The experimental investigation of the effects of non-homogeneously mixed gases (on the compressor performance) has been conducted thanks to an introduction of passage divider upstream from the compressor housing and injection of gas into one of the passages. Due to the performance penalties caused by the divider (pressure and accuracy drop) the data gathered with the installed passage divider cannot be directly compared with the closed-loop homogenous gas data. Instead, to create a baseline case, two compressor speed lines were generated by mapping the compressor with the installed passage divider but without any injection (divider open at both ends). Unbalanced mass fractions within the divider and jet streams caused by the injection method were considered to be a major cause of the efficiency drop (despite no degradation of pressure ratio). The increment of the CO2 concentrations in the injected cases have caused a small drop

of the total-to-total pressure ratio (similar trend as in the case of homogeneous mixtures). The comparison of the measured efficiencies shown some inconsistencies with the data obtained during the homogeneous tests.

The CFD analysis of the compressor performance at the chosen non-dimensional speed line have not shown substantial differences (pressure ratio nor efficiency) between the homogeneous and non-homogeneous introduction of the gas at the chosen concentrations of CO2 in the mixture (10% by mass).

Experimental analysis carried out for the increased temperature of the injected gas has shown that the measurement of the compressor efficiency can be highly underestimated if the temperature of the injected gas is unaccounted for. The change of the temperature of the gas mixture also affects the calculation of corrected mass flow and speed and therefore the measurement of the actual temperature of the gas mixture is important for the correct determination of the compressor operating point. In extreme case, the maximum temperature at the high pressure side of the compressor can be violated leading to the damage of the wheel.

The mapping tests carried out for a selected LP EGR mixing valve and intake piping have revealed that the addition of the 90 degree bend directly upstream of compressor inlet has caused a slightly larger surge margin (when compared with the straight pipe configuration) but also a pressure drop. The installation of the pre-whirl device caused a further pressure drop and enlargement of surge margin. Various openings of the EGR valve have resulted with the large reduction of pressure ratio (and efficiency) in the high mass flow region of the map (significantly lowered operation range of the map) despite no visible change in the surge margin size.

9. Future work suggestions

Following the findings of this study, there is a number of directions in which this research can be further progressed. Some of the proposals are listed below:

9.1 Uncertainty of the turbocharger performance maps

- Study the possibility of the turbocharger performance map extrapolation improvement based on the experimentally obtained low speed data (both in hot and adiabatic conditions).
- Within the 1d simulation environment quantify the influence of various turbocharger performance map uncertainties on the predicted engine fuel consumption and emission generation.

9.2 Compressor surge measurement and mitigation

- Further investigate the post-compressor pressure data in the mild surge area of the map. Can the development of pressure oscillations be used in an active process of surge mitigation algorithm both in steady-state and on-engine conditions?
- Understanding the steady-state gas stand and engine-gas stand installation differences find the relationship between the compressor surge onset and various sizes of the pre and post compressor pipework.

9.3 Compressor mapping with substitute gas

- Conduct the closed-loop experimental analysis of the compressor performance map with gases of various ratios of specific heat – carry out the tests in adiabatic and diabatic test conditions.
- Quantify the effects (1D wave-action simulations) of an uncorrected performance map (with respect to gas properties) on the fuel consumption.
- Investigate on the efficiency correction formulas that take into account the heat transfer effects.

Bibliography

1. Burke, R.D., C.D. Copeland, and T. Duda, *Investigation into the assumptions for lumped capacitance modelling of turbocharger heat transfer*, in *6th International conference on simulation and testing*. 2014: Germany.
2. Burke, R.D., et al., *Lumped Capacitance and Three-Dimensional Computational Fluid Dynamics Conjugate Heat Transfer Modeling of an Automotive Turbocharger.* Journal of Engineering for Gas Turbines and Power, 2016. 138(9): p. 092602-092602-9.
3. Avola, C., et al. *Compressor surge for fully and semi fluctuating flows in automotive turbochargers*. in *Proceedings of the 1st Global Power and Propulsion Forum*. 2017. Zurich, Switzerland.
4. Jaaskelainen, H. and M.K. Khair, *Turbocharger Fundamentals.*
5. Nice, K., *How Turbochargers Work*. 04 December 2000.
6. March 12th, 2015];

Available from: http://www.turbobygarrett.com/turbobygarrett/compressor_maps.

7. Watson, N. and M.S. Janota, *Turbocharging the internal combustion engine.* 1982.
8. *Exhaust gas recirculation and control with Pierburg components*. KSPG Automotive.
9. Morey, B., *Cooled EGR shows benefits for gasoline engines*. September 17th, 2014, Automotive Engineer.
10. Reifarth, S., *EGR-Systems for Diesel Engines*, in *Department of Machine Design*. 2010, KTH Royal Institute of Technology in Stockholm. p. 57.
11. Schwartz, J.B. and D.N. Andrews, *Considerations for gas stand measurement of turbocharger performance*, in *11th International Conference on Turbochargers and Turbocharging*. 2014, Woodhead Publishing: Oxford. p. 253-265.
12. *SAE J1826 - Turbocharger Gas Stand Test Code*. 1995, SAE International.
13. *SAE J1723 - Supercharger Testing Standard*. 1995, SAE International.
14. ASME, *Performance Test Code on Compressors and Exhausters; ASME PTC 10-1997* 1998.
15. Benson, R.S. and K.H. Scrimshaw, *An Experimental Investigation of Non-Steady Flow in a Radial Gas Turbine.* Proceedings of the Institution of Mechanical Engineers, Conference Proceedings, 1965. 180(10): p. 74-85.
16. Payri, F., et al., *Experimental Methodology to Characterize Mechanical Losses in Small Turbochargers.* 2010(44007): p. 413-423.
17. Arcoumanis, C., et al., *Performance and Exit Flow Characteristics of Mixed-Flow Turbines.* International Journal of Rotating Machinery, 1997. 3(4).

18. Serrano, J.R., et al., *Contribution to the Understanding of Cold Pulsating Flow Influence in the Efficiency of Small Radial Turbines for Turbochargers.* 2012(44717): p. 571-580.
19. Karamanis, N. and R.F. Martinez-Botas, *Mixed-flow turbines for automotive turbochargers: Steady and unsteady performance.* International Journal of Engine Research, 2002. 3(3): p. 127-138.
20. Capobianco, M., A. Gambarotta, and G. Cipolla, *Effect of Inlet Pulsating Pressure Characteristics on Turbine Performance of an Automotive Wastegated Turbocharger*. 1990, SAE International.
21. J.S., S., *Extended Turbocharger Mapping and Engine Simulation*, in *Mechanical Engineering* 2010, University of Aachen.
22. Naundorf, D. and H. Bolz, *Turbocharger Test Stand with a Hot Gas Generator for High-Performance Supercharging Systems*, in *MTZ Worldwide*. 2008, Springer. p. 22-25.
23. Young, M.Y. and D.A. Penz, *The Design of a New Turbocharger Test Facility*. 1990, SAE International.
24. *Evaluation of measurement data - Guide to the expression of uncertainty in measurement*. 2008, JCGM 100:2008.
25. *SAE J1826 - Surface Vehicle Recommended Practice*. 1995, SAE International.
26. SAE, *SAEJ1723 - Supercharger Code of Practise.* 1995.
27. Kline, S.J. and F.A. McClintock, *Describing uncertainties in single sample experiments*.
28. Mohtar, H., P. Chesse, and D. Chalet, *Describing Uncertainties Encountered during Laboratory Turbocharger Compressor Tests.* Experimental Techniques, 2012. 36(5): p. 53-61.
29. Guillou, E., *Uncertainty and Measurement Sensitivity of Turbocharger Compressor Gas Stands*. 2013, SAE International.
30. Olmeda, P., et al., *Uncertainties in power computations in a turbocharger test bench.* Measurement, 2015. 59: p. 363-371.
31. Bolz, H., A. Rinaldi, and A. Kaufmann, *Critical aspects in turbocharger testing - Engineers, Institute of Mechanical*, in *11th International Conference on Turbochargers and Turbocharging*. 2014, Woodhead Publishing: Oxford. p. 265-277.
32. Shiva Kumar, S., B. van Leeuwen, and A. Costall, *Quantification and Sensitivity Analysis of Uncertainties in Turbocharger Compressor Gas Stand Measurements Using Monte Carlo Simulation*. 2014, SAE International.
33. Mai, H., et al., *Impact of Measurement Uncertainty in the Characteristic Maps of a Turbocharger on Engine Performance.* Journal of Engineering for Gas Turbines and Power, 2013. 136(2): p. 021201-021201.

34. Otobe, T., et al., *Method of performance measurement for low turbocharger speeds*, in *9th International Conference on Turbochargers and Turbocharging*. 2010: London.
35. Serrano, J., et al., *Importance of Heat Transfer Phenomena in Small Turbochargers for Passenger Car Applications.* 2013.
36. Chesse, P., D. Chalet, and X. Tauzia, *Impact of the Heat Transfer on the Performance Calculations of Automotive Turbocharger Compressor.* Oil & Gas Science and Technology – Revue d'IFP Energies nouvelles, 2011. 66: p. 791-800.
37. Sutton, A.J. and A. Whitfield, *The effect of vaneless diffuser geometry on the surge margin of turbocharger compressors.* ARCHIVE: Proceedings of the Institution of Mechanical Engineers, Part D: Transport Engineering 1984-1988 (vols 198-202), 1989. 203(24): p. 91-98.
38. Engeda, A., *The unsteady performance of a centrifugal compressor with different diffusers.* Proceedings of the Institution of Mechanical Engineers, Part A: Journal of Power and Energy, 2001. 215(5): p. 585-599.
39. Jager, B.d. *Rotating stall and surge control: A survey*. in *Conference on Decision & Control*. 1995. New Orleans, LA.
40. Fink, D.A., N.A. Cumpsty, and E.M. Greitzer, *Surge Dynamics in a Free-Spool Centrifugal Compressor System.* Journal of Turbomachinery, 1992. 114(2): p. 321-332.
41. Dehner, R., et al., *Simulation of Mild Surge in a Turbocharger Compression System.* 2010.
42. Dehner, R., et al., *Prediction of Surge in a Turbocharger Compression System vs. Measurements.* 2011.
43. Nguyen-Schäfer, H., *Aero and Vibroacoustics of Automotive Turbochargers*. 2013: Springer Berlin Heidelberg.
44. Galindo, J., et al., *Surge limit definition in a specific test bench for the characterization of automotive turbochargers.* Experimental Thermal and Fluid Science, 2006. 30(5): p. 449-462.
45. Boyce, M.P., *6 - Centrifugal Compressors*, in *Gas Turbine Engineering Handbook (Fourth Edition)*, M.P. Boyce, Editor. 2012, Butterworth-Heinemann: Oxford. p. 253-301.
46. Eynon, P.A. and A. Whitfield, *The effect of low-solidity vaned diffusers on the performance of a turbocharger compressor.* Proceedings of the Institution of Mechanical Engineers, Part C: Journal of Mechanical Engineering Science, 1997. 211(5): p. 325-339.
47. Harp, J. and T. Oatway, *Centrifugal Compressor Development for a Variable Area Turbocharger.* SAE Technical Paper 790066, 1979.
48. Simon, H., T. Wallmann, and T. Mönk, *Improvements in Performance Characteristics of Single-Stage and Multistage Centrifugal Compressors by Simultaneous Adjustments of*

Inlet Guide Vanes and Diffuser Vanes. Journal of Turbomachinery, 1987. 109(1): p. 41-47.

49. Senoo, Y., *Senoo Y. Japanese Pat. Application Disclosure 119411/78, 1978*. 1978: Japan.
50. Senoo, Y. and Y. Kinoshita, *Influence of Inlet Flow Conditions and Geometries of Centrifugal Vaneless Diffusers on Critical Flow Angle for Reverse Flow.* Journal of Fluids Engineering, 1977. 99(1): p. 98-102.
51. Abdel-Hamid, A.N., *A New Technique for Stabilizing the Flow and Improving the Performance of Vaneless Radial Diffusers.* Journal of Turbomachinery, 1987. 109(1): p. 36-40.
52. Jaatinen, A., et al., *Effect of vaneless diffuser width on the overall performance of a centrifugal compressor.* Proceedings of the Institution of Mechanical Engineers, Part A: Journal of Power and Energy, 2011. 225(5): p. 665-673.
53. Mohtar, H., et al., *Effect of Diffuser and Volute on Turbocharger Centrifugal Compressor Stability and Performance: Experimental Study.* Oil & Gas Science and Technology – Revue d'IFP Energies nouvelles, 2011. 66(5): p. 779-790.
54. Fisher, F.B., *Application of Map Width Enhancement Devices to Turbocharger Compressor Stages.* SAE Technical Paper 880794, 1988.
55. Chalet, D., P. Chesse, and H. Mohtar, *Effect of a map width enhancement system on turbocharger centrifugal compressor performance and surge margin.* Proceedings of the Institution of Mechanical Engineers, Part D: Journal of Automobile Engineering, 2011. 225(3): p. 395-405.
56. Sivagnanasundaram, S., S. Spence, and J. Early. *Map width enhancement technique for a turbocharger compressor*. in *Proceedings of ASME Turbo Expo 2012*. 2012.
57. Hu, L., et al., *Numerical and experimental investigation of a compressor with active self-recirculation casing treatment for a wide operation range.* Proceedings of the Institution of Mechanical Engineers, Part D: Journal of Automobile Engineering, 2013. 227(9): p. 1227-1241.
58. Chen, H. and V.-M. Lei, *Casing Treatment and Inlet Swirl of Centrifugal Compressors.* Journal of Turbomachinery, 2013. 135(4): p. 041010.
59. Ding, L., et al., *Experimental investigation of the casing treatment effects on steady and transient characteristics in an industrial centrifugal compressor.* Experimental Thermal and Fluid Science, 2013. 45: p. 136-145.
60. Freeman, C., et al., *Experiments in Active Control of Stall on an Aeroengine Gas Turbine.* Journal of Turbomachinery, 1998. 120(4): p. 637-647.
61. Suder, K.L., et al., *Compressor Stability Enhancement Using Discrete Tip Injection.* Journal of Turbomachinery, 2000. 123(1): p. 14-23.

62. Stein, A., S. Niazi, and L.N. Sankar, *Computational Analysis of Centrifugal Compressor Surge Control Using Air Injection.* Journal of Aircraft, 2001. 38(3): p. 513-520.

63. Hirano, T., T. Uchida, and H. Tsujita, *Control of Surge in Centrifugal Compressor by Using a Nozzle Injection System: Universality in Optimal Position of Injection Nozzle.* International Journal of Rotating Machinery, 2012. 2012: p. 1-8.

64. Spakovszky, Z.S., *Backward Traveling Rotating Stall Waves in Centrifugal Compressors.* Journal of Turbomachinery, 2004. 126(1): p. 1-12.

65. Skoch, G.J., *Experimental Investigation of Diffuser Hub Injection to Improve Centrifugal Compressor Stability*. 2004, NASA.

66. Wallace, F.J., A. Whitfield, and R.C. Atkey, *Experimental and theoretical performance of a radial flow turbocharger compressor with inlet prewhirl.* Proceedings of the Institution of Mechanical Engineers, Part A: Journal of Power and Energy, 1975. 189(1): p. 177-186.

67. Whitfield, A. and A.H. Abdullah, *The Performance of a Centrifugal Compressor With High Inlet Prewhirl.* Journal of Turbomachinery, 1998. 120: p. 487-493.

68. Galindo, J., et al., *Potential of flow pre-whirl at the compressor inlet of automotive engine turbochargers to enlarge surge margin and overcome packaging limitations.* International Journal of Heat and Fluid Flow, 2007. 28(3): p. 374-387.

69. Mohtar, H., et al., *Variable Inlet Guide Vanes in a Turbocharger Centrifugal Compressor: Local and Global Study*, in *World Congress*. 2008: Detroit, Michigan.

70. Mohseni, A., et al., *Novel IGV Designs for Centrifugal Compressors and Their Interaction With the Impeller.* Journal of Turbomachinery, 2012. 134(2): p. 021006.

71. TOUSSAINT, M. and P. PODEVIN, *Guide vanes upstream the impeller of centrifugal compressor*. http://turbo-moteurs.cnam.fr/pdf/EUROT5.PDF.

72. Grigoriadis, P., et al. *Variable trim compressor - a new approach to variable compressor geometry*. in *10th International Conference on Turbochargers and Turbocharging*. 2012. London: IMecheE.

73. Iwakiri, Y. and H. Uchida, *Numerical Fluid Analysis of a Variable Geometry Compressor for use in a Turbocharger*. R&D Review of Toyota CRDL.

74. Tomita, I., B. An, and T. Nanbu. *A new operating range enhancement device combined with a casing treatment and inlet guide vanes for centrifugal compressors*. in *11th International Conference on Turbochargers and Turbocharging*. 2014. London.

75. Andersen, J., F. Lindström, and F. Westin, *Surge Definitions for Radial Compressors in Automotive Turbochargers.* 2008.

76. Hansen, K.E., P. Jørgensen, and P.S. Larsen, *Experimental and Theoretical Study of Surge in a Small Centrifugal Compressor.* Journal of Fluids Engineering, 1981. 103(3): p. 391-395.

77. ASME, *Performance Test Code on Compressors and Exhausters; ASME PTC 10-1997* 1998.

78. Galindo, J., et al., *Experiments and modelling of surge in small centrifugal compressor for automotive engines.* Experimental Thermal and Fluid Science, 2008. 32(3): p. 818-826.

79. Galindo, J., et al., *On the effect of pulsating flow on surge margin of small centrifugal compressors for automotive engines.* Experimental Thermal and Fluid Science, 2009. 33(8): p. 1163-1171.

80. Galindo, J., et al., *Measurement and Modeling of Compressor Surge on Engine Test Bench for Different Intake Line Configurations.* 2011.

81. Galindo, J., et al., *On-Engine Measurement of Turbocharger Surge Limit.* Experimental Techniques, 2013. 37(1): p. 47-54.

82. Boyce, M.P., *6 - Centrifugal Compressors*, in *Gas Turbine Engineering Handbook (Third Edition)*. 2006, Gulf Professional Publishing: Burlington. p. 219-273.

83. Greitzer, E.M., *Surge and Rotating Stall in Axial Flow Compressors—Part I: Theoretical Compression System Model.* Journal of Engineering for Gas Turbines and Power, 1976. 98(2): p. 190-198.

84. van Helvoirt, J. and B. de Jager, *Dynamic model including piping acoustics of a centrifugal compression system.* Journal of Sound and Vibration, 2007. 302(1–2): p. 361-378.

85. Harley, P.X.L., S.W.T. Spence, and J. Early. *Inlet recirculation in automotive turbocharger centrifugal compressors*. in *11th International Conference on Turbochargers and Turbocharging*. 2014. London: IMechE.

86. Sivagnanasundaram, S., S. Spence, and J. Early, *Experimental and numerical analysis of a classical bleed slot system for a turbocharger compressor.*

87. Harley, P., et al., *Meanline Modeling of Inlet Recirculation in Automotive Turbocharger Centrifugal Compressors.* Journal of Turbomachinery, 2015. 137(1).

88. Margot, X., et al., *Combination of CFD and Experimental Techniques to Investigate the Flow in Centrifugal Compressors Near Surge Line.* 2008.

89. Mostafa, N.H., A.F. Abdul-gawad, and M.S. Emeara, *A numercial/experimental study of a multi-stage centrifugal compressor.* EIJEST, 2011. 14: p. 792-801.

90. Day, I.J., *Active Suppression of Rotating Stall and Surge in Axial Compressors.* Journal of Turbomachinery, 1993. 115(1): p. 40-47.

91. Whitfield, A. and N.C. Baines. *Design of radial turbomachines*. 1990.

92. Weigel, C. and C.L. Ball, *Reynolds number effect on overall performance of a 10.8-centimeter sweptback bladed centrifugal compressor*. 1972, NASA; United States: NASA Lewis Research Center; Cleveland, OH, United State.

93. Wiesner, F.J., *A New Appraisal of Reynolds Number Effects on Centrifugal Compressor Performance.* Journal of Engineering for Power, 1979. 101(3): p. 384-392.

94. Simon, H. and A. Bülskämper, *On the Evaluation of Reynolds Number and Relative Surface Roughness Effects on Centrifugal Compressor Performance Based on Systematic Experimental Investigations.* Journal of Engineering for Gas Turbines and Power, 1984. 106(2): p. 489-498.

95. Strub, R.A., et al., *Influence of the Reynolds Number on the Performance of Centrifugal Compressors.* Journal of Turbomachinery, 1987. 109(4): p. 541-544.

96. Casey, M.V., *The Effects of Reynolds Number on the Efficiency of Centrifugal Compressor Stages.* Journal of Engineering for Gas Turbines and Power, 1985. 107(2): p. 541-548.

97. Casey, M.V. and C.J. Robinson, *A unified correction method for Reynolds number, size, and roughness effects on the performance of compressors.* Journal of Power and Energy, 2011.

98. Roberts, S.K. and S.A. Sjolander, *Effect of the Specific Heat Ratio on the Aerodynamic Performance of Turbomachinery.* Journal of Engineering for Gas Turbines and Power, 2002. 127(4): p. 773-780.

99. Karstadt, S., et al., *Effect of Water Droplets Caused by Low Pressure EGR on Spinning Compressor Wheels*, in *19th Supercharging Conference* 2014: Dresden.

100. M Burkinshaw, U Mukhtar, and L. Sullivan, *The development of a long route EGR turbocharger for commercial engine applications*, in *The 12th International Conference on Turbochargers and Turbocharging*. 2016: London.

101. Münz, S., et al., *Turbocharger for emission concepts with low-pressure-end exhaust-gas recirculation*. 2007: Borg Warner.

102. *GT-Suite. Flow Theory Manual. Version 7.5 by Gamma Technologies*. 2015.

103. Baines, N.C., *Fundamentals of Turbocharging*. 2005: Concepts NREC.

104. *An introduction to differential-pressure flow meters. Good practice guide*. National Measurement System.

105. www.tcdirect.co.uk. June 10th 2017].

106. Avola, C., et al., *Preliminary DoE Analysis and Control of Mapping Procedure for a Turbocharger on an Engine Gas-Stand.* 2016(49866): p. V008T23A008.

107. Tu, J., G.H. Yeoh, and C. Liu, *Chapter 1 - Introduction*, in *Computational Fluid Dynamics*. 2008, Butterworth-Heinemann: Burlington. p. 1-28.

108. Pinto, R.N., et al., *Computational Fluid Dynamics in Turbomachinery: A Review of State of the Art.* Archives of Computational Methods in Engineering, 2016: p. 1-13.

109. Shih, T.-H., et al., *A New K-epsilon Eddy Viscosity Model for High Reynolds Number Turbulent Flows: Model Development and Validation*. 1994, NASA Lewis Research Center; Cleveland, OH, United States.

110. Jones, W.P. and B.E. Launder, *The prediction of laminarization with a two-equation model of turbulence.* International Journal of Heat and Mass Transfer, 1972. 15(2): p. 301-314.

111. Rodi, W., *Experience with two-layer models combining the k-epsilon model with a one-equation model near the wall*, in *29th Aerospace Sciences Meeting*. 1991, American Institute of Aeronautics and Astronautics.

112. *SAE J922 - Turbocharger Nomenclature and Terminology*. 2011, SAE International.

113. CIMAC, *Turbocharging efficiencies - definitions and guidelines for measurement and calculation.* 2007(Recommendation 27).

114. Serrano, J.R., et al., *Influence of Environmental Conditions and Thermodynamic Considerations in the Calculation of Turbochargers Efficiency*. 2009, SAE International.

Appendix A - Compressor uncertainty formulas

Uncertainty of $c_{p_{c,1}}$ (dependent on $R, \gamma_{c,1}$)

$$c_{p_{c,1}} = R\frac{\gamma_{c,1}}{\gamma_{c,1}-1}$$

$$\delta c_{p_{c,1}} = \sqrt{(\frac{\partial c_{p_{c,1}}}{\partial R}\delta R)^2 + (\frac{\partial c_{p_{c,1}}}{\partial \gamma_{c,1}}\delta\gamma_{c,1})^2}$$

$$\delta c_{p_{c,1}} = \sqrt{(\frac{\gamma_{c,1}}{\gamma_{c,1}-1})\delta R)^2 + ((\frac{R}{\gamma_{c,1}-1}) - \frac{(\gamma_{c,1}R)}{(\gamma_{c,1}-1)^2})\delta\gamma_{c,1})^2}$$

Uncertainty of $c_{p_{c,2}}$ (dependent on $R, \gamma_{c,2}$)

$$c_{p_{c,2}} = R\frac{\gamma_{c,2}}{\gamma_{c,2}-1}$$

$$\delta c_{p_{c,2}} = \sqrt{(\frac{\partial c_{p_{c,2}}}{\partial R}\delta R)^2 + (\frac{\partial c_{p_{c,2}}}{\partial \gamma_{c,2}}\delta\gamma_{c,2})^2}$$

$$\delta c_{p_{c,2}} = \sqrt{(\frac{\gamma_{c,2}}{\gamma_{c,2}-1})\delta R)^2 + ((\frac{R}{\gamma_{c,2}-1}) - \frac{(\gamma_{c,2}R)}{(\gamma_{c,2}-1)^2})\delta\gamma_{c,2})^2}$$

Uncertainty of $c_{p_{c,avg}}$ (dependent on $c_{p_{c,1}}, c_{p_{c,2}}$)

$$c_{p_{c,avg}} = \frac{(c_{p_{c,1}} + c_{p_{c,2}})}{2}$$

$$\delta c_{p_{c,avg}} = \sqrt{(\frac{\partial c_{p_{c,avg}}}{\partial c_{p_{c,1}}}\delta c_{p_{c,1}})^2 + (\frac{\partial c_{p_{c,avg}}}{\partial c_{p_{c,2}}}\delta c_{p_{c,2}})^2}$$

$$\delta c_{p_{c,avg}} = \sqrt{[\frac{1}{2}\delta c_{p_{c,1}}]^2 + [\frac{1}{2}\delta c_{p_{c,2}}]^2}$$

Uncertainty of $\gamma_{c,1}$ (dependent on T_{1s})

$$\gamma_{c,1} = 1.42592 - 8.03974(10^{-5})T_{1s}$$

$$\delta\gamma_{c,1} = -8.03974(10^{-5})$$

Uncertainty of $\gamma_{c,2}$ (dependent on T_{2s})

$$\gamma_{c,2} = 1.42592 - 8.03974(10^{-5})T_{2s}$$

$$\delta\gamma_{c,2} = -8.03974(10^{-5})$$

Uncertainty of $\gamma_{c,avg}$ (dependent on $\gamma_{c,1}, \gamma_{c,2}$)

$$\gamma_{c,avg} = \frac{\gamma_{c,1} + \gamma_{c,2}}{2},$$

$$\delta\gamma_{c,avg} = \sqrt{[\frac{1}{2}\delta\gamma_{c,1}]^2 + [\frac{1}{2}\delta\gamma_{c,2}]^2}$$

Uncertainty of ρ_1 (dependent on P_{1s}, T_{1s})

$$\rho_1 = \frac{P_{1s}}{RT_{1s}}$$

$$\delta\rho_1 = \sqrt{(\frac{\partial\rho_1}{\partial P_{1s}}\delta P_{1s})^2 + (\frac{\partial\rho_1}{\partial T_{1s}}\delta T_{1s})^2}$$

$$\delta\rho_1 = \sqrt{(\frac{1}{RT_{1s}}\delta P_{1s})^2 + (-\frac{P_{1s}}{RT_{1s}{}^2}\delta T_{1s})^2}$$

$$\delta\rho_1 = \frac{1}{R}\sqrt{(\frac{1}{T_{1s}}\delta P_{1s})^2 + (-\frac{P_{1s}}{T_{1s}{}^2}\delta T_{1s})^2}$$

Uncertainty of ρ_2 (dependent on P_{2s}, T_{2s})

$$\rho_2 = \frac{P_{2s}}{RT_{2s}}$$

$$\delta\rho_2 = \sqrt{(\frac{\partial\rho_2}{\partial P_{2s}}\delta P_{2s})^2 + (\frac{\partial\rho_2}{\partial T_{2s}}\delta T_{2s})^2}$$

$$\delta\rho_2 = \sqrt{(\frac{1}{RT_{2s}}\delta P_{2s})^2 + (-\frac{P_{2s}}{RT_{2s}{}^2}\delta T_{2s})^2}$$

$$\delta\rho_2 = \frac{1}{R}\sqrt{(\frac{1}{T_{2s}}\delta P_{2s})^2 + (-\frac{P_{2s}}{T_{2s}{}^2}\delta T_{2s})^2}$$

Uncertainty of V_1 (dependent on $\dot{m}_c$, T_{1s}, P_{1s})

$$V_1 = \frac{\dot{m}_c}{q_1 A_1} = \frac{\dot{m}_c RT_{1s}}{P_{1s}A_1}$$

$$\delta V_1 = \sqrt{(\frac{\partial V_1}{\partial\dot{m}_c}\delta\dot{m}_c)^2 + (\frac{\partial V_1}{\partial T_{1s}}\delta T_{1s})^2 + (\frac{\partial V_1}{\partial P_{1s}}\delta P_{1s})^2}$$

$$\delta V_1 = \sqrt{(\frac{RT_{1s}}{P_{1s}A_1}\delta\dot{m}_c)^2 + (\frac{\dot{m}_c R}{P_{1s}A_1}\delta T_{1s})^2 + (-\frac{\dot{m}_c RT_{1s}}{P_{1s}{}^2 A_1}\delta P_{1s})^2}$$

$$\delta V_1 = \frac{R}{A_1}\sqrt{(\frac{T_{1s}}{P_{1s}}\delta\dot{m}_c)^2 + (\frac{\dot{m}_c}{P_{1s}}\delta T_{1s})^2 + (-\frac{\dot{m}_c T_{1s}}{P_{1s}{}^2}\delta P_{1s})^2}$$

Uncertainty of V_2 (dependent on $\dot{m}_c$, T_{2s}, P_{2s})

$$V_2 = \frac{\dot{m}_c}{q_2 A_1} = \frac{\dot{m}_c R T_{2s}}{P_{2s} A_1}$$

$$\delta V_2 = \sqrt{(\frac{\partial V_2}{\partial \dot{m}_c}\delta \dot{m}_c)^2 + (\frac{\partial V_2}{\partial T_{2s}}\delta T_{2s})^2 + (\frac{\partial V_2}{\partial P_{2s}}\delta P_{2s})^2}$$

$$\delta V_2 = \sqrt{(\frac{R T_{2s}}{P_{2s} A_1}\delta \dot{m}_c)^2 + (\frac{\dot{m}_c R}{P_{2s} A_1}\delta T_{2s})^2 + (-\frac{\dot{m}_c R T_{2s}}{{P_{2s}}^2 A_1}\delta P_{2s})^2}$$

$$\delta V_2 = \frac{R}{A_1}\sqrt{(\frac{T_{2s}}{P_{2s}}\delta \dot{m}_c)^2 + (\frac{\dot{m}_c}{P_{2s}}\delta T_{2s})^2 + (-\frac{\dot{m}_c T_{2s}}{{P_{2s}}^2}\delta P_{2s})^2}$$

Uncertainty of T_{1t} (dependent on T_{1s}, V_1, $c_{p_{c,1}}$)

$$T_{1t} = T_{1s} + \frac{{V_1}^2}{2c_{p_{c,1}}}$$

$$\delta T_{1t} = \sqrt{(\frac{\partial T_{1t}}{\partial T_{1s}}\delta T_{1s})^2 + (\frac{\partial T_{1t}}{\partial V_1}\delta V_1)^2 + (\frac{\partial T_{1t}}{\partial c_{p_{c,1}}}\delta c_{p_{c,1}})^2}$$

$$\delta T_{1t} = \sqrt{{\delta T_{1s}}^2 + [(\frac{V_1}{c_{p_{c,1}}})\delta V_1)]^2 + [\left(-\frac{{V_1}^2}{2{c_{p_{c,1}}}^2}\right)\delta c_{p_{c,1}}]^2}$$

Uncertainty of T_{2t} (dependent on T_{2s}, V_2, $c_{p_{c,2}}$)

$$T_{2t} = T_{2s} + \frac{{V_2}^2}{2c_{p_{c,2}}}$$

$$\delta T_{2t} = \sqrt{(\frac{\partial T_{2t}}{\partial T_{2s}}\delta T_{2s})^2 + (\frac{\partial T_{2t}}{\partial V_2}\delta V_2)^2 + (\frac{\partial T_{2t}}{\partial c_{p_{c,2}}}\delta c_{p_{c,2}})^2}$$

$$\delta T_{2t} = \sqrt{{\delta T_{2s}}^2 + [(\frac{V_2}{c_{p_{c,2}}})\delta V_2)]^2 + [\left(-\frac{{V_2}^2}{2{c_{p_{c,2}}}^2}\right)\delta c_{p_{c,2}}]^2}$$

Uncertainty of P_{1t} (dependent on P_{1s}, ρ_1, V_1)

$$P_{1t} = P_{1s} + \frac{\rho_1 {V_1}^2}{2}$$

$$\delta P_{1t} = \sqrt{(\frac{\partial P_{1t}}{\partial P_{1s}}\delta P_{1s})^2 + (\frac{\partial P_{1t}}{\partial \rho_1}\delta \rho_1)^2 + (\frac{\partial P_{1t}}{\partial V_1}\delta V_1)^2}$$

$$\delta P_{1t} = \sqrt{[\delta P_{1s}]^2 + [(\frac{1}{2}V_1^2)\delta \rho_1]^2 + [(\rho_1 V_1)\delta V_1]^2}$$

Uncertainty of P_{2t} (dependent on $P_{2s}, T_{2t}, T_{2s}, \gamma_{c,2}$)

$$P_{2t} = P_{2s}(\frac{T_{2t}}{T_{2s}})^{\left(\frac{\gamma_{c,2}}{\gamma_{c,2}-1}\right)} = P_{2s}{T_{2t}}^{\left(\frac{\gamma_{c,2}}{\gamma_{c,2}-1}\right)}{T_{2s}}^{-(\frac{\gamma_{c,2}}{\gamma_{c,2}-1})}$$

$$\delta P_{2t} = \sqrt{(\frac{\partial P_{2t}}{\partial P_{2s}}\delta P_{2s})^2 + (\frac{\partial P_{2t}}{\partial T_{2t}}\delta T_{2t})^2 + (\frac{\partial P_{2t}}{\partial T_{2s}}\delta T_{2s})^2 + (\frac{\partial P_{2t}}{\partial \gamma_c}\delta \gamma_{c,2})^2}$$

$$\frac{\partial P_{2t}}{\partial P_{2s}} = (\frac{T_{2t}}{T_{2s}})^{(\frac{\gamma_{c,2}}{\gamma_{c,2}-1})}$$

$$\frac{\partial P_{2t}}{\partial T_{2t}} = \frac{P_{2s}\gamma_{c,2}\frac{T_{2t}}{T_{2s}}^{(\left(\frac{\gamma_{c,2}}{\gamma_{c,2}-1}\right)-1)}}{(\gamma_{c,2}-1)T_{2s}}$$

$$\frac{\partial P_{2t}}{\partial T_{2s}} = -\frac{\gamma_{c,2}P_{2s}T_{2t}\frac{T_{2t}}{T_{2s}}^{(\left(\frac{\gamma_{c,2}}{\gamma_{c,2}-1}\right)-1)}}{{T_{2s}}^2(\gamma_{c,2}-1)}$$

$$\frac{\partial P_{2t}}{\partial \gamma_{c,2}} = P_{2s}\ln(\frac{T_{2t}}{T_{2s}})(\frac{1}{\gamma_{c,2}-1} - \frac{\gamma_{c,2}}{\left(\gamma_{c,2}-1\right)^2})(\frac{T_{2t}}{T_{2s}})^{\left(\frac{\gamma_{c,2}}{\gamma_{c,2}-1}\right)}$$

Uncertainty of PR_c (dependent on P_{1t}, P_{2t})

$$PR_c = (\frac{P_{2t}}{P_{1t}})$$

$$\delta PR_c = \sqrt{(\frac{\partial PR_c}{\partial P_{1t}}\delta P_{1t})^2 + (\frac{\partial PR_c}{\partial P_{2t}}\delta P_{2t})^2}$$

$$\delta PR_c = \sqrt{(-\frac{P_{2t}}{P_{1t}^2}\delta P_{1t})^2 + (\frac{1}{P_{1t}}\delta P_{2t})^2}$$

Uncertainty of η_c (dependent on $T_{1t}, T_{2t}, PR_c, \gamma_{c,avg}$)

$$\eta_c = \frac{T_{1t}[\left(PR_c^{\left(\frac{\gamma_{c,avg}-1}{\gamma_{c,avg}}\right)}\right) - 1]}{T_{2t} - T_{1t}}$$

$$\delta \eta_c = \sqrt{(\frac{\partial \eta_c}{\partial T_{1t}}\delta T_{1t})^2 + (\frac{\partial \eta_c}{\partial T_{2t}}\delta T_{2t})^2 + (\frac{\partial \eta_c}{\partial PR_c}\delta PR_c)^2 + (\frac{\partial \eta_c}{\partial \gamma_c}\delta \gamma_{c,avg})^2}$$

$$\frac{\partial \eta_c}{\partial T_{1t}} = \frac{T_{1t}\left[\left(PR_c^{\left(\frac{\gamma_{c,avg}-1}{\gamma_{c,avg}}\right)}\right) - 1\right]}{(T_{1t}-T_{2t})^2} - \frac{\left[\left(PR_c^{\left(\frac{\gamma_{c,avg}-1}{\gamma_{c,avg}}\right)}\right) - 1\right]}{(T_{1t}-T_{2t})}$$

$$\frac{\partial \eta_c}{\partial T_{2t}} = \frac{-T_{1t}\left[\left(PR_c^{\left(\frac{\gamma_{c,avg}-1}{\gamma_{c,avg}}\right)}\right)-1\right]}{(T_{1t}-T_{2t})^2}$$

$$\frac{\partial \eta_c}{\partial PR_c} = -\frac{PR_c^{\left[\left(\frac{\gamma_{c,avg}-1}{\gamma_{c,avg}}\right)-1\right]} T_{1t}(\gamma_{c,avg}-1)}{\gamma_{c,avg}(T_{1t}-T_{2t})}$$

$$\frac{\partial \eta_c}{\partial \gamma_{c,avg}} = \frac{PR_c^{\left(\frac{\gamma_{c,avg}-1}{\gamma_{c,avg}}\right)} T_{1t} lnPR_c\left(\frac{1}{\gamma_{c,avg}} - \frac{\gamma_{c,avg}-1}{{\gamma_{c,avg}}^2}\right)}{T_{1t}-T_{2t}}$$

Uncertainty of $\dot{Q}_c$ (dependent on Y_{cv1}, ΔP_{cv1}, ρ_{cv1})

$$\dot{Q}_c = F_a C_d Y_{cv1} k_1 \sqrt{\frac{\Delta P_{cv1}}{\rho_{cv1}}}$$

$$\delta \dot{Q}_c = \sqrt{\left(\frac{\partial \dot{Q}_c}{\partial Y_{cv1}}\delta Y_{cv1}\right)^2 + \left(\frac{\partial \dot{Q}_c}{\partial \Delta P_{cv1}}\delta \Delta P_{cv1}\right)^2 + \left(\frac{\partial \dot{Q}_c}{\partial \rho_{cv1}}\delta \rho_{cv1}\right)^2}$$

$$\frac{\partial \dot{Q}_c}{\partial Y_{cv1}} = F_a C_d k_1 \sqrt{\frac{\Delta P_{cv1}}{\rho_{cv1}}}$$

$$\frac{\partial \dot{Q}_c}{\partial \Delta P_{cv1}} = \frac{F_a C_d Y_{cv1} k_1}{2\rho_{cv1}\sqrt{\frac{\Delta P_{cv1}}{\rho_{cv1}}}}$$

$$\frac{\partial \dot{Q}_c}{\partial \rho_{cv1}} = -\frac{C_d \Delta P_{cv1} F_a k_1 Y_{cv1}}{2{\rho_{cv1}}^2\sqrt{\left(\frac{\Delta P_{cv1}}{\rho_{cv1}}\right)}}$$

Uncertainty of Y_{cv1} (dependent on, ΔP_{cv1}, P_{cv1s})

$$Y_{cv1} = 1 - (0.649 + 0.696\beta^4)\frac{\Delta P_{cv1}}{k_{cv1}P_{cv1s}}$$

$$\delta Y_{cv1} = \sqrt{\left(\frac{\partial Y_{cv1}}{\partial \Delta P_{cv1}}\delta \Delta P_{cv1}\right)^2 + \left(\frac{\partial Y_{cv1}}{\partial P_{cv1s}}\delta P_{cv1s}\right)^2 + \left(\frac{\partial Y_{cv1}}{\partial k_{cv1}}\delta k_{cv1}\right)^2}$$

$$\frac{\partial Y_{cv1}}{\partial \Delta P_{cv1}} = -(0.649 + 0.696\beta^4)\frac{1}{k_{cv1}P_{cv1s}}$$

$$\frac{\partial Y_{cv1}}{\partial P_{cv1s}} = -(0.649 + 0.696\beta^4)\left(-\frac{\Delta P_{cv1}}{k_{cv1}{P_{cv1s}}^2}\right)$$

Uncertainty of $\dot{m}_c$ (dependent on $\dot{Q}_c$, ρ_{cv1})

$$\dot{m}_c = \dot{Q}_c \rho_{cv1}$$

$$\delta\dot{m}_c = \sqrt{(\frac{\partial\dot{m}_c}{\partial\dot{Q}_c}\delta\dot{Q}_c)^2 + (\frac{\partial\dot{m}_c}{\partial\rho_{cv1}}\delta\rho_{cv1})^2}$$

$$\delta\dot{m}_c = \sqrt{(\rho_{cv1}\delta\dot{Q}_c)^2 + (\dot{Q}_c\delta\rho_{cv1})^2}$$

Uncertainty of $\dot{m}_{c,cor}$ (dependent on $\dot{m}_c$, T_{1s}, P_{1s})

$$\dot{m}_{c,cor} = \dot{m}_c \frac{\sqrt{\frac{T_{1t}}{T_{ref}}}}{\frac{P_{1t}}{P_{ref}}}$$

$$\delta\dot{m}_{c,cor} = \sqrt{(\frac{\partial\dot{m}_{c,cor}}{\partial\dot{m}_c}\delta\dot{m}_c)^2 + (\frac{\partial\dot{m}_{c,cor}}{\partial T_{1t}}\delta T_{1t})^2 + (\frac{\partial\dot{m}_{c,cor}}{\partial P_{1t}}\delta P_{1t})^2}$$

$$\delta\dot{m}_{c,cor} = \sqrt{(\sqrt{\frac{T_{1t}}{T_{ref}}}\frac{P_{ref}}{P_{1t}}\delta\dot{m}_c)^2 + (-\frac{\dot{m}_c P_{ref}}{2P_{1t}T_{ref}\sqrt{\frac{T_{1t}}{T_{ref}}}}\delta T_{1t})^2 + (\dot{m}_c\sqrt{\frac{T_{1t}}{T_{ref}}}(-\frac{P_{ref}}{{P_{1t}}^2})\delta P_{1t})^2}$$

Uncertainty of ρ_{cv1} (dependent on P_{cv1s}, T_{cv1s})

$$\rho_{cv1} = \frac{P_{cv1s}}{RT_{cv1s}}$$

$$\delta\rho_{cv1} = \sqrt{(\frac{\partial\rho_{cv1}}{\partial P_{cv1s}}\delta P_{cv1s})^2 + (\frac{\partial\rho_{cv1}}{\partial T_{cv1s}}\delta T_{cv1s})^2}$$

$$\delta\rho_{cv1} = \sqrt{(\frac{1}{RT_{cv1s}}\delta P_{cv1s})^2 + (-\frac{P_{cv1s}}{{RT_{cv1s}}^2}\delta T_{cv1s})^2}$$

$$\delta\rho_{cv1} = \frac{1}{R}\sqrt{(\frac{1}{T_{cv1s}}\delta P_{cv1s})^2 + (-\frac{P_{cv1s}}{{T_{cv1s}}^2}\delta T_{cv1s})^2}$$

Uncertainty of $N_{c,cor}$ (dependent on N_{act}, T_{1s})

$$N_{c,cor} = N_{act}\sqrt{\frac{T_{ref}}{T_{1t}}}$$

$$\delta N_{c,cor} = \sqrt{(\frac{\partial N_{c,cor}}{\partial N_{act}}\delta N_{act})^2 + (\frac{\partial N_{c,cor}}{\partial T_{1t}}\delta T_{1t})^2}$$

$$\delta N_{c,cor} = \sqrt{(\sqrt{\frac{T_{ref}}{T_{1t}}}\delta N_{act})^2 + (-\frac{N_{act}T_{ref}}{2{T_{1t}}^2\sqrt{\frac{T_{ref}}{T_{1t}}}})\delta T_{1t})^2}$$

Appendix B - Turbine uncertainty formulas

Uncertainty of $c_{p_{t,3}}$ (dependent on $R, \gamma_{t,3}$)

$$c_{p_{t,3}} = R\frac{\gamma_{t,3}}{\gamma_{t,3}-1}$$

$$\delta c_{p_{t,3}} = \sqrt{(\frac{\partial c_{p_{t,3}}}{\partial R}\delta R)^2 + (\frac{\partial c_{p_{t,3}}}{\partial \gamma_{t,3}}\delta\gamma_{t,3})^2}$$

$$\delta c_{p_{t,3}} = \sqrt{(\frac{\gamma_{t,3}}{\gamma_{t,3}-1})\delta R)^2 + ((\left(\frac{R}{\gamma_{t,3}-1}\right) - \frac{(\gamma_{t,3}R)}{\left(\gamma_{t,3}-1\right)^2})\delta\gamma_{t,3})^2}$$

Uncertainty of $c_{p_{t,4}}$ (dependent on $R, \gamma_{t,4}$)

$$c_{p_{t,4}} = R\frac{\gamma_{t,4}}{\gamma_{t,4}-1}$$

$$\delta c_{p_{t,4}} = \sqrt{(\frac{\partial c_{p_{t,4}}}{\partial R}\delta R)^2 + (\frac{\partial c_{p_{t,4}}}{\partial \gamma_{t,4}}\delta\gamma_{t,4})^2}$$

$$\delta c_{p_{t,4}} = \sqrt{(\frac{\gamma_{t,4}}{\gamma_{t,4}-1})\delta R)^2 + ((\left(\frac{R}{\gamma_{t,4}-1}\right) - \frac{(\gamma_{t,4}R)}{\left(\gamma_{t,4}-1\right)^2})\delta\gamma_{t,4})^2}$$

Uncertainty of $c_{p_{t,avg}}$ (dependent on $c_{p_{t,3}}, c_{p_{t,4}}$)

$$c_{p_{t,avg}} = \frac{(c_{p_{t,3}} + c_{p_{t,4}})}{2}$$

$$\delta c_{p_{t,avg}} = \sqrt{(\frac{\partial c_{p_{t,avg}}}{\partial c_{p_{t,3}}}\delta c_{p_{t,3}})^2 + (\frac{\partial c_{p_{t,avg}}}{\partial c_{p_{t,4}}}\delta c_{p_{t,4}})^2}$$

$$\delta c_{p_{t,avg}} = \sqrt{[\frac{1}{2}\delta c_{p_{t,3}}]^2 + [\frac{1}{2}\delta c_{p_{t,4}}]^2}$$

Uncertainty of $\gamma_{t,3}$ (dependent on T_{3s})

$$\gamma_{t,3} = 1.42592 - 8.03974(10^{-5})T_{3s}$$

$$\delta\gamma_{t,3} = -8.03974(10^{-5})$$

Uncertainty of $\gamma_{t,4}$ (dependent on T_{4s})

$$\gamma_{t,4} = 1.42592 - 8.03974(10^{-5})T_{4s}$$

$$\delta\gamma_{t,4} = -8.03974(10^{-5})$$

Uncertainty of $\gamma_{t,avg}$ (dependent on $\gamma_{t,3}, \gamma_{t,4}$)

$$\gamma_{t,avg} = \frac{\gamma_{t,3} + \gamma_{t,4}}{2},$$

$$\delta\gamma_{t,avg} = \sqrt{[\frac{1}{2}\delta\gamma_{t,3}]^2 + [\frac{1}{2}\delta\gamma_{t,4}]^2}$$

Uncertainty of ρ_3 (dependent on P_{3s}, T_{3s})

$$\rho_3 = \frac{P_{3s}}{RT_{3s}}$$

$$\delta\rho_3 = \sqrt{(\frac{\partial\rho_3}{\partial P_{3s}}\delta P_{3s})^2 + (\frac{\partial\rho_3}{\partial T_{3s}}\delta T_{3s})^2}$$

$$\delta\rho_3 = \sqrt{(\frac{1}{RT_{3s}}\delta P_{3s})^2 + (-\frac{P_{3s}}{{RT_{3s}}^2}\delta T_{3s})^2}$$

$$\delta\rho_3 = \frac{1}{R}\sqrt{(\frac{1}{T_{3s}}\delta P_{3s})^2 + (-\frac{P_{3s}}{{T_{3s}}^2}\delta T_{3s})^2}$$

Uncertainty of V_3 (dependent on $\dot{m}_t$, T_{3s}, P_{3s})

$$V_3 = \frac{\dot{m}_t}{q_3 A_1} = \frac{\dot{m}_t R T_{3s}}{P_{3s} A_1}$$

$$\delta V_3 = \sqrt{(\frac{\partial V_3}{\partial\dot{m}_t}\delta\dot{m}_t)^2 + (\frac{\partial V_3}{\partial T_{3s}}\delta T_{3s})^2 + (\frac{\partial V_3}{\partial P_{3s}}\delta P_{3s})^2}$$

$$\delta V_3 = \sqrt{(\frac{RT_{3s}}{P_{3s}A_1}\delta\dot{m}_t)^2 + (\frac{\dot{m}_t R}{P_{3s}A_1}\delta T_{3s})^2 + (-\frac{\dot{m}_t RT_{3s}}{{P_{3s}}^2 A_3}\delta P_{3s})^2}$$

$$\delta V_3 = \frac{R}{A_1}\sqrt{(\frac{T_{3s}}{P_{3s}}\delta\dot{m}_t)^2 + (\frac{\dot{m}_t}{P_{3s}}\delta T_{3s})^2 + (-\frac{\dot{m}_t T_{3s}}{{P_{3s}}^2}\delta P_{3s})^2}$$

Uncertainty of T_{3t} (dependent on T_{3s}, V_3, $c_{p_{t,3}}$)

$$T_{3t} = T_{3s} + \frac{{V_3}^2}{2c_{p_{t,3}}}$$

$$\delta T_{3t} = \sqrt{(\frac{\partial T_{3t}}{\partial T_{3s}}\delta T_{3s})^2 + (\frac{\partial T_{3t}}{\partial V_3}\delta V_3)^2 + (\frac{\partial T_{3t}}{\partial c_{p_{t,3}}}\delta c_{p_{t,3}})^2}$$

$$\delta T_{3t} = \sqrt{{\delta T_{3s}}^2 + [(\frac{V_3}{c_{p_{t,3}}})\delta V_3)]^2 + [\left(-\frac{{V_3}^2}{2{c_{p_{t,3}}}^2}\right)\delta c_{p_{t,3}}]^2}$$

Uncertainty of P_{3t} (dependent on $P_{3s}, T_{3t}, T_{3s}, \gamma_{t,3}$)

$$P_{3t} = P_{3s}(\frac{T_{3t}}{T_{3s}})^{\left(\frac{\gamma_{t,3}}{\gamma_{t,3}-1}\right)} = P_{3s}{T_{3t}}^{\left(\frac{\gamma_{t,3}}{\gamma_{t,3}-1}\right)}{T_{3s}}^{-(\frac{\gamma_{t,3}}{\gamma_{t,3}-1})}$$

$$\delta P_{3t} = \sqrt{(\frac{\partial P_{3t}}{\partial P_{3s}}\delta P_{3s})^2 + (\frac{\partial P_{3t}}{\partial T_{3t}}\delta T_{3t})^2 + (\frac{\partial P_{3t}}{\partial T_{3s}}\delta T_{3s})^2 + (\frac{\partial P_{3t}}{\partial\gamma_{t,3}}\delta\gamma_{t,3})^2}$$

$$\frac{\partial P_{3t}}{\partial P_{3s}} = (\frac{T_{3t}}{T_{3s}})^{(\frac{\gamma_{t,3}}{\gamma_{t,3}-1})}$$

$$\frac{\partial P_{3t}}{\partial T_{3t}} = \frac{P_{3s}\gamma_{t,3}\frac{T_{3t}}{T_{3s}}^{((\frac{\gamma_{t,3}}{\gamma_{t,3}-1})-1)}}{(\gamma_{t,3}-1)T_{3s}}$$

$$\frac{\partial P_{3t}}{\partial T_{3s}} = -\frac{\gamma_{t,3}P_{3s}T_{3t}\frac{T_{3t}}{T_{3s}}^{((\frac{\gamma_{t,3}}{\gamma_{t,3}-1})-1)}}{{T_{3s}}^2(\gamma_{t,3}-1)}$$

$$\frac{\partial P_{3t}}{\partial \gamma_{t,3}} = P_{3s}\ln(\frac{T_{3t}}{T_{3s}})(\frac{1}{\gamma_{t,3}-1} - \frac{\gamma_{t,3}}{(\gamma_{t,3}-1)^2})(\frac{T_{3t}}{T_{3s}})^{(\frac{\gamma_{t,3}}{\gamma_{t,3}-1})}$$

Uncertainty of PR_t (dependent on $P_{3t}, P_{4s},$)

$$PR_t = (\frac{P_{3t}}{P_{4s}})$$

$$\delta PR_t = \sqrt{(\frac{\partial PR_t}{\partial P_{3t}}\delta P_{3t})^2 + (\frac{\partial PR_t}{\partial P_{4s}}\delta P_{4s})^2}$$

$$\delta PR_t = \sqrt{(\frac{1}{P_{4s}}\delta P_{3t})^2 + (-\frac{P_{3t}}{P_{4s}^2}\delta P_{4s})^2}$$

Uncertainty of P_c (dependent on $\dot{m}_c$, ${c_p}_{c,avg}$, T_{2t}, T_{1t})

$$P_c = \dot{m}_c {c_p}_{c,avg}(T_{2t} - T_{1t})$$

$$\delta P_c = \sqrt{(\frac{\partial P_c}{\partial \dot{m}_c}\delta \dot{m}_c)^2 + (\frac{\partial P_c}{\partial {c_p}_{c,avg}}\delta {c_p}_{c,avg})^2 + (\frac{\partial P_c}{\partial T_{2t}}\delta T_{2t})^2 + (\frac{\partial P_c}{\partial T_{1t}}\delta T_{1t})^2}$$

$$\delta \dot{m}_c = -{c_p}_{c,avg}(T_{1t} - T_{2t})$$

$$\delta {c_p}_{c,avg} = -\dot{m}_c(T_{1t} - T_{2t})$$

$$\delta T_{2t} = {c_p}_{c,avg}\dot{m}_c$$

$$\delta T_{1t} = -{c_p}_{c,avg}\dot{m}_c$$

Uncertainty of η_t (dependent on $P_c, \dot{m}_t, {c_p}_{t,avg}, T_{3t,} PR_t, \gamma_{t,avg}$)

$$\eta_t = \frac{P_c}{\eta_{mech}\dot{m}_t {c_p}_{t,avg} T_{3t}[1-(\frac{1}{PR_t})^{(\frac{\gamma_{t,avg}-1}{\gamma_{t,avg}})}]}$$

where: $\eta_{mech} = 0.95$

$$\delta\eta_t = \sqrt{\begin{matrix}\left(\frac{\partial\eta_t}{\partial P_c}\delta P_c\right)^2 + \left(\frac{\partial\eta_c}{\partial\dot{m}_t}\delta\dot{m}_t\right)^2 + \left(\frac{\partial\eta_c}{\partial c_{p_{t,avg}}}\delta c_{p_{t,avg}}\right)^2 \\ + \left(\frac{\partial\eta_c}{\partial T_{3t}}\delta T_{3t}\right)^2 + \left(\frac{\partial\eta_c}{\partial PR_T}\delta PR_T\right)^2 + (\frac{\partial\eta_c}{\partial\gamma_{t,avg}}\delta\gamma_{t,avg})^2\end{matrix}}$$

$$\frac{\partial\eta_t}{\partial P_c} = -\frac{1}{c_{p_{t,avg}}\dot{m}_t\eta_{mech}T_{3t}[(\frac{1}{PR_t})^{\left(\frac{\gamma_{t,avg}-1}{\gamma_{t,avg}}\right)} - 1]}$$

$$\frac{\partial\eta_t}{\partial\dot{m}_t} = \frac{P_c}{c_{p_{t,avg}}\dot{m}_t{}^2\eta_{mech}T_{3t}[(\frac{1}{PR_t})^{\left(\frac{\gamma_{t,avg}-1}{\gamma_{t,avg}}\right)} - 1]}$$

$$\frac{\partial\eta_t}{\partial c_{p_{t,avg}}} = \frac{P_c}{c_{p_{t,avg}}{}^2\dot{m}_t\eta_{mech}T_{3t}[(\frac{1}{PR_t})^{\left(\frac{\gamma_{t,avg}-1}{\gamma_{t,avg}}\right)} - 1]}$$

$$\frac{\partial\eta_t}{\partial T_{3t}} = \frac{P_c}{c_{p_{t,avg}}\dot{m}_t\eta_{mech}T_{3t}{}^2[(\frac{1}{PR_t})^{\left(\frac{\gamma_{t,avg}-1}{\gamma_{t,avg}}\right)} - 1]}$$

$$\frac{\partial\eta_t}{\partial PR_t} = -\frac{P_c(\gamma_{t,avg}-1)(\frac{1}{PR_t})^{\left(\frac{\gamma_{t,avg}-1}{\gamma_{t,avg}}\right)-1}}{c_{p_{t,avg}}\gamma_{t,avg}\dot{m}_t\eta_{mech}PR_t{}^2T_{3t}[(\frac{1}{PR_t})^{\left(\frac{\gamma_{t,avg}-1}{\gamma_{t,avg}}\right)} - 1]^2}$$

$$\frac{\partial\eta_t}{\partial\gamma_{t,avg}} = \frac{P_c ln\left(\frac{1}{PR_t}\right)\left(\frac{1}{\gamma_{t,avg}} - \frac{\gamma_{t,avg}-1}{\gamma_{t,avg}{}^2}\right)\left(\frac{1}{PR_t}\right)^{(\frac{\gamma_{t,avg}-1}{\gamma_{t,avg}})}}{c_{p_{t,avg}}\dot{m}_t\eta_{mech}T_{3t}[(\frac{1}{PR_t})^{\left(\frac{\gamma_{t,avg}-1}{\gamma_{t,avg}}\right)} - 1]^2}$$

Uncertainty of $\dot{Q}_t$ (dependent on Y_{tv3}, ΔP_{tv3}, ρ_{tv3}) – flow through turbine V-cone 3

$$\dot{Q}_t = F_a C_d Y_{tv3} k_3 \sqrt{\frac{\Delta P_{tv3}}{\rho_{tv3}}}$$

$$\delta\dot{Q}_t = \sqrt{(\frac{\partial\dot{Q}_t}{\partial Y_{tv3}}\delta Y_{tv3})^2 + (\frac{\partial\dot{Q}_t}{\partial\Delta P_{tv3}}\delta\Delta P_{tv3})^2 + (\frac{\partial\dot{Q}_t}{\partial\rho_{tv3}}\delta\rho_{tv3})^2}$$

$$\frac{\partial\dot{Q}_t}{\partial Y_{tv3}} = F_a C_d k_3 \sqrt{\frac{\Delta P_{tv3}}{\rho_{tv3}}}$$

$$\frac{\partial\dot{Q}_t}{\partial\Delta P_{tv3}} = \frac{F_a C_d Y_{tv3} k_3}{2\rho_{tv3}\sqrt{(\frac{\Delta P_{tv3}}{\rho_{tv3}})}}$$

$$\frac{\partial \dot{Q}_t}{\partial \rho_{tv3}} = -\frac{C_d \Delta P_{tv3} F_a k_1 Y_{tv3}}{2{\rho_{tv3}}^2 \sqrt{(\frac{\Delta P_{tv3}}{\rho_{tv3}})}}$$

Uncertainty of Y_{tv3} (dependent on ΔP_{tv3}, P_{tv3s})

$$Y_{tv3} = 1 - (0.649 + 0.696\beta^4)\frac{\Delta P_{tv3}}{k_{tv3} P_{tv3s}}$$

$$\delta Y_{tv3} = \sqrt{(\frac{\partial Y_{tv3}}{\partial \Delta P_{tv3}}\delta \Delta P_{tv3})^2 + (\frac{\partial Y_{tv3}}{\partial P_{tv3s}}\delta P_{tv3s})^2 + (\frac{\partial Y_{tv3}}{\partial k_{tv3}}\delta k_{tv3})^2}$$

$$\frac{\partial Y_{tv3}}{\partial \Delta P_{tv3}} = -(0.649 + 0.696\beta^4)\frac{1}{k P_{tv3s}}$$

$$\frac{\partial Y_{tv3}}{\partial P_{tv3s}} = -(0.649 + 0.696\beta^4) * \left(-\frac{\Delta P_{tv3}}{k_{tv3}{P_{tv3s}}^2}\right)$$

Uncertainty of $\dot{m}_t$ (dependent on $\dot{Q}_t$, ρ_{tv3})

$$\dot{m}_t = \dot{Q}_t \rho_{tv3}$$

$$\delta \dot{m}_t = \sqrt{(\frac{\partial \dot{m}_t}{\partial \dot{Q}_t}\delta \dot{Q}_t)^2 + (\frac{\partial \dot{m}_t}{\partial \rho_{tv3}}\delta \rho_{tv3})^2}$$

$$\delta \dot{m}_t = \sqrt{(\rho_{tv3}\delta \dot{Q}_t)^2 + (\dot{Q}_t \delta \rho_{tv3})^2}$$

Uncertainty of $\dot{m}_{t,cor}$ (dependent on $\dot{m}_t$, T_{3t}, P_{3t})

$$\dot{m}_{t,cor} = \dot{m}_t \frac{\sqrt{\frac{T_{3t}}{T_{ref}}}}{\frac{P_{3t}}{P_{ref}}}$$

$$\delta \dot{m}_{t,cor} = \sqrt{(\frac{\partial \dot{m}_{t,cor}}{\partial \dot{m}_t}\delta \dot{m}_t)^2 + (\frac{\partial \dot{m}_{t,cor}}{\partial T_{3t}}\delta T_{3t})^2 + (\frac{\partial \dot{m}_{t,cor}}{\partial P_{3t}}\delta P_{3t})^2}$$

$$\delta \dot{m}_{t,cor} = \sqrt{(\sqrt{\frac{T_{3t}}{T_{ref}}}\frac{P_{ref}}{P_{3t}}\delta \dot{m}_t)^2 + (-\frac{\dot{m}_t P_{ref}}{2P_{3t}T_{ref}\sqrt{\frac{T_{ref}}{T_{3t}}}}\delta T_{3t})^2 + (\dot{m}_t \sqrt{\frac{T_{3t}}{T_{ref}}}(-\frac{P_{ref}}{{P_{3t}}^2})\delta P_{3t})^2}$$

Uncertainty of ρ_{tv1} (dependent on P_{tv3s}, T_{tv3s})

$$\rho_{tv3} = \frac{P_{tv3s}}{R T_{tv3s}}$$

$$\delta \rho_{tv3} = \sqrt{(\frac{\partial \rho_{tv3}}{\partial P_{tv3s}}\delta P_{tv3s})^2 + (\frac{\partial \rho_{tv3}}{\partial T_{tv3s}}\delta T_{tv3s})^2}$$

$$\delta\rho_{tv3} = \sqrt{(\frac{1}{RT_{tv3s}}\delta P_{tv3s})^2 + (-\frac{P_{tv3s}}{RT_{tv3s}^{\ 2}}\delta T_{tv3s})^2}$$

$$\delta\rho_{tv3} = \frac{1}{R}\sqrt{(\frac{1}{T_{tv3s}}\delta P_{tv3s})^2 + (-\frac{P_{tv3s}}{T_{tv3s}^{\ 2}}\delta T_{tv3s})^2}$$

Uncertainty of $N_{t,cor}$ (dependent on N_{act}, T_{3t})

$$N_{t,cor} = N_{act}\sqrt{\frac{T_{ref}}{T_{3t}}}$$

$$\delta N_{t,cor} = \sqrt{(\frac{\partial N_{t,cor}}{\partial N_{act}}\delta N_{act})^2 + (\frac{\partial N_{t,cor}}{\partial T_{3t}}\delta T_{3t})^2}$$

$$\delta N_{t,cor} = \sqrt{(\sqrt{\frac{T_{ref}}{T_{3t}}}\delta N_{act})^2 + (-\frac{N_{act}T_{ref}}{2T_{3t}^{\ 2}\sqrt{\frac{T_{ref}}{T_{3t}}}})\delta T_{3t})^2}$$

Appendix C – Fox Compressor FFT plots

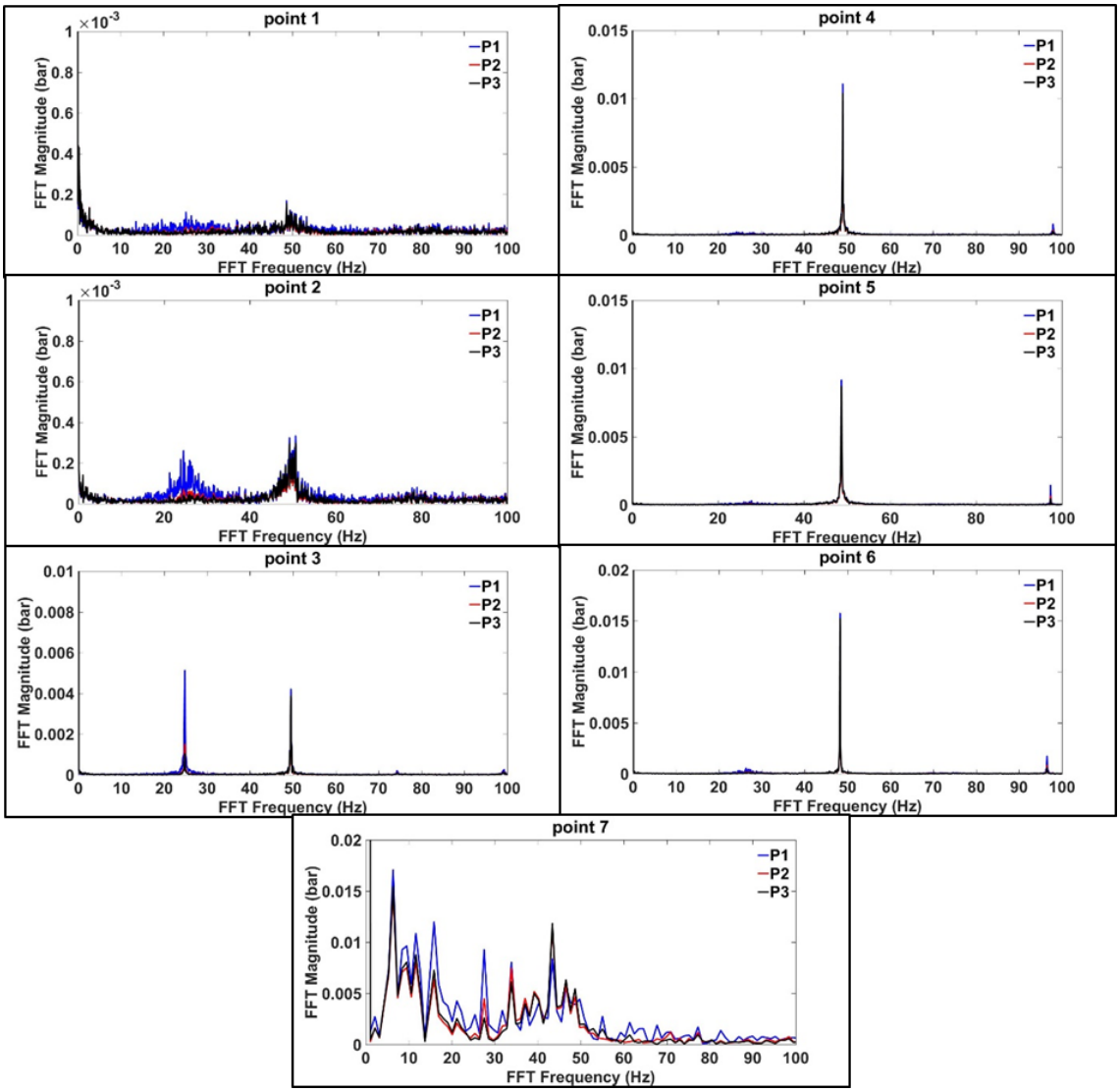

Figure 9-1. Inlet pressure based FFT plots of operating points at 194 krpm

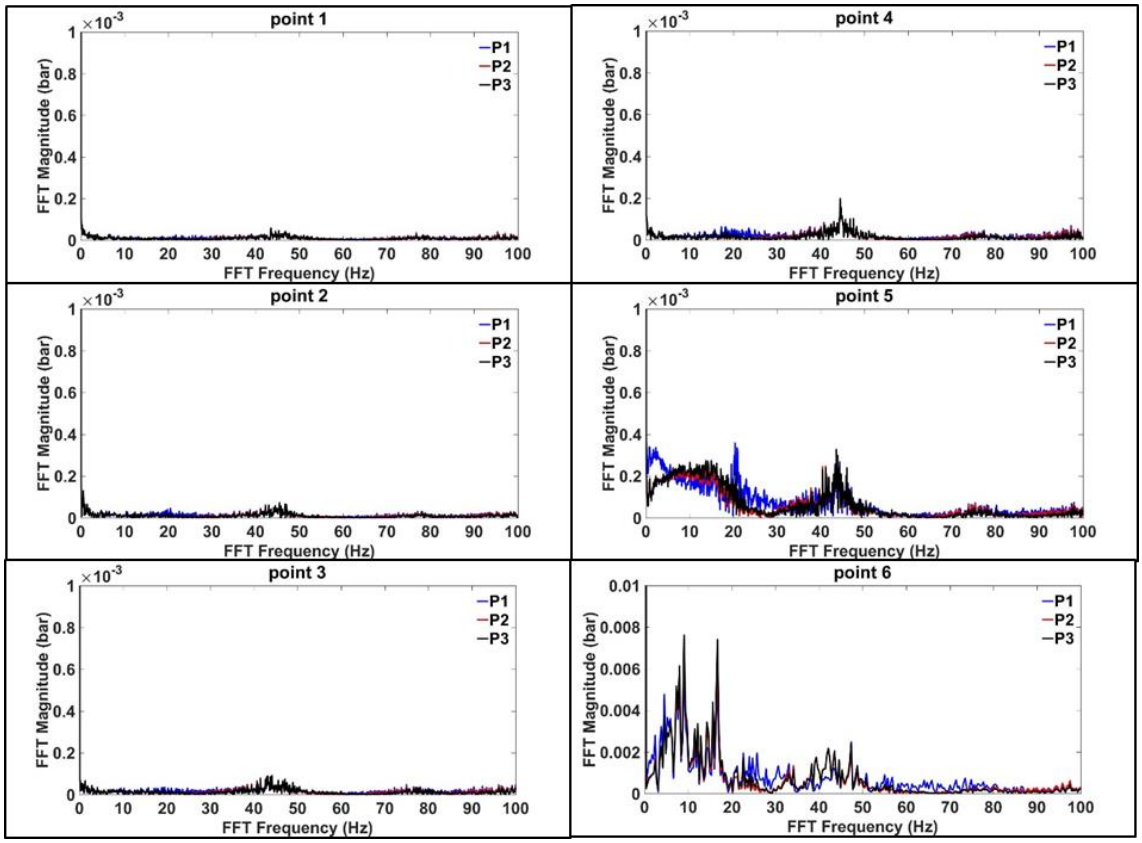

Figure 9-2. Inlet pressure based FFT plots of operating points at 158 krpm

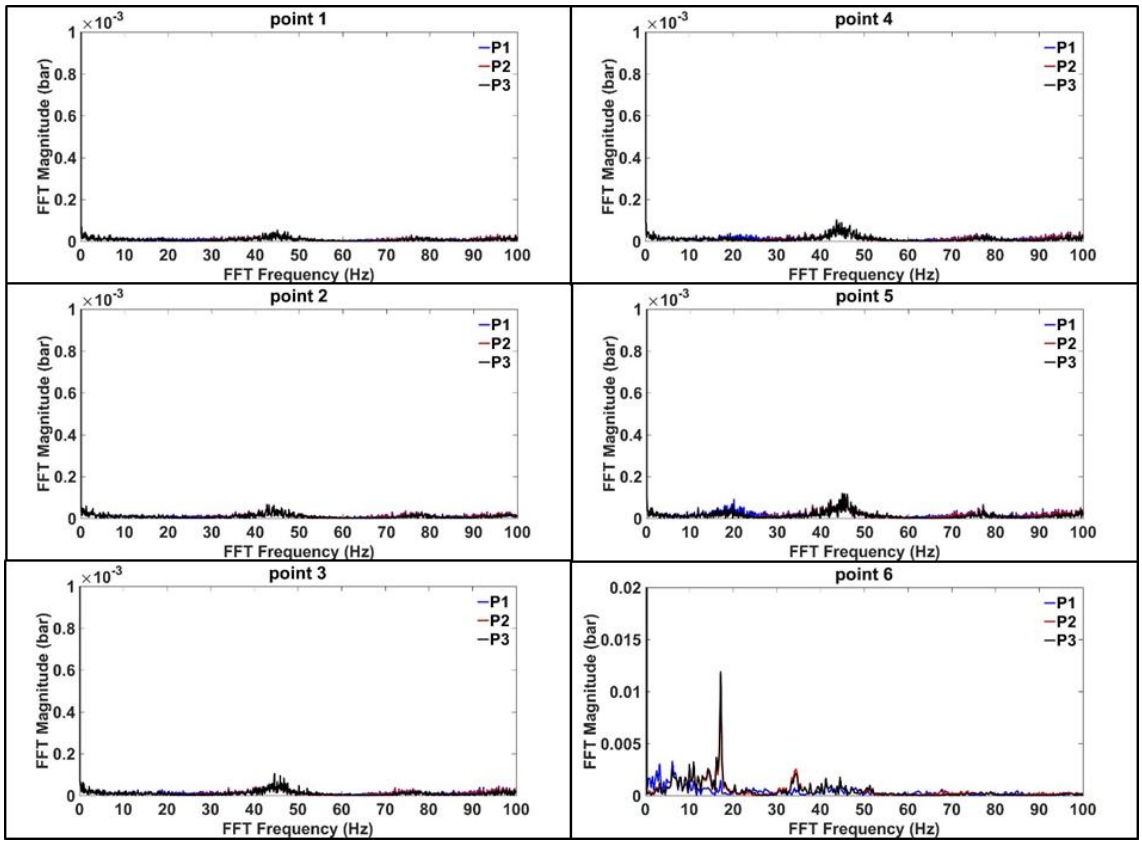

Figure 9-3. Inlet pressure based FFT plots of operating points at 139 krpm

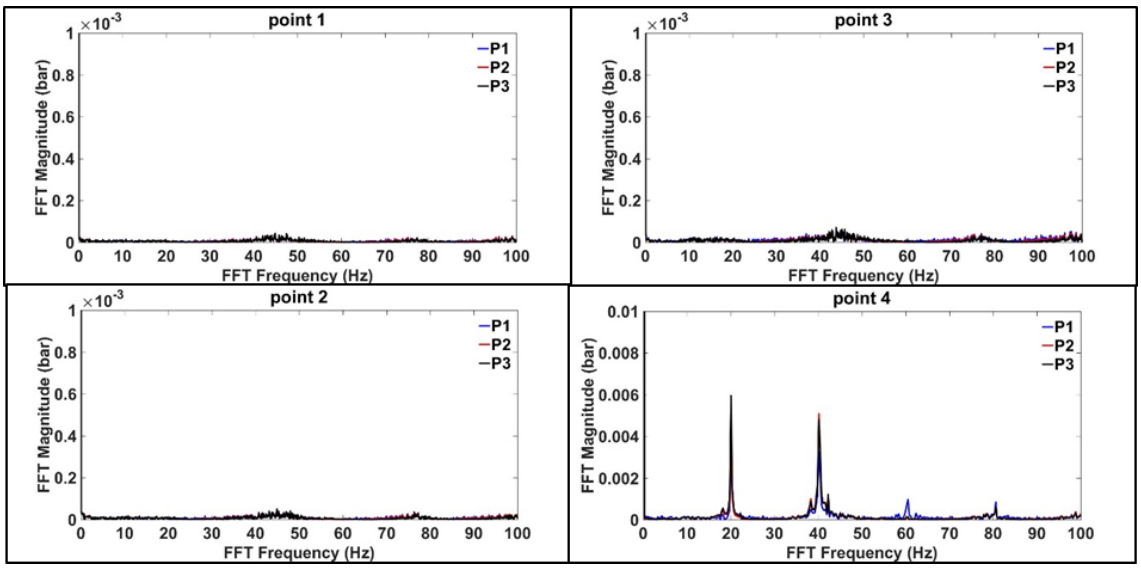

Figure 9-4. Inlet pressure based FFT plots of operating points at 88 krpm

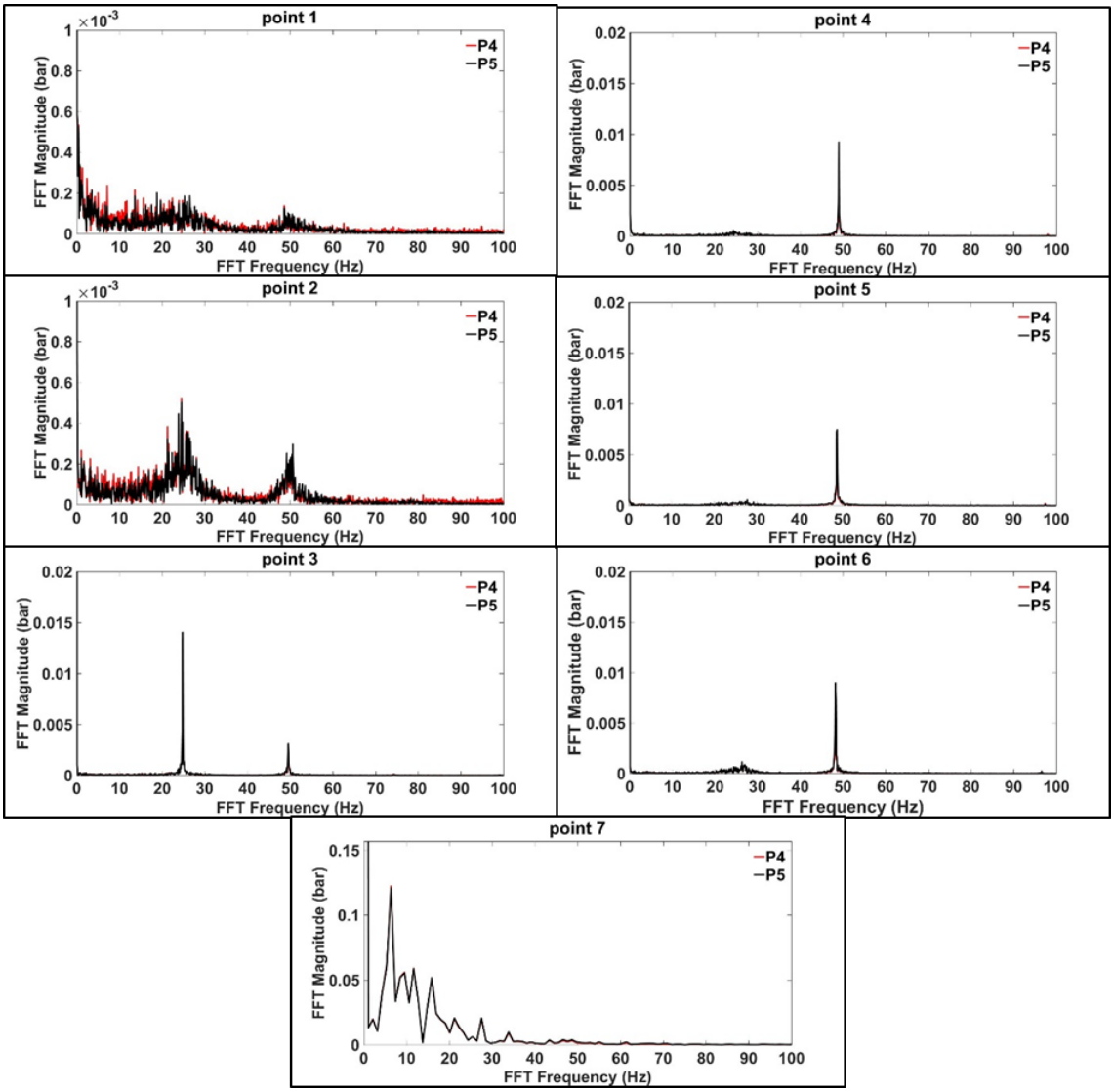

Figure 9-5. Post compressor pressure based FFT plots of operating points at 194 krpm

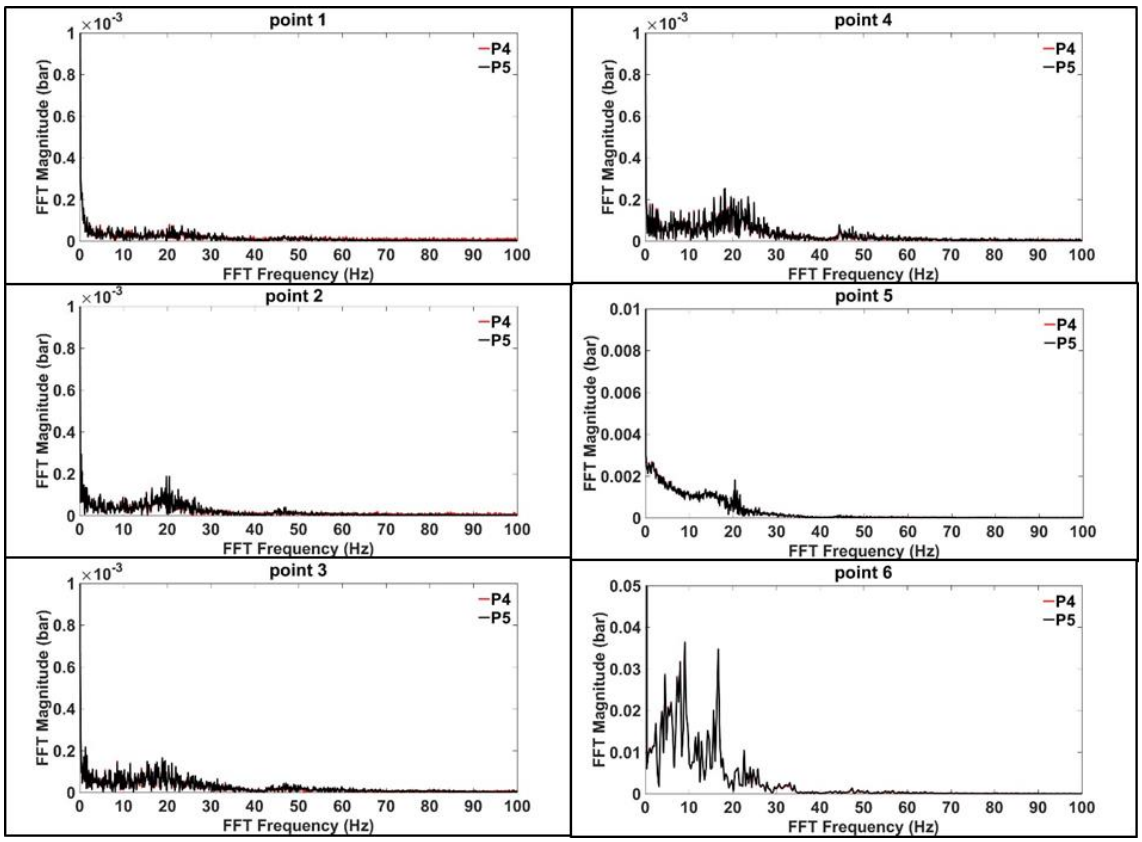

Figure 9-6. Post compressor pressure based FFT plots of operating points at 158 krpm

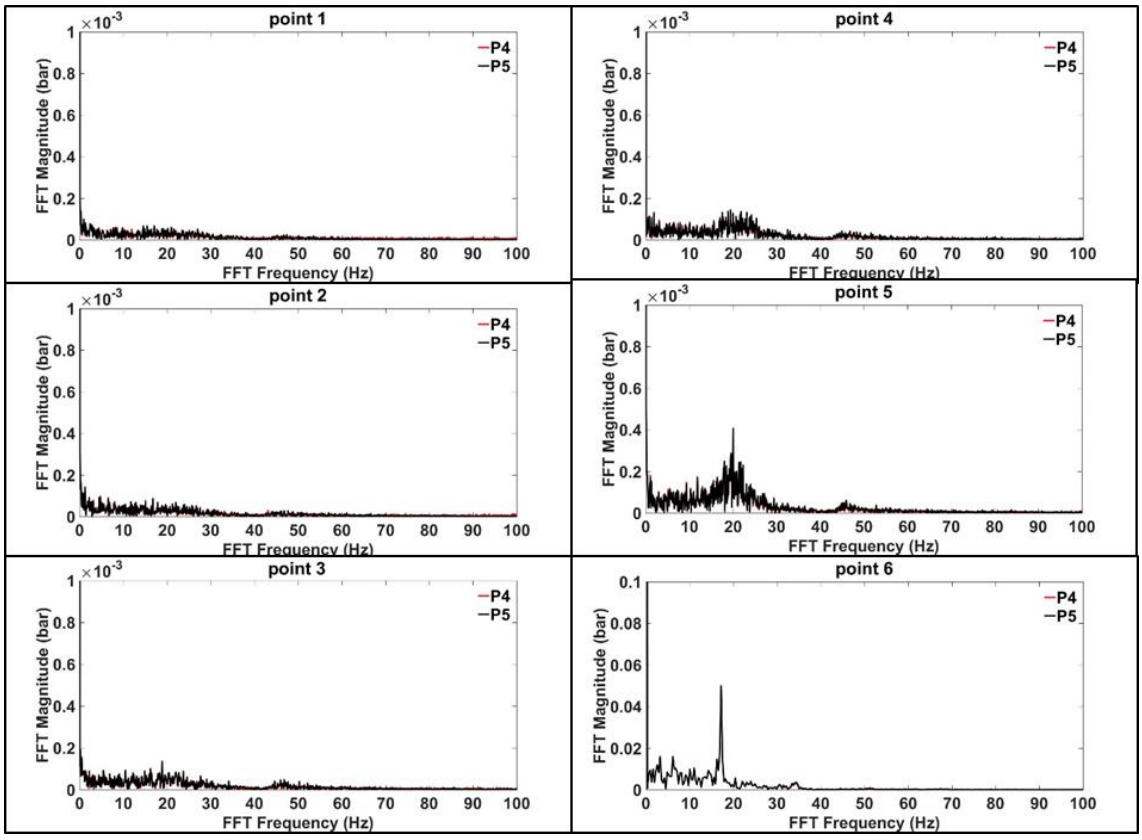

Figure 9-7. Post compressor pressure based FFT plots of operating points at 139 krpm

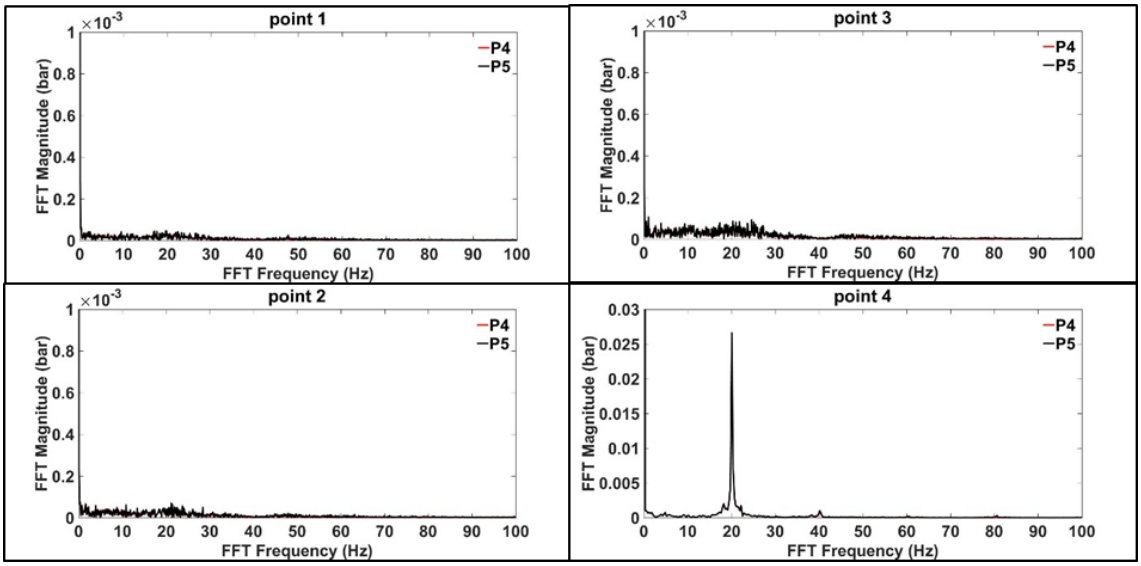

Figure 9-8. Post compressor pressure based FFT plots of operating points at 88 krpm

Appendix D – Puma Compressor FFT plots

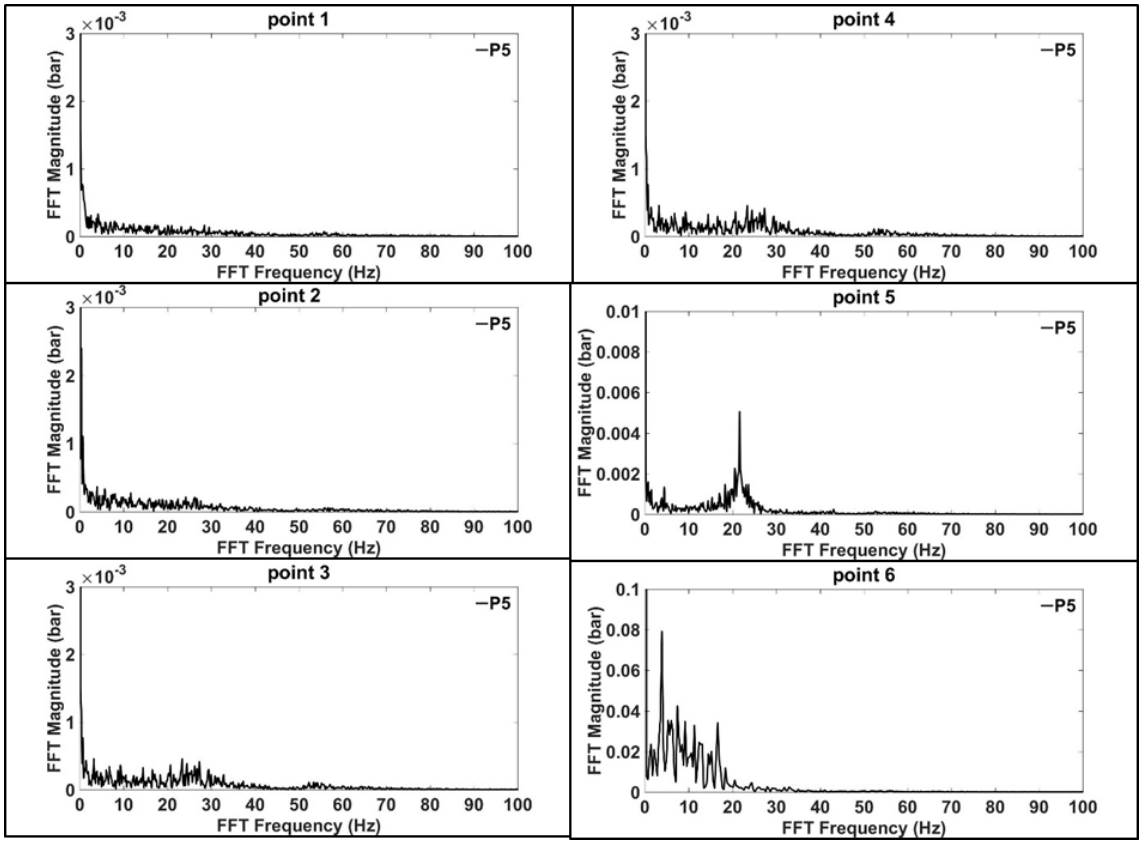

Figure 9-9. Post-compressor pressure based FFT plots of operating points at 170 krpm

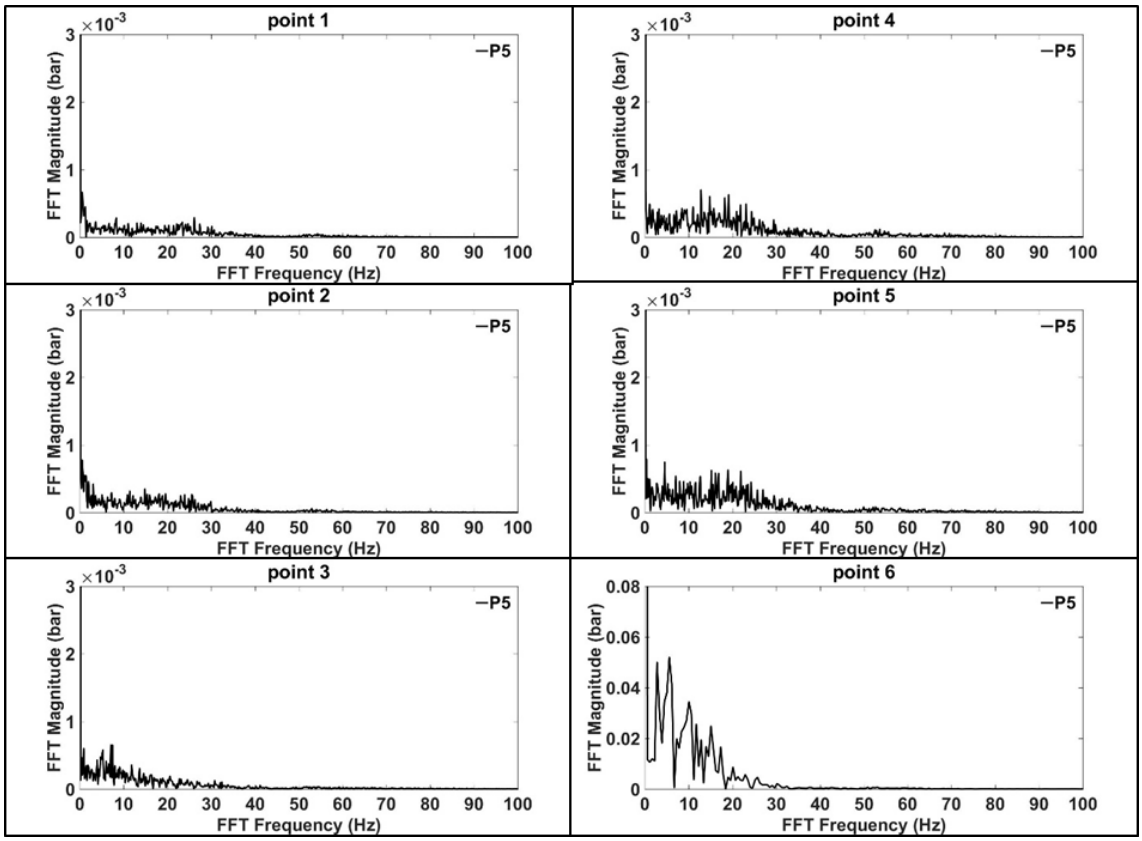

Figure 9-10. Post-compressor pressure based FFT plots of operating points at 150 krpm

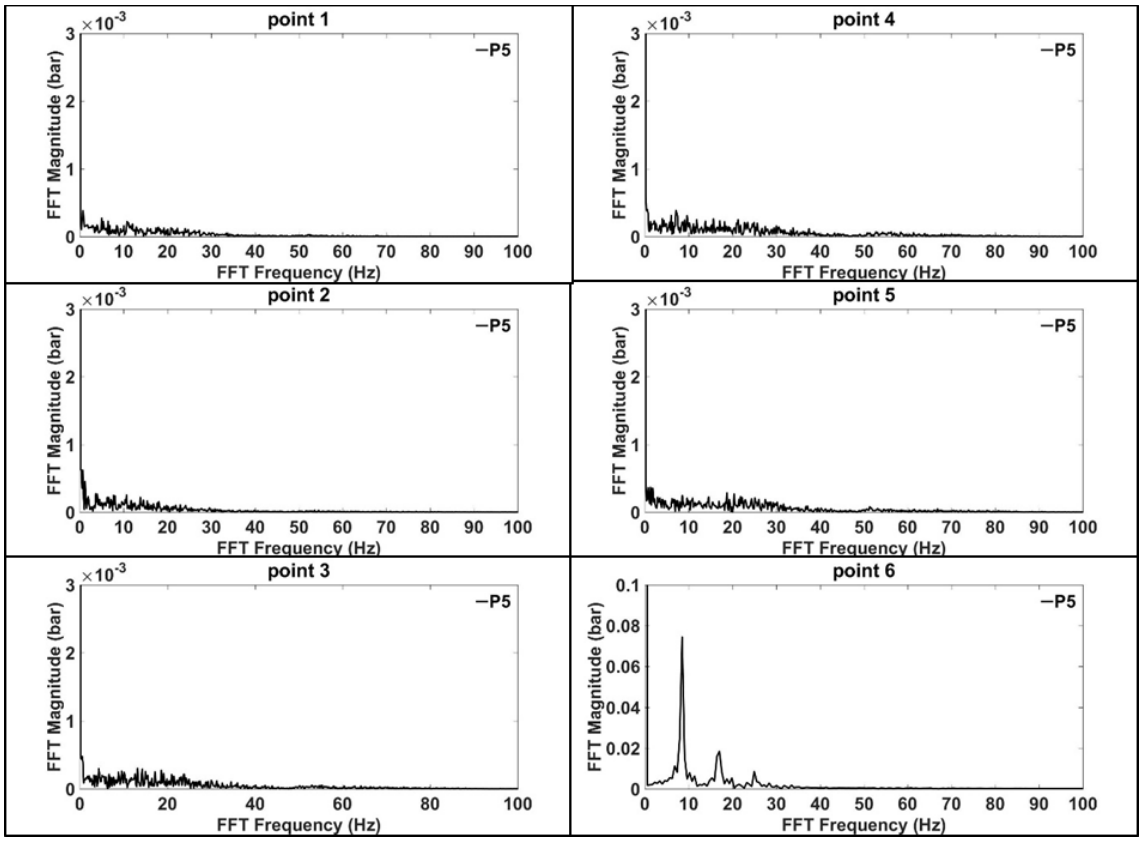

Figure 9-11. Post-compressor pressure based FFT plots of operating points at 130 krpm

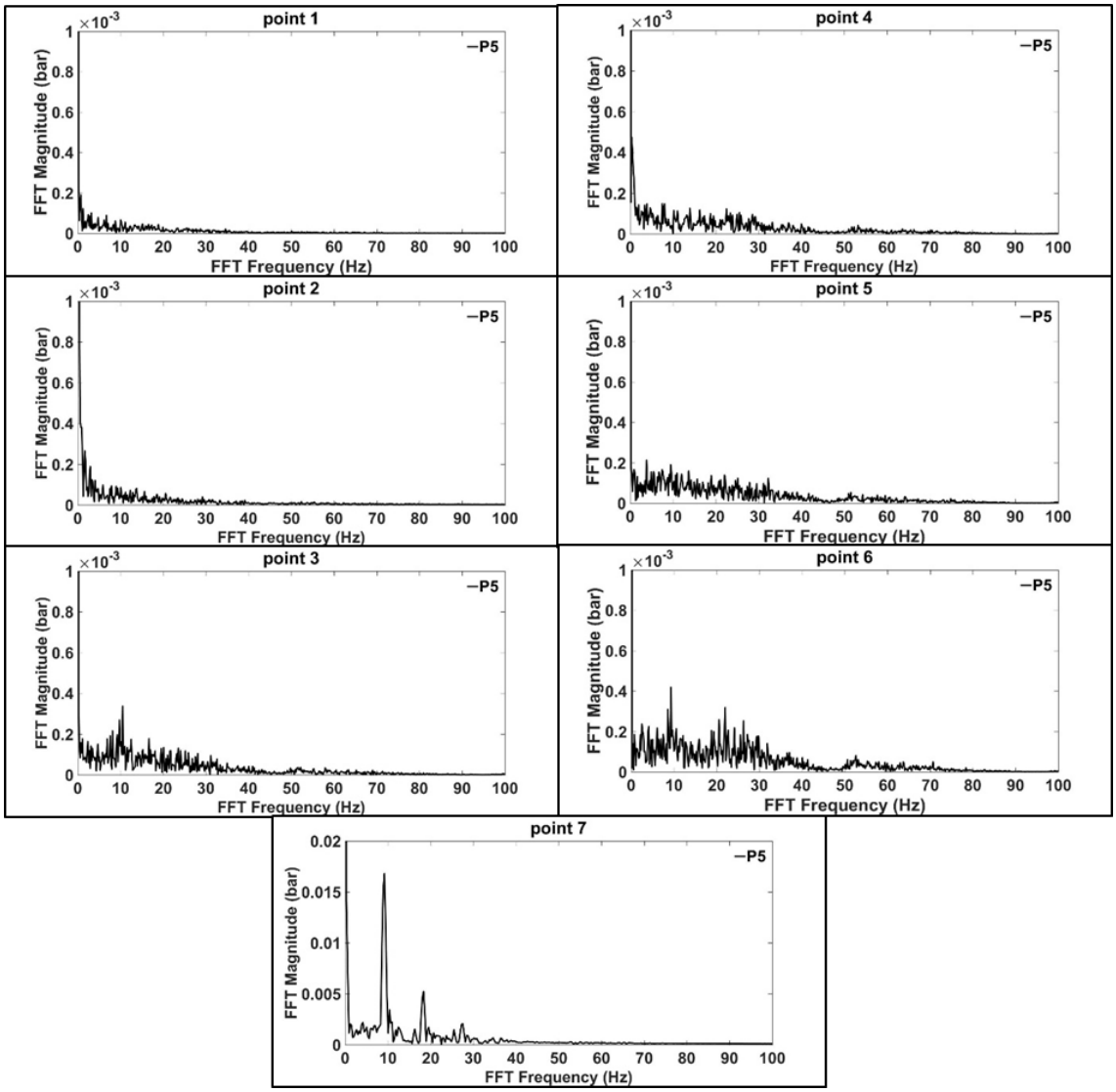

Figure 9-12. Post-compressor pressure based FFT plots of operating points at 90 krpm